The Validation and Application of CFD-generated Aircraft Carrier Airwakes for Flight Simulation

Thesis submitted in accordance with the requirements of the University of Liverpool for the degree of

Doctor of Philosophy

By

Neale Alexander Watson

School of Engineering

University of Liverpool

United Kingdom

January 2021

The Validation and Application of CFD-generated Aircraft Carrier Airwakes for Flight Simulation

Abstract

This thesis describes an extensive experimental and computational study of the air flow over the UK Royal Navy's Queen Elizabeth Class (QEC) aircraft carriers, including how the air flow will affect aircraft flying operations, particularly rotorcraft. Maritime fixed- and rotary-wing aircraft routinely perform launch and recovery manoeuvres to and from ships at sea, often in challenging environmental conditions. Pilots performing such manoeuvres must contend with ship motion, sea spray, and an unsteady airwake generated by the air flow shedding off the ship’s superstructure. The main aim of the research was to investigate the use of modelling and simulation to improve understanding of the flying environment over the flight deck of the QEC.

The unsteady air flow over the QEC was created using Computational Fluid Dynamics (CFD) and incorporated into flight simulators at the University of Liverpool (UoL) and at BAE Systems, Warton. Experimental data to confirm the validity of the computed air flow was obtained from a small-scale experiment in which a 1.4 m long (1:200) scale model of the QEC was submerged in a water channel and Acoustic Doppler Velocimetry (ADV) was used to measure the unsteady flow around the ship. The results show generally very good agreement between the model-scale experiment and CFD.

Piloted flight simulation trials were conducted using the UoL’s HELIFLIGHT-R full-motion flight simulator in which a test pilot conducted simulated deck landings of a representative Sikorsky SH-60B Seahawk helicopter to the flight deck of the QEC under a range of wind conditions. Results for aircraft performance and pilot workload are presented. These trials demonstrated how flight simulation could be used to support flight trials and helicopter clearance activities, but also notes that real-world trials data are needed to compare with the simulations before the techniques can be beneficially deployed. A non-piloted simulation technique was also deployed in which the unsteady forces and moments imposed by the air flow onto the helicopter fuselage were quantified; the results were correlated with the pilot workload ratings from the piloted simulation trials. The results have demonstrated how modelling and simulation can be effectively used to inform real-world flight trials.

The simulations reaffirmed how important it is that helicopter flight models respond to the very different velocity components that are imposed on different parts of the aircraft by the highly unsteady three-dimensional air flow. Fixed-wing flight models, however, are not typically designed to capture the unsteady moments created during hover in a highly turbulent flow at low speeds. A new aerodynamic model of a fixed-wing aircraft has been developed which uses strip theory to create the overall forces and moments acting on the aircraft when hovering in a ship airwake. The results show the effect of the QEC airwakes on a hovering fixed-wing aircraft and provide recommendations for the number of strips required to accurately capture the effect of the flow.

Acknowledgements

I would like to thank my supervisors, Prof Mark White and Prof Ieuan Owen for their guidance, effort, support, and endless patience throughout the project. I am very grateful for their mentorship and kindness which has made this project thoroughly enjoyable. A special thanks goes to my industrial supervisor Dr Steve Hodge for his support, insight, and invaluable contributions to the research. I could not have asked for better supervisors.

The financial support from the Engineering and Physical Sciences Research Council through an Industrial CASE Award jointly funded with BAE Systems is acknowledged (REF: 1794920), as is the support from ANSYS U.K., Ltd.

Thanks to Michael Kelly for introducing me to CFD and to Wajih Memon for all his help with the flight simulator and trials. Thanks to Jamie Varney who helped code the ADV traverse. Thanks to everyone in the office for endless laughs and CFD chat; Sarah Scott, Rebecca Mateer, Jade Adams-White, Chris Dadswell, Matt Hudson, Nick Fernandez, Isaac Stephens, Josie Roscoe and Neil Cameron.

I would like to thank John Curran and the workshop staff for their perpetual production of experimental models, to Derek Neary for his efforts in keeping the flume running and also, to Maria White who was always there to help me out. The expert contributions of test pilots Andy Berryman and Charlie Brown are acknowledged, as is their skill in telling their remarkable stories.

I would like to thank all my friends and family, especially my parents, for their encouragement and support since before I can remember. The biggest thank you goes to my amazing wife for her limitless support, love, and encouragement.

Thank you all.

Research Outcomes

Journal Publications

- **Watson, N. A.**, Kelly, M. F., Owen, I., Hodge, S. J., and White, M. D., "Computational and experimental modelling study of the unsteady airflow over the aircraft carrier HMS Queen Elizabeth," *Ocean Engineering*, Vol. 172, No. 1, 2019, pp. 562-574. https://doi.org/10.1016/j.oceaneng.2018.12.024
- **Watson, N. A.**, Owen, I., and White, M. D., "Piloted Flight Simulation of Helicopter Recovery to the Queen Elizabeth Class Aircraft Carrier," *Journal of Aircraft*, Vol. 57, No. 4, 2020, pp. 742-760. https://doi.org/10.2514/1.C035733

Conference Proceedings

- Kelly, M. F., **Watson, N. A.**, Hodge, S. J., White, M. D. and Owen, I., "The Role of Modelling and Simulation in the Preparations for Flight Trials Aboard the Queen Elizabeth Class Aircraft Carriers," *14th International Naval Engineering Conference (INEC)*, Glasgow, UK, Institute of Marine Engineering Science & Technology, Oct. 2018. https://doi.org/10.24868/issn.2515-818x.2018.037
- **Watson, N. A.**, Kelly, M. F., Owen, I., Hodge, S. J. and White, M. D., "The Aerodynamic Effect Of An Oblique Wind On Helicopter Recovery To The Queen Elizabeth Class Aircraft Carrier," *Vertical Flight Society's 75th Annual Forum & Technology Display*, Philadelphia, USA, Vertical Flight Society, May 2019.
- **Watson, N. A.**, Owen, I. and White, M. D., "Experimental Validation of the Unsteady CFD-generated Airwake of the HMS Queen Elizabeth Aircraft Carrier*,"* *AIAA Aviation 2019 Forum*, Dallas, USA, AIAA, Jun. 2019. – **Best Applied Aerodynamics Student Paper** https://doi.org/10.2514/6.2019-3029
- **Watson, N. A.**, Owen, I. and White, M. D., "Modelling the Effect of Unsteady Turbulent Wakes on a Short Take-off and Vertical Landing (STOVL) Aircraft*,"* *AIAA Aviation 2019 Forum*, Dallas, USA, AIAA, Jun. 2019. https://doi.org/10.2514/6.2019-3244
- **Watson, N. A.**, Memon, W. A., Owen, I. and White, M. D., "Dynamic Interface Modelling and Simulation. Part 1: Preparation and Analysis for High-Fidelity Helicopter-

Ship Flight Simulations," *8th Asian/Australian Rotorcraft Forum*, Ankara, Turkey, Nov. 2019.

- Memon, W. A., **Watson, N. A.**, Owen, I. and White, M. D., "Dynamic Interface Modelling and Simulation. Part 2: Developing Robust Fidelity Requirements for Maritime Rotorcraft Flight Simulators," *8th Asian/Australian Rotorcraft Forum*, Ankara, Turkey, Nov. 2019.
- **Watson, N. A.,** Owen, I. and White, M. D., "The Effect of Atmospheric Turbulence on Helicopter Recovery to a Twin-Island Aircraft Carrier," *Vertical Flight Society's 77th Annual Forum & Technology Display*, West Palm Beach, USA, Vertical Flight Society, May 2021.

Presentations

- **Watson, N. A.**, "Initial validation of CFD generated airwakes using Acoustic Doppler Velocimetry," *UK Vertical Lift Network – 3rd Annual Technical Workshop*, Cheshire, UK, Vertical Lift Network (VLN), May 2017.
- **Watson, N. A.**, "Generating ship airwakes for piloted flight simulation," *Science and Technology Organization's STEM Early Career Professionals' Day*, Glasgow, UK, North Atlantic Treaty Organization (NATO), Sep. 2018.
- **Watson, N. A.**, "Modelling the Airflow over the HMS Queen Elizabeth for Flight Simulation in Support of Aircraft-Ship Integration," *International Powered Lift Conference*, Bristol, UK, Royal Aeronautical Society, Nov. 2018.
- **Watson, N. A.** and Memon, W. A., "Design and development of modelling and simulation tools to inform ship-helicopter dynamic interface research," *Royal Aeronautical Society Rotorcraft Simulation - Trends and Future Applications*, London, UK, Nov. 2019.
- **Watson, N. A.**, "Super-Computing HMS Queen Elizabeth's Airwake For F-35B Flight Simulation," *UK Parliament STEM For Britain Event*, London, UK, UK Parliamentary and Scientific Committee, Mar. 2020.
- **Watson, N. A.**, "The University of Liverpool's Role in Preparations for Flight Trials Aboard the Queen Elizabeth Class Aircraft Carriers," *HMS Prince of Wales UKNEST Event*, Liverpool, UK, United Kingdom Naval Engineering Science & Technology (UKNEST), Mar. 2020.

Awards

- **Air Europe and International Business Leaders Chairman's Award** by BAE Systems in the 'Innovating for Success' category for the University of Liverpool's collaboration with BAE Systems in supporting the preparation of F-35B's First of Class Flight Trials with HMS Queen Elizabeth through flight simulation and airwake analysis, Oct. 2018.
- **Executive Committee Chairman's Award** by BAE Systems for University of Liverpool's collaboration with BAE Systems in supporting the preparation of F-35B's First of Class Flight Trials with HMS Queen Elizabeth through flight simulation and airwake analysis, Feb. 2019.
- **Aerospace Speakers Travel Grant (AeSTG)** by Royal Aeronautical Society to their work entitled "The Aerodynamic Effect Of An Oblique Wind On Helicopter Recovery To The Queen Elizabeth Class Aircraft Carrier" at the Vertical Flight Society's 75th Annual Forum & Technology Display in Philadelphia, USA, Jun. 2019.
- **AIAA Applied Aerodynamics Best Student Paper** by American Institute of Aeronautics and Astronautics Applied Aerodynamics Technical Committee for the presented paper "Experimental Validation of the Unsteady CFD-generated Airwake of the HMS Queen Elizabeth" at the AIAA Aviation 2019 Forum in Dallas, USA, Oct. 2019.

Table of Contents

Notation

A	*area*	m^2
BL	*bottom reflection loss*	dB
c	*chord of aerodynamic surface*	m
c_d	*drag coefficient of incremental surface area*	
c_l	*lift coefficient of incremental surface area*	
c_r	*chord of surface at the root*	m
C	*Courant number*	
C_{DES}	*DES constant*	
$C_{l_{max}}$	*maximum lift coefficient*	
d	*distance to the wall*	m
$\tilde{d}$	*modified turbulent length scale*	m
D	*drag force*	N
ΔD	*drag on incremental surface element*	N
h	*roughness height*	m
e	*internal energy per unit mass*	J/kg
f	*frequency*	Hz
F	*force*	N
F_{DDES}	*DDES parameter*	
F_{DES}	*DES parameter*	
F_{SST}	*SST model blending function*	
H_{ASL}	*height above sea level*	m
k	*turbulent kinetic energy*	J/kg
l	*length of ship*	m
l_y	*semi-span of surface (positive for starboard surfaces)*	m
L	*lift force*	N
L_t	*turbulent length scale*	m
ΔL	*lift on incremental surface element*	N
M	*rotational moment*	Nm
N	*number of incremental surface elements*	
p	*pressure*	Pa
R	*reflection/Rayleigh coefficient*	
R_a	*Rayleigh criterion*	
Ra	*arithmetic average roughness*	μm
R_{coh}	*coherent reflection*	
S	*magnitude of the strain rate tensor*	s^{-1}
t_{sett}	*settling time*	s
$\Delta\mathrm{t}$	*time-step size*	s

u	*velocity in the longitudinal direction*	m/s
u'	*fluctuating velocity in the longitudinal direction*	m/s
u^+	*non-dimensional velocity*	
$\bar{u}$	*mean longitudinal velocity*	m/s
U_∞	*freestream velocity*	m/s
$\overline{u'v'}$	*Reynolds Stress*	m^2/v^2
v	*velocity in the lateral direction*	m/s
$\hat{v}$	*WOD unit vector*	
v'	*fluctuating velocity in the lateral direction*	m/s
$\bar{v}$	*mean lateral velocity component*	m/s
V	*airspeed*	m/s
$\boldsymbol{V}$	*vector velocity field*	m/s
V_{ref}	*Reference wind speed*	m/s
V_{WOD}	*relative wind speed over deck*	m/s
w	*velocity in the vertical direction*	m/s
w'	*fluctuating velocity in the vertical direction*	m/s
$\bar{w}$	*mean vertical velocity component*	m/s
x	*distance in the longitudinal direction*	m
$\Delta\mathrm{x}$	*grid cell size in the longitudinal direction*	m
X_{b4}	*x location of one-quarter chord incremental surface area*	m
y	*distance in the lateral direction*	m
$\Delta\mathrm{y}$	*grid cell size in the lateral direction*	m
y^+	*non-dimensional wall distance*	
z	*distance in the vertical direction*	m
Z	*specific acoustic impedance*	$Pa \cdot s/m$
$\Delta\mathrm{z}$	*grid cell size in the vertical direction*	m
z_{ref}	*height ASL of reference wind speed*	m
z_0	*sea surface roughness length*	m

Greek Notation

α	*angle of attack*	deg
Δ	*boundary layer thickness*	m
Δ	*area incremental surface area*	m^2
ε	*angle of rotation about z axis of surface axis system (related to sweep angle)*	deg
η	*rotation about x axis of surface axis system relative to body axis system (related to dihedral)*	deg
θ_w	*grazing angle*	deg
θ_b	*boundary angle*	deg
κ	*angular wavenumber*	$rads/m$
λ	*taper ratio*	

μ_t	*turbulent viscosity*	$Pa \cdot s$
ξ	*DDES constant*	
ρ	*density*	kg/m^3
σ	*RMS roughness*	µm
τ	*stress*	Pa
ψ, θ, ϕ	*euler angles of body axis system relative to earth axis system*	deg
$\Delta\varphi$	*phase difference*	$rads$
Ψ	*wind azimuth*	deg
ω	*specific turbulence dissipation*	s^{-1}
Ω	*magnitude of vorticity*	s^{-1}

Subscripts

b	*body axis system*
c	*critical*
cg	*centre of gravity*
e	*earth axis system*
h	*horizontal tail*
i	*incident*
s	*aerodynamic surface axis system*
v	*vertical tail*
w	*wing*
x, y, z	*x, y, z direction*
ε	*rotation about z axis (related to sweep)*

Non-dimensional variables

$Re = \frac{\rho V l}{\mu}$	*Reynolds number*
$St = \frac{f l}{u}$	*Strouhal number*
$Ti = \frac{\sqrt{\frac{1}{3}\left(u'^2 + v'^2 + w'^2\right)}}{U_\infty}$	*Turbulence intensity*
$C_l = \frac{L}{\frac{1}{2}\rho V^2 A}$	*Coefficient of lift*
$C_d = \frac{D}{\frac{1}{2}\rho V^2 A}$	*Coefficient of drag*

Abbreviations

ABL	Atmospheric Boundary Layer
ABS	Acrylonitrile Butadiene Styrene
ACA	Aircraft Carrier Alliance
ACP	Aerodynamic Computation Points
ADV	Acoustic Doppler Velocimetry
AIAA	American Institute of Aeronautics and Astronautics
ASTOVL	Advanced Short Take-Off and Vertical Landing
CAD	Computer Aided Design
CAUM	Corrected All-Up Mass
CFD	Computational Fluid Dynamics
CFL	Courant-Friedrichs-Lewy
COG	Centre of Gravity
CONOPS	Concept of Operations
DDES	Delayed Detached Eddy Simulation
DES	Detached Eddy Simulation
DIPES	Deck Interface Pilot Effort Scale
DLP	Digital Light Processing
DNS	Direct Numerical Simulation
DRDC	Defence Research and Development Canada
EPSRC	Engineering and Physical Sciences Research Council
ESDU	Engineering Science Data Unit
FDM	Finite Difference Method
FLYCO	Flying Control
FOCFTs	First of Class Flight Trials
FVM	Finite Volume Method
GIS	Grid Induced Separation
HMDS	Helmet-Mounted Display System
HMS	Her Majesty's Ship
HPC	High Performance Computing
ICASE	Industrial Cooperative Award in Science & Technology
ITF	Integrated Test Force
LDA/LDV	Laser Doppler Anemometry/Velocimetry
LES	Large Eddy Simulation
LHA	Landing Helicopter Assault
LSO	Landing Signal Officer
MAUM	Maximum All Up Mass
MILES	Monotone Integrated Large Eddy Simulation
MSD	Modelled Stress Depletion
MTE	Mission Task Element
MUSCL	Monotone Upstream-Centred Schemes for Conservation Laws
NACA	National Advisory Committee for Aeronautics
NASA	National Aeronautics and Space Administration

NATO	North Atlantic Treaty Organization
NLDE	Non-Linear Disturbance Equations
PIV	Particle Image Velocimetry
PMMA	Polymethyl methacrylate
PSD	Power Spectral Density
QEC	Queen Elizabeth Class
RAF	Royal Air Force
RAM	Random Access Memory
RANS	Reynolds Averaged Navier-Stokes
RMS	Root Mean Square
RN	Royal Navy
RNG	Re-Normalisation Group
SA	Spalart-Allmaras
SAI	Ship-Air Interface
SAS	Stability Augmentation System
SFS	Simple Frigate Shape
SGS	Sub-grid Scale
SHOL	Ship Helicopter Operating Limit
SIMPLEC	Semi-Implicit Method for Pressure Linked Equations-Consistent
SNR	Signal to Noise Ratio
SRVL	Shipborne Rolling Vertical Landing
SST	Shear Stress Transport
STO	Ski-jump Take-Off
STOVL	Short Take-Off and Vertical Landing
TTCP	The Technical Cooperation Program
UoL	University of Liverpool
URANS	Unsteady Reynolds Averaged Navier-Stokes
VAD	Virtual AirDyn
VL	Vertical Landings
VLA	Visual Landing Aids
VLM	Vortex Lattice Method
VTOL	Vertical Take-off and Landing
WOD	Wind Over Deck

Blank Page

Chapter 1

Introduction

This thesis describes a detailed study of the air flow over the UK's two new aircraft carriers, collectively known as the Queen Elizabeth Class (QEC) aircraft carriers. The flow of air over a ship, commonly referred to as the 'airwake' is due to a combination of the prevailing wind and the forward motion of the ship. Turbulent wakes may be formed as the air flow moves past the ship's superstructure resulting in a highly disturbed air flow that can often affect aircraft operating to and from the ship. Due to a combination of both the unsteady airwake and the motion of the ship's flight deck, launching or recovering an aircraft from a ship is recognised as one of the most challenging manoeuvres a pilot may perform. To ensure aircraft are operating to the ship within a safe envelope, a set of operational limits are defined for each aircraft-ship combination, referenced to the magnitude and direction of the wind over the ship's flight deck. The operational limits are defined during flight trials at-sea in which an aircraft conducts multiple landings to a ship in a variety of wind, ship motion, aircraft Corrected All-Up Masses (CAUM) and visual conditions; because these flight tests are conducted for each aircraft to the first ship of its class, they are known as the First of Class Flight Trials (FOCFTs). A significant risk is imposed on test pilots, their aircraft, the ship, and its crew during FOCFTs. Test pilots have to account for the unsteadiness of the airwake affecting the aircraft and for the motion of the ship while also attempting to push the aircraft and themselves to operational limits.

Simulation technologies, including motion platforms, visual projection systems and high-performance computing, have now advanced to the stage whereby the environment of a ship/aircraft combination can be recreated as a high-fidelity simulation to augment at-sea testing [1]. Piloted flight simulations can now be used to reduce time and costs by conducting part of the trials in the safety of a simulator.

FOCFTs require the aircraft and pilot to perform a variety of manoeuvres to and from the ship in a large number of operating conditions. Achieving each of the required conditions at-sea is often challenging and, due to time constraints may limit the potential operational envelope of the aircraft. As piloted flight simulation has the ability to create environmental conditions, at-sea trials may be augmented with the results of piloted simulated flight trials reducing the time at-sea and cost. In a typical flight testing schedule, test points with the lowest assumed risk to the pilot and aircraft are performed first, after which there is a gradual increase in the difficulty of manoeuvre and operating condition. If piloted flight simulation is used to augment at-sea flight trials, as the difficulty of the conditions are increased, higher confidence in the modelling can be achieved allowing pilots to perform repeated simulated trials at the operational edge of the flight envelope in a safe environment that may lead to greater operational capability.

The QEC aircraft carriers primarily operate the 5th generation Lockheed Martin F-35B Lightning II Short Take-Off and Vertical Landing (STOVL) fighter jet; the ship also operates with a variety of helicopters. In preparation for the F-35B FOCFTs with the QEC aircraft carriers, a high-fidelity simulation facility was developed at BAE Systems in which a motion-base piloted flight simulator, with a flight dynamics model of the F-35B, was integrated with unsteady airwakes produced using computational methods [2]. Research into the method used to create full-scale airwakes for simulation, and the subsequent production of QEC airwakes, was conducted in a collaborative research programme between BAE Systems Warton and the UoL through two Engineering and Physical Sciences Research Council (EPSRC) Industrial Cooperative Award in Science & Technology (ICASE) PhD studentships. The primary focus of the second ICASE PhD award, reported in this thesis, was to provide experimental validation and confidence in the accuracy of the computed airwakes. Mean and turbulent velocity data of the airwake, produced by an experimental setup of a 1:200 scale model of the QEC submerged in a large water channel, were measured and compared with computational solutions of the ship's airwake. As well as providing experimental validation of the computed airwakes for the BAE Systems F-35B flight simulator, this study has also developed simulation techniques to investigate how the airwake will affect a helicopter operating to the ship. Simulated flight trials using a generic helicopter flight model were conducted in a range of wind magnitudes and directions by former Royal Navy (RN) test pilots in an effort to both understand the effect of the airwake on the helicopter and the suitability of the method for defining the operational limits of the aircraft/ship combination. The simulated flight trials of a helicopter landing to the deck of the ship, in the unsteady air flow being shed from the superstructure, demonstrated the complex interaction between an aircraft and the unsteady three-dimensional air flow. A second simulation technique, used to assess how the airwakes affect a helicopter was conducted through the use of an offline (unpiloted) helicopter flight dynamics tool, the results which are also presented in the thesis. During the course of the research project, BAE Systems, the industrial research collaborator, expressed an interest in the complex interactions of the unsteady airwake produced by the ship on a fixed-wing aircraft, such as the F-35B. A high-fidelity aerodynamic model of a generic STOVL aircraft was developed. The development of this aerodynamic model, its integration with the ship's airwake and comparison with lower fidelity aerodynamic models applied to the generic STOVL aircraft are also presented in the Appendix.

1.1 Queen Elizabeth Class (QEC) Aircraft Carriers

HMS Queen Elizabeth, Figure 1-1, is the first of the United Kingdom's two new aircraft carriers. Commissioned in December 2017, she has already successfully conducted sea-trials and flight testing and is on track to become fully operational in 2020. The second carrier in the class, HMS Prince of Wales, was commissioned in December 2019 and is expected to be operational in 2023. At 65,000 tonnes each, with a length of 280 m and a beam of 73 m, they are the largest and most capable warships ever built for the Royal Navy. Characteristic features of the QEC, as can be seen in Figure 1-1, include the twin island superstructure, and the ramp, or 'ski-jump', located at the bow to facilitate short take-off [3]. The forward island is primarily for ship control and navigation and the aft island houses the Flying Control, or FLYCO, which is primarily for directing flight operations. The QEC carriers have been primarily designed to operate the 5th generation Lockheed Martin F-35B Lightning II, Figure 1-2, which is the world's first supersonic stealth STOVL fighter jet [4].

Figure 1-1 HMS Queen Elizabeth during FOCFTs © Crown 2019.

Figure 1-2 F-35B aboard HMS Queen Elizabeth © Crown 2019.

The means by which the F-35B will launch and recover from the QEC are illustrated in Figure 1-3. There are two methods by which the F-35B will be recovered to the ship; Vertical Landing (VL), which is the primary means of recovery, and the Shipborne Rolling Vertical Landing (SRVL). SRVL is a new recovery method unique to the UK F-35B/QEC combination and involves the aircraft recovering along a 7 deg glideslope over the stern of the ship, at a low forward speed, and stopping on deck using the wheel-brake [5, 6]. The advantage of the SRVL over the primary 'hover-translate-land' technique is an additional capacity to recover to the ship at higher gross weights (e.g., with more fuel and/or stores), by using wing-lift to augment the lift available from the aircraft's propulsion system.

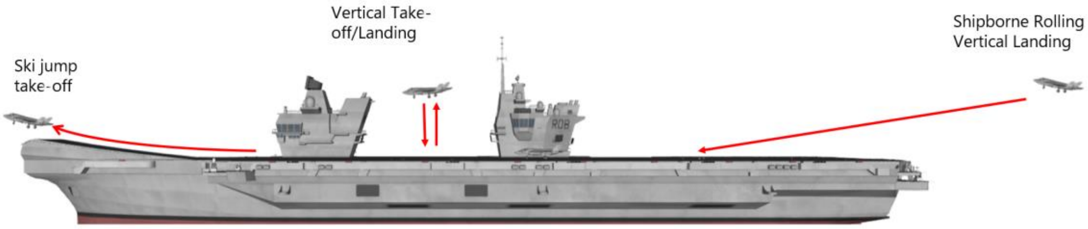

Figure 1-3 F-35B take-off and landing capabilities to the QEC.

As well as the fixed-wing F-35B, the QEC carriers will also operate a range of RN and Royal Air Force (RAF) rotary-wing assets (Figure 1-4) including Merlin, Wildcat, Chinook, and Apache helicopters. Figure 1-5 shows the six primary landing spots designated for VL recovery for both the F-35B and rotorcraft, with spot 6 being designated solely for rotorcraft operations.

Figure 1-4 Chinook and Wildcat helicopters during operations with HMS Queen Elizabeth © Crown 2019.

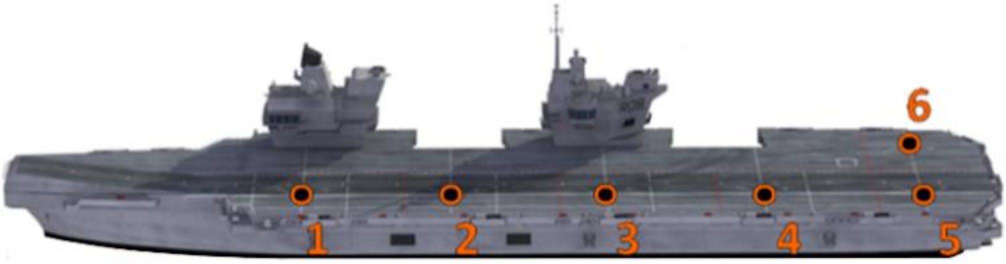

Figure 1-5 Queen Elizabeth Class aircraft carrier with VL spots identified.

Figure 1-6 HMS Queen Elizabeth (left) conducting simultaneous fixed- and rotary-wing operations © Crown 2019.

Figure 1-6 depicts typical concurrent fixed- and rotary-wing flight operations aboard a QEC aircraft carrier and shows that although the flight deck of the QEC carrier covers an area of approximately four acres, the space available for an aircraft to be recovered to will be constrained by other aircraft, personnel, and equipment on deck. On-deck obstacles, a pitching, rolling, and heaving deck, degraded visibility, and the presence of a highly dynamic airwake over the flight deck are all issues the pilot may have to contend with when recovering their aircraft to the ship.

1.2 The Ship-Air Interface (SAI)

Maritime aircraft are routinely deployed with modern combat ships and provide extended tactical capability. Tasks such as anti-submarine warfare, surveillance, troop transfer, and supply replenishment at sea are often performed by the ship's rotary-wing aircraft. Fixed-wing shipborne aircraft provide further capability such as air superiority, strike missions, electronic warfare, and reconnaissance. Although aircraft-ship operations are now considered routine, the recovery and launch of aircraft to and from ships at sea, particularly in adverse weather conditions, is regarded as one of the most demanding and dangerous environments in which a pilot may operate [7]. Flying conditions can deteriorate to the level at which the aircraft is no longer cleared to operate, thereby reducing the ship's overall capability.

Figure 1-7 F-35B operating within the SAI © Crown 2019.

During aircraft-ship operations, pilots must contend with the at-sea weather conditions which can lead to rolling, heaving and pitching of the flight deck, and to the unsteady airwake. The airwake is dependent on the ship's forward motion and the strength and direction of the prevailing wind. Visual cues for the pilot are also often impaired by sea spray or fog, and night-time operations are also routinely performed. Due to the time-varying and sometimes volatile nature of these conditions, the environment around the ship's landing deck is referred to as the Ship-Air Interface (SAI). The combination of the ship's motion, the local weather conditions and the ship's airwake all contribute to the degradation in the handling qualities of the aircraft and increase in pilot workload [8, 9]. When pilot workload increases, the margins for error are reduced and the safe operational envelope of the combined aircraft/ship system is affected. Several studies have been performed in an effort to understand the SAI effect on helicopter pilot workload [7, 10]. Even complex STOVL aircraft with highly augmented digital flight control systems, such as the F-35B, are not considered 'immune' to the effect of a ship's airwake, as the unsteady airflow will require a response from the aircraft's air-data system. To mitigate the risk associated with aircraft launch and recovery operations to a ship's flight deck, it is beneficial to understand the effects of the airwake on aircraft well ahead of FOCFTs.

1.3 First of Class Flight Trials (FOCFT)

The environment in which maritime aircraft operate can be challenging, and operational limits must be adhered to. Typically, these limits are expressed in terms of the relative magnitude and direction of the wind over the ship's landing deck, commonly referred to as the Wind Over Deck (WOD). The limits are also significantly affected by the deck motion, and so the WOD and deck motion will define the operational envelope for each aircraft type operating from each ship [11, 12]. These envelopes are traditionally determined through FOCFTs, in which numerous deck landings are carried out in a variety of wind, ship motion and visual conditions, e.g. The Merlin and Chinook performed a total of 960 deck landings during FOCFTs with the HMS Queen Elizabeth [13]. FOCFTs are expensive, time-consuming, and hazardous. Reliant on the available wind and sea conditions, FOCFTs can be limited in their scope leading to a reduced ship/aircraft operational envelope.

Prior to the planned F-35B FOCFTs with HMS Queen Elizabeth, a number of new challenges were presented. F-35B pilots had to not only contend with SAI (in particular, the effect of the ship's airwake on the F-35B) but also had to perform new manoeuvres such as the SRVL whilst in a single-seat cockpit. As shipborne STOVL operations have not been conducted by the UK RAF/RN since the retirement of the Harrier in 2010, and as the combination of F-35B/QEC is seen as a critical component of UK defence capability, efforts to reduce the level of risk and uncertainty during F-35B/QEC FOCFTs were conducted, identifying the use of simulation to provide risk mitigation.

Similarly, rotorcraft, although having been deployed and operated to several RN ships, typically frigates and destroyers, had also to contend with the SAI of the much larger QEC aircraft carriers.

1.4 Ship Helicopter Operating Limits

As discussed above, operational limits for every in-service ship/aircraft combination are determined during the FOCFTs, to ensure the safety of pilots and crew operating within the SAI. The operating limits are determined through a series of launch and recovery tasks, completed with the ship and aircraft at sea for winds of varying strength and direction; aircraft load, sea state and visibility are also considered.

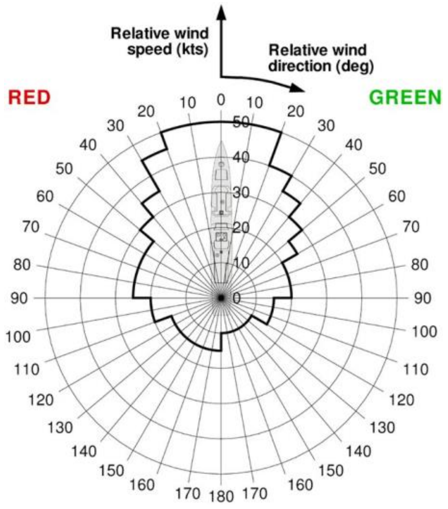

Figure 1-8 Simulated SHOL diagram [14].

Figure 1-8 is a polar diagram, known as a Ship-Helicopter Operating Limits (SHOLs), that shows the limiting relative wind conditions for a maritime helicopter operating to a particular ship. SHOLs are used by operators and fleet pilots to ensure that for given conditions they are operating within the safety envelope. The SHOL diagram in Figure 1-8 is for a standard RN port side approach [14]; the bold black line indicates the edge of the operational boundary. Winds approaching from the starboard side of the ship are termed 'green' winds and those from the portside are 'red' winds.

The limit of the safety envelope is determined by a team of flight test engineers and test pilots who assess the difficulty of the landing task. For helicopters, this is achieved using the Deck Interface Pilot Effort Scale (DIPES), Figure 1-9, which is widely used by North Atlantic Treaty Organization (NATO) member countries to determine limiting conditions for ship-helicopter combinations. A similar diagram is provided for fixed-wing STOVL aircraft in combination with each ship. During FOCFTs, the test pilot will give DIPES ratings considering the perceived workload of the average fleet pilot to complete each flight task. The ratings are then used to produce the SHOL for each ship/aircraft combination. As well as pilot workload, DIPES also identifies limits due to aircraft physical control activity and influencing environmental factors such as deck motion and turbulence [11]. The DIPES rating scale is, therefore, particularly well-suited for qualification testing where, although pilot workload may be low, control limits can be encountered. The DIPES rating scale shown in Figure 1-9 is used by test pilots to give a rating of 1-5 for a launch/recovery task. A rating of 1-3 ranks effort from slight to the highest tolerable while still being considered within acceptable bounds and within the capabilities of an average fleet pilot. A rating of 4 is deemed to be unacceptable on the basis that an average fleet pilot would not be able to complete the task in a consistently safe manner. A rating of 5 indicates that the task cannot be safely completed by fully proficient crews even under controlled test conditions. The DIPES rating scale also includes a list of suffixes the test pilot may assign to a given rating to specify the causes of the workload.

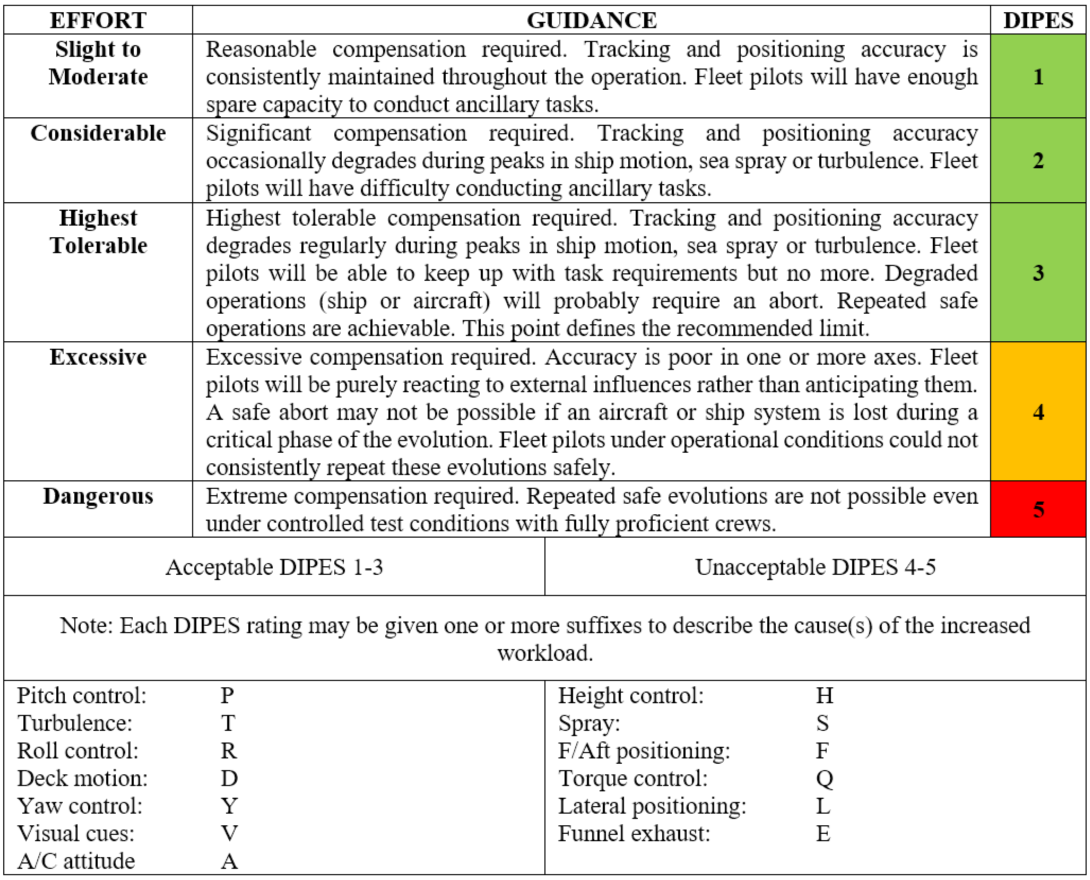

EFFORT	**GUIDANCE**	**DIPES**
Slight to Moderate	Reasonable compensation required. Tracking and positioning accuracy is consistently maintained throughout the operation. Fleet pilots will have enough spare capacity to conduct ancillary tasks.	**1**
Considerable	Significant compensation required. Tracking and positioning accuracy occasionally degrades during peaks in ship motion, sea spray or turbulence. Fleet pilots will have difficulty conducting ancillary tasks.	**2**
Highest Tolerable	Highest tolerable compensation required. Tracking and positioning accuracy degrades regularly during peaks in ship motion, sea spray or turbulence. Fleet pilots will be able to keep up with task requirements but no more. Degraded operations (ship or aircraft) will probably require an abort. Repeated safe operations are achievable. This point defines the recommended limit.	**3**
Excessive	Excessive compensation required. Accuracy is poor in one or more axes. Fleet pilots will be purely reacting to external influences rather than anticipating them. A safe abort may not be possible if an aircraft or ship system is lost during a critical phase of the evolution. Fleet pilots under operational conditions could not consistently repeat these evolutions safely.	**4**
Dangerous	Extreme compensation required. Repeated safe evolutions are not possible even under controlled test conditions with fully proficient crews.	**5**

Acceptable DIPES 1-3	Unacceptable DIPES 4-5

Note: Each DIPES rating may be given one or more suffixes to describe the cause(s) of the increased workload.

Pitch control:	P	Height control:	H
Turbulence:	T	Spray:	S
Roll control:	R	F/Aft positioning:	F
Deck motion:	D	Torque control:	Q
Yaw control:	Y	Lateral positioning:	L
Visual cues:	V	Funnel exhaust:	E
A/C attitude	A		

Figure 1-9 DIPES rating scale [11].

Due to the unpredictable nature of the wind and sea conditions encountered during the FOCFTs, it is not always possible to complete the full SHOL envelope test points. Conditions in some areas of the flight envelope may not be attained, requiring interpolation/extrapolation of previously recorded data, known as 'read-across', reducing confidence in the limits and leading to a conservative SHOL [15]. FOCFTs may also take several weeks to complete and are inevitably very expensive. Modelling and simulation has the potential to provide a more cost-effective option that offers augmentation of SHOL testing at-sea with simulated flight trials, an option that is made more feasible by ongoing developments in flight simulation fidelity.

1.5 Modelling and Simulation of the SAI

Engineering modelling and simulation is the solution of practical engineering analysis and design problems using physics-based computational models. Once these simulations have been created and validated to demonstrate how well they represent the real system, they can be used to safely explore the performance of the system for a large variety of conditions.

The multi-faceted SAI, with many complex features, is well suited to the potential benefits of modelling and simulation due to the considerable risk to the pilot and aircraft/ship systems. Over the last 15 years or more, UoL has been conducting research into the use of modelling and simulation tools to understand the SAI of primarily UK naval ships, such as single-spot frigates, destroyers, and more recently, aircraft carriers. The two principal aims of this ongoing work are to (i) create a flight simulation environment for realistic aircraft launch and recovery operations [1, 8, 15-17], and (ii) develop guidance for ship designers to minimise the effect of ship superstructure aerodynamics on helicopter operations [18]; both aims being directed towards maximising operational capability and reducing pilot workload during aircraft launch and recovery.

1.5.1 Piloted Flight Simulation

To provide a realistic flight simulation environment for launch and recovery of aircraft to and from ships, each contributing factor to pilot workload must be considered and included. Due to the significant contribution of the ship's airwake to pilot workload [7], a high-fidelity model of the airwake must be included in any SAI flight simulation. A ship's airwake is a complex three-dimensional unsteady air flow characterised by steep velocity gradients, shear layers and vortices shed from the ship's superstructure. Contemporary ship airwake research has been focused on the use of Computational Fluid Dynamics (CFD) to model the flow over the ship for both analysis and integration with piloted flight simulation; this has only been possible through the advancement of computing power over the last two decades [19, 20]. The generation of high-fidelity airwakes allows a comprehensive study of the flow features present over the ship's flight deck in varying wind conditions and their effect on aircraft operating within the SAI. While flight simulation can be used to support flight trials and aircraft clearance activities, there is a need for real-world trials data to compare with simulations before the techniques utilised to their full potential.

1.5.2 Ship Design

Although many practical requirements for aircraft operations to a ship are taken account of during the ship's design stage, little to no consideration is given to the effect the ship's superstructure has on the airwake generated and the consequential effect on aircraft operations. The first time the ship airwake effect on operational aircraft is observed is during the FOCFTs. At this stage of the ship's development any structural modifications will be expensive and if pilot workload or aircraft handling issues are detected during the FOCFTs, the only alternative is to certify a restricted flight envelope with reduced operational capability. Modelling and simulation of the ship's airwake has the potential to analyse the superstructure's effect on the flow field, identifying geometry features which may be altered early in the development of the ship design to increase the operational capability of the aircraft/ship system.

Placement of the anemometers aboard ships is also a concern for designers. Ship anemometers measure the local wind speed and direction (i.e., WOD); pilots and operators then use this information to ensure they are operating within the SHOL [21]. If the anemometers are within the disturbed flow of the ship's airwake, the readings given will not reflect the true wind conditions. During FOCFTs, a number of independent reference sources of the WOD conditions are set up to verify the ship's anemometer readings. Although corrections could be applied to the anemometer measurements, there will be an associated degree of error in the final readings. To maximise the capability of aircraft operations on board, it is desirable to have a true reading of the wind conditions. If the readings taken from the anemometer are not true to the local wind conditions, the pilot may unknowingly be flying in conditions outside the operational envelope or, conversely, flight operations may be inadvertently restricted, so reducing overall capability. Modelling of the airwake can also allow designers to assess the effect of anemometer placement on the flow readings obtained, or to evaluate the difference between the readings at freestream conditions, thereby increasing operational capability and reducing costs of relocating the anemometers late in the ship's development.

1.5.3 Training

Flight simulators are in widespread use as training devices for pilots, flight crew and flight deck operators due to the versatility of current modelling and simulation techniques. A simulation that is more representative of the real-world, allows more of the real-world training to be augmented within a simulator, and reduces the overall cost and risk associated with real-world training.

By implementing a high-fidelity airwake within a flight simulation of a ship at-sea, trainee pilots can practise manoeuvres and emergency procedures to further their understanding of the flight environment in the safety of a flight simulator before live operations. For F-35B pilots operating to and from QEC carriers, flight simulation allows pilots to both experience the airwake over the ship during VL and to practice the SRVL recovery technique.

Modelling and Simulation of the SAI therefore has the potential to mitigate risk and reduce cost and time for FOCFTs. It is of note, that while a high-fidelity model of the ship's airwake may be analysed in isolation to identify noteworthy flow features, when integrated with flight simulation, the effect of the airwake on aircraft handling and pilot workload may also be investigated. By allowing the potential ship/aircraft operating envelope to be developed using modelling and simulation of the SAI, and then exercised, the envelope can be refined, enabling a case to be made for the optimal position of the minimum number of FOCFT test and build up points.

Modelling and Simulation of the SAI may also be used to inform ship design [22]. Significant research has been conducted to improve the fidelity of the airwake and flight simulation, to better inform designers, operators, and pilots [18, 21, 23, 24].

Working with BAE Systems and the UK Ministry of Defence, UoL has implemented its research to provide and analyse airwakes of the Type 23 Frigate, the Wave Class Auxiliary Oiler and the Hunter Class Type 26 Global Combat Ship; in addition, UoL has also informed the design of the UK Type 26 Global Combat Ship by providing airwakes at several design iterations. Specific to the research being reported in this thesis, UoL has been tasked by BAE Systems to compute airwakes over the QEC aircraft carriers for integration with their piloted flight simulation of the F-35B/QEC environment.

1.6 **Modelling a Ship's Airwake**

The SAI environment around the ship's flight deck is a combination of the ship's unsteady airwake and deck motion in which the pilot has to compensate for, while also being close to the ship's deck and superstructure. The fidelity of the SAI simulation is highly dependent on realistic modelling of the unsteady turbulent airwake [17]. A significant amount of research has been dedicated to the understanding of the ship airwake and to accurately recreating the flow field for simulation.

1.6.1 Empirical Measurements

Early attempts at capturing the effect of the airwake on aircraft focused on identifying regions of high turbulence by using model-scale ships attached to the floor of a wind tunnel working section at angles to the freestream flow to represent different wind directions [25, 26]. Flow visualization techniques such as smoke, oil flow, tufts and helium soap bubbles were used in the wind tunnel to detect areas of significant flow disturbance and to identify the flow features over the flight deck [27]. Hot wire anemometers were used to measure the unsteady three-dimensional velocity data [22-25]. Similar experimental measurements were conducted using hot wire and hot film anemometers to map the airwake velocities along specific helicopter flight paths over a DD-963 Class Destroyer and conduct flow visualization [31, 32]. Fortenbaugh, collected empirical data measured in wind tunnel testing to create several numerical models through an analytical method described in [25, 33], and used these data in real-time flight simulation.

1.6.2 Computational Fluid Dynamics

As the computing power over the last two decades has increased, the modelling focus has shifted from experiment to CFD [34]. Capable of producing flow data across the whole domain of the ship, CFD has become the standard method of high-fidelity airwake simulation, as reviewed by Shukla et al. [35]. Many studies have been conducted using a variety of CFD methods with the aim of generating an accurate model of the ship airwake for analysis and flight simulation. The choice of CFD method used to generate a ship airwake is an important consideration. Strengths and limitations of each method must be understood. An appropriate method must not only accurately capture the flow features of interest, but also remain within the constraints of computational resources.

Numerical limitations along with the large size and the high Reynolds number associated with a full-scale ship present a complex problem [15, 36-43]. The first use of a Finite Volume Method CFD to compute a ship's airwake was reported by Tai and Carico [44], who produced the airwake of a DD-963 destroyer using the CFL3D Navier-Stokes code with a Baldwin-Lomax turbulence model. Dominant features of the flow observed in parallel wind tunnel experiments were observed in the CFD solution.

To aid individuals and groups who were researching the flow phenomenon found in the ship's airwake, a baseline ship model was conceived by The Technical Cooperation Program

(TTCP), an international framework for the research and defence agencies of member countries to share and combine research effort [45]. Consisting of the five nations: UK, US, Canada, Australia and New Zealand, the TTCP panel developed a simplified representation of the landing deck of a single-spot frigate known as the Simple Frigate Shape (SFS, also later known as SFS1) in 1985. In 1998 the SFS1 model was extended forward to include a bow, a ship's superstructure and a funnel resulting in a more realistic representation of a frigate, the SFS2; the geometry of the SFS1/SFS2 is shown in Figure 1-10.

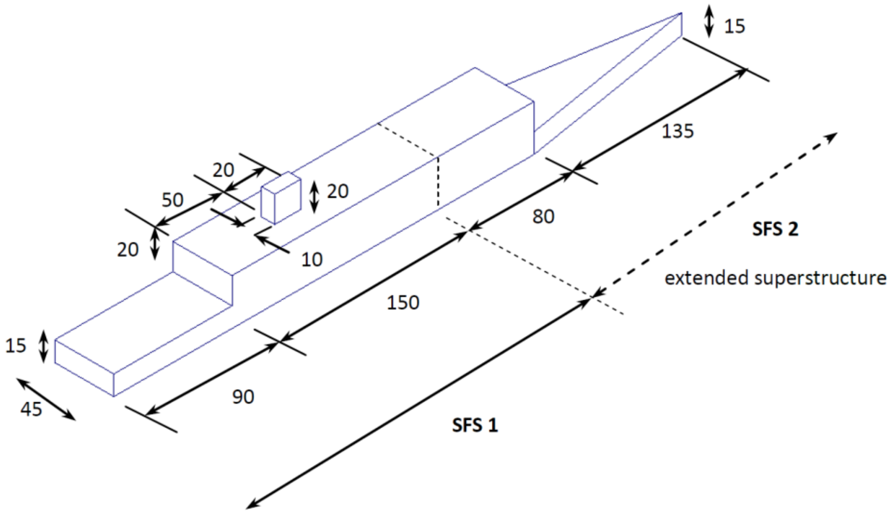

Figure 1-10 The SFS1 & SFS2 geometry. All dimensions are in feet.

In 1998, Liu et al. produced an unsteady CFD simulation of the SFS1 airwake using an inviscid Non-Linear Disturbance Equations (NLDE) Navier-Stokes method [38]. Initial comparison of the results with experimental studies [30] showed good agreement; however, oil-flow visualizations performed by Cheney and Zan [46] and Zan [47] did not agree well. A steady computation of the flow over the SFS was conducted by Reddy et al. in 2000 using the Re-Normalisation Group (RNG) k-e turbulence model which highlighted re-circulation zones and numerous flow features [48]; consistent with the flow features reported by Cheney and Zan. Reddy et al. also demonstrated the variation of the velocity field due to changes in grid sizes on which the fluid around the ship had been discretized.

The first reported application of an unsteady CFD method to simulate a ship airwake was by Long et al. in 1998 using an NDLE technique with a Navier-Stokes Solver [38]. A comparison of time-accurate unsteady CFD and steady-state CFD with experimental measurements was performed by Polsky and Bruner in 2000, using a Landing Helicopter Assault (LHA) ship and the COBALT Navier-Stokes solver with Monotone Integrated Large Eddy Simulation (MILES) [40]. Results showed that the unsteady method aligned closer with the experimental data than the steady state CFD solution. The LHA simulation of Polsky and Bruner was the first reported instance of CFD being used to model the flow over an aircraft carrier and demonstrated that, after accounting for Reynolds number, the airwake can be scaled as the flow features do not change much with different wind speeds for a given wind direction. In 2003, Polsky computed the flow over the LHA in a beam wind to study the complex flow features over the flight deck [42]. The results of the CFD solution, which was computed using a parallel Navier-Stokes solver, COBALT, with MILES on an unstructured grid of 4-7 million cells, were compared with at-sea measurements aboard the LHA. Although some reasonable agreement was shown, it was observed that the results matched more closely when an Atmospheric Boundary Layer (ABL) was included in the CFD boundary conditions. Poor agreement with experimental results was still observed over one spot on the deck, which Polsky attributed to the turbulence modelling, and recommended a time-accurate hybrid RANS-LES approach, such as Detached Eddy Simulation (DES), for future airwake studies.

Roper et al. [15] produced steady CFD simulations of the two TTCP SFS models, using the Finite-Volume Method (FVM) based CFD solver Fluent with two-equation turbulence models, and showed reasonably good agreement with the experimental measurements reported by Zan et al. [46] and Lee [49]; multiple wind conditions were compared as suggested by Zan [50]. The CFD-generated airwake data was converted into look-up tables and integrated with a piloted flight simulation of a Lynx-like helicopter and the SFS2. This research was extended by Forrest et al. [8] in 2012, using DES with an ABL, to compute the unsteady airwake over a Type 23 Frigate and a Wave Class Auxiliary Oiler.

The time-accurate airwakes created by Forrest et al. were integrated with the generic research flight simulator at the UoL, HELIFLIGHT-R [51], and simulated SHOL trials were performed. Results indicated that shortcomings due to steady-state airwakes identified by Roper et al. were greatly improved. Using the computed airwakes, Forrest et al. were able to discern that differences in the SHOL data between the Type 23 and Wave Class Auxiliary Oiler were due to the relative size of each ship. As Forest et al. showed, high-fidelity simulation of the airwake is key to assessing the flow features of the airwake and for flight simulation; Shukla et al. [35] considers this work a milestone in accomplishing high-fidelity simulation. Forrest et al. outlined the CFD method in more detail in [16], where good agreement was shown when comparing the results with wind tunnel and at-sea airwake data; further improvements in the results were achieved by the application of an ABL.

The QEC aircraft carriers are significantly larger multi-spot platforms, each possessing an approximately four-acre flight deck, and with a requirement to operate both fixed- and rotary-wing aircraft. The generation of time-accurate CFD airwakes for a multiple-spot aircraft carrier requires a significant increase in computational power when compared with the CFD solution for a single-spot frigate. As part of the two BAE Systems/EPSRC ICASE studentships, Kelly produced airwakes of the QEC aircraft carriers and performed initial validation of the CFD method against at-sea measurements of an LHA [52]; reasonably good agreement was shown. The CFD methodology used by Kelly et al. [52] to produce the QEC airwakes was adapted from that used by Forrest et al. to produce time accurate flow over a single spot frigate [16], and has also been adopted for the research presented in this thesis, as described in detail in Chapter 3. The QEC airwakes were then integrated into the fixed-wing STOVL F-35B Lightning II piloted flight simulator at BAE Systems Warton [52], and used to inform the FOCFTs.

1.7 Modelling and Simulation of the QEC/F-35B Dynamic Interface

The concurrent development of the QEC and F-35 programmes presented a unique opportunity to deploy modelling and simulation to investigate the SAI and maximise the combined capabilities of these two assets [53]. As previously mentioned, the development of high-fidelity ship airwakes of the QEC aircraft carriers for simulation was conducted in a collaborative research programme between BAE Systems and UoL [52]. The QEC airwakes generated at UoL were employed by BAE Systems in its fixed-wing flight simulator at Warton in which test pilots performed simulated flights to and from the flight deck, exploring the flight envelope for a variety of wind over deck conditions. Numerous operational scenarios were examined, providing experience for the test pilots and the ship's FLYCO team ahead of FOCFTs. Results of these simulated trials were then used to inform the FOCFTs at-sea and subsequent operational procedures.

The main components required to construct a high-fidelity simulation of the aircraft-ship dynamic interface are shown in Figure 1-11. These components are specifically related to the flight simulator at BAE Systems, Warton, for an F-35B operating to and from the QEC. Components similar to those shown in Figure 1-11 have also been integrated into the UoL research simulator to assess the effect of the environment on rotary-wing aircraft, results of which will be shown in Chapter 4. Each of the simulation components are described below; note that certain restricted features, such as the ship systems model, were not implemented in the UoL simulator.

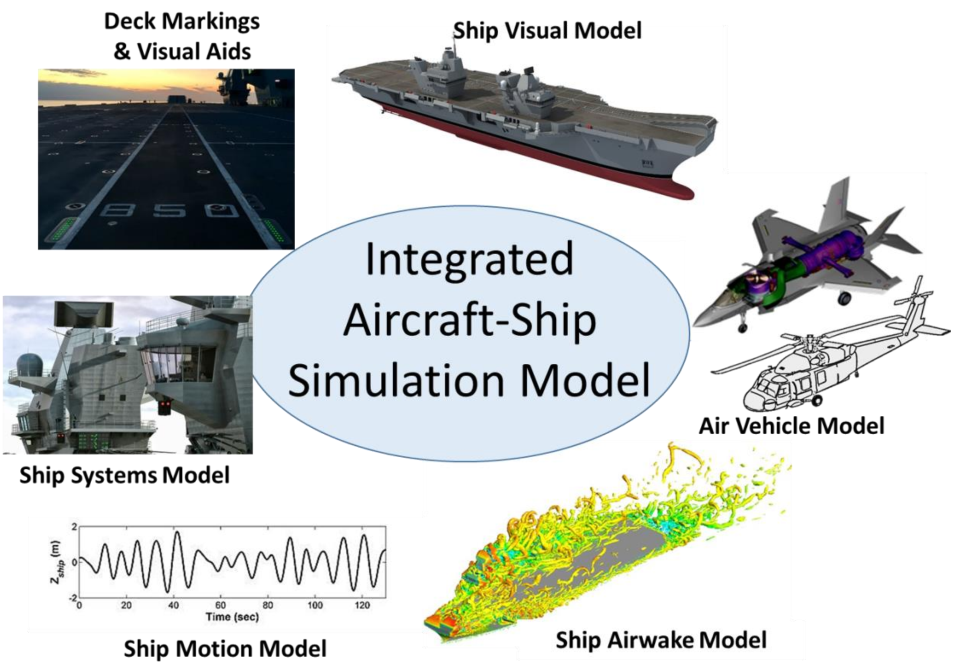

Figure 1-11 Principal components of an integrated aircraft-ship simulation.

The mathematical air vehicle flight model used in the BAE Systems simulator is a comprehensive non-linear simulation of the F-35B aircraft, developed by Lockheed Martin Aeronautics and its partners. The model is constructed from a set of federated sub-system components, each being designed, built, validated, and maintained by the appropriate domain experts. These subsystem models cover the entire range of aircraft systems, including but not limited to aerodynamics, flight controls, air-data systems and sensors, propulsion systems, actuators, landing gear, electrical power, navigation, and vehicle management systems.

Using general arrangement CAD data supplied by the Aircraft Carrier Alliance (ACA), a three-dimensional model representative of a version of a QEC carrier was developed. Pilots often use relatively small features on the island superstructures as position and height reference cues while hovering alongside and over the deck, so the level of detail incorporated into the ship visual model is an important factor in creating a realistic and immersive cueing environment. The deck markings and Visual Landing Aids (VLA) were designed by the ACA and their VLA suppliers. Models of the VLA and deck markings were incorporated into the visual model of the ship [54]. These models define the size, shape, colour, and position of each VLA or deck marking and, for VLAs, the brightness, viewable angle / range, and signal format (e.g., colours, flash rate, duty cycle etc.). The ship systems model represents the ship's sensors and systems, specifically those relating to the launch and recovery of fixed- and rotary-wing aircraft (e.g., approach radar, and VLA control algorithms etc.).

The ship motion model represents the sea-keeping characteristics of the vessel. Realistic ship motion data was derived from a series of tow-tank experiments conducted by the ACA and integrated into the BAE Systems simulation. The ship motion model employed in the UoL's HELIFLIGHT-R simulator incorporates a generic set of ship motion data which can be scaled to represent a range of different sized ships.

The QEC airwake models were created at UoL using CFD techniques that will be outlined in Chapter 3. For realistic flight simulation it is essential that the airwake is computed using time-accurate CFD, i.e., the three components of velocity in the airwake are computed at different time intervals (every 0.01 seconds in this case) so that unsteady velocities can be imposed on the air vehicle model as it is 'flown' through the airwake. The generation of the CFD airwakes and their implementation into a real-time flight simulator, is a major part of the modelling and simulation process for the SAI.

The BAE Systems simulator includes a fully representative F-35B cockpit, mounted on a six-axis electric motion system, housed inside a fixed 3.65 m radius dome (Figure 1-12 a). The cockpit is an accurate replica of that in the F-35B (Figure 1-12 b and c), including active sidestick and throttle units, a large-area touchscreen display and ejection seat model. A representative Helmet-Mounted Display System (HMDS) was also provided to give the pilots flight guidance and navigation symbology. The motion system uses state-of-the-art electric-motion technology, although the actuator stroke length (640 mm) is considerably shorter than most civil airline training simulators. The fact that the visual system is mounted off-board (i.e., not mounted on-top of the moving platform) reduces platform payload resulting in a highly agile motion system with a relatively small footprint. The visual system uses 16 WQXGA projectors, the images from each being seamlessly blended to provide the pilot with a continuous field-of-view of 360 deg in azimuth by 10 deg in elevation. The projected scene includes a high-fidelity model of the QEC carrier together with a realistic and dynamic sea surface.

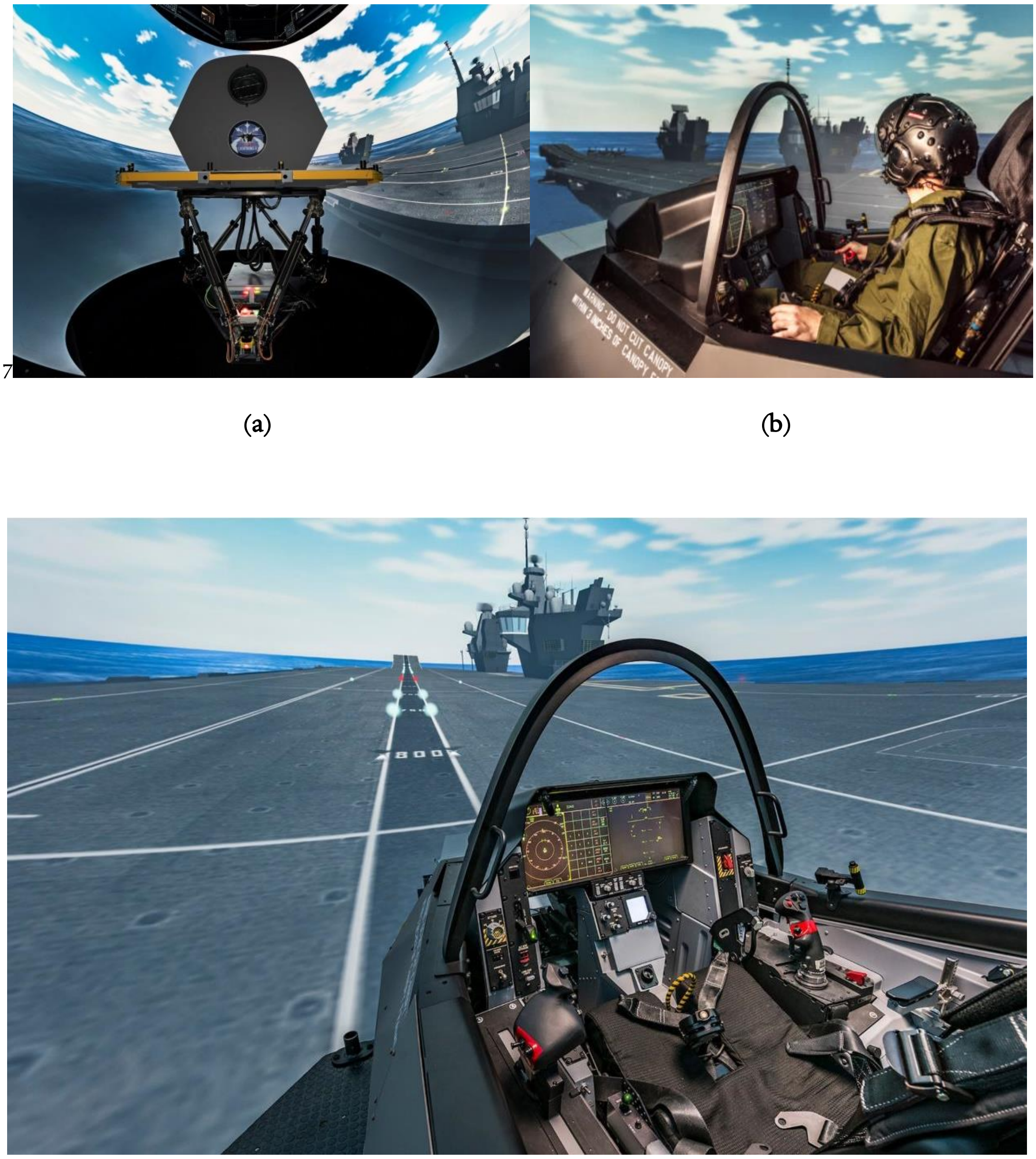

(a) (b)

(c)

Figure 1-12 F-35/QEC simulation facility at BAE Systems Warton, showing (a) motion system and dome, (b) inside the cockpit, and (c) F-35B cockpit and QEC visual environment.

Figure 1-13 F-35/QEC simulation facility at BAE Systems Warton, showing inside of networked FLYCO simulator.

The piloted simulator is networked with a second, adjacent, simulator facility which provides a replica of the QEC carrier FLYCO (Figure 1-13), which, on the ship, is located in the aft island. The outside world scene in this simulator presents the view from FLYCO including pre-recorded F-35B and rotorcraft take-off and recovery manoeuvres, as well as live flights being conducted by the pilot in the flight simulator. The coupled simulators allow the ship's FLYCO team, including the Landing Signal Officer (LSO) who, together with the pilot is responsible for the safe launch and recovery of fixed-wing aircraft to the ship, to work together to refine the Concept of Operations (CONOPS), dictating how fixed-wing aircraft will operate from the carrier.

From 2016, engineers, test pilots and LSOs from the UK Royal Navy and Royal Air Force, and the F-35 Integrated Test Force (ITF) used the BAE Systems simulator at Warton to 'fly' thousands of simulated deck landings and ski-jump launches from the deck of HMS Queen Elizabeth in a variety of wind conditions, with the aim of gathering the data to ensure that the real-world flight trials were as safe, efficient and effective as possible. Prior to FOCFTs, Commander Nath Gray, a F-35B test pilot said of the simulator facility at BAE Systems Warton:

'The facility is unique in providing the most realistic environment and conditions that I've ever experienced in a simulator. The flying qualities, aircraft handling, air wakes and way the ship rolls are as real as it gets' [55].

The bespoke F-35B/QEC simulator at BAE Systems, Warton, has played, and continues to play, a vital role in the development and qualification of the F-35B/QEC aircraft-ship interface [56, 57].

1.8 Westlant 18-19 FOCFTs

The F-35B's first landing aboard QEC was accomplished on the 25th of September 2018 as part of the FOCFTs during 'Operation Westlant 18' held off the eastern coast of the USA. Over a period of 11 weeks, two F-35B test aircraft conducted a variety of flight manoeuvres, providing data to determine operational limits for the jet operating to the QEC. During these trials, the F-35B successfully performed 202 take-offs from the ship's ski-jump (Figure 1-14), 187 vertical landings and 15 SRVL manoeuvres (Figure 1-15); low-visibility night-time landings and a aft-facing landing were also completed.

Figure 1-14 HMS Queen Elizabeth during F-35B First of Class Flight Trials, October 2018 © Crown.

Two F-35B aircraft flew for a total of 75 hrs, completing Development Test 1 and 2 ahead of schedule, allowing a significant portion of Development Test 3, originally planned for the following year, to be started. Commenting after completion of the trials, Commander Nathan Gray, one of the four F-35B test pilots, was quoted as saying:

> '*The preparations we did in the simulator gave us the perfect foundation to get these trials started and everything we have done so far has built on those foundations. There have already been many times during the trials where we are in a position we have been in during the simulator trials and everything felt familiar, which give us huge confidence*'

Figure 1-15 F-35B performing an SRVL manoeuvre to the flight deck of HMS Queen Elizabeth © Crown 2019.

HMS Queen Elizabeth left Portsmouth on the 30th of August 2019 to take part in the second Westlant deployment as part of the UK Carrier Strike Group (Figure 1-16), which saw British F-35B aircraft embarking from the QEC for the first time. Building on the success of the Westlant 18 FOCFTs, Westlant 19 focussed on maximising the capabilities of the F-35B onboard through operational testing. Trials were led by the joint RN/RAF 17 Test and Evaluation Squadron operating alongside personnel and aircraft from the UK Lightning Force based out of RAF Marham. Over five weeks, the F-35B was put through 'end-to-end' testing, including armament and using the ship's automated weapon handling system. Following the Westlant 19 deployment, the Commanding Officer of HMS Queen Elizabeth, Commodore Steve Moorhouse said:

'*This has been an extremely successful deployment for HMS Queen Elizabeth*' [58].

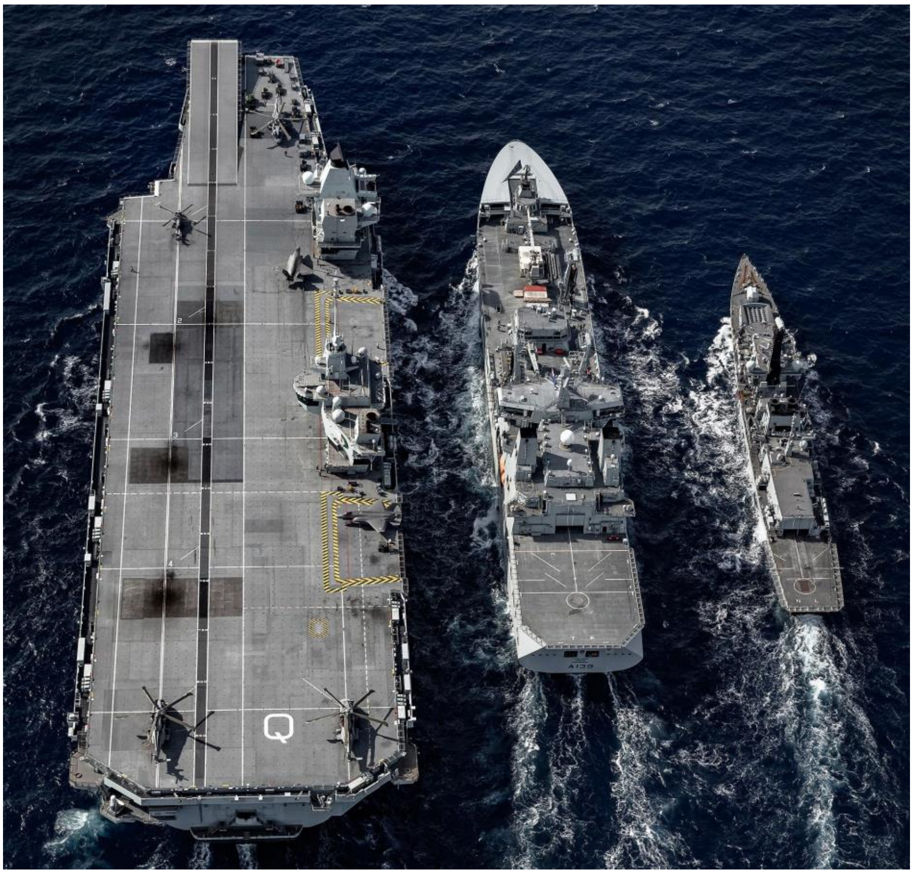

Figure 1-16 From left to right: HMS Queen Elizabeth, Royal Fleet Auxiliary Tideforce and Type 23 Frigate HMS Northumberland © Crown 2019.

The success of Westlant 18 and 19 can be attributed in part to over 3000 flight tests conducted in the high-fidelity flight simulator at BAE Systems Warton. Pilots, engineers, and operators were able to investigate the air flow over the carrier and its effect on the aircraft; furthermore, due to the addition of the FLYCO simulator, operators were also able practice landing, take-off, and emergency procedures. The integration of high-fidelity QEC airwakes, computed using CFD, into the flight simulator, was critical in providing pilots and operators with an accurate representation of the flow environment in which to assess its effect on the aircraft and pilot workload.

It is not currently feasible for flight simulation, as described above, to completely replace at-sea testing; nevertheless, intelligent application of modelling and simulation, backed-up by appropriate validation evidence, has been a powerful tool for informing the flight trials planning process. In the future, improvements in computing power and simulation technology are likely to lead to further breakthroughs in the application of modelling and simulation to the challenging aircraft-ship dynamic interface environment, but these improvements must always be underpinned by fundamental research such as that described in this thesis.

As mentioned in Section 1.7, the first BAE Systems QEC EPSRC ICASE PhD studentship was successful in developing the method used to generate and integrate high-fidelity QEC airwakes into the flight simulator, at BAE Systems Warton, to provide a realistic SAI simulation environment [52]. For modelling and simulation to be exploited successfully, the individual models and the overall simulation must be validated with real-world data to give confidence that the simulated results can be trusted. Creating unsteady CFD airwakes over a ship the size of the QEC, and for a significant distance downstream of the ship, where the disturbed air can still affect the aircraft, is a significant challenge. The research from the second BAE Systems QEC EPSRC ICASE PhD studentship is detailed in this thesis and was concerned with both the need to validate the CFD method using experimental measurements, and to further develop tools to analyse the ship airwake on fixed- and rotary-wing aircraft.

1.9 CFD Validation

To ensure the reliability and accuracy of the CFD method, it is necessary to compare the computed solution with measured ‘true’ data from exact solutions or through experimental measurements [59]. Due to the size and complex geometry of a ship, an exact solution using analytical CFD methods is infeasible. Several experimental measurements have previously been conducted, typically using a small-scale model ship housed in a wind tunnel, to compare velocity and turbulence data with a CFD solution. Multi-hole probes are one method that have been used to measure mean flow velocities for initial CFD validation [46, 47]. As the airwake is inherently unsteady due to its bluff body nature, a more comprehensive CFD validation requires a comparison with transient flow measurements [60]. Hot film anemometry, a method of measuring the velocity by maintaining a constant temperature and measuring the variable electrical resistance across a heated wire in an air flow, was used by Zan et al. to obtain mean and unsteady data to compare with the CFD solution of the TTCP SFS2 ship [61]. Other unsteady flow measurement techniques include non-intrusive laser techniques such as Laser Doppler Anemometry (LDA/LDV), which measures the velocities at a point in the flow, and 2D Particle Image Velocimetry (PIV), which measures velocities in a 2D plane [62-66]. Although LDA and PIV systems provide a good quantitative measurement of the unsteady flow, the equipment is expensive, and requires additional safety constraints during testing due to the application of high-powered lasers. In the present study there was also an issue with optical access to the working section containing a scale model of the QEC which will be discussed later. Chapter 2 of this thesis outlines the experimental measurement of the flow over the QEC using ADV for comparison with the results of the CFD method detailed in Chapter 3.

1.9.1 CFD of Scale Model QEC Experiment

Chapter 2 will describe the experimental measurements that were used in this study to validate the CFD method. The volume of flow to be investigated, both experimentally and computationally, corresponds to the flow over, and astern of, the aircraft carrier's flight deck. The Reynolds number of the experimental flow, based on the length of the small-scale model of the carrier was approximately 1.57×10^6, compared with approximately 2×10^8 for the full-scale ship with a wind speed of 10 m/s (~20 kts). In experimental bluff body aerodynamics, especially where the body has sharp edges, it is common practice to assume that the flow characteristics are independent of Reynolds number [67]. This is because the flow separates cleanly from sharp edges, unlike, for example, the separation from the curved surface of an aerofoil. For the flow around rectangular blocks, ESDU [68] notes that the force coefficients do not change over the Reynolds number range of 10^4 to $10^{6.}$ However, if the blocks are long in the direction of the flow then there will be a reattachment that is seen to be Reynolds number dependent. As shown earlier in Figure 1-1, the leading edges of the QEC flight deck and the ski-jump both have a radius, a precaution to prevent flow separation; it can also be seen from Figure 1-1 that the front of the ship is rather blunt. Drawing upon studies into the aerodynamics of large road vehicles [69, 70], the rounded leading edge of the small-scale model of the QEC can be expected to have flow separation, while the full-scale ship will not; the CFD methodology was therefore applied to both the experimental and full-scale situations. The inlet velocity profile between the two is also different with a uniform velocity profile applied at the experimental inlet, whilst at full-scale a profile approximating the atmospheric boundary layer over the open ocean was applied at the inlet. By performing CFD simulations of both the experiment and full-scale the differences in Reynolds number and inlet conditions were investigated.

1.10 **Analysis of Airwake Effects on Shipborne Aircraft**

The generation of high-fidelity ship airwakes at varying WOD conditions using CFD provides a database which can be integrated with different analysis tools to allow interrogation of the airwake's effect on the aircraft's forces and moments, as well as aircraft handling and pilot workload. When the airwake is integrated within a piloted flight simulation environment, such as described in Section 1.7, investigations into the airwake's effect on the aircraft and pilot workload may be conducted. A major part of the research reported in this thesis (Chapter 5) involved integrating the QEC airwakes with a generic helicopter model in a piloted flight simulation to provide an in-depth analysis of the effect of the airwake on the pilot and the helicopter during recovery to the QEC.

While piloted flight simulation is an effective SAI analysis tool, it requires expensive simulation facilities and the availability of highly trained test pilots. Tools such as the Virtual AirDyn (VAD), a helicopter forces and moments analysis technique [71] described in detail in Chapter 6, does not require a pilot in-the-loop and provides an objective interrogation of the airwake's effect on the aircraft. By conducting a VAD analysis of the QEC SAI, an investigation into the effect of the QEC airwakes on a helicopter's forces and moments was conducted. The results of this analysis were compared with the simulated flight test data to identify any correlation in the two airwake analysis techniques.

As in the research being reported in this thesis, previous research into the interaction of ship airwakes with aircraft has largely been focussed on maritime helicopters. Although the BAE Systems F-35B simulator successfully integrated the QEC airwakes with a fixed-wing aircraft model, it has not been possible to conduct a detailed analysis of how the air velocities within the airwake affect the forces and moments on the aircraft model used in the Warton Simulator (because of security restrictions). However, as a first step to investigating the requirements for fixed-wing integration, an aerodynamic model of a generic STOVL aircraft has been developed (Appendix A), which allows the airwake velocity components to be distributed across the surfaces of the aircraft, thereby generating both unsteady forces and moments on the airframe.

1.11 Project Aims and Objectives

The aim of the research reported in this thesis is to improve the understanding of the air flow over the Queen Elizabeth Class aircraft carriers and how it affects aircraft operations. A major objective of that aim is to provide experimental data to compare with the preliminary full-scale airwakes that were obtained in a previous project. How the air flow affects aircraft operations has been pursued through rotary-wing flight simulation and the development of an aerodynamic model of a generic fixed-wing STOVL aircraft.

To meet the overall aim, the following objectives were pursued:

- Develop an experiment to provide unsteady velocity measurements of the flow over a model of the QEC.

- Develop a CFD model of the experiment.

- Perform experimental measurements and compare results with CFD of the experimental study, and of the full-scale ship for multiple WOD azimuths.

- Perform a simulated helicopter flight trial in a piloted simulator to investigate wind conditions and angles over the QEC and, by in-depth analysis of the results, demonstrate the potential for using modelling and simulation to support helicopter FOCFTs.

- Analyse the effect of the airwake on a helicopter using the Virtual AirDyn (VAD), an unpiloted airwake analysis technique, and compare the results with the piloted simulation.

- Develop a high-fidelity method to integrate the unsteady flow velocities contained in a ship's airwake with a generic fixed-wing STOVL aircraft.

- Compare the high-fidelity fixed-wing airwake integration method with existing techniques.

1.12 Chapter Summary and Thesis Outline

This chapter has described the challenge pilots face when operating aircraft to and from the flight deck of a ship. The pilot will often encounter dynamic ship motion, a degraded visual environment, and the presence of an invisible airwake produced by the air flow shedding off the ship's superstructure. The risk to the pilots and operators is increased during FOCFTs when the aircraft will be operating with the ship for the first time, and at the limits of the operational envelope. Modelling and simulation of the SAI was successfully used by BAE Systems prior to the F-35B's FOCFTs with HMS Queen Elizabeth to reduce the risk by providing a safe environment for pilots and operators to conduct simulated trials. The CFD methods used to compute the ship's airwake are complex and validation of the computed flow must be performed by comparing the CFD solution with experimental measurements. High-fidelity modelling of the airwake not only provides a highly realistic simulation environment for pilots, once integrated with a flight simulator, but also allows the flow to be investigated using offline tools (without a pilot in-the-loop).

Chapter 2 will outline the development of the experimental method used to measure the flow over a small-scale model of the QEC submerged in a large water channel. Chapter 3 introduces the CFD method and its application to both the experimental study and the full-scale ship. Chapter 4 compares the measurements obtained from the experiment with CFD of the experimental flow. A comparison of the data with the full-scale ship is also provided to investigate the effect of Reynolds number on the airwake flow features. Chapter 5 describes how the airwakes were integrated with a full-motion flight simulator and provides results from simulated flight trials, conducted in a piloted simulator, which show how the QEC airwakes affect helicopter pilot workload. Chapter 6 details the VAD method used to quantify the unsteady loads imposed onto the helicopter by the airwake. To advance the development of unsteady simulation tools for fixed-wing aircraft, Appendix A describes a method used to integrate the unsteady velocities of the airwake over the wingspan of a fixed-wing generic STOVL aircraft model. Finally, Chapter 7 summarises the main findings of the research and provides conclusions and recommendations.

Chapter 2

Experimental Study of the QEC Carrier Airwake

As described in Chapter 1, the project being reported in this thesis has followed an earlier PhD project [52], in which CFD was used to compute the unsteady air flow over the full-scale HMS Queen Elizabeth for implementation in the BAE Systems F-35B/QEC flight simulator. It was recognised from the outset of Kelly's research that it would be necessary to provide experimental data to compare with the CFD computations and preparations were made for this, i.e., an experimental facility was designed and commissioned by Kelly [52]. However, because of the size of the task, the validation phase of the research was not completed and therefore forms a major part of the research this thesis. This chapter describes the development and application of the experimental method used for measuring the unsteady velocity components in the airwake; a comparison of the measurements with the CFD will be presented in Chapter 3.

The experiment was carried out by submerging a 1.4 m long small-scale model (1:200) of the QEC in UoL's recirculating water channel; flow velocities over and around the ship were measured using ADV. Because of the large differences in scale, and hence Reynolds number, between the full and experimental scale, the CFD method was applied to both the experimental conditions and the full scale. Good agreement between each CFD solution and experimental measurements of the steady and unsteady velocities will provide confidence in the CFD method to simulate realistic disturbances to the aircraft during flight simulation by accurately modelling the flow over the QEC.

2.1 The Recirculating Water Channel

The experimental measurements were carried out in the recirculating water channel shown schematically in Figure 2-1. The working section is 3.7 m long, 1.4 m wide, and has an adjustable floor to give water depths between 0.15 m and 0.85 m; for this study, the water depth was 0.8 m. While water speeds can be carefully controlled up to a maximum speed of 6 m/s, for the current experiments an inlet velocity of 1 m/s was adopted to minimise disturbance at the generally smooth water surface in the open channel. A brass honeycomb flow-straightener in combination with a contraction upstream of the open channel working section ensures a uniform velocity profile at the section entry, while water jet injection at the start of the working section adds flow across the width of the channel at the free surface to maintain the uniform velocity profile at the surface [72]. Figure 2-1 shows the position of the 1:200 scale ship model submerged in the working section of the water channel; the ship was attached to the smooth floor of the water channel using suction-cups.

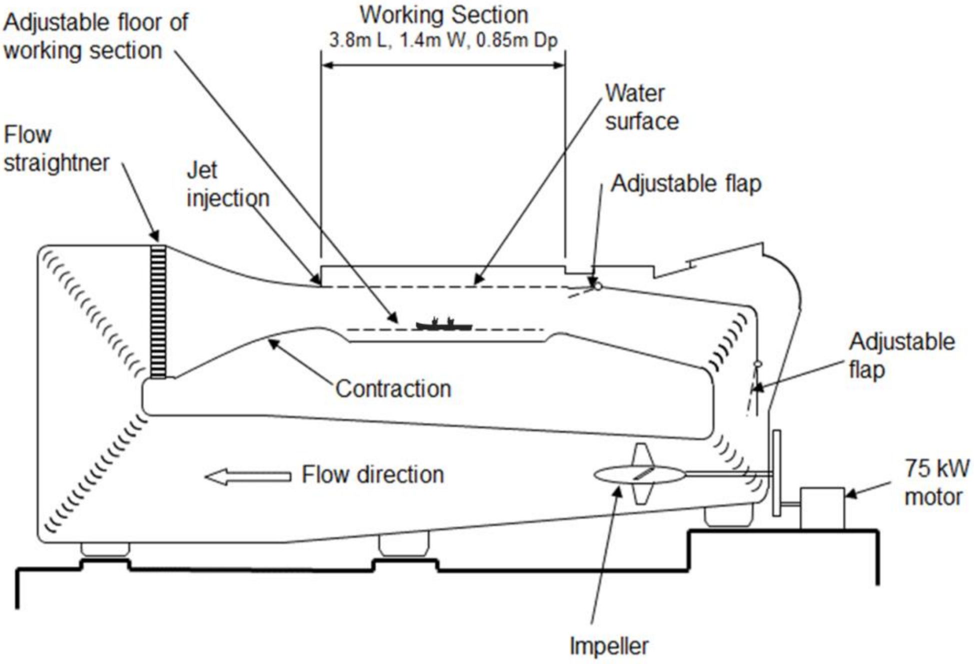

Figure 2-1 Schematic of the University of Liverpool recirculating water channel.

2.2 3D-Printed Scale Model of the QEC

Detailed digital drawings of the QEC were used to create both the 1:200 physical small-scale model and the geometry for the CFD computations. To provide a suitable model for CFD meshing, QEC geometry features smaller than 30 cm (full-scale) were removed. The same QEC geometry used for CFD was used to manufacture a 3D-printed model of QEC to allow direct comparison of geometries.

The size of the model was constrained to maintain a blockage ratio beneath acceptable levels. Defined as the ratio of model frontal area to the experimental test section cross-sectional area, the blockage ratio is typically kept beneath a level of 7.5% for aerodynamic testing to avoid artificial flow acceleration over the model that would not be experienced in the real world [73]. When the ship is placed directly into the flow, i.e., equivalent to a headwind, the working section blockage is approximately 3.2%. The 1.4 m long model also allows the ship to be placed across the full width of the water channel if a side-on (beam) flow was needed.

The experimental model, Figure 2-2, was manufactured using three-dimensional printing techniques to create a water-resistant model with sufficient stiffness and rigidity to withstand the oncoming flow when submerged in the water channel. The hull was manufactured from ABS (Acrylonitrile Butadiene Styrene) in three interlocking sections using Fused Deposition Modelling, as were the ski-jump and islands; the main mast located on the aft island was manufactured from cobalt chrome using Direct Metal Laser Sintering, due to the higher stiffness required for this slender component. All the manufacturing was carried out at BAE Systems' Additive Layer Manufacturing Centre. The ABS components, particularly the sloping ski-jump, required some additional finishing to obtain a smooth surface due to the effect of rasterization, which is inherent to the additive layering process. The Reynolds number of the 1.4 m long scale model of the ship in a uniform flow of 1 m/s was 1.57×10^{6} which, although not as high as the typical full-scale Reynolds number (of the order of 10^{8}), is still well in excess of 10^{4} which is commonly recognised as being required for Reynolds number independence for flows over bluff bodies [74].

Figure 2-2 Assembled 1:200 scale model of HMS Queen Elizabeth.

The hull had been designed by Kelly [52] to be hollow to reduce manufacturing time and cost, as well as the overall weight. Five suction cups were attached to the underside of the hull sections to secure the model to the smooth floor of the water channel using a vacuum pump; a CAD model showing the suction cups (in blue) attached to the underside of the QEC model can be seen in Figure 2-3. The model was secured to the floor of the water channel to allow convenient access over the flight deck for flow measurement. A more detailed description of the design and manufacture of the model is given by Kelly in [52].

Figure 2-3 Underside of the QEC 1:200 scale model.

2.3 Traverse System

A Nortek Vectrino Plus ADV probe, was attached to a traverse system that had been mounted on the water channel by Kelly [52]. To achieve positional accuracy and repeatability for each chosen measurement point, a three-dimensional programmable traverse system was used. Each traverse component is driven by a stepper motor controlled via stepper cards mounted in a control unit, which is connected to a computer via USB. The user is able to input a series of commands to move the attached instrument to a specified location. The positional accuracy of the traverse is 0.1 mm in each direction of movement. Using the in-built distance tool of the ADV probe, the sample volume could be positioned within 1 mm in the x, y and z direction producing a total approximate positional accuracy of 1.1 mm, which was checked at regular intervals.

A program was developed by the author to integrate the movement of the traverse with the ADV measuring software, allowing a series of sample points to be measured consecutively without the need for further user input, decreasing the time required to measure multiple sample points. The traverse, with its three stepper motors providing movement in three axes, was controlled through the software MINT Workbench [75]. The ADV measurement probe was controlled through the Vectrino Plus Software. MINT workbench and Vectrino Plus may be controlled through ActiveX allowing integration of the probe and the traverse with the National Instruments software LabVIEW [76]. The LabView program was developed in order to provide a return to a fixed datum of the ADV after each use in addition to datum selection, live view of the probe metrics such as signal/noise ratio (SNR). A number of point locations can be fed into the program via a text file to be measured automatically.

2.4 Acoustic Doppler Velocimetry

ADV is a velocity measurement technique that was originally developed for measuring water velocities in rivers and marine currents. Over the years, ADV has been refined and is now also used as a laboratory-based instrument and was selected for this project because it is relatively inexpensive, easy to use and provides good accuracy. Although there are disadvantages, as discussed in the following section, it has proved to be a very convenient and effective instrument.

2.4.1 ADV Method

ADV measures three-dimensional velocity components at a point in a flow through the detection of small variations in acoustic signal frequency due to the Doppler effect [77]. First developed in the 1990s to characterize fluid flow and turbulence [78], the ADV probe consists of a central transmitter around which several receive transducers are attached and focussed on a small sampling area typically 5 cm from the transmitter. The original ADV probe was developed with three receivers; however, the more recently updated Vectrino Plus probe shown in Figure 2-4 has a fourth receiver, added to improve turbulence measurements and to provide redundancy.

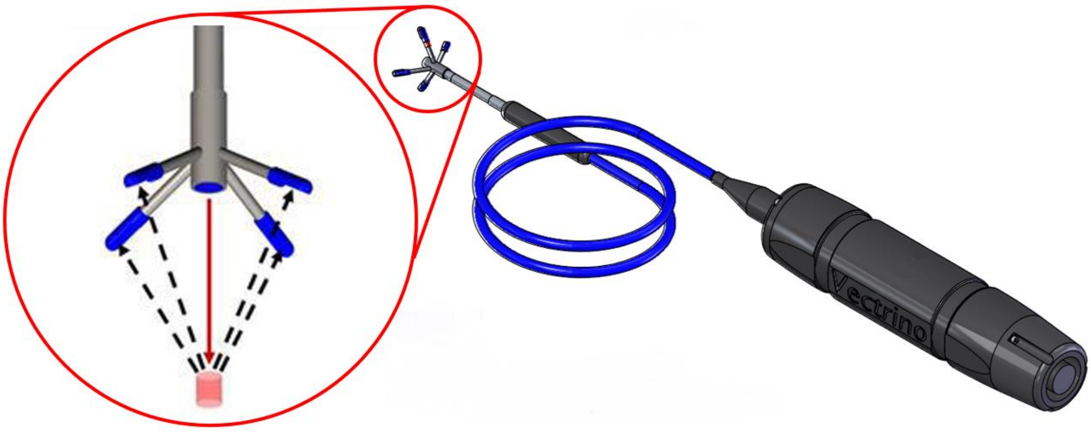

Figure 2-4 Nortek Vectrino Plus ADV downward-facing probe showing the arrangement of transmitter and receivers focussed on the sampling volume.

A short 10 MHz ultrasonic pulse is sent from the central transmitter to a location at which each of the receivers are focussed, called the sampling volume. The reflection of the transmitted pulse from particles within the sampling volume are then detected by the receivers shown in Figure 2-4. The recorded reflection from each of the receivers is processed to find the Doppler shift, enabling the velocity in each of the three components to be measured. The quality of the velocity measurements relies on the strength of the reflected signal from the particles in the sampling volume. The signal strength (amplitude) is used by the ADV software as a signal-to-noise ratio (SNR) to measure the data quality. A consistent SNR value of above 15 dB is recommended for valid mean and turbulence measurements [79]. Both the amount of seeding within the fluid and the transmitted acoustic power will affect the SNR value. Another measure of data quality is correlation, which quantifies the similarity between the two pulses being measured [79]. The Vectrino normalizes the correlation to an interval between 0 and 100%. A high correlation provides confidence that the probe is receiving the two original pulses initially transmitted and is computing a valid phase shift. By discarding measurements, a certain correlation threshold, beneath 70%, the variance of the dataset can be reduced. However, care must be taken as high correlation is not always indicative of a valid measurement of the flow and should be used alongside SNR to provide confidence in the accuracy of the measured values.

When conducting field measurements, such as in rivers, oceans or basins, the water often contains naturally occurring suspended material that reflects the transmitted signal back to the receivers. However, in the laboratory, the water is normally 'clean' and requires the user to add seeding particles [80]. The recommended seeding for use in the laboratory should be spherical in shape, have a density close to that of water to give almost neutral buoyancy, and be around 10 μm in size [78]. As the centre of the roughly cylindrical sampling volume is located approximately 50 mm from the pulse transmitter, ADV velocimeters are considered to be non-intrusive [81]. The diameter of the sampling volume is 6 mm, and the height of the sampling volume may be adjusted in the range 3-15 mm by the user. A sampling volume of 7 mm was used for all experimental measurements taken in this study to reduce signal noise.

2.4.2 Speed of Sound

The speed of sound in water, used to calculate the Doppler shift, is dependent on the water temperature, pressure and salinity [82]. Figure 2-5 shows the effect of salinity for a range of temperatures at a depth of 0.6 m [83]. Although the salinity and pressure of the water used in the laboratory is known and remains constant, the temperature of the water can fluctuate hourly. Therefore, to accurately compute the velocity of each component a temperature reading must be taken regularly. Most modern ADV probes such the Nortek Vectrino shown in Figure 2-4 have a thermistor embedded in the probe to provide up-to-date temperature readings at 1 Hz [84]. The Vectrino temperature measurement of the water was regularly checked against a handheld mercury thermometer.

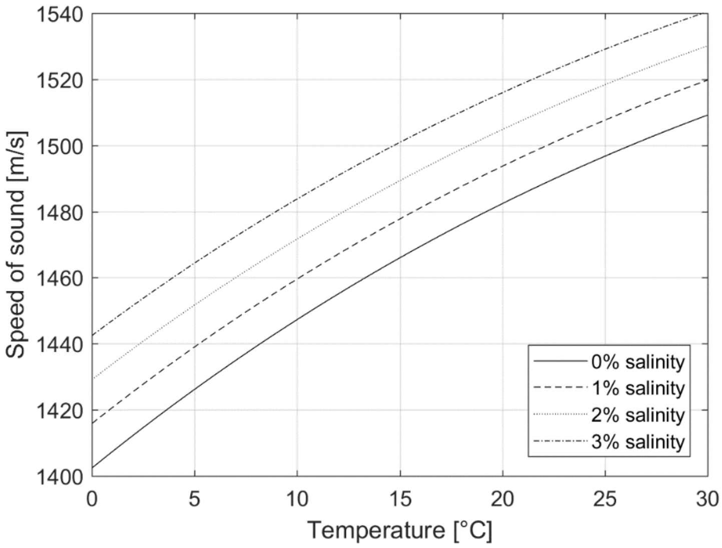

Figure 2-5 Speed of sound in water at 0.6 m depth.

2.4.3 Post-processing of Raw Data

The raw measurements recorded by the probe should not be used without post-processing due to the presence of erroneous 'spikes' in the data [85]. Spikes can occur in the raw signal due to aliasing of the Doppler signal in which a phase shift between the transmitted and reflected pulse exceeds the phase angles range $-\pi$ and π. Other spikes are caused by the flow velocity exceeding the user's chosen velocity range, or by proximity to a boundary, which reflects previously transmitted pulses to the receiver, thereby contaminating the signal. A method to eliminate spikes in the data was proposed by Goring and Nikora [86], which was then modified and implemented in the widely used software program WinADV [87]. Figure 2-6 shows an example of the despiking method used to remove spurious data. The data was obtained by placing the ADV probe sampling volume in the centre of the water channel at mid-height and recording data for 10 seconds. The uniform inlet velocity was set to 1 m/s. Several large spikes can be seen in the unfiltered *u*-velocity data in the top plot of Figure 2-6 which, after processing by WinADV, have been removed as can be seen in the bottom plot of Figure 2-6 showing the despiked (filtered) time history of *u*-velocity.

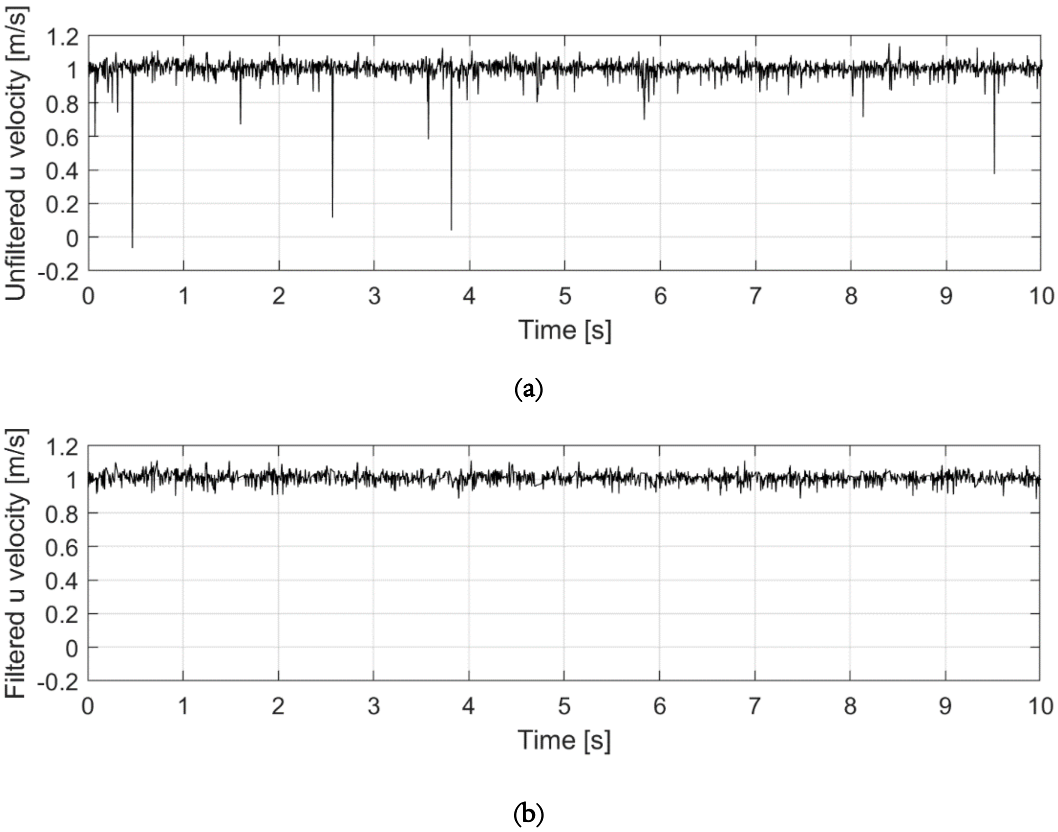

Figure 2-6 Freestream velocity time history (a) before and (b) after despiking.

2.4.4 Probe Orientation

ADVs have been shown, in a range of laboratory and field conditions, to provide mean three-component velocities and Reynold stress values to within 1% when compared with LDV [88]. However, due to the geometry of the probe and the presence of signal noise, the ability of the ADV to report accurate turbulent measurements is compromised; this is the disadvantage of using ADV referred to above. The signal recorded by the ADV's receivers contains a level of noise from a combination of Doppler noise, signal aliasing and velocity gradient across the sampling volume, with Doppler noise producing the largest impact upon measured data in the two velocity components normal to the acoustic transmitter [89, 90]. As Doppler noise is characterised as unbiased white noise, averaging the data leaves the mean three-component velocities unaffected [91, 92]. However, turbulent statistics from the data recorded in the two velocity components normal to the probe's transmitter cannot be recovered accurately due to increased levels of Doppler noise. As a result, only the turbulence in the direction of the flow aligned with the transmitter is measured accurately for each probe orientation, along with the three mean-velocity components. Two differently orientated probes (sidewards- and downward-facing) have been used in this study to obtain the turbulence measurements in the vertical and lateral components.

According to the manufacturer, the probe transmitter should not be placed in the direction of the freestream flow, because it will interfere with the flow, so preventing reliable turbulence measurements in the freestream direction [79]. The sideward-looking probe, shown in the left of Figure 2-7, allows turbulence to be measured in the lateral direction, while the downward-facing probe in the right of Figure 2-7 allows turbulence measurements in the vertical direction. When using the two probes, care must be taken to position the two sampling volumes so they coincide. As the mean velocity in each component is accurate for both probes, they can be compared to ensure consistency of flow measurements.

Figure 2-7 Nortek Vectrino Plus ADV sideward- and downwards-looking probes

Before conducting any experimental measurements, both probes were placed in the open channel to measure the water velocity at the same position to compare the mean and turbulent statistics of the undisturbed freestream flow; turbulence is calculated as the root-mean-square (RMS) of the unsteady velocity fluctuations from the mean. Each probe was aligned in the centre of the channel with a uniform inflow velocity of 1 m/s and a background turbulence intensity of around 1%. Velocity measurements were then sampled over one minute at 200 Hz. Figure 2-8 shows the three components of velocity of the downward-facing probe. Only 10 seconds of data are shown, but the means and standard deviations were calculated for 60 seconds of data. Figure 2-8 (a) shows that the freestream *u*-component is within 1% of the value that was set for the freestream flow, consistent with the probe manufacturer's specification. The mean *v*- and *w*-velocity components, as shown in Figure 2-8 (b) and (c) respectively, are essentially zero and are within the specified accuracy of 1% of the freestream velocity. The signal is noisy in the *u*- and *v*-components, and significantly less so in the *w* component, which is aligned with the acoustic transmitter. Figure 2-9 shows the corresponding data for the sideward-facing probe. The mean *u*-, *v*- and *w*-velocities are again within 1% of the expected values, and the *v*-velocity component, which is aligned with the transmitter, has much lower noise than the other two components.

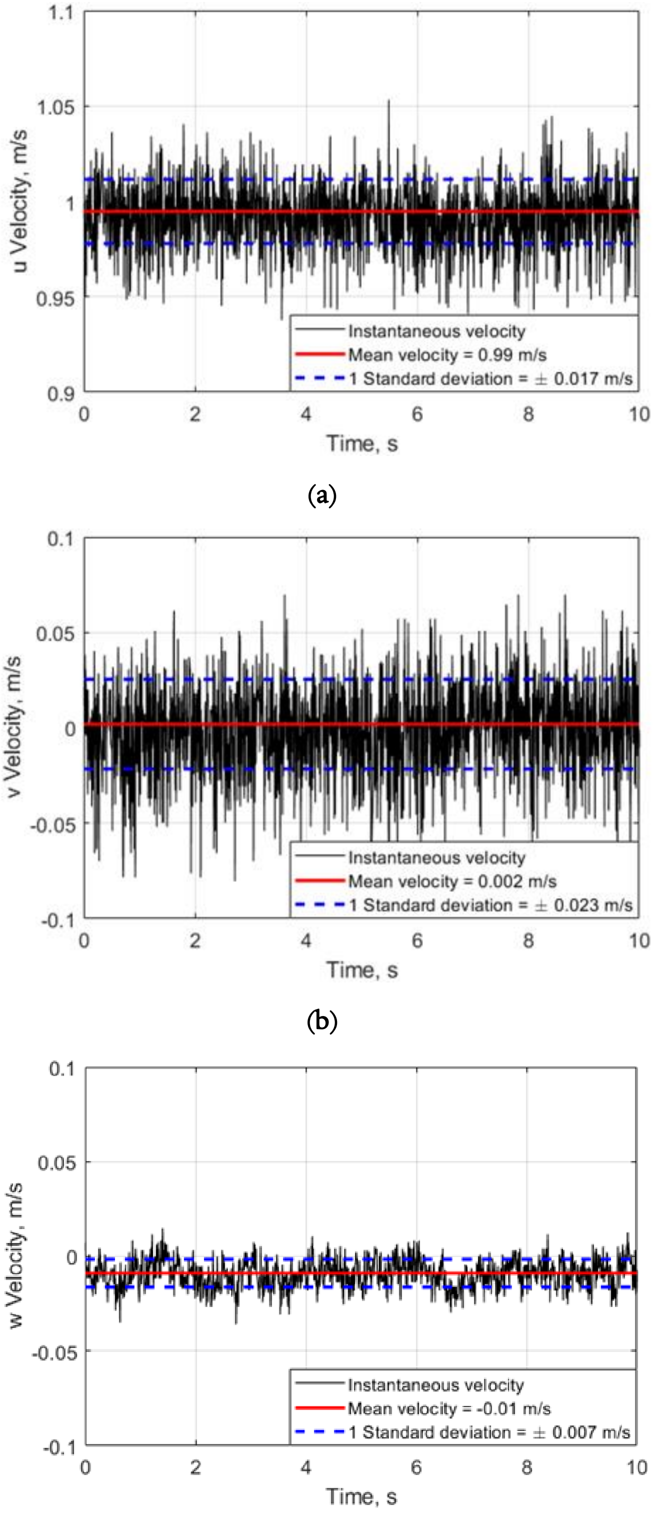

(a)

(b)

(c)

Figure 2-8 Free-stream time histories of velocity components measured by downward-facing ADV probe.

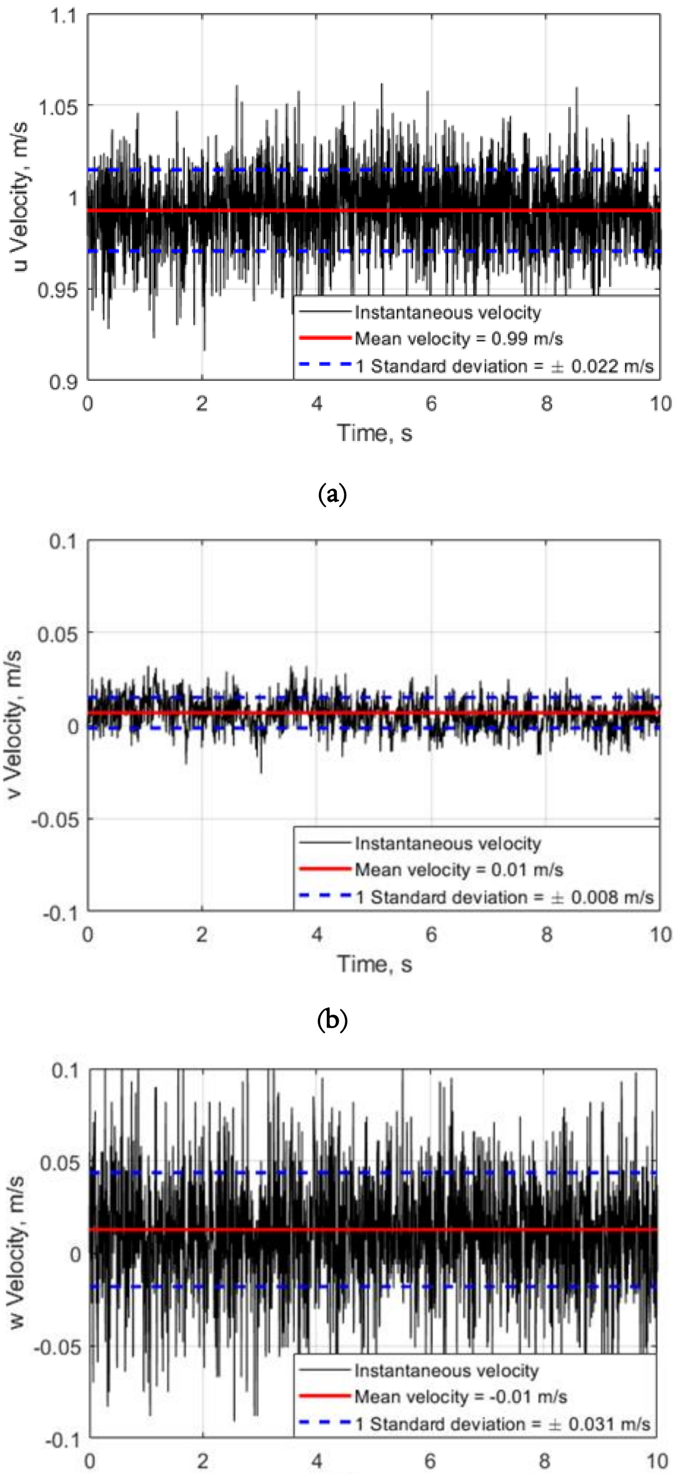

(a)

(b)

(c)

Figure 2-9 Free-stream time histories of velocity components measured by sideward-facing ADV probe.

Figure 2-10 shows histograms of the velocity components for each probe orientation; a low spread of values, and a high occurrence, is seen in the *w*- and *v*-components of velocity for the downward and sideward-facing probes respectively, corresponding with the alignment of the transmitter. The velocity components normal to the transmitter direction have a wider spread of data that fit well with the overlaid normal distribution shown in Figure 2-10. Both probes gave a turbulence intensity of about 1% in the correctly aligned lateral and vertical components, indicating that the inlet turbulence was isotropic, as expected.

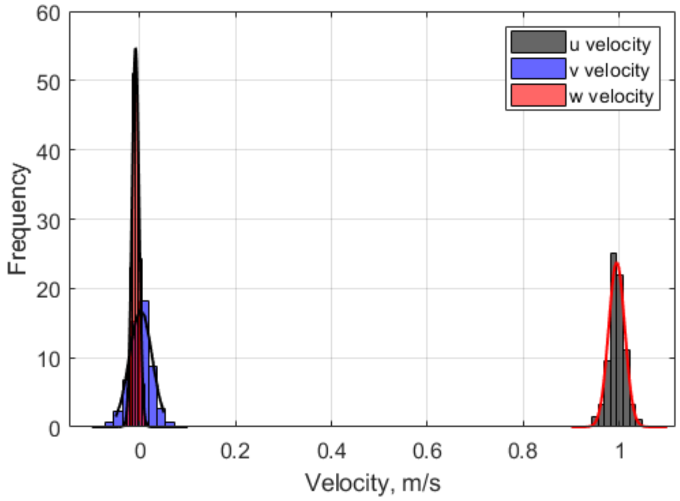

(a)

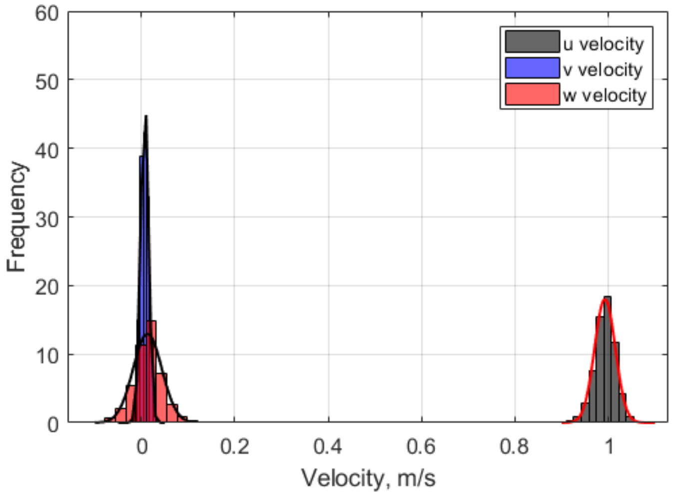

(b)

Figure 2-10 Histograms of velocity components measured by (a) downward and (b) sideward-facing probes for a 1 m/s freestream condition.

2.4.5 Water Tunnel Inlet condition

A uniform inlet was chosen for simplicity and to allow direct comparison with CFD of the water channel experiment. Prior to experimental testing the flow inlet condition of the water channel was measured. Figure 2-11 shows the water channel inlet profile measured using the sideways-facing probe positioned 1 m from the inlet of the working section (along the centreline of the water channel) at intervals in height from the floor up to a maximum height of 37.5 cm (the QEC model is 17.5 cm high).

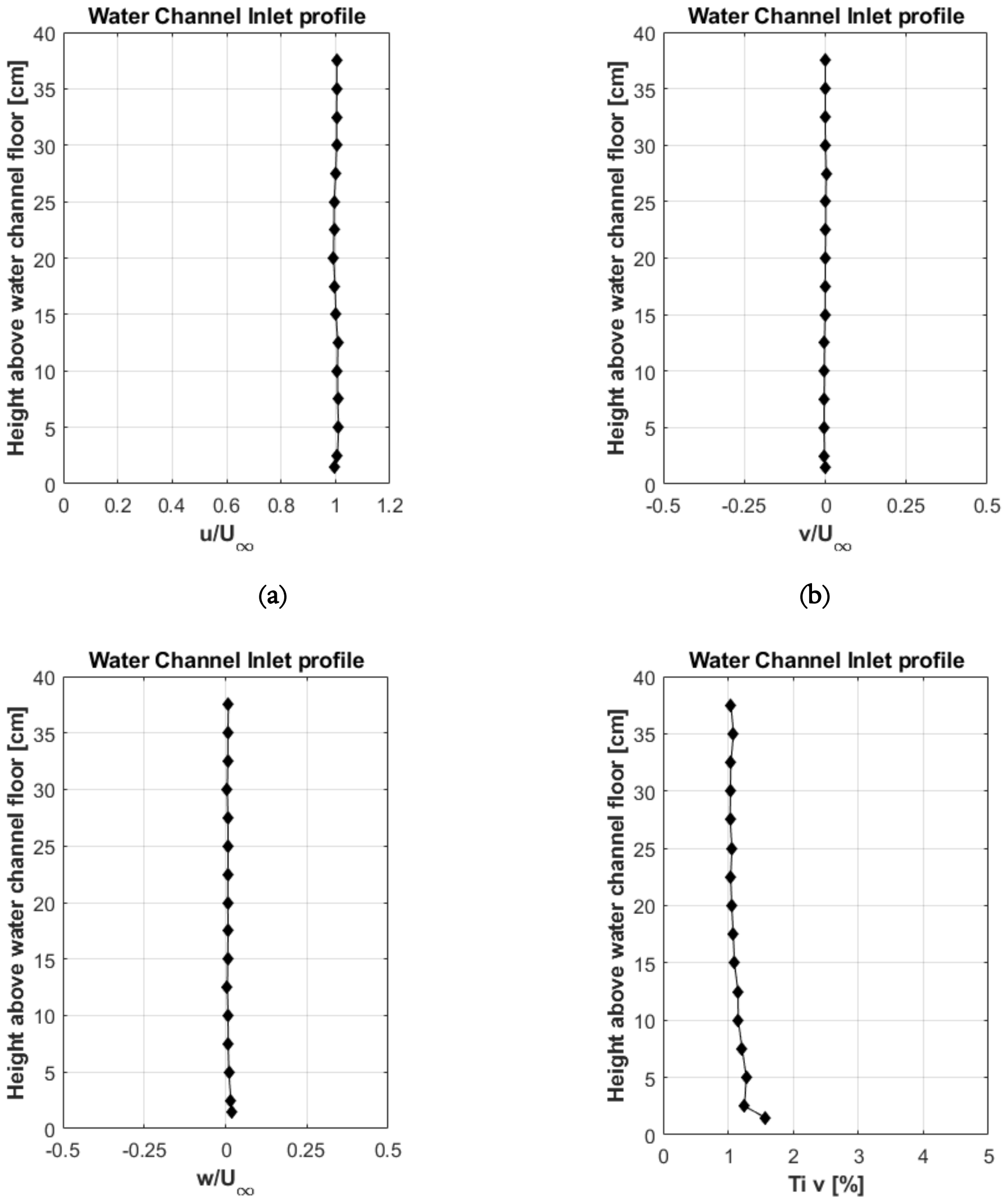

(a)

(b)

(c)

(d)

Figure 2-11 Water Channel Inlet profile (a) *u*-velocity (b) *v*-velocity (c) *w*-velocity and (d) lateral turbulence intensity.

2.4.6 ADV Near-Boundary Measurements

As the velocity measurements are to be used to compare with CFD predictions of the QEC airwake, it is desirable to measure experimental velocities close to the surface of the experimental model. The ADV probe transmits a signal which is reflected off the particles within the sampling volume to provide mean and turbulence measurements of the flow. When the probe is placed close to the boundary of a surface the transmitted signal may be reflected, by the boundary, back to the receivers, so causing interference. There is also some uncertainty about what happens when the 7 mm deep sampling volume comes up against the solid surface of a boundary.

2.4.6.1 Reflectivity Due to Boundary Composition

As identified above, ADV point measurements taken near a boundary (e.g., a solid wall or a muddy riverbed) are subject to interference from reflections of the transmitted signal off the boundary. If the strength of the signal reflected from the boundary is comparable with the signal from the flow seeding, the velocity measurements may become biased [93]. It has been previously shown that the level of near-boundary interference is dependent on the boundary composition, surface angle and roughness [94]. The magnitude of the reflected signal from boundaries of varying compositions may be modelled using fluid ray theory [95]. In the present study it was necessary to take velocity measurements as close as possible to the solid surface of the ship model to understand how well the boundary layer is captured by the CFD. Therefore, to provide further information on the performance of the ADV for near-wall measurements, a supplementary study was conducted where the ADV probe was used to obtain velocity measurements close to surfaces made of five different materials; the experiment will be described in the next section.

The transmitted acoustic signal from the probe in water can be approximated as a plane wave. When a plane wave encounters a boundary with a sharp change in density, a fraction of the sound energy will be transmitted into the boundary, while the remaining sound energy will be reflected [95]. Figure 2-12 shows an idealized fluid ray theory model of a two-dimensional representation of a planar boundary at $z = 0$, between two materials of dissimilar density and speed of sound. The arrows indicate the wave vector for an incident plane wave at grazing angle θ_w, the angle of the incident/reflected wave with the surface, and the resulting reflected and transmitted plane waves. All three have the same horizontal components.

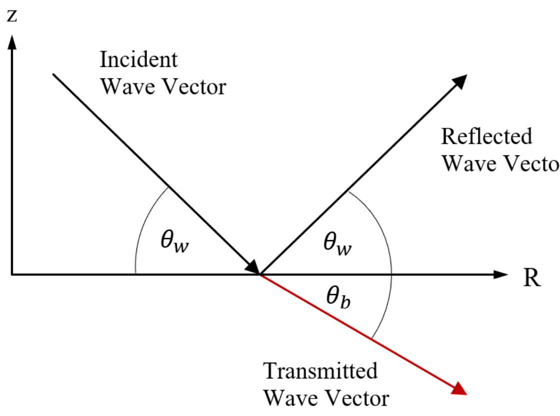

Figure 2-12 Two-dimensional representation of a planar boundary, z = 0, between two dissimilar fluids.

According to Snell's Law, shown in equation 2.1, the angle of the transmitted wave depends on the angle at which the incident wave interacts with the boundary, and the speed of sound, *c*, of each material.

$$\frac{c_w}{\cos\theta_w} = \frac{c_b}{\cos\theta_b} \tag{2.1}$$

By imposing the continuity of pressure condition across the boundary, $z = 0$, the Rayleigh or reflection coefficient can be solved:

$$R(\theta_W) = \frac{Z_b - Z_w}{Z_b + Z_w} \tag{2.2}$$

with

$$Z_w = \rho_w c_w / \sin\theta_w \qquad Z_b = \rho_b c_b / \sin\theta_b \tag{2.3}$$

where Z_b and Z_w are the specific acoustic impedances of each material, being equal to the ratio of acoustic pressure to particle velocity in the direction normal to the boundary and evaluated at the boundary. The plane wave, or Rayleigh, reflection coefficient, *R*, gives the magnitude of the reflected pressure wave and is defined as the ratio between the two characteristic acoustic impedances. At grazing angles below a critical value, the boundary will reflect all of the energy back into the water medium, i.e., total internal reflection occurs. Transmitted waves at the critical angle and above will propagate into the boundary material, reducing the magnitude of the reflected signal. The critical grazing angle is given by Snell's law in equation 2.4 and shows that as the ratio of c_b/c_w increases, the critical angle will also increase.

$$\theta_c = \cos^{-1}(c_w/c_b) \tag{2.4}$$

$$BL = -20\log|R| \tag{2.5}$$

Bottom reflection loss (*BL*) is defined in equation 2.5 and is a measure of the energy lost by sound propagating into the boundary layer medium. When $|R| = 1$, the reflection loss is 0 dB, total internal reflection has occurred, and no sound energy is lost to the boundary medium. The reader will note the similarity between fluid ray theory and optical theory, albeit with its own terminology such as 'grazing angle' and 'bottom reflection losses'.

The reflection coefficient and bottom reflection loss as a function of grazing angle were calculated for each of the five materials used in the experimental study: ABS, wood (pine), aluminium, polymethyl methacrylate (PMMA), and stainless steel, using the acoustic properties listed in Table 2-1 for each material. Attenuation was assumed to be negligible. Table 2-1 also gives the critical angle calculated using equation 2.4 at which a transmitted wave in water will propagate sound energy into the boundary medium.

Table 2-1 Acoustic properties of materials tested.

	Density	Speed of Sound	Specific Acoustic Impedance	Critical Angle (with water)
	kg/m^3	m/s	$Pa \cdot s/m$	deg
Water [96]	998	1482	1,479,036	-
ABS [97]	1023	2040	2,086,920	43.41
Wood (Pine) [98]	550	3360	1,848,000	63.83
Aluminium [98]	2710	5190	14,064,900	73.41
PMMA [97]	1191	2690	3,203,790	56.57
Steel (stainless) [98]	7500	5083	38,122,500	73.05

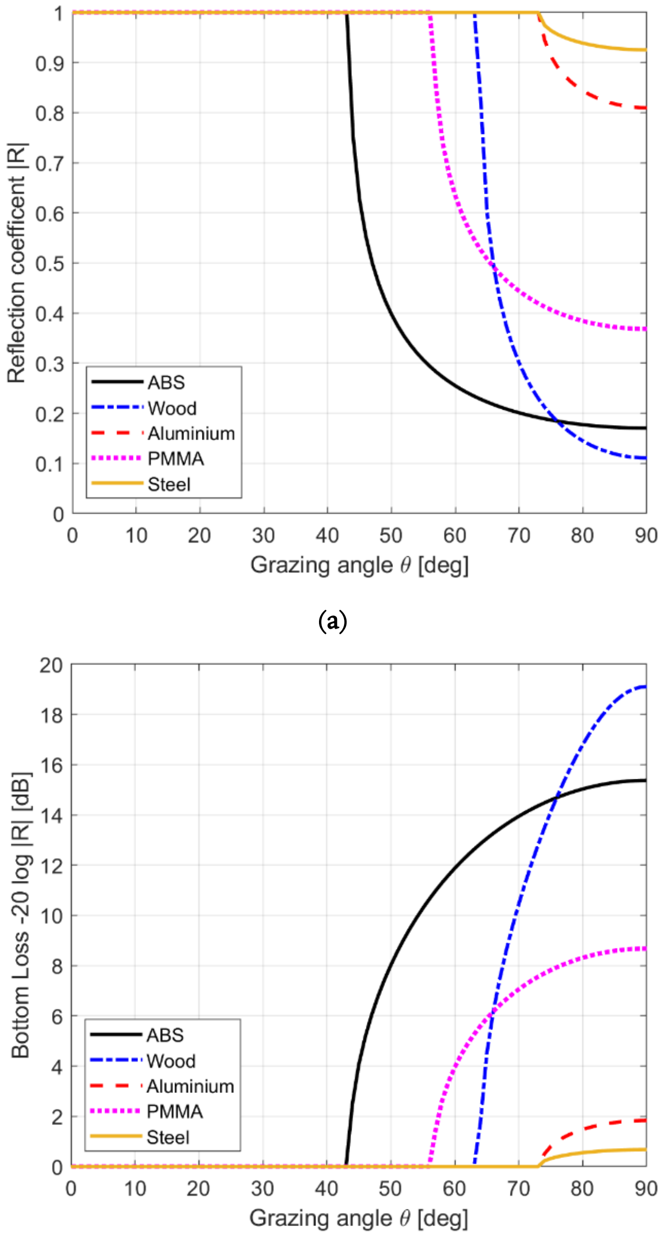

(a)

(b)

Figure 2-13 Sampled materials (a) Reflection coefficient and (b) BL.

Figure 2-13 shows the reflection coefficient and BL for each material as a function of grazing angle calculated using equations 2.4 and 2.5. To improve the SNR for measurements, close to the surface, it is desirable that the surface does not reflect acoustic energy from the transmitter so that it is detected by the receivers. Although the transmitter of the ADV probe is typically orientated towards the normal of a boundary, such as the floor or sidewalls of a water channel, the geometry of an experimental model around which the probe is measuring within the water channel may present an inclined boundary surface; the grazing angle shows this effect on the reflection characteristics. Wood shows the highest signal attenuation when the transmitted signal is normal to the boundary, $\theta = 90$ deg, as seen in Figure 2-13. Although ABS, from which the QEC model has been manufactured, does not provide the maximum signal attenuation of the materials modelled at 90 deg, it does give a relatively high BL for a larger range of grazing angles down to a critical angle value of about 43 deg. The metals, steel and aluminium, both exhibit low bottom loss for high angles of attack and reflect all the transmitted signal energy back into the water for grazing angles below 73 deg. PMMA shows higher attenuation of the signal for a larger range of grazing angles in comparison with the metals. Figure 2-13 suggests that materials such as plastic and wood will present lower boundary interference compared with metals.

2.4.6.2 Boundary Material ADV Experiment

ADV point flow measurements in the water channel were taken at increasing distances from boundaries made of each of the five materials in Table 2-1 to identify the effect of boundary material on measurement quality. An aerofoil shaped blade, with an insert for a sample of each material, as shown in

Figure **2-14**, was submerged in the water channel with the aerofoil pointed into the freestream flow. A wire with a diameter of 0.7 mm, calculated to trip the boundary layer [74], was placed at 10% of the aerofoil chord to ensure the flow over the sample material was consistent by transitioning the boundary layer from laminar to turbulent. The streamlined geometry of the aerofoil shaped blade and the turbulent boundary layer generated by the trip wire provide flow over the material sample broadly independent of sample material roughness; eddies generated by the roughness of the sample material are absorbed in the local turbulence of the boundary layer without significantly altering the boundary layer structure [99].

A sideward-facing ADV probe was then positioned with the transmitter pointed normal to the sample material. The distance of the sampling volume from the material was found with the probe distance check to an accuracy of ± 0.2 mm. The inlet condition was set to a uniform freestream velocity profile of 1 m/s. A total of 16 measurements were taken with the centre of the measurement volume placed at intervals starting 10 mm below the sample material boundary, to a maximum distance from the surface of 30 mm. Clearly, when the ADV is focussed on a point that is within the solid boundary it will not obtain a valid measurement, but the probe was then incrementally moved away from the surface until the measurement volume emerged into the flow. The velocities were recorded for two minutes at each point with the sampling volume set to 7 mm. Each of the point measurements were processed to remove erroneous spikes in the data using the WinADV software.

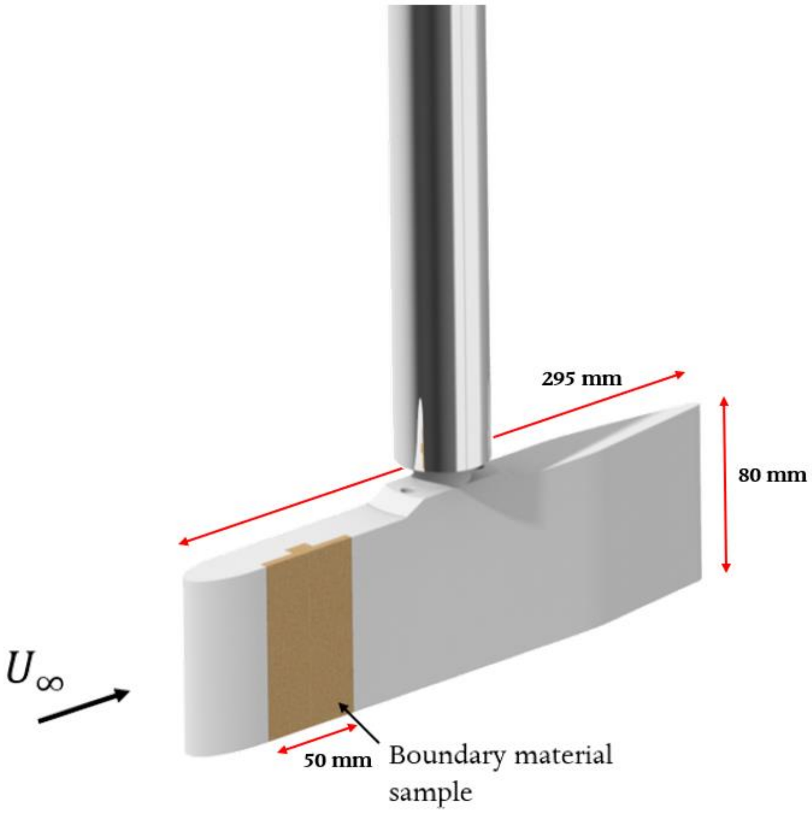

Figure 2-14 Experimental setup of aerofoil blade with interchangeable boundary material sample.

Figure 2-15 shows the average SNR and correlation recorded during the velocity measurements taken at distances from each sample material, the dotted line indicates the boundary/surface of the material. SNR is dependent on both the number of seeding particles and the homogeneity of seeding particle concentration in the water. The seeding particles tends to settle to the bottom of the water channel working section over time. SNR measurements were taken near freestream conditions several times over a period of 7.5 hrs of testing during which the water flume was turned on and off several times. The SNR of these measurements showed a percentage change of less than 0.5% over the 7.5 hrs which indicates that any variation in the SNR was mostly independent on the settling of the seeding particles during material changes.

The SNR of each recorded sample in Figure 2-15 (a) is above the recommended lower limit of 15 dB, and as the height above the boundary is increased, the SNR is relatively constant. When the sampling volume is placed beneath the boundary, the SNR increases and becomes erratic. Figure 2-15 (a) shows that different boundary materials create a change in the SNR ratio of the probe, due to the reflected acoustic signal. The order in which the materials' SNR increases agrees with the level of attenuation shown in Figure 2-13, at a grazing angle of 90 deg. For example, wood shows the highest attenuation in Figure 2-13 (a) and the lowest overall SNR in Figure 2-15 (a) while, steel shows the lowest attenuation in Figure 2-13 (a) and the highest overall SNR.

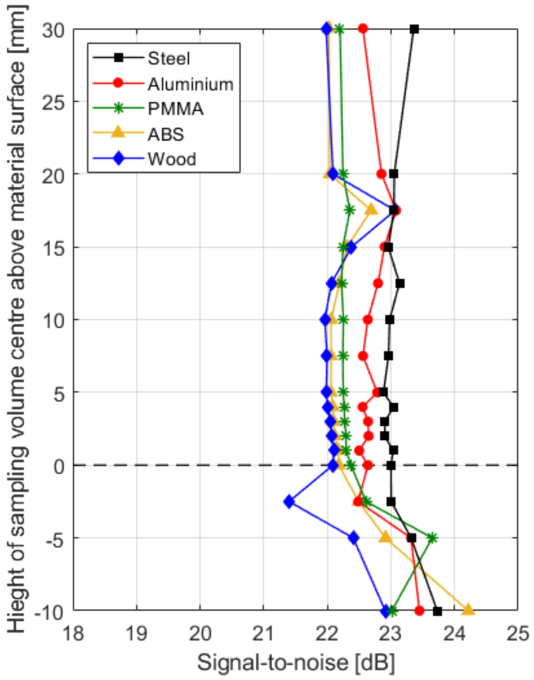

(a)

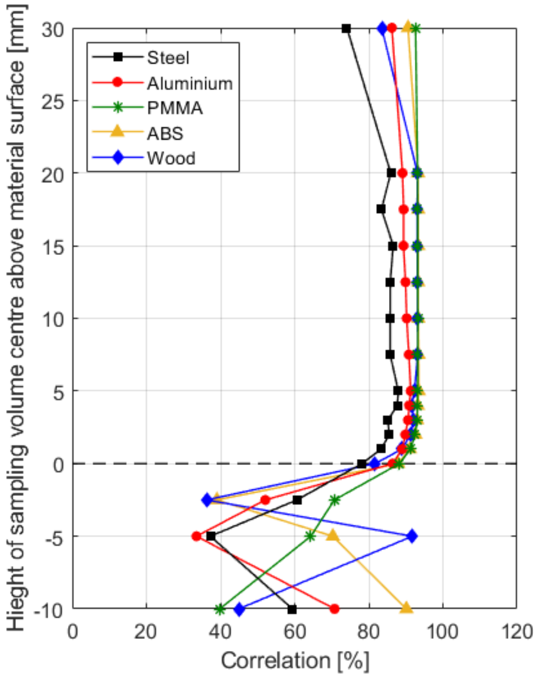

(b)

Figure 2-15 Signal-to-Noise ratio (a) and Correlation (b) of measured data at sampling volume heights above material surface.

The effect of the increase in SNR shown in Figure 2-15 (a) can be seen in the corresponding correlation in Figure 2-15 (b). As the total sampling volume is placed beneath the boundary surface, the correlation reduces significantly, as expected, and becomes erratic. The materials exhibiting lower overall SNR show high correlation values of approximately 93%. Boundaries made of metal, however, show a reduction in correlation, consistent with the observed increase in SNR, as demonstrated by the steel sample which shows the highest SNR and the lowest correlation at each height above the boundary.

The raw ADV flow measurements taken over 2 minutes at each point were filtered to remove any spurious spikes in the data. The remaining data were used to calculate the three mean velocity components and the single component of turbulence of the flow at each point (with the sideways probe, the v-velocity component was aligned with the transmitter). As discussed above, spikes in the data can be caused by velocity aliasing, flow velocities beyond the probe's velocity range, or an indication of contamination in the return signal to the probe caused by reflected pulses off nearby boundaries [86]. If the raw measurements require many spikes to be removed, the sample number is reduced, leading to a decrease in the accuracy of the mean and turbulence. Figure 2-16 (a) shows the percentage of the signal retained after filtering of the raw measurement data by the software WinADV. The non-metallic materials required a low percentage of spikes to be removed. As the centre of the sampling volume was brought below 4 mm and moved towards the boundary, the percentage of spikes in the signal increased to approximately 5%. However, a much higher percentage of spurious data was present in the raw measurements above the metallic surfaces, aluminium and stainless steel. The flow measurements over the aluminium sample required 10 – 40% of the signal to be removed due to the large amount of sample points identified as erroneous data. Raw measurements above the steel sample required a larger range of data, up to a maximum of 50%, to be removed. Consistent with the increase in SNR in Figure 2-15 (a) and the reduction in correlation in Figure 2-15 (b) for the metals, it can be concluded that the corresponding increase in erroneous data, identified as spikes, is due to the material of the surface contaminating the return signal to the ADV probe.

To determine the effect of the reduction in quality of the signal, the turbulence intensity in the lateral direction and the mean velocity in the freestream and lateral components are shown in Figure 2-16 (b) and Figure 2-17, respectively. The turbulence intensity in the *v*-component, Figure 2-16, is calculated by dividing the RMS of the velocity fluctuations by the free stream velocity U_∞ (i.e., 1 m/s).

When the sampling volume is placed beneath the surface, Figure 2-16 (b) shows that the turbulence can 'apparently' be very high and is erratic. The turbulence intensity in the lateral component is approximately 0.7% for all the samples, with the metals showing slightly higher values when the sampling volume is placed 4 mm above the material surface. As the sampling volume is brought closer to the surface from a height of 4 mm, an increase in lateral turbulence intensity is shown for each material, consistent with turbulence characteristics measured in the boundary layer on a flat plate at zero incidence [100].

Figure 2-17 shows the u and v mean velocity components at distances from each boundary material. The lateral, v, component can be expected to be close to zero, while the streamwise, u, velocity should be 1 m/s, although the presence of the experimental aerofoil section will locally distort the flow. As in the figures above, the measurements apparently taken below the surface are erratic, while those above the surface are close to what would be expected, even close to the surface. The measurements for the non-metallic materials are clustered closer together, but even so the mean velocities measured over the steel and aluminium surfaces are also close to the others, despite the effect of the material on the signal quality as discussed above.

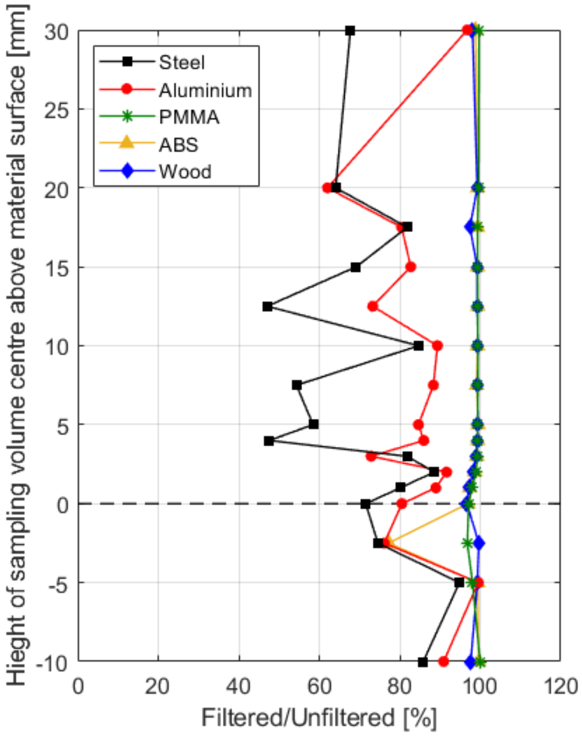

(a)

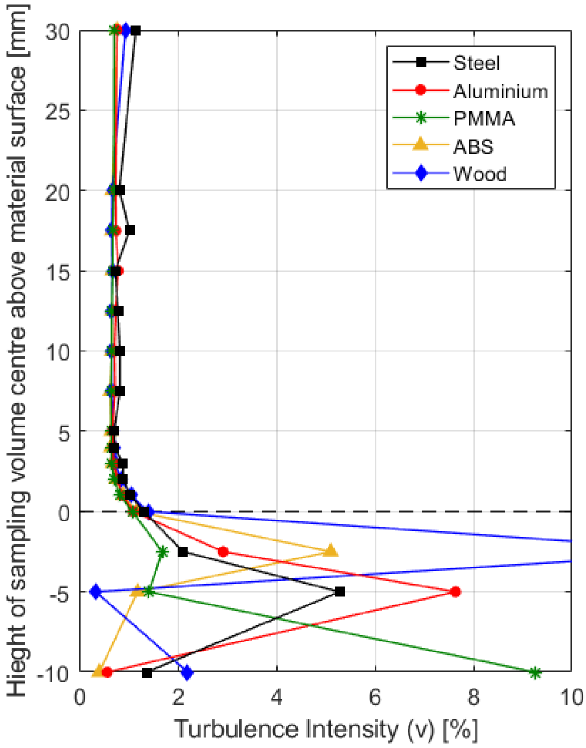

(b)

Figure 2-16 Despiking filter ratio (a) and lateral turbulence intensity (b) of measured data at sampling volume heights above material surface.

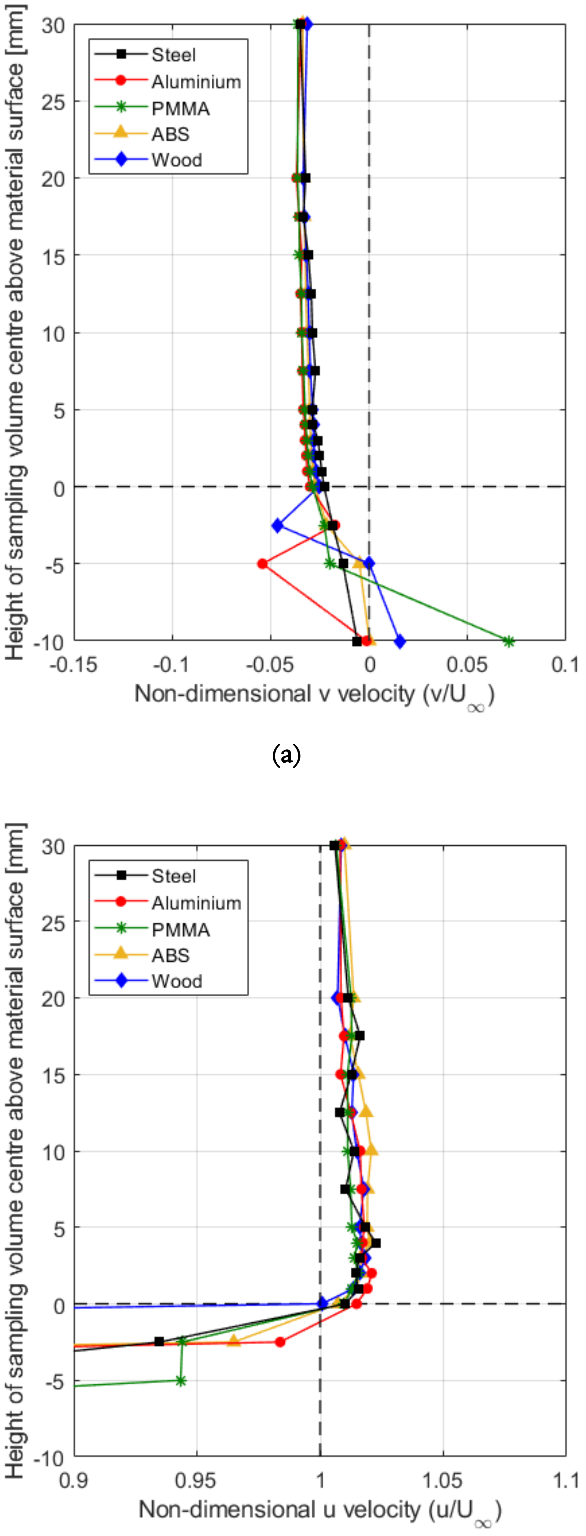

(a)

(b)

Figure 2-17 Non-dimensional mean *u* (a) and *v* (b) velocities of measured data at sampling volume heights above material surface.

The results of the experiment suggest that the quality of the flow measurements near a boundary are dependent on the material of the solid surface. Although the final effect of surface material choice on the velocity measurements was not significant, it is prudent to select a material that has a similar specific acoustic impedance to the fluid, in this case water, to provide higher attenuation of the reflected signal reducing the acoustic noise at the ADV probes receivers. This experiment shows that as the scale-model is ship is built from ABS, the reflected signal will be highly attenuated, compared with metals, reducing the acoustic noise within the ADV signal and providing more accurate measurements.

2.4.6.3 Reflectivity Due to Surface Roughness

As well as the material from which the boundary surface is made affecting the reflected acoustic signal, so too does its surface roughness [101]. A second experiment was, therefore, carried out to provide more information on the effect of surface roughness on near-surface flow velocity measurements; in this case only steel and aluminium were used as they provided the highest reflected signal.

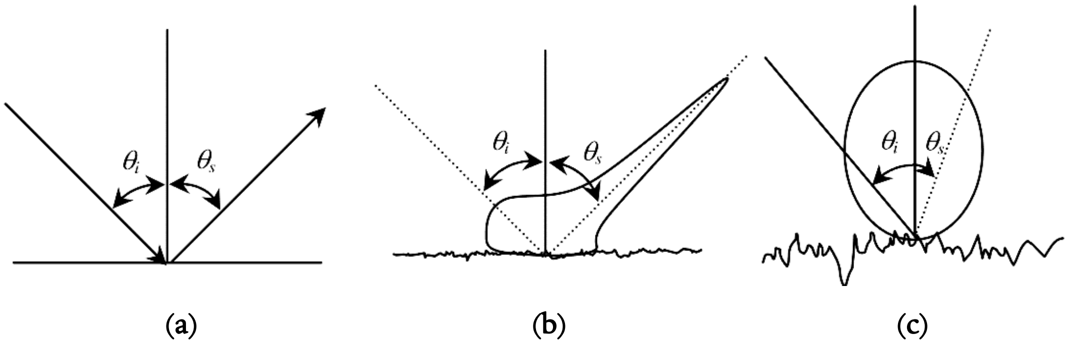

Figure 2-18 Relative contributions of coherent and diffuse scattering components for different surface-roughness conditions: (a) specular, (b) slightly rough, (c) very rough [102].

The reflection of acoustic waves from a boundary creates scattered waves which can consist of coherent and diffuse components. Understanding and predicting these effects could be important for the quality of ADV measurements near a rough surface. Figure 2-18 illustrates the effect of surface roughness on signal scattering [101]. The coherent scattered field is clearly visible in Figure 2-18 (a) and (b), while in Figure 2-18 (c) only a diffuse scattered field is present. The coherent component of the wave propagating in the direction of specular reflection is of particular importance, as the transmitted wave from the ADV probe is often normal to a boundary which reflects the coherent signal back to the ADV's receivers.

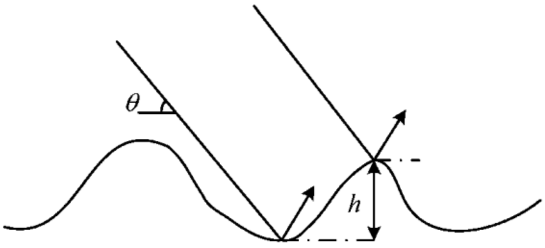

Figure 2-19 Rayleigh roughness parameter.

The Rayleigh criterion is often used to characterise the surface roughness for scattering [103]. If a plane monochromatic wave is incident at angle θ, as shown in Figure 2-19, with a medium wavenumber, κ, then the phase difference can be calculated between two heights on the surface. The phase difference is dependent on the wavelength of the incident wave and for specular scattering is:

$$\Delta\varphi = 2\kappa\Delta h \sin\theta_W \tag{2.6}$$

If $\Delta\varphi \ll \pi$ there is little scattering as the waves interfere constructively. If $\Delta\varphi{\sim}\pi$, there is strong scattering due to destructive interference. By measuring the change in height over the surface by the RMS roughness, σ, the Rayleigh criterion is defined by equation 2.7.

$$R_a = 2\kappa\sigma \sin\theta_W \tag{2.7}$$

Equation 2.7 shows that the roughness parameter used to find the scattering of the wave depends on the wave number and the incident angle, as well as the surface roughness. Through the application of the Kirchoff approximation (tangent plane approximation), the reduction in coherent reflection is given by:

$$R_{coh} = Rexp\left(-\frac{{R_a}^2}{2}\right) \tag{2.8}$$

2.4.6.4 Boundary Surface Roughness ADV Experiment

The Rayleigh criterion shows that the reflectivity of an incident monochromatic wave can be altered by changing the wavelength of the wave or the roughness of the surface boundary. The reflectivity of a boundary, as the previous section suggests, impacts the quality of the return signal of an ADV probe to its receivers. By changing the surface roughness of the boundary, the reflectivity of the boundary may be reduced, resulting in an increase in the quality of the return signal to the ADV probe. This section compares experimental ADV measurements close to a boundary of differing materials and surface roughness with the theoretically calculated noise attenuation by each sample. Two metals, steel and aluminium, each with an arbitrarily rough and smooth surface finish were used as the boundary close to which ADV probe flow measurements were taken. The reflectivity of each metal (when smooth) is high in comparison with other materials previously tested, as shown earlier in Figure 2-13, which led to lower quality ADV data, as shown in Figure 2-15. By changing the surface roughness, the high reflectivity of these metals may be reduced to provide higher quality ADV flow measurements close to their surface. Table 2-2 gives the surface roughness of each metal sample tested measured perpendicular to the surface pattern lay using a Surftest 301 profilometer.

Table 2-2 Surface roughness of materials tested.

	Arithmetic Average, Ra	RMS roughness, σ
	μm	μm
Steel (smooth)	0.73	0.91
Steel (rough)	5.86	7.15
Aluminium (smooth)	0.75	0.98
Aluminium (rough)	24.96	30.38

The impact on coherent reflectivity from each sample was calculated using the Rayleigh criterion, equation 2.7, with surface roughness from Table 2-2 and the 10 MHz wavelength of the transmitted ADV signal. The total bottom loss of each material sample, smooth and rough, was then computed using the reflectivity due to the surface material, as previously shown in Figure 2-13 (a), and the reflectivity due to surface roughness. Figure 2-20 shows the theoretical total bottom loss calculated for each sample. The inclusion of surface roughness for each smooth metal sample shows there is little difference to the bottom loss calculated in Figure 2-13. However, as the surface roughness of the steel sample was increased to 7.15 μm from 0.91 μm, the bottom loss increased from 1.8 dB to 3.4 dB at a grazing angle of 90 deg. The surface roughness of the rough aluminium sample was measured at 30.38 μm, resulting in a much higher bottom loss of 29.5 dB at 90 deg grazing angle compared with the 0.7 dB bottom loss calculated from the smooth aluminium sample with a surface roughness of 0.98 μm. The larger increase in surface roughness of the aluminium sample increases the bottom loss to more than 5 dB in the grazing angle range of 25-90 deg. Figure 2-20 suggests that by increasing the surface roughness of a boundary material, the bottom loss will increase, resulting in a higher quality of ADV flow measurements near a surface as less noise is reflected back to the ADV's receivers.

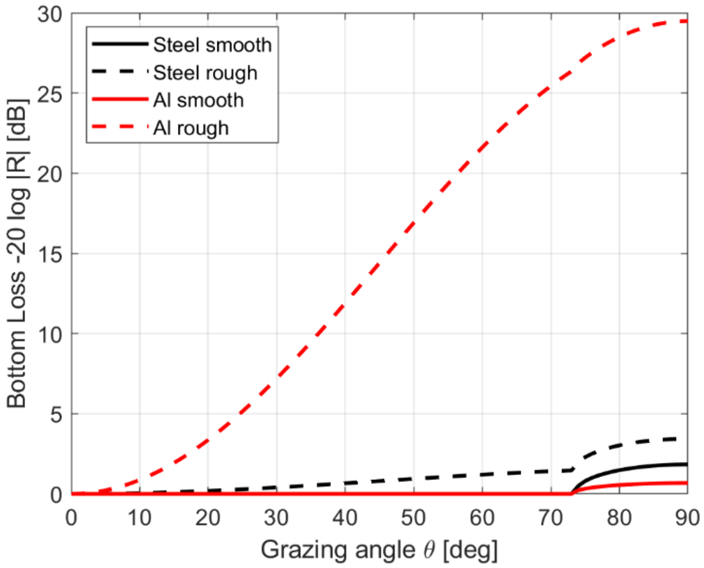

Figure 2-20 BL of steel and aluminium due to reflectivity and surface roughness.

ADV measurements were taken in the water channel at increasing distances from the smooth and rough metallic surfaces to identify the effect of boundary surface roughness on measurement quality. The acoustic properties of each metal were those listed in Table 2-1. The experiment was performed in the same manner as previously described for investigating the effect of surface materials and using the sideways facing probe. Each sample was inserted into the aerofoil shaped blade shown in

Figure 2-14. A total of 16 measurements were taken for the different surfaces with the sampling volume placed at intervals starting 10 mm below the sample surface, to a maximum height of 30 mm. The flow was recorded for two minutes at each point. Each of the point measurements were processed by the WinADV software to remove erroneous spikes in the data. Figure 2-21 (a) shows the average SNR over the two-minute sampling time at the different distances from each of the four surfaces. The increase in surface roughness of aluminium and steel is seen to decrease the SNR and is consistent with the increase in bottom loss calculated for each rough sample and shown in Figure 2-20. The SNR of each rough sample in Figure 2-21 (a) is comparable with the SNR found for materials of a lower reflectivity such as ABS, shown in Figure 2-15 (a). The average correlation of the ADV measurement at each distance from the sample surfaces is shown in Figure 2-21 (b). At sample volume heights above 7.5 mm the rough samples give higher correlation values compared with the smooth samples. Below 7.5 mm the rough steel sample maintains correlation values above the smooth steel sample. The aluminium rough sample produces lower correlation values than the aluminium smooth sample below 7.5 mm, and it is suggested that the surface of the particularly rough aluminium sample is altering the flow field above the surface, creating more turbulence and reducing the correlation.

Figure 2-22 (a) shows the percentage of unfiltered data retained after de-spiking has been applied to the raw data to remove any spurious measurements. As shown earlier in Figure 2-16 (a), measurements in the flow over each of the smooth metal samples contained a large number of spikes resulting in a much lower number of samples compared with the other materials tested. Increasing the roughness of the steel and aluminium surfaces reduces the number of data points that are filtered, and this is believed to be due to the rough surfaces scattering the reflected signals so there is less corruption of the acoustic signals detected by the ADV receivers.

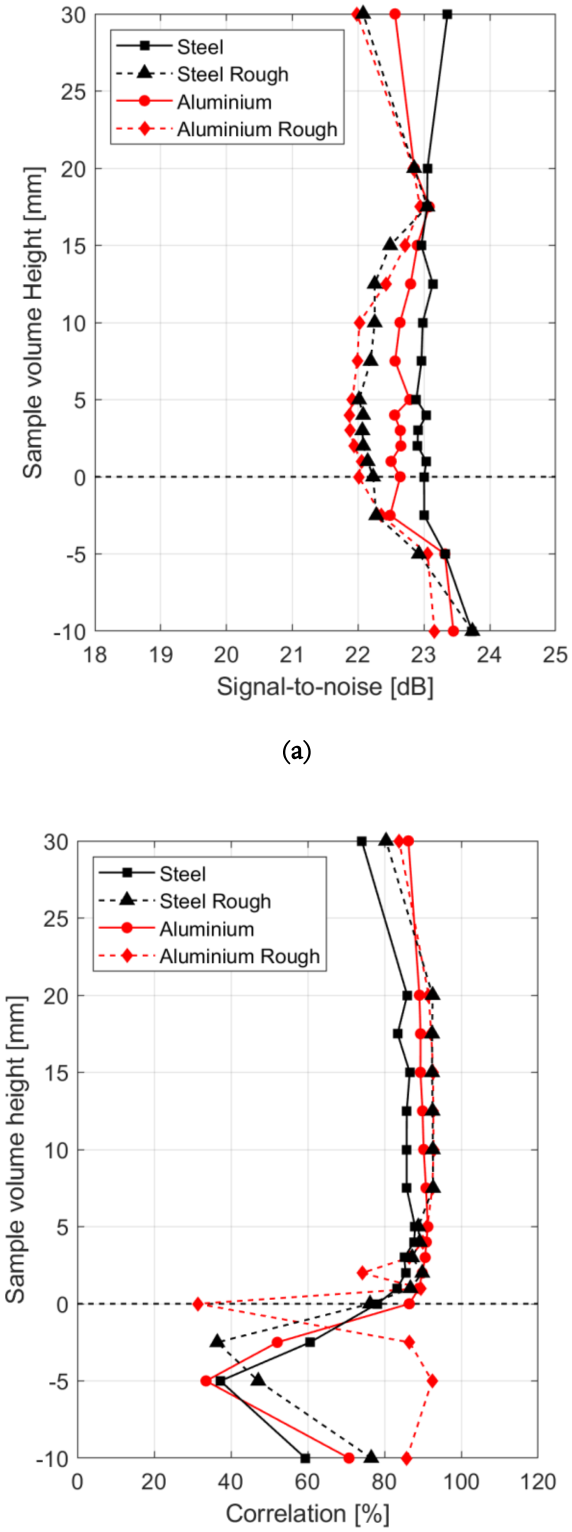

(a)

(b)

Figure 2-21 Signal-to-Noise ratio (a) and Correlation (b) of measured data at sampling volume heights above material surface.

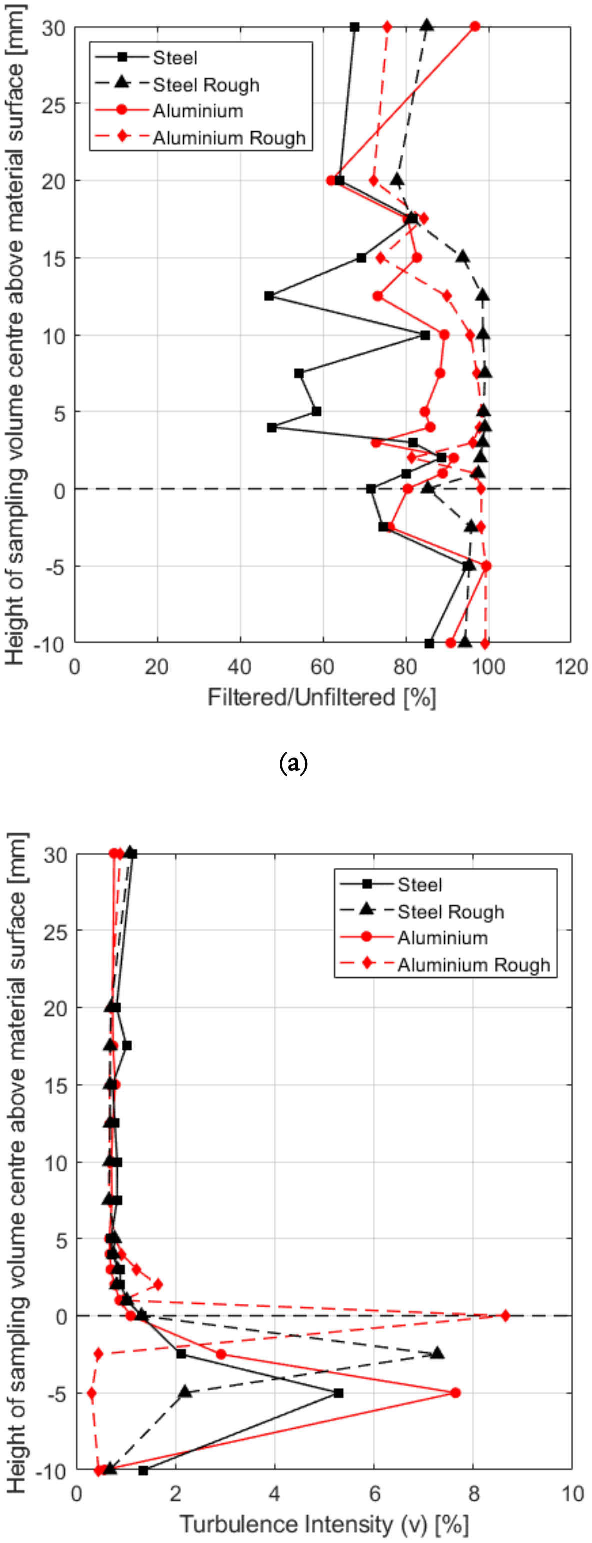

(a)

(b)

Figure 2-22 Despiking filter ratio and lateral turbulence intensity of measured data at sampling volume heights above material surface.

Turbulence intensity in the lateral direction, normal to the surface, for each measurement at distances away from the surface is shown in Figure 2-22 (b). In general, the effect of roughening the surfaces on the measurement of lateral turbulence is inconclusive and not particularly significant, except that closer to the surface, within 5 mm, the particularly rough aluminium surface may have increased the turbulence in the flow. Figure 2-23 shows the measured lateral and streamwise velocity components; as mentioned above, these would be expected to be close to 0 and 1 m/s, respectively, with some local distortion due to the presence of the test plate. As can be seen in Figure 2-23, the measured velocities are close to what was expected and, while there are some differences for the different surfaces, these are not significant except close to the surface, where the roughness may have affected the local water velocity and turbulence.

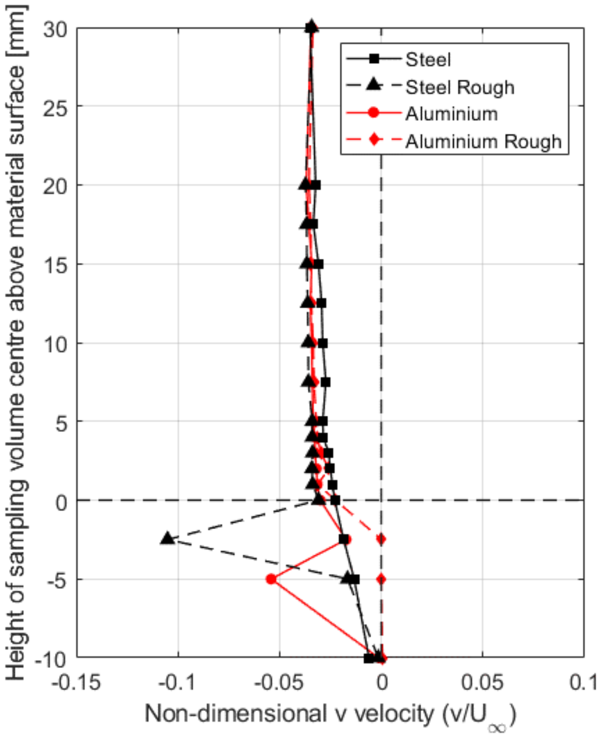

(a)

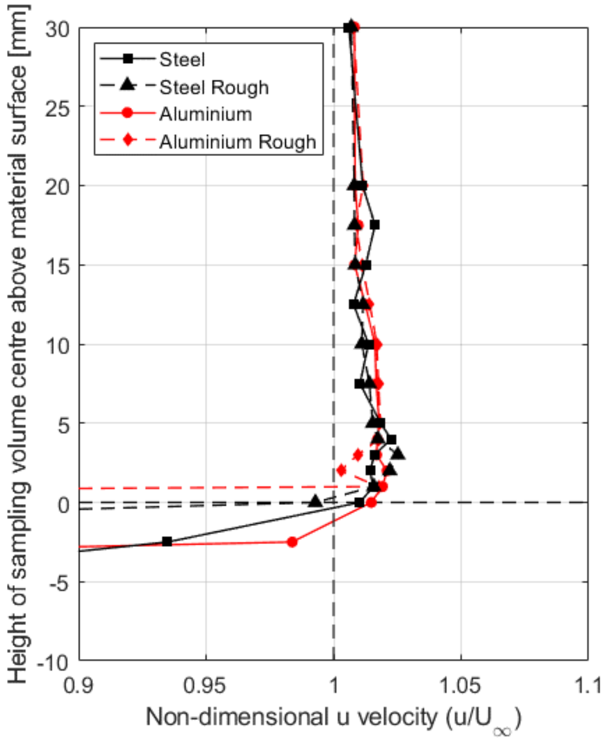

(b)

Figure 2-23 Non-dimensional mean *u* and *v* velocities of measured data at sampling volume heights above material surface

Overall, therefore, the investigation into the use of ADV close to a surface has demonstrated that even though half of the sample volume will be obscured by the wall when the measurement point is at the surface, good measurements of mean velocity and turbulence are still possible. The investigation into the acoustic reflections from the surface show that a smooth acoustically reflective material, such as steel and aluminium, will adversely affect the signal detected by the ADV receivers due to the transmitted acoustic signal being reflected from the boundary surface. Roughening the surface can be beneficial in that the uneven surface scatters the reflected signal. The material of the QEC experimental model is ABS, which has been shown to have a low reflectively. An added benefit of the detailed study into the ability of the ADV to measure water velocities close to the surface of the QEC model is that much has been learnt about the instrument and the signal processing requirements. The ADV has been found to be a very effective instrument, even though each prone orientation can only measure turbulence in one component.

2.5 QEC Experimental Model Testing Procedure

Ships can sail in any heading relative to the wind; however, for an aircraft carrier deploying fixed-wing aircraft, the captain will typically steer the ship into wind so that the relative winds approach from close to Ahead. It was, therefore, decided that the experiments to measure the airwake over the ship would be conducted with the ship aligned with the flow or with a small yaw angle. Figure 2-24 shows a schematic of the QEC models position within the water channel's working section in Ahead WOD. Beam (90 deg) winds could also be of interest, because they present very different flying conditions. However, even though the experiment was designed so that the scale model could be placed across the water channel, the option to measure the beam airwake was not pursued as it was outside the scope of this project.

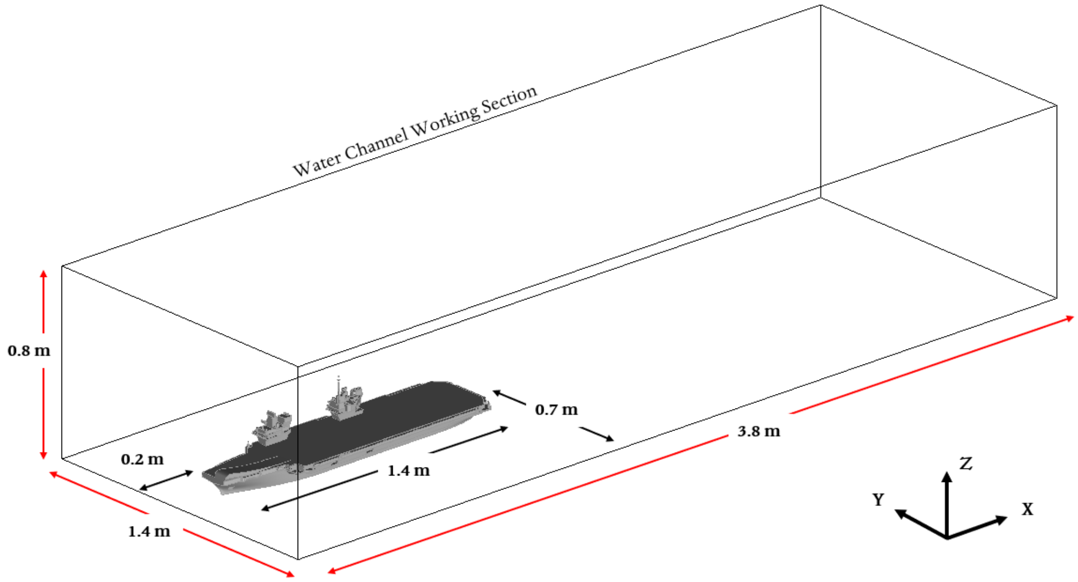

Figure 2-24 Schematic of the QEC model in the water channel working section.

2.5.1 WOD Conditions

The 1:200 scale QEC model was submerged in the working section of the flume and aligned with the flow to simulate a headwind as shown in Figure 2-25 (a), and 10 deg off the ship's centreline to simulate the flow coming from 10 deg off the starboard side of the ship shown in Figure 2-25 (b); this wind direction is referred to as Green 10. For each orientation, the model was positioned close to the working section inlet to allow measurements of the ship's airwake to be conducted further downstream of the ship in the area where the F-35B descends along a sloping approach path towards the ship for landing, i.e., the SRVL, as shown in Figure 1-3. The water channel inlet velocity was set to 1 m/s which, as well as being a convenient value for nondimensionalization, also created minimal disturbance at the generally smooth water surface in the open channel.

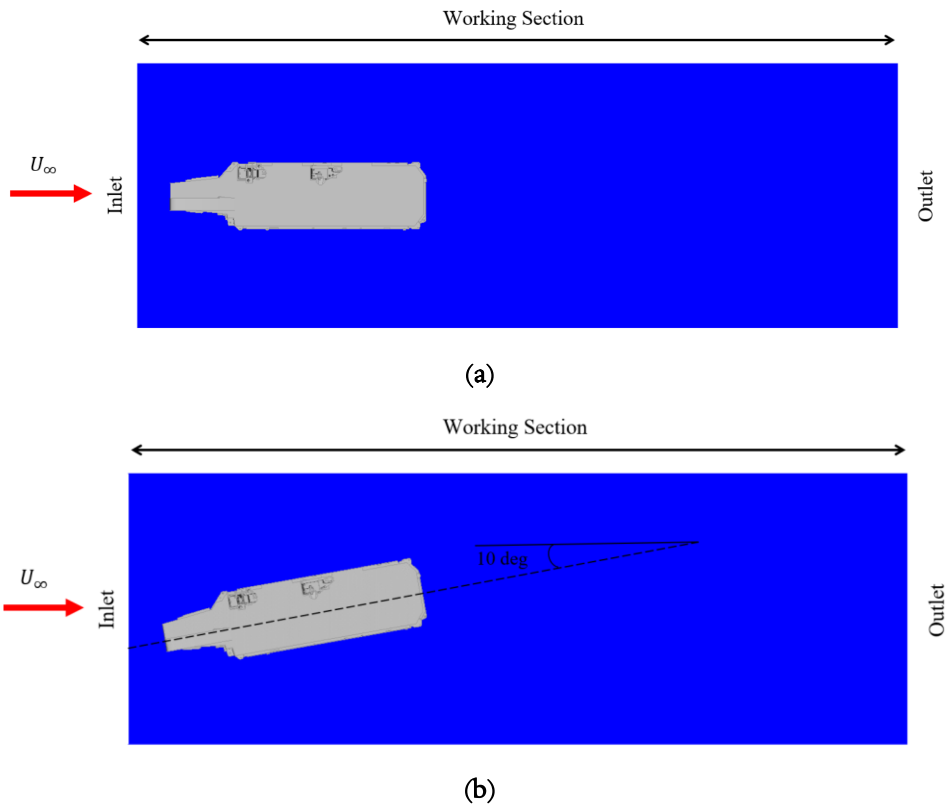

(a)

(b)

Figure 2-25 QEC Model Orientation in Water Channel in a (a) Ahead and (b) Green 10.

2.5.2 Location of Measurement Points

The three-dimensional electronic programmable traverse system enabled a large number of measurements to be taken in a much shorter time period compared with previous testing regimes in the water channel. Additionally, it was possible to more easily move the ADV along the sloping approach flight path with the ship yawed at 10 deg. Figure 2-26 illustrates the complete experimental setup showing the ADV probe, attached to the 3D traverse system, measuring the flow over the 1:200 scale model of the QEC. Below the water surface, as shown in Figure 2-27, the probe can be seen positioned between the two islands measuring the wake velocities for comparison with the numerical CFD predictions. Figure 2-28 shows a schematic of the probe and the sampling volume relative to the ship model in the water channel.

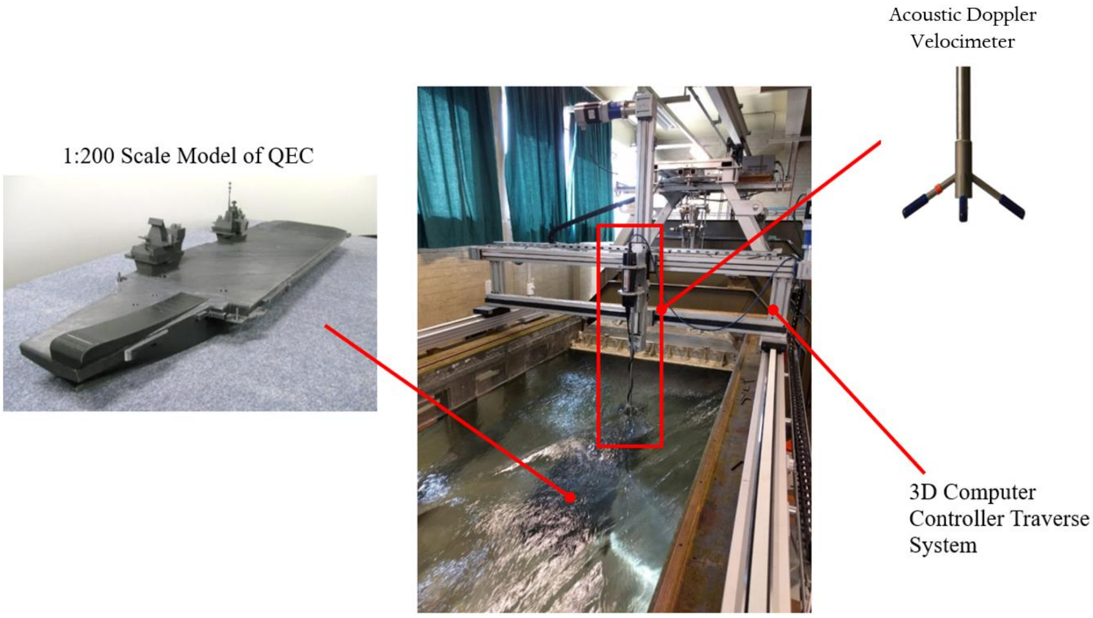

Figure 2-26 Water channel Experimental Setup.

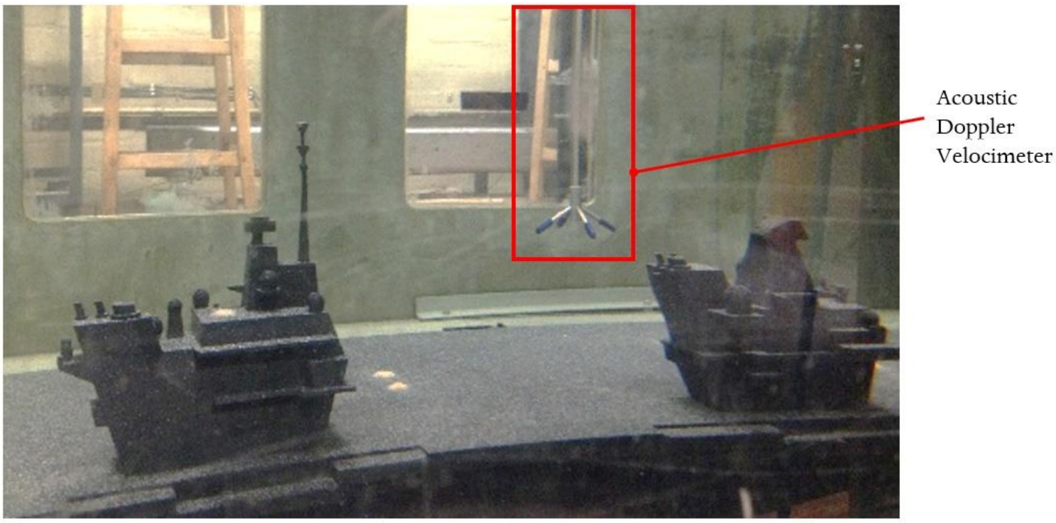

Figure 2-27 ADV flow measurement of a sample point in the wake of the submerged QEC model.

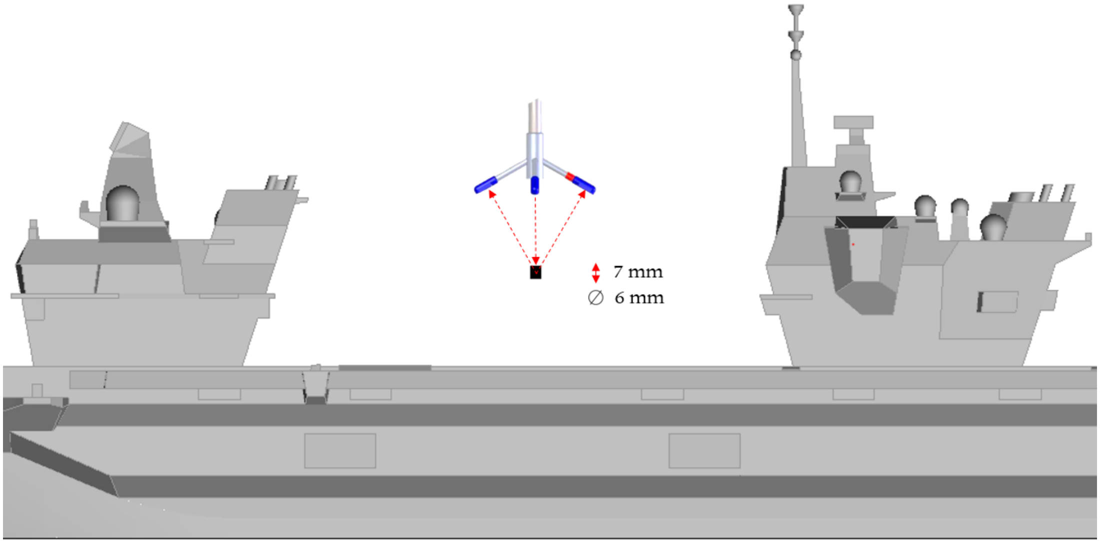

Figure 2-28 ADV probe and sample volume relative to the ship model.

As discussed previously, the ADV is capable of measuring mean velocities effectively in three directions but can only measure turbulence in the direction of the transmitter. The flow over the model ship was, therefore, measured separately with a downward facing probe and a sideways probe, so that profiles of turbulence could be obtained in the lateral (*v*) and vertical (*w*) directions. Measurements taken using the sideways facing probe were used to compare the mean velocity and turbulence in the lateral *v*-component, while measurements taken using the downwards facing probe were used to compare the mean velocity and turbulence in the vertical *w*-component. As each probe measured the mean velocities in each of the three components and the lateral/vertical turbulence intensities, regular comparison of the equivalent measurements from each probe was conducted to identify any anomalous data. The mean measurement data in each component at each sample point showed consistently good agreement. The mean *u*-velocity component used to compare the experimental wake with the CFD was taken from the sideways facing probe. It was important to be sure that the two probes were taking measurements at the same points, which was achieved using the programmable traverse. In total, approximately 1,500 measurements were made for each ship orientation. At each sample point, for each probe orientation, the velocity components were measured over a period of 60 seconds at a sample rate of 200 Hz giving a total of 12,000 individual samples per velocity time history, a much larger sample size than is required to achieve minimum errors on first- and second-order statistical moments of the velocity components [92]. Figure 2-29 shows a series of lines over and around the QEC along which ADV point measurements were taken. From the perspective of BAE Systems, the areas of interest were over the landing spots on the flight deck and along the 7 deg SRVL approach path, shown as a red line in Figure 2-29. However, from the point of view of the research, the more complex flow due to the ship's islands, the ski-jump at the bow and the backward facing step formed by the stern of the ship were more interesting. Therefore, all together, velocity measurements were taken over the bow of the ship, along the centreline of the islands, over the deck, over the vertical landing positions, at the stern of the ship and along the approach path used for the SRVL.

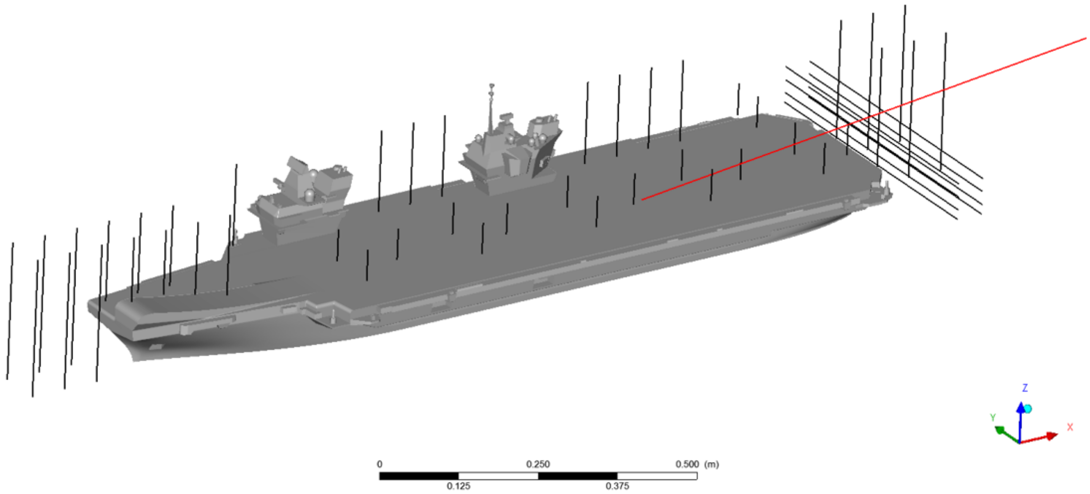

Figure 2-29 ADV measurement locations around the QEC 1:200 scale model.

2.6 Chapter Summary

This chapter has described the experimental setup that was used to measure the flow field over and around a 1:200 scale model of the QEC which was submerged in a large re-circulating water channel. The scale model of the QEC, manufactured from ABS in sections using a 3D printer, was attached to the floor of the water channel's working section using suction cups located on the underside of the model. The water channel has a uniform velocity profile at its inlet that was set to 1 m/s. ADV, the method of flow measurement, along with the recommended procedure to ensure high-quality data without the presence of erroneous spikes in the data, has been described. Two differently orientated ADV probes were used to measure points in the flow around the ship for one minute at 200 Hz, allowing the mean velocities in three components and the turbulence in the lateral and vertical components to be obtained. Exploratory experiments were conducted with the ADV to assess the ability of the probe to capture high-quality data close to the surface of a boundary. Acoustic theory was used to inform and explain the experimental velocity measurements close to surfaces made of different materials and with different surface roughness. Overall, the ADV was confirmed to be a suitable instrument with the capability to measure velocities close to the surface, as well as in the complex three-dimensional unsteady flow that will occur, for example, in the lee of the islands. Experimental ADV measurements were conducted with the ship aligned with the flow and at an angle of 10 deg. The next Chapter will describe how CFD was used to compute the unsteady flow field of the QEC's airwake, first using the geometry of the water channel to define the flow domain and to match fully the conditions of the small-scale experiment in water channel, and second using the full-scale ship geometry in a large domain to represent the at-sea conditions. The experimental measurements will be compared with both the small- and full-scale CFD.

Chapter 3

CFD Modelling of the QEC Carrier Airwake

As discussed in Chapter 1, realistic flight simulation for launch and recovery of aircraft to and from ships requires the inclusion of a high-fidelity model of the ship's airwake. CFD has been identified as a suitable method to accurately generate the complex three-dimensional unsteady air flow characteristics of the ship airwake. The initial CFD-generated airwakes for the full-scale QEC that were implemented in the F-35B piloted flight simulation facility at BAE Systems, and used to inform the FOCFTs, were produced by Kelly [52]. The required validation of the CFD methodology was obtained as part of the present study using the experimental measurements described in Chapter 2. As bluff body flows are often independent of the Reynolds number [67], small-scale experiments are commonly used to represent large-scale bluff body flows. However, in the case of the aircraft carrier, not only were the Reynolds number of the small-scale experiment and the full-scale ship very different, but so too were the velocity profiles of the flow approaching the ship, and the bow of the ship has rounded edges, which could create local flows that are dependent on Reynolds number. Therefore, the CFD used in this research has been implemented in two stages; one was to apply the methodology to the experiment described in Chapter 2, to obtain validation data; the second was to apply it to the full-scale ship to obtain new additional airwakes for the flight simulators, to drive the external flow for fixed-/rotary-wing simulations, and also to enable a comparison between the small and full-scale CFD. This chapter will first give a background to the CFD methodology used and will then describe how it was implemented for the small-scale experiment and the full-scale ship.

3.1 CFD Methodology

3.1.1 The Governing Equations

CFD numerical modelling is based on the fundamental physical principles that govern fluid dynamics: the conservation of mass, conservation of momentum (Newton's second law), and the conservation of energy (not shown here as it was not used in this research). By applying mass, momentum and energy conversation to a finite control volume within the fluid, the governing equations for fluid dynamics can be derived. The following equations include the dissipative transport phenomena of friction (mass diffusion is not included) and are used to model unsteady, three-dimensional, compressible and viscous fluid flow [104]. The governing fluid dynamics equations are derived by considering an infinitesimally small element in a general flow field with a differential volume fixed in space and are conventionally presented in conservation/partial-differential form below:

Mass Continuity Equation:

$$\frac{\partial \rho}{\partial t} + \nabla \cdot (\rho \boldsymbol{V}) = 0 \tag{3.1}$$

Momentum Equations (Navier-Stokes):

$$\frac{\partial (\rho u)}{\partial t} + \nabla \cdot (\rho u \boldsymbol{V}) = -\frac{\partial p}{\partial x} + \frac{\partial \tau_{xx}}{\partial x} + \frac{\partial \tau_{yx}}{\partial y} + \frac{\partial \tau_{zx}}{\partial z} + \rho f_x \tag{3.2}$$

$$\frac{\partial (\rho v)}{\partial t} + \nabla \cdot (\rho v \boldsymbol{V}) = -\frac{\partial p}{\partial y} + \frac{\partial \tau_{xy}}{\partial x} + \frac{\partial \tau_{yy}}{\partial y} + \frac{\partial \tau_{zy}}{\partial z} + \rho f_y \tag{3.3}$$

$$\frac{\partial (\rho w)}{\partial t} + \nabla \cdot (\rho w \boldsymbol{V}) = -\frac{\partial p}{\partial z} + \frac{\partial \tau_{xz}}{\partial x} + \frac{\partial \tau_{yz}}{\partial y} + \frac{\partial \tau_{zz}}{\partial z} + \rho f_z \tag{3.4}$$

The Navier-Stokes equations (including the continuity equation) are generally accepted to form a closed set of equations that describe laminar and turbulent flows, however, as they form a coupled system of nonlinear partial differential equations they are difficult to solve analytically, especially for turbulent fluid flow which is unsteady, irregular and chaotic by nature. Although there is a limited number of analytic solutions to trivial flow problems, there is currently no general solution. Due to the widespread use and importance of the Navier-Stokes Equations their solution has been listed as one of seven millennium prizes since 2000 by the Clay Mathematics Institute [105].

Since no general solution exists, more complex fluid flows are solved numerically through a process known as discretization, where the partial differential equations are transformed into a system of algebraic expressions applied at discrete points on a grid that is constructed within the fluid volume. Discretization is achieved through Finite-Difference Method (FDM), or FVM, methods which represent the flow field in space and time at each grid point within the fluid, known as nodes. A more detailed description of the discretization scheme used in this work will be given in Section 3.1.3.

3.1.2 Turbulence Modelling

As previously discussed, pilot workload during launch and recovery of aircraft to a ship is largely dependent on the unsteady nature of the air flow over the ship's flight deck. The airwake often contains turbulent structures of varying size and frequency that are shed from the ship's superstructure and it is essential that the CFD captures these. To model the unsteady turbulent flow at a high Reynolds number, a suitable level of turbulence must be resolved within the CFD solution.

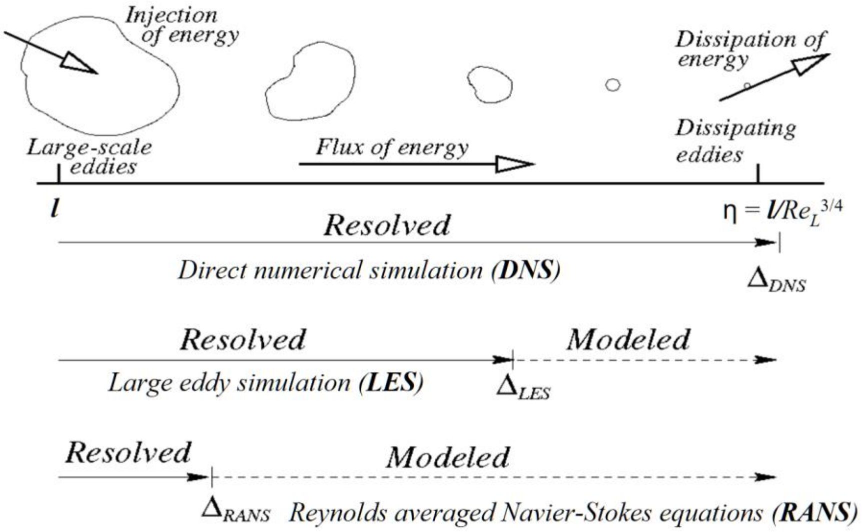

Figure 3-1 Varying scale of eddies resolved by turbulence modelling approaches [106].

Figure 3-1 provides an example of the scale of eddies resolved by different turbulence model approaches (DNS, LES, RANS). Direct Numerical Simulation (DNS) allows the Navier-Stokes equations to be numerically solved without any modelling of the turbulence, however, as the smallest spatial and temporal scales of the turbulence are resolved, the computational expense in doing so is prohibitive. While DNS provides the most accurate approach, it is only practical for very low Reynolds numbers and was not considered feasible for the high Reynolds numbers and complex geometry associated with ship airwake modelling.

A more practical solution is found by modelling some or all of the effects of turbulence. Small-scale dissipative turbulence can be modelled as it is generally isotropic; however, larger turbulent length scales are more difficult to model, as they can be highly non-isotropic, dependent on the geometry of the problem, and tend to have a larger effect on the mean flow. Researchers have produced numerous turbulence models with varying levels of turbulent flow resolution and computational expense. The suitability of each model is dependent on the fluid properties, the flow conditions and the geometry of the problem. The following section will discuss several turbulence models and describe the method chosen for the research being reported in this thesis.

3.1.2.1 Reynolds Averaging Navier-Stokes

The Reynolds Averaging Navier-Stokes (RANS), method describes the transport of averaged flow quantities whereby all of the turbulent length scales are modelled, greatly reducing the computational expense. RANS decomposes the instantaneous flow variables into a mean and fluctuating term:

$$u = \bar{u} + u' \tag{3.5}$$

where $\bar{u}$ is the mean flow velocity and u' is the fluctuating component. Substituting equation 3.5 into the Navier-Stokes equations for each velocity component and taking a time average will result in the RANS equations. Equation (3.6) gives the Reynolds averaged continuity equation. The three-dimensional incompressible flow equations for the conservation of momentum are given in equations (3.7) to (3.9) using the substantial derivative $\frac{D}{Dt}$.

$$\frac{\partial \bar{u}}{\partial x} + \frac{\partial \bar{v}}{\partial y} + \frac{\partial \bar{w}}{\partial z} = 0 \tag{3.6}$$

$$\rho \frac{D\bar{u}}{Dt} = -\frac{\partial \bar{p}}{\partial x} + \mu \nabla^2 \bar{u} - \rho \frac{\partial}{\partial x}\left(\overline{u'^2}\right) - \rho \frac{\partial}{\partial y}\left(\overline{u'v'}\right) - \rho \frac{\partial}{\partial z}\left(\overline{u'w'}\right) + \rho \overline{f_x} \tag{3.7}$$

$$\rho \frac{D\bar{v}}{Dt} = -\frac{\partial \bar{p}}{\partial y} + \mu \nabla^2 \bar{v} - \rho \frac{\partial}{\partial x}\left(\overline{v'u'}\right) - \rho \frac{\partial}{\partial y}\left(\overline{v'^2}\right) - \rho \frac{\partial}{\partial z}\left(\overline{v'w'}\right) + \rho \overline{f_y} \tag{3.8}$$

$$\rho \frac{D\bar{w}}{Dt} = -\frac{\partial \bar{p}}{\partial z} + \mu \nabla^2 \bar{w} - \rho \frac{\partial}{\partial x}\left(\overline{w'u'}\right) - \rho \frac{\partial}{\partial y}\left(\overline{w'v'}\right) - \rho \frac{\partial}{\partial z}\left(\overline{w'^2}\right) + \rho \overline{f_z} \tag{3.9}$$

As a result of the averaging process, however, several additional terms are introduced ($\overline{u'^2}$, $\overline{u'v'}$) known as the Reynolds normal and shear stress terms which can be thought of as additional momentum fluxes due to the unsteady turbulent motions. As the RANS method describes an open series of equations, the Reynolds stresses must be modelled to achieve closure. The majority of RANS turbulence models used to achieve closure are based on the Boussinesq concept of eddy-viscosity which relates transfer of momentum to the Reynolds stresses, for example:

$$-\overline{u'v'} = \mu_t \frac{\bar{u}}{\partial y} \tag{3.10}$$

Turbulence models based on the Boussinesq hypothesis assume that eddy-viscosity, μ_t, is isotropic which can lead to errors due complex interactions between the Reynolds stresses and the mean flow field not being accurately captured. Commonly used turbulence models for RANS solutions, all of which are based on empirical data, include the $k - \varepsilon$ [107], $k - \omega$ [108], and Menter's Shear Stress Transport (SST) models [109]. The $k - \varepsilon$ turbulence model was originally proposed as an improvement over the mixing-length model, which defines two additional transport equations for turbulent kinetic energy (k) and dissipation rate (ε). The $k - \varepsilon$ is suitable for a large number of flows, however, it has been shown to overpredict turbulent kinetic energy upstream of high shear regions [110].

The $k - \omega$ contains transport equations for turbulent kinetic energy (k) and specific dissipation rate (ω) and performs well in free-shear flows, however, similarly to the $k - \varepsilon$ model, it is highly empirical. The SST model was developed by blending the $k - \varepsilon$ and $k - \omega$ models and adding terms for the transport of turbulent shear stresses to create an enhanced turbulence model which improves on each model's standalone merits.

Widely adopted for practical engineering applications, RANS is a relatively computationally inexpensive method, as the mean flow field and turbulence can be computed by iteration to a steady state; however, it is unable to capture unsteady three-dimensional complex structures present in a typical ship's airwake.

3.1.2.2 Unsteady RANS

Maintaining the time differential during derivation of the RANS equations and solving in a time-accurate manner in an effort to resolve any unsteadiness in the solution leads to a method known as Unsteady-RANS (URANS). Although URANS is effective in modelling large-scale unsteady flows, such as vortex shedding behind a cylinder, it is unsuitable for bluff body wake simulation dominated by quasi-periodic large-scale structures and chaotic small-scale features. In previous cases of ship airwake modelling, the use of URANS resulted in the unsteady solution converging in time to an approximate steady-state solution [111, 112]. Forrest el al. suggests that a combination of high eddy-viscosity dissipation due to the RANS turbulence modelling and further dissipation caused by upwind schemes results in the damping of solution perturbations [113].

3.1.2.3 Large Eddy Simulation

Large Eddy Simulation (LES), assumes that because large vortices are responsible for the majority of energy transfer in a flow, large scale turbulent structures are more important than the smaller dissipative length scales. First introduced to model atmospheric turbulence by Smagorinksy [114], LES is now often used to model turbulence in engineering CFD solutions involving large Reynolds numbers. Large eddies within the LES model are explicitly resolved in a time-dependent simulation while small eddies are filtered out of the Navier-Stokes equations. By explicitly resolving larger eddies, less of the turbulence is modelled, reducing the modelling error. Filtering of the eddies is based on an appropriate length scale which is often defined as the local grid spacing. Similar to Reynolds averaging, the filtering process creates additional unknown terms due to temporal and spatial averaging which must be modelled by a sub-grid-scale (SGS) model to achieve closure, and is generally based on the Boussinesq hypothesis. LES allows variables in the time-varying flow fields, such as velocity and pressure, to be recorded and used to obtain time-averaged and RMS turbulence values which, in general, are of most engineering interest.

As eddy filtering is based on the local grid spacing, accurately resolving a flow with a high Reynolds number requires high spatial resolution, especially near wall boundaries where eddies produced are typically small compared with the vortical structures that will develop downstream, resulting in a computationally expensive solution. To resolve the flow over the flight deck of a ship solely using LES would require a very large cell count and would be impractical.

3.1.2.4 Hybrid RANS/LES

Hybrid RANS/LES models were first introduced to combine the benefits of the large-scale eddy-resolving capabilities of LES with the near-wall modelling capabilities of RANS to allow flows with high Reynolds numbers to be accurately computed in more practical time scales. Detached

Eddy Simulation, DES, is a hybrid RANS/LES model that was first introduced by Spalart [115] as a modification to the one-equation Spalart-Allmaras model. DES utilises the eddy-resolving power of LES in areas of large separation, and a RANS approach in the boundary layer; this is achieved through the replacement of the distance to the wall term, d, in the underlying Spalart-Allmaras (SA) turbulence model by $\tilde{d}$, where:

$$\tilde{d} = \min(d, C_{DES}\Delta) \tag{3.11}$$

The modified turbulent length scale, $\tilde{d}$, which drives the production of eddy-viscosity, is therefore linked to the local grid spacing, Δ. In regions where the grid is 'fine enough', eddy-viscosity production is limited, allowing medium to large scale turbulent structures to be explicitly resolved using LES. This reduction in eddy-viscosity prevents artificial dampening of the flow field perturbations by the turbulence model and allows turbulent structures to propagate.

DES is often used with the SST $k - \omega$ model, which requires a modification to the term which governs the dissipation of turbulent kinetic energy as described by Menter [109], Y_k, where:

$$Y_k = \rho\beta^* k\omega F_{DES} \tag{3.12}$$

Set to a constant of 1 in the standard model, the parameter F_{DES}, is modified for DES computations to be:

$$F_{DES} = max\left(\frac{L_t}{C_{DES}\Delta}, 1\right) \tag{3.13}$$

where the turbulent length scale is expressed as:

$$L_t = \frac{\sqrt{k}}{\beta^*\omega} \tag{3.14}$$

C_{DES} is usually defined as 0.61, a slight change from a typical S-A value of 0.65. In regions of flow where the grid spacing is small, F_{DES} will increase above unity, resulting in an increase in dissipation of turbulent kinetic energy.

In a typical DES simulation, a RANS SGS model with a low-Reynolds number correction is utilised throughout the boundary layer; however, as the turbulent length scale is linked to the local grid spacing, care must be taken so that the streamwise grid spacing is longer than the boundary layer thickness (δ) to ensure LES is not resolving the flow. Figure 3-2 shows a comparison of typical near-wall grids used by both RANS/DES and LES. The bottom of Figure 3-2 depicts a mesh near the boundary where the streamwise grid spacing is shorter than the boundary layer thickness, or 'ambiguous' grid, which activates the DES limiter roughly in the upper two-thirds of the boundary layer. Therefore, LES is activated prematurely inside the boundary layer where the grid is not fine enough for LES to resolve the velocity fluctuations. The subsequent reduction in eddy-viscosity and modelled Reynolds stresses due to the grid spacing is known as Modelled Stress Depletion (MSD) and it can also result in Grid Induced Separation (GIS) in areas where the unresolved Reynolds stresses lead to an artificially reduced skin friction coefficient [116].

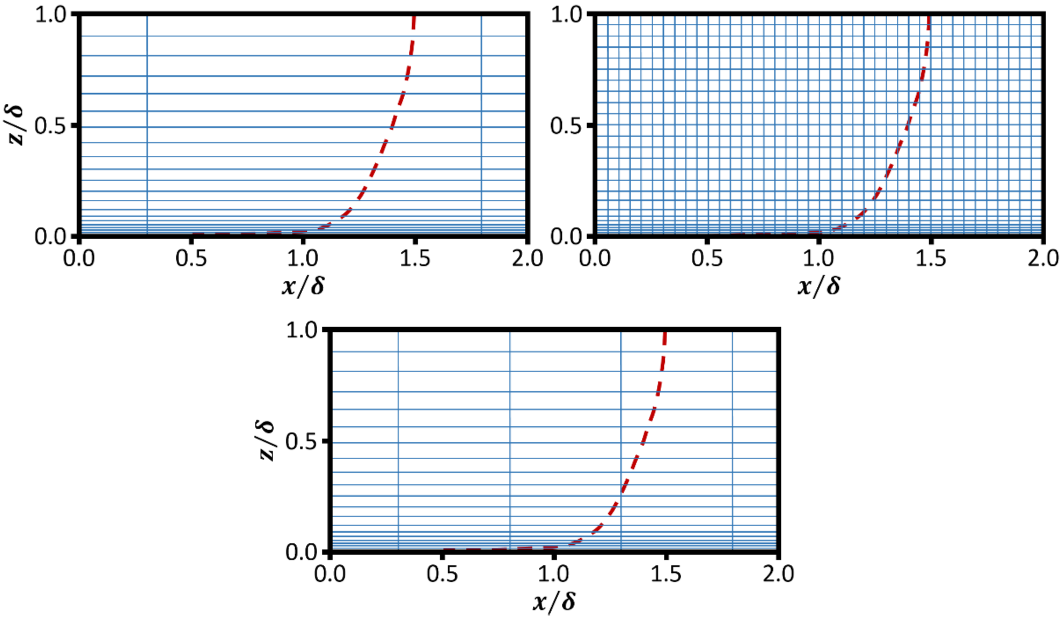

Figure 3-2 Comparison of RANS/DES (left) and LES (right) meshes across the near-wall boundary layer. A grid with a more ambiguous spacing is also shown (bottom), similar to that used in some regions of the QEC geometry [117].

Retaining an unambiguous grid near the wall is a challenge for the complex geometry of the QEC and the full range of wind azimuths. To reduce the effect of the grid and the DES-limiter on the RANS part of the boundary layer a zonal formulation of the underlying SST model was developed. F_{DES} is modified to:

$$F_{DES} = max\left(\frac{L_t}{C_{DES}\Delta}(1 - F_{SST}, 1\right) \tag{3.15}$$

with $F_{SST} = 0, F_1, F_2$, where F_1 and F_2 are blending functions of the SST model. A more general form of the shielding function was developed which depends only on the eddy-viscosity and the wall distance which, in principle, can be applied to any eddy-viscosity based DES model [117]. The resulting model was termed Delayed Detached Eddy Simulation (DDES). The F_{DDES} blending function is given by:

$$F_{DDES} = \tanh[(C_{d1}r_d)^{C_{d2}}] \tag{3.16}$$

where C_{d1}= 20, C_{d2}= 3, and r_d is expressed as:

$$r_d = \frac{v_t + v}{\xi^2 y^2 \sqrt{0.5 \cdot (S^2 + \Omega^2)}} \tag{3.17}$$

S is the magnitude of the strain rate tensor, Ω is the magnitude of vorticity, $\xi = 0.41$, and y is the wall distance.

3.1.2.5 Choice of Turbulence Modelling

A suitable turbulence model was therefore required to provide realistic ship airwakes which accurately capture the complex three-dimensional unsteady flow generated by the air moving over and around the ship's superstructure. While steady-state RANS method offers the least computationally expensive model of the flow, unsteady airwake data is required. Unsteady RANS was investigated as a possible technique for ship airwake generation [16], however, it was found that the computations became damped and converged to a steady-state solution. Due to the near-wall meshing requirements of LES and the complex geometry of the QEC LES was not chosen as a flow solver method.

First identified by Forrest et al. [16], DES allows the large-scale, high Reynolds number, wall-bounded flows which are characteristic of ship airwakes, to be accurately modelled without the computationally expensive flow resolution near the boundaries required by LES. However, for the present work, DDES was selected over DES as the suitable method for turbulence modelling. While the premature switching to LES caused by the DES formulation will have little impact on the solution of a frigate, the solution of the aircraft carrier with its long flat-plate flight deck and aerodynamic ski-jump ramp is more susceptible to GID; therefore, DDES was chosen as the more suitable method.

Another concern with the application of CFD to ship airwake modelling is the potential for artificial dissipation of turbulent energy, especially in the significantly large region over the carrier flight deck and along the approach path astern of the ship. The dissipation of turbulence may be attributed in part to the overly dissipative SGS model applied when the turbulent length scale is less than the grid spacing in LES mode [118]. A sufficiently fine grid is therefore required in the wake region of the ship to minimise this unphysical dissipation in the focus region; this was achieved using a 'density box' which constrains the grid elements in a volume to a maximum size when producing the computational mesh. The application of density boxes will be described in Section 3.3.

3.1.3 Discretization Schemes

As previously mentioned in Section 3.1.1, as there is no general solution for the Navier-Stokes equations for viscous flow, the flow domain is discretized into a number of cells collectively known as a grid, or mesh, and the algebraic form of the equations are solved iteratively. There are many different types of cell/elements that are used to define the mesh, as shown in Figure 3-3. The choice of cell types generated in each mesh is dependent on the fluid problem and capabilities of the CFD solver. Certain cell types may also be used for specific purposes, e. g., several layers of triangular based prisms are often generated adjacent to boundaries due to their efficiency in resolving the boundary layer.

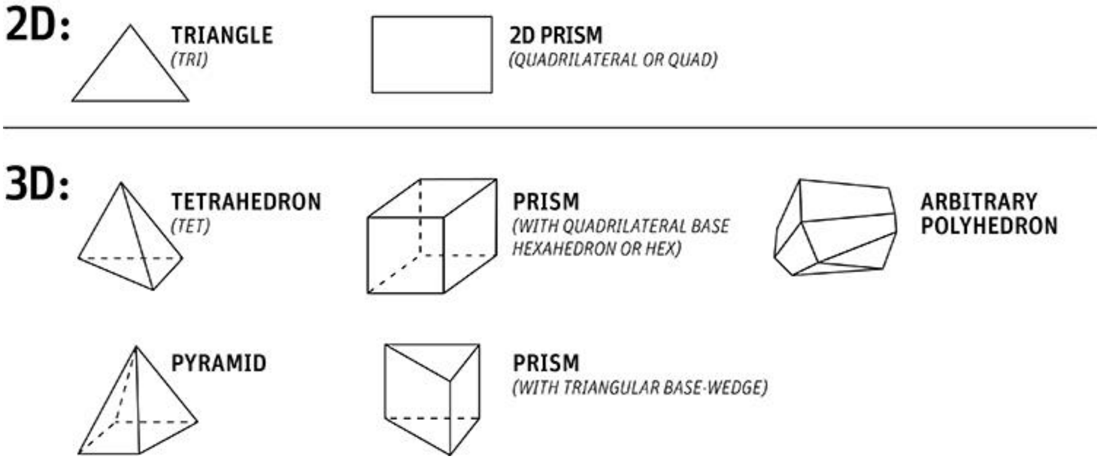

Figure 3-3 Common CFD mesh cell types [119].

The discretization method by which the flow is approximated numerically has an impact on the accuracy of the solution; artificial dissipation can occur in the form of numerical diffusion. For an unstructured, tetrahedral grid, that is not always aligned with the freestream flow, as used in this study, a second-order discretization method is required to reduce the numerical error. In the overall CFD solution, an initial steady-state solution was implemented first to provide an initialisation case before switching to the unsteady DDES; the steady-state solution was computed with first-order discretization. After initialisation, the solver was switched to DDES. Pressure discretization was set to second-order, and momentum was set to the third-order Monotone Upstream-Centred Schemes for Conservation Laws (MUSCL) scheme, which is a blend of a central-differencing scheme and second-order upwind scheme [119]. A second-order implicit time scheme was used to provide temporal discretization. Momentum and pressure corrections were solved together in the coupled algorithm to compute pressure-velocity coupling.

3.1.4 ANSYS Fluent Flow Solver

Ship airwake computations were performed using the FVM ANSYS Fluent general-purpose CFD solver. Fluent accommodates both structured and unstructured grids and provides a wide range of physical modelling capabilities, including:

- Steady-state or transient solutions
- Multi-phase flows
- Heat transfer from natural, forced and mixed convection
- Laminar, transient or turbulent flows
- Dynamic mesh modelling
- Incompressible and compressible flows
- Parallel processing

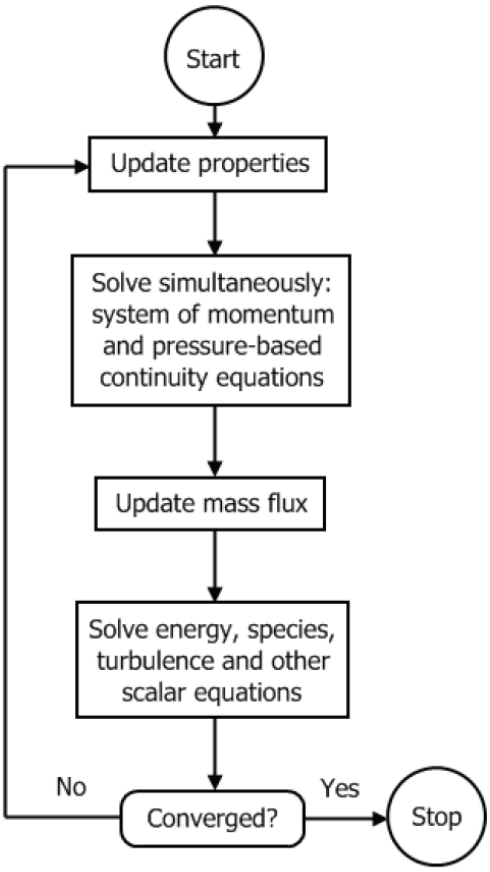

Figure 3-4 Fluent's pressure-based coupled algorithm [119].

Figure 3-4 depicts Fluent's pressure-based coupled algorithm used to solve a coupled system of equations comprised of the momentum equations and the pressure-based continuity equation. Solving the coupled momentum and continuity equations results in an improvement in the rate of solution convergence compared with a segregated algorithm; however, it requires an increase in memory of 1.5-2 times that of the segregated solver.

3.2 Computer Aided Design Geometry of the QEC Aircraft Carrier

CFD simulations require the geometry of the physical structure which the fluid is moving over and/or through. The geometry (in this case the QEC) and the surrounding domain in which the fluid will flow are typically defined as a digital drawing, i.e. a Computer Aided Design (CAD) model. The level of geometric detail of the structure in the fluid domain is governed by the type and required fidelity of the CFD solution.

3.2.1 Preparation of CAD

A CAD model of the QEC's geometry was produced using the software ANSYS ICEM from digital drawings of the QEC above the waterline as provided by BAE Systems [52]. Previous CFD grid-dependence studies performed by Forrest et al. for full-scale ship airwakes recommend a surface triangle edge length of 0.3 m. To provide a good quality surface mesh of the QEC, features smaller than 0.3 m were removed (e.g. handrails, aerials and antenna etc.) and some larger features simplified. Due to the large bluff body nature of the QEC, fine geometric detail of the ship is not required and will have little effect on the airwake. The same CAD geometry used to create the 3D printed model of the ship, shown earlier in Figure 2-2, was used to produce the mesh for each CFD investigation.

3.2.2 Domain Sizing/Shape

Once the CAD model of the ship had been generated it was necessary to enclose the ship within solid boundaries, known as the computational domain, which defines the region of fluid flow the CFD solver will compute. The size and shape of the domain is dependent on the CFD application. Section 3.4.1 and 3.5.1 will describe the computational domains used for the experimental model and the full-scale QEC respectively.

3.3 **Mesh Generation**

The method by which the grid, or mesh, is generated, and the quality of the mesh used for solving the Navier-Stokes equations, has a large impact on the accuracy of the solution. The following sections outline the method used to generate the mesh for computing the airwakes for the QEC. The general methodology applies to both the experimental model and the full-scale ship.

3.3.1 General Meshing Process for Ship Airwake CFD Applications

An unstructured mesh was chosen to produce a grid for the QEC due to the complex nature of the ship's geometry. Unstructured meshes are much quicker and more straightforward to generate compared with structured meshes. The quality of the mesh can be affected by the quality of the CAD geometry; therefore, the process for mesh generation is often iterative. The stages used to generate each mesh in ANSYS ICEM are listed below, and are followed by further explanation:

1. A density box with a defined maximum cell size is placed in regions of interest, i.e. in areas of expected flight operations.

2. Minimum and maximum cell size along with the growth ratio are specified for each domain surface.
3. An unstructured volume mesh is generated using the Robust Octree method.
4. The volume mesh is deleted leaving only the unstructured surface mesh.
5. The surface mesh is smoothed using a Laplacian algorithm.
6. The mesh is checked for quality and to ensure no holes or penetrating elements exist.
7. A volume mesh is generated using the Quick Delauney method from the smoothed surface mesh.
8. The unstructured Delauney mesh is smoothed.
9. Initial surface prism layers are generated using a post-inflation method in ICEM.
10. Prism layers are split and redistributed to ensure the correct wall distance and to provide the required number of cells to capture boundary layer effects.
11. The quality of the mesh is checked before being exported as a .msh file.

This method of unstructured mesh generation first produces the surface mesh from which the volume cells will be grown. The specified maximum and minimum cell size on each surface are important as they will determine the surface mesh size and the cell growth away from the surfaces. The Octree method is used to create the triangular surface mesh. Once the surface mesh has been smoothed to give an even growth transition, the Delauney method is used to create the volume mesh. As the volume mesh is made up of tetrahedral elements, the highest quality cell shape has triangular faces in equilateral proportions. ICEM and FLUENT provide a cell quality metric from 0-1, 1 being the highest quality, based on the node point distribution, smoothness and skewness of the cell. As the surface mesh is grown, the cells will naturally deform around the geometry of the ship; a minimum cell quality of 0.3 is recommended for both the Delauney and surface mesh. Prism cells are then created using post-inflation (after the generation of the Delauney mesh) to capture the boundary layer. Prism cells are used in the boundary layer. Generating the prism layers will deform the cells, further reducing mesh quality; it is recommended that prism cells should have a minimum quality value of 0.03-0.05. The success of the mesh will only be evident through initial computation attempts due to the complex geometry of the ship and several iterations of the mesh may be required.

3.3.2 Boundary Layer Meshing for Bluff Body Aerodynamics

Ship-airwake CFD is primarily concerned with the modelling of the wake produced by the bluff body geometry of the ship; resolving the boundary layer is nevertheless important in predicting flow phenomena such as flow reattachment across large flat surfaces. Many parts of the QEC geometry will generate areas of low pressure and recirculating flow, such as the backward facing step at the stern of the ship, which require accurate capture of the boundary layer [48].

The mesh sizing near each surface should reflect the level of boundary layer modelling required for each CFD application. The dimensionless wall distance value, known as y^+, is a key parameter in determining accurate capture of the boundary layer flow for each specific flow problem. The boundary layer consists of three separate regions: the viscous sub-layer, the buffer zone and the log-law zone as shown in Figure 3-5 [74].

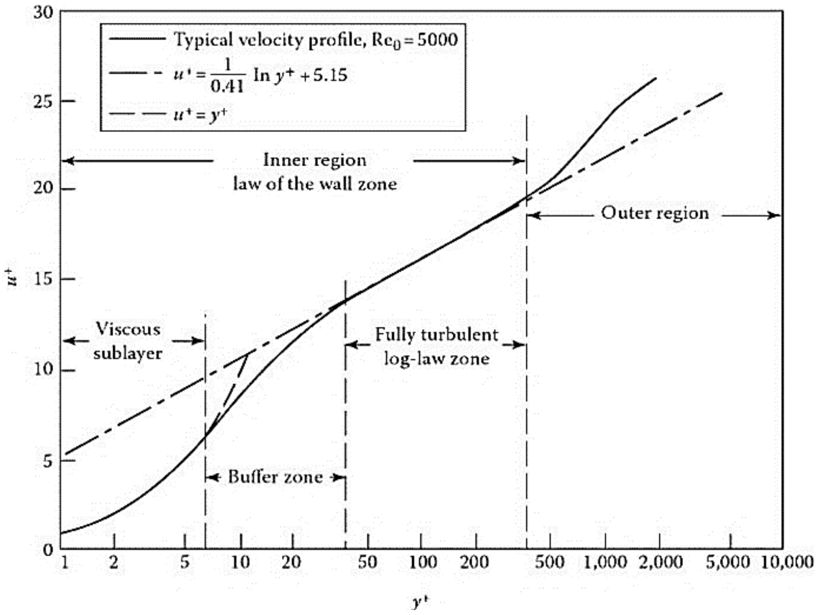

Figure 3-5 Graph depicting the presence of each boundary layer zone according to dimensionless wall distance [74].

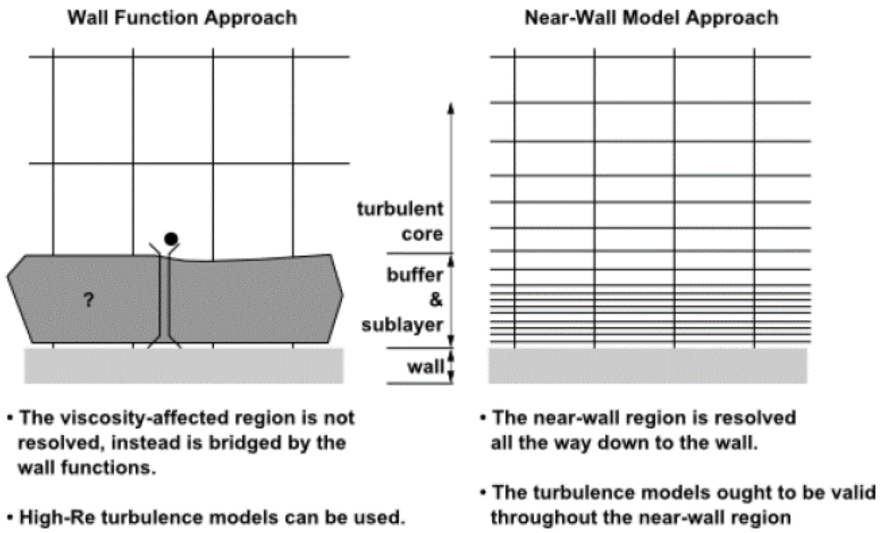

Figure 3-6 Visual explanation of the two wall modelling approaches; Wall Function Approach and Near-Wall Model Approach [120].

Generally, there are two approaches to modelling the flow in the near-wall region of a surface: calculating the entire laminar sublayer, or using a wall function to model up to the log-law zone. Calculating the entire laminar sublayer requires the mesh to be refined to allow the viscous sublayer and buffer layer to be resolved with the first cell height typically beneath a y^+ value of less than 1, as seen on the right of Figure 3-6. Alternatively, the wall function approach models the sublayer and buffer zone entirely in the first prism layer requiring the first cell height to be within the log-law zone with a typical y^+ value of greater than 30 and less than 300 [121] as shown to the left of Figure 3-6. The wall function approach requires a much lower cell count and is less computationally expensive compared with the near-wall model approach. All CFD calculations completed in this work have used the more appropriate wall function approach, with the added benefit of a lower cell count and a reduction in computational time.

3.3.3 Mesh focal regions

As previously described, extensive airwake modelling research has previously been carried out at UoL [1], largely focussed on 'single-spot' ships (i.e., frigate-sized vessels). The QEC aircraft carriers are significantly larger multi-spot platforms, each possessing an approximately four-acre flight deck, and with a requirement to operate both fixed- and rotary-wing aircraft. The generation of time-accurate CFD airwakes for a multiple-spot aircraft carrier requires a significant increase in computational power compared with the CFD solution for a single-spot frigate. To adequately resolve the turbulent length scales passing over a ship's flight deck, it is necessary for the mesh size in the region of interest to be sufficiently refined. It is therefore necessary for the grid density to be carefully controlled in the CFD region of interest, or ‘focus region’ [118]. In the case of creating CFD airwakes for simulated aircraft operations to/from the QEC, the focus region was defined as the area through which aircraft will pass on approach to the ship during the VL, which is the primary means of recovery, and the SRVL, extending the focus region approximately 1.5 ship lengths aft of the ship and the STO.

Figure 3-7 shows the interpolation boxes, or export domains, used in the BAE Systems (black box) and UoL (pink box) flight simulators, compared with that used in previous experiments at UoL focussed on single-spot frigates (light blue filled box). The unsteady velocity components generated by the CFD models, within these interpolation boxes, are interpolated onto a uniform grid and exported to the flight simulator host software as look-up tables. Compared with the previous studies, focussed on single-spot frigates, the difference in the export volumes graphically illustrates the size of the challenge faced during implementation of the aircraft carrier airwakes, in terms of computational resources and real-time data storage and processing.

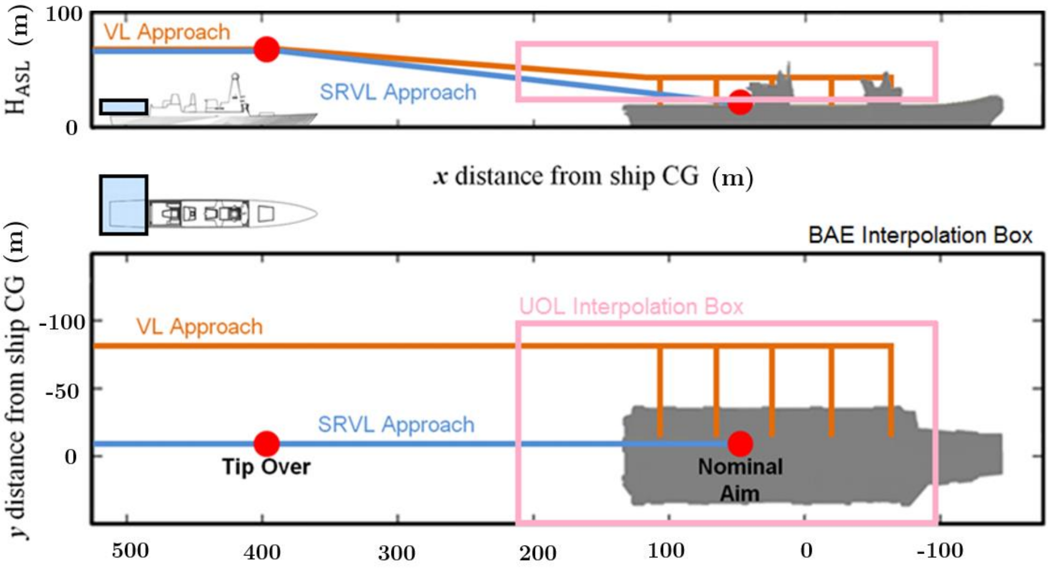

Figure 3-7 CFD exported domains for UoL and BAE Systems flight simulators.

3.4 Model Scale QEC Computational Setup

This section outlines the procedure used to create the computational mesh and to compute the airwake over the 1.4 m scale model of the QEC submerged in the water channel under the experimental conditions described in Chapter 2.

3.4.1 Water Channel Domain and Boundary Conditions

For the small-scale CFD study, the computational domain was given the same height and width as the water channel, outlined in blue in Figure 3-8 and described in Section 2.1. The upstream length of the domain was increased by 2.5 m to minimise any spurious effects from the inlet boundary conditions and is shown in Figure 3-8 as a red box. The detailed ship geometry was simplified so that at full-scale all features less than 0.3 m were removed. Positive x runs from the ship's bow toward the stern, positive y runs laterally from port to starboard and z is positive in the vertically upward direction from the floor of the water channel.

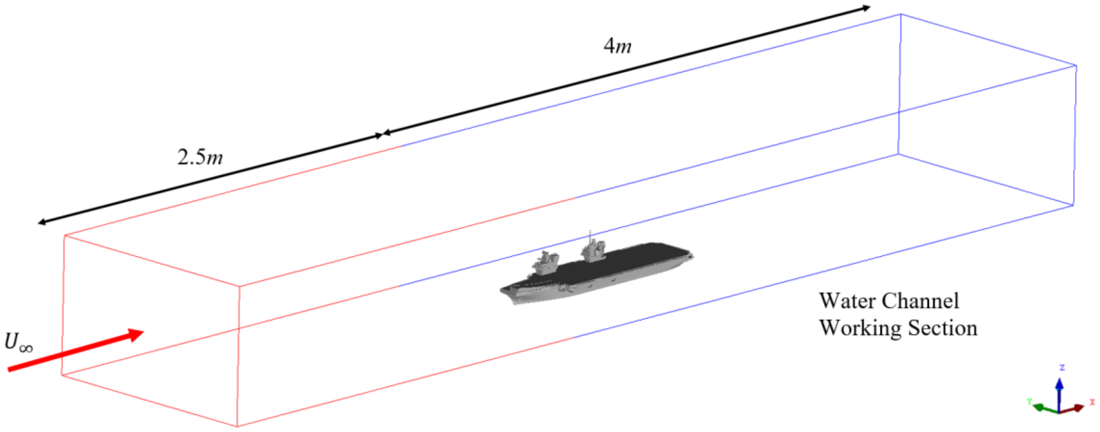

Figure 3-8 Computational domain for QEC in water channel CFD

Defining the boundary conditions is necessary for the CFD solver to compute a solution to the system of differential equations. Each surface of the computational domain must be specified with appropriate boundary conditions to ensure the fluid flow over the ship is modelled to accurately represent the flow over the model ship in the water channel. The ship surface, the water channel side walls and the floor of the water channel which were assumed to be hydraulically smooth (the characteristic roughness height of the surface is less than the boundary layer height) were defined as zero-slip walls, which specifies that the fluid immediately adjacent to the surface is stationary (equation 3.18), allowing the natural development of a boundary layer.

$$u = v = w = 0 \tag{3.18}$$

The free surface of the water was set as a slip surface, i.e., frictionless with no velocity gradient normal to the surface. The walls of the extended water channel section shown in red, in Figure 3-8, were also defined as slip surfaces so that no boundary layer would grow, replicating the conditions of the water channel. The flow velocity at the inlet of the domain was set as a uniform 1.0 m/s, to replicate the experimental conditions shown in Section 2.4.5, the outlet plane was set as an outflow boundary condition, and the internal fluid was set as water with a constant density.

3.4.2 Water Channel Mesh

The method outlined in Section 3.3 was used to produce the mesh of the QEC model submerged in the water channel. The ship was aligned with the flow to represent a headwind and turned through 10 deg to represent a Green 10 wind. From previous experience [18], the surface cell size normally applied to a full-scale ship is approximately 0.3 m; for the small-scale model this proportion was retained and so was set at 1.485 mm. Twelve prism layers, used to efficiently capture the boundary layer, were applied on the non-slip surfaces. Using a non-dimensionalised first layer height (y^+) of 30 and a growth ratio of 1.2, the height of the next layer was calculated using the exponential prism growth law. A mesh density box was created to represent the focus region (shown earlier in Figure 3-7) within which the cells are restricted to a maximum size of 5 mm (equivalent to 1 m at full-scale), allowing the flow to be resolved with a higher fidelity in the region of interest over the deck and astern of the ship. For each WOD condition the focus region was aligned with the axis of the water channel, outlined as a red rectangular box in Figure 3-9. These configurations each had a total mesh size of approximately 100 million cells.

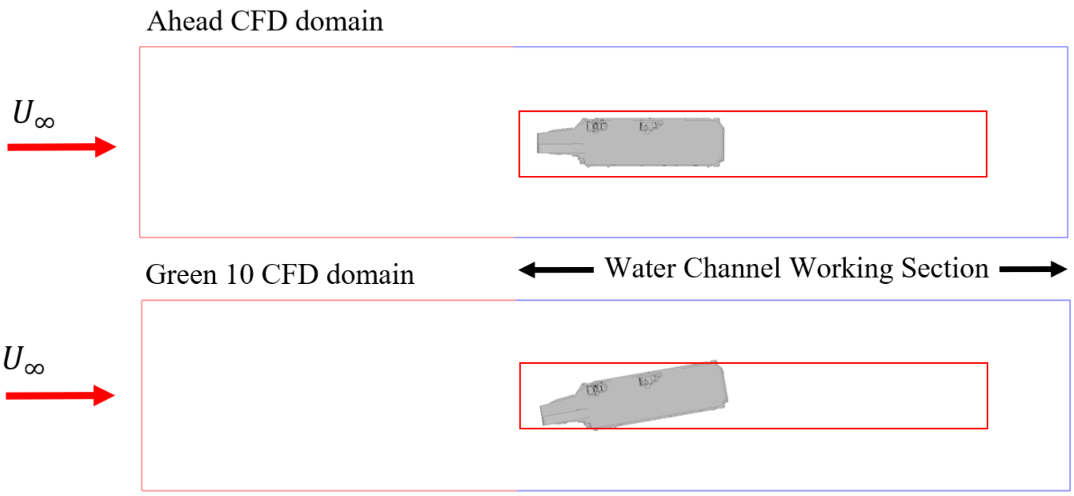

Figure 3-9 Computational domain and focus regions for QEC in water channel CFD in Ahead and Green 10 WOD conditions.

3.4.3 Time Step

The time-step chosen for unsteady CFD must be carefully considered to ensure that the development of turbulent structures in the flow field are adequately resolved. Too large a time-step could lead to instability in the solution, divergence and the loss of dominant frequencies in the flow. Too small a time-step will lead to a large increase in computational time. Care must also be taken with DES-based simulations to choose an appropriate time-step to ensure that the SGS filter is not unduly activated in the LES region of the mesh.

A method to calculate a suitable time-step sizing is suggested by Spalart [118] in which the Courant-Friedrichs-Lewy (CFL) number is set below unity so that the smallest eddies in the smallest grid cells are convected by the time-marching scheme resulting in error levels close to the spatial discretization error. The CFL equation relates the velocity of the fluid and time-marching simulation to the size of a computational grid cell as shown in equation 3.19, where Δ_n is the grid spatial dimension, Δt is the time-step, u_n is fluid velocity, and C is the Courant number.

$$C = \frac{u_x \Delta_t}{\Delta_x} + \frac{u_y \Delta_t}{\Delta_y} + \frac{u_z \Delta_t}{\Delta_z} \leq 1 \qquad (3.19)$$

If C is below unity then the fluid particle will not move from one cell to another within one time-step, whereas a C above unity indicates that the fluid particle moves more than one cell within a time-step, resulting in lower resolution of the turbulent structures. As the Courant number is not specified in the ANSYS Fluent solver, the time-step and grid-spacing must be carefully defined to ensure the CFL condition is met. The time-step for the CFD simulation was determined by setting the grid spacing, Δ_n, as the minimum cell size in the domain, taking the flow velocity, u_n, as 1.5 times the freestream velocity to account for flow acceleration in the fluid domain and specifying the C number to be approximately one. The time-step chosen for each of the model-scale QEC CFD simulations was 0.001 seconds (equivalent to approximately 100 Hz at full-scale).

3.4.4 Parallel Computation

Generating time-accurate unsteady CFD simulations of large flow domains such as ship airwakes requires the use of High Performance Computing (HPC) with parallel processing capabilities due to the large mesh size, computationally expensive DDES method and large data sets. ANSYS Fluent allows the CFD simulation to be processed in parallel using either multiple processors on a single computer or multiple computers connected by a network to reduce the overall computation time. Although increasing the number of computers running in parallel will initially decrease the computational time, the time taken for communication over the network will eventually increase the computational time, so optimal system sizing is important for simulations. Parallel processing in ANSYS Fluent is performed using a utility called Cortex which interfaces ANSYS Fluent with a host process and one or more compute node(s). Figure 3-10 shows a diagram of the ANSYS Fluent Architecture for parallel processing. During parallel computations the mesh is split into multiple partitions and assigned to individual compute nodes. Each node is virtually connected to every other compute node for inter-process communication, which is managed by a message passing library such as the Message Passing Interface (MPI) standard depicted in Figure 3-10.

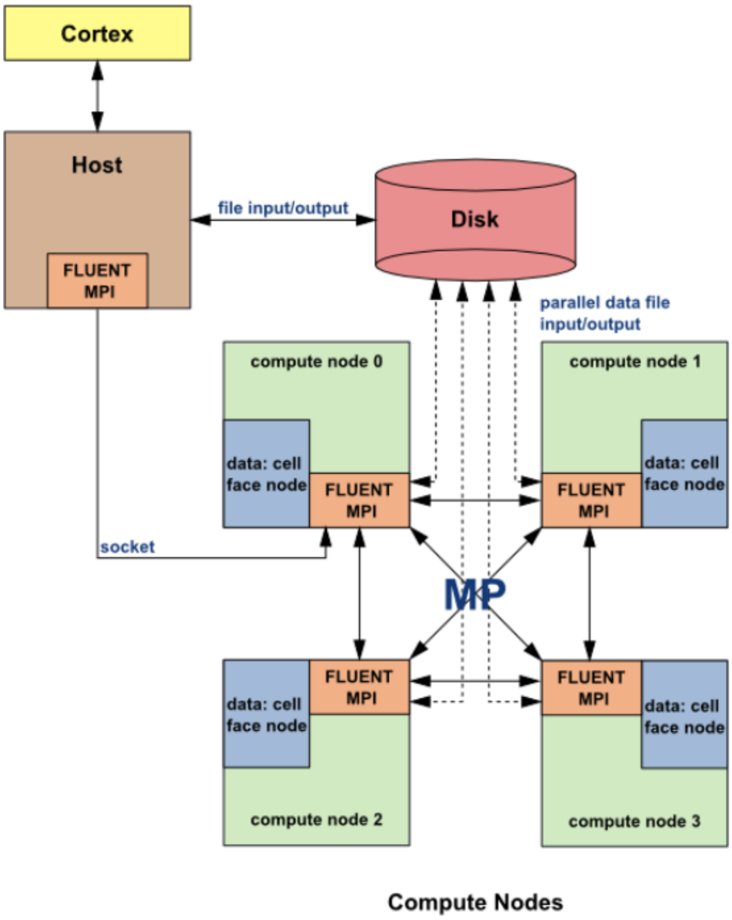

Figure 3-10 ANSYS Fluent Architecture [119].

All airwake computations were performed on Chadwick, the University of Liverpool's Unix-based HPC facility. Chadwick, first commissioned in 2014, is comprised of 118 nodes with 16 cores (a total of 1888 cores) each connected by InfiniBand connection providing speeds of 40 Gigabits per second between nodes. Each node has 16 Sandy Bridge quad-core processors each with 64 GB of RAM, permitting memory intensive parallel simulations. Access to Chadwick was provided using a secure shell (SSH) from a Linux terminal. Text-based commands to ANSYS Fluent on the HPC were provided from a journal file written using the scripting language Scheme for each CFD ship airwake simulation.

3.4.5 CFD Execution

As discussed earlier in Section 3.1.3, prior to each full DDES simulation of the flow, a steady-state RANS simulation was completed to aid convergence of the solution by approximating the mean flow in each cell. During the steady-state RANS initialisation, the SST $k-\omega$ turbulence model was applied in order to maintain consistency within the boundary layer with the unsteady turbulence model used during the subsequent DDES simulation. As first-order accuracy is sufficient for flow initialisation, the first-order upwind discretization scheme was used for momentum, turbulent kinetic energy, and specific turbulence dissipation rate. Pressure was discretized using the Standard scheme, while the SIMPLEC algorithm was applied to achieve pressure-velocity coupling. All of the boundary conditions were kept the same during the RANS initialisation and the DDES simulation. Once the steady-state RANS simulation was computed to an acceptable level of convergence, a synthetic instantaneous turbulence was applied to initiate unsteadiness in the DDES simulation. The flow solution was initiated as steady-state with 3000 iterations, the unsteady solution was then run with a time step of 0.001 seconds.

Before the DDES simulation can be sampled to produce airwake data, the unsteadiness in the flow must be allowed to settle into periodic turbulence, ensuring that the solution is repeatable. Previous work has used equation 3.20 to determine the settling time, which states that the freestream flow will pass at least twice over the length of the ship [113, 122, 123].

$$t_{sett} = \frac{2l}{U_\infty} \tag{3.20}$$

where l is the ship length and U_∞ is the freestream velocity.

Although this rule of thumb is useful, the settling time for each solution may vary due to a number of factors such as changes in wind direction, time-step, mesh quality or boundary conditions. To ensure the flow was settled for each ship airwake CFD solution, the velocity at a number of monitor points were recorded at each time-step in the fluid domain to assess whether the mean unsteady flow was converged at those points and to monitor the turbulence.

The CFD solution settling period was typically 5 seconds, allowing a water particle to pass through the working section at least 2.5 times, and thereby allowing periodic flow features to fully develop. For the small-scale solution, the unsteady flow field was solved for 3 seconds, which in total required around 30 days computing time running on 128 processors on the Chadwick HPC. The CFD solution was output as a case (.cas) file and a data (.dat) file in which unsteady statistics were recorded over the final 3 seconds of the solution allowing mean and turbulent variables to be compared with the experimental measurements taken in the water channel. Each CFD solution, including mesh generation/CFD execution, of the experimental setup was performed by the author. A table of the CFD computations completed by each individual is included in Appendix B.

3.5 Full-Scale QEC Carrier Computational Setup

This section provides further details of the CFD approach used to generate realistic airwakes for the full-scale QEC for implementation in fixed-wing and rotary-wing piloted flight simulation. The CFD method is largely consistent with the CFD method used in Section 3.4 and, as well as providing airwake for flight simulation, the results will also be compared with the model-scale CFD and the experimental measurements.

3.5.1 Full-Scale QEC Domain

The CFD domain for the full-scale QEC is shown in Figure 3-11. The QEC CAD model was placed in the centre of a cylindrical domain. Unlike the domain constraints imposed by the geometry of the water channel, the cylindrical geometry allows the wind angle to be varied through 360 deg by changing the u and v components of the freestream velocity without having to alter the computational domain. Similar to the model-scale CFD simulation, a CFD focus region was placed in the area of interest to accurately resolve turbulence with a maximum grid size of 1 m. The rectangular red box around the ship is the region in which the velocity data was interpolated for integration with BAE Systems F-35B simulator; the box has a length of 700 m, a width of 200 m and a height of 72 m.

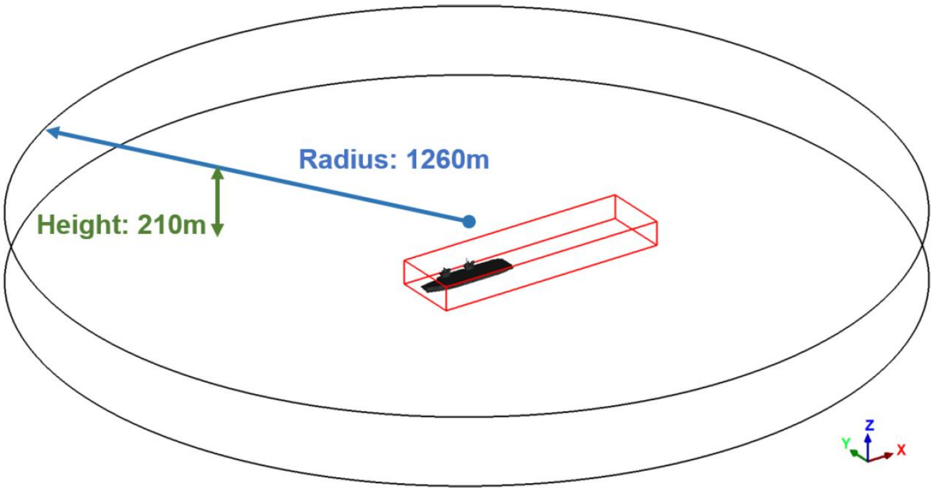

Figure 3-11 Computational domain for full-scale QEC CFD including rectangular interpolated box for CFD integration with simulation [52].

The overall CFD domain in Figure 3-11 needs to be large enough to ensure that boundaries are at a sufficient distance from the rectangular volume to avoid interfering with the flow computations. The CFD computational domain height was set at 0.75 ship length (210 m), while the radius was set to 4.5 ship lengths (1260 m), placing the ship geometry and the rectangular box at a sufficient distance from far-field boundaries to ensure that the fluid flow in the focus region is not impacted by physically unrealistic/unrepresentative effects which may occur near to the domain boundaries; the dimensions of the cylindrical domain are consistent with the approach used by Forrest and Owen for smaller ships [16]. The bottom surface of the cylindrical domain represents the waterline. Positive x runs from the ship's bow toward the stern, positive y runs laterally from port to starboard and z is positive in the vertically upward direction from the sea surface. The direction of flow entering the domain is specified by unit direction vectors given in equation 3.21 and shown in relation to the ship axis in Figure 3-12. For each airwake computation the WOD condition is specified in terms of wind direction and magnitude as shown in Figure 3-12. The ship speed is accounted for in x-component of the WOD.

$$\begin{aligned} \hat{v}_x &= \cos\Psi \\ \hat{v}_y &= \sin\Psi \qquad (3.21) \\ \hat{v}_z &= 0 \end{aligned}$$

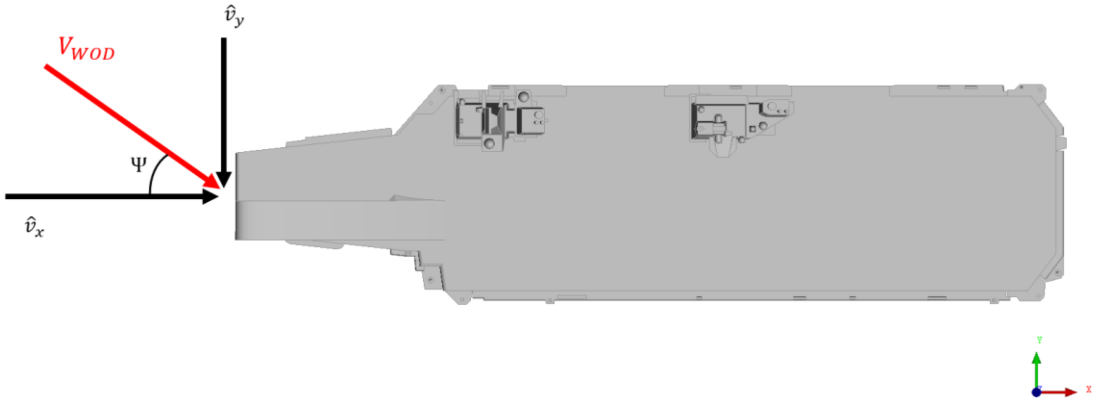

Figure 3-12 Unit vector formation to determine prevailing wind condition.

3.5.2 Full-Scale Mesh

The QEC domain was meshed using the method outlined in Section 3.3. Twelve layers of prism elements were grown from the surface to resolve the viscous boundary layer, consistent with the number of layers used in the model-scale CFD simulations. The cell size in the focal region was limited to 1 m and the overall cell count for the whole domain was approximately 100 million. Figure 3-13 shows a slice through the domain along the centre of the ship's islands in which the density region can be distinguished over the flight deck and off the stern of the ship to ensure the turbulence is adequately resolved over the areas employed during fixed-wing and rotary-wing approaches.

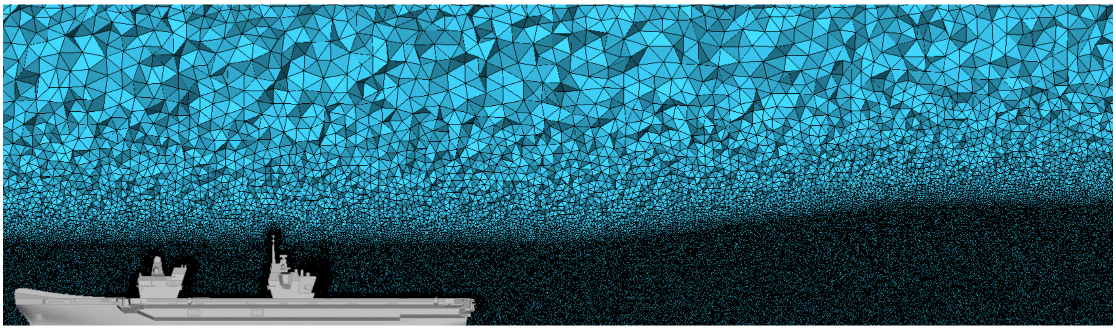

Figure 3-13 Slice through centre of the islands showing the mesh density region.

3.5.3 Full-Scale Boundary Conditions

Similarly, to the experimental CFD domain, the surfaces of the carrier were assumed to be hydrodynamically smooth and were defined as zero-slip walls, i.e. zero velocity on the surfaces. The upper surface of the domain was set as a pressure-far-field, allowing static pressure to be specified at the boundary, and thus minimising any potential blockage effects. While a real boundary does occur at the sea-air interface, a representative model to account for this along with the ship's motion would incur high computational cost. As the CFD modelling is performed to provide a ship airwake database for flight simulations, the sea surface boundary was limited to a slip condition, thereby allowing the prescribed velocity profile, detailed in 3.5.4, to be maintained throughout the domain. The boundary conditions specified are typical for ship airwake computations [16, 113].

3.5.4 Atmospheric Boundary Layer Profile

While the inlet of the model-scale CFD simulation was defined as a uniform profile of 1 m/s to replicate the flow through the water channel, the freestream flow over the full-scale ship was given an inlet velocity profile to represent an oceanic Atmospheric Boundary Layer (ABL) using equation 3.22, where V_{ref} is the reference wind-speed measured at a known height above sea-level, z_{ref}, and z_0 is the sea-surface roughness length-scale which, according to Garratt [124], can be taken to equal 0.001 m for oceanic conditions.

$$V = V_{ref}\left(\frac{ln\left(\frac{Z}{Z_0}\right)}{ln\left(\frac{Z_{ref}}{Z_0}\right)}\right) \tag{3.22}$$

The reference wind speed, V_{ref}, is the desired wind speed at the mean height of the ship's anemometers. The application of a steady ABL has previously been shown to produce more accurate results for ship airwake CFD computations than does a uniform inlet profile [42].

The ABL is illustrated in Figure 3-14, which shows a computed full-scale airwake for a headwind as contours of the mean *u*-velocity; the ABL is seen just ahead of the ship, and the vertical plane is through the centre of the islands. The inlet flow is described by the velocity at the mean height of the ship's three island-mounted anemometers, which is approximately 34 m above the sea surface. The velocity at anemometer height in Figure 3-14 is 25 kts (12.86 m/s).

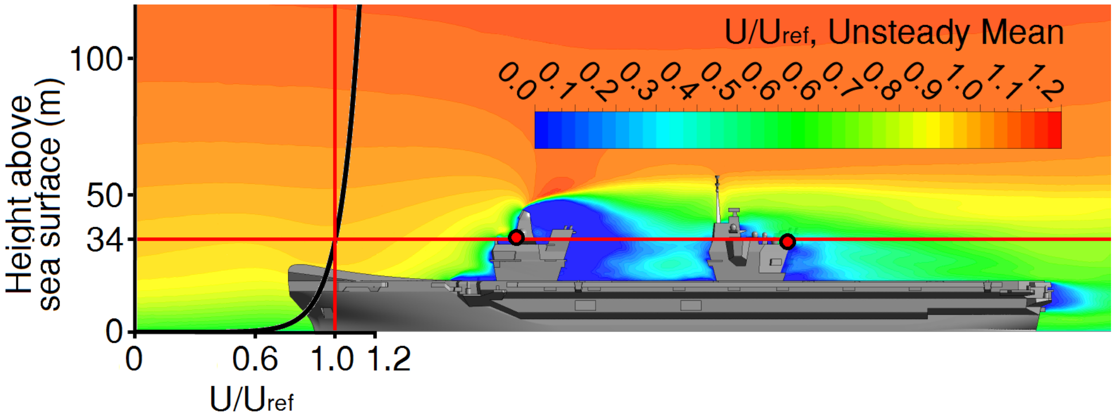

Figure 3-14 Contours of mean normalised *u*-velocity components in a plane through the centre of the islands, including the ABL inlet profile.

3.5.5 Full-Scale CFD Execution

Consistent with the CFD method outlined in Section 3.4, an initial steady-state solution was computed for 3000 iterations before the solver was switched to the transient DDES solver with a time-step of 0.01 seconds (100 Hz). A further consideration of the time-step sizing is to ensure that the frequency content of the flow shed from the ship's superstructure, which affects the aircraft and pilot workload, is adequately captured in the CFD solution. Previous research has shown that frequencies of turbulent flow perturbations in the range 0.2-2 Hz are the main contributors to pilot workload [125]. This range is known as the pilot closed-loop response frequency range; the pilot will respond to, or compensate for, disturbance frequencies within this, through movement of the cockpit control inputs. At frequencies much below this range, disturbances will be 'quasi-steady' and manifest themselves as a drift, which the pilot can easily counteract through low frequency 'trim' corrections. Frequencies above 2 Hz are experienced as vibrations through the airframe that will mainly impact ride quality. The minimum time period of 2 Hz equates to 0.5 seconds, which is well within the frequency of computation.

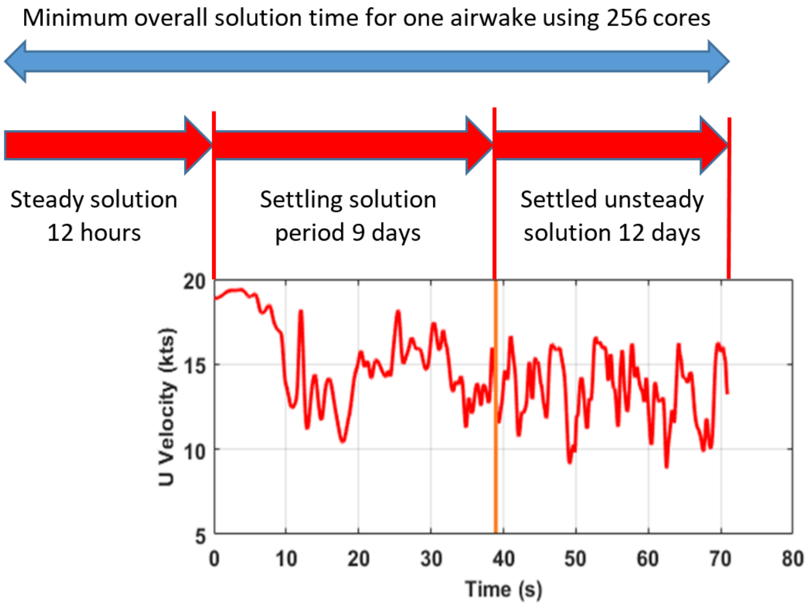

Figure 3-15 Sampled airwake velocity used for monitoring progress of unsteady solution [52].

Figure 3-15 shows the time to create a full-scale airwake when using 256 processors in an HPC cluster; the progress of the solution was monitored by recording the velocity components at several points in the flow. The initial steady-state solution took around 12 hours, the settling period was in the region of 9 days and the time for computing the 30 seconds of unsteady airwake required for export to the flight simulator was a further 12 days, giving a total time of approximately three weeks. While the unsteady solution was computed using a time-step of 0.01 seconds (100 Hz), the airwake data for the flight simulators was exported at 25 Hz producing instantaneous time-step files of approximately 4.68 GB in size and generating 3.52 TB of airwake data in total. A CFD output data file containing mean data for flow over the total domain was also generated along with velocity measurements at each monitor point. In total each CFD QEC airwake WOD condition generated approximately 4 TB of data.

The process for QEC airwake generation was repeated for a range of relative wind conditions. Airwakes were produced in a sequence specified by BAE Systems as they developed their F-35B/QEC simulated flight trials, in total 16 airwakes at different WOD azimuths and magnitudes were generated for rotary-wing and fixed-wing flight simulation and analysis. The majority of the full-scale QEC airwakes were produced by Kelly [52]. The author contributed to the final QEC airwake computations, and was a main contributor to the interpolation, and integration with the UoL HELIFLIGHT-R simulator discussed in Chapter 5. Table B-1 in Appendix B provides a list of the computations and interpolations performed, and by which individual, for both the experimental and full-scale CFD.

3.6 Airwake Velocity Scaling

It is clear from the discussion so far that creating airwakes for the QEC is very time-consuming and is expensive in terms of computing resources; however, it is possible to make some significant savings. For example, an airwake computed at one velocity can then be scaled to a different velocity [126]. Polsky [127] first showed how the average velocities in the airwake could simply be scaled since the flow topology is independent of Reynolds number. So, for example, if the airwake is computed at 40 kts, a 20 kts airwake can be obtained by halving all the velocity components throughout the domain. Zan [22] further noted that the unsteadiness within the airwake can also be scaled because the frequencies of the various vortical structures being shed from the superstructure is also directly related to the flow velocity, through the Strouhal number, shown in equation 3.23. At sufficiently high Reynolds number, such as found in ship airwakes, the Strouhal number, *St*, is a constant value and can, therefore, be used to scale the airwake frequency, f, to a required flow speed, u, for a ship of characteristic length, l.

$$St = \frac{fl}{u} \tag{3.23}$$

Hodge et al. [17], in a study where CFD-generated ship airwakes were applied to flight simulation, demonstrated that the Strouhal scaling of CFD airwake data from 40 to 30 kts gave good results when compared to a computed 30 kts airwake. In the present study, therefore, Strouhal scaling was applied to the computed QEC airwakes for use in flight simulation.

3.7 Chapter Summary

This chapter has described the CFD method used to model the flow over the QEC for both the experimental-scale model submerged in a water channel, and the full-scale ship in an open environment. For the small-scale model, an unstructured mesh of 100 million cells was required to compute the flow over the ship using the time-accurate DDES turbulence model, performed during 30 computational days on an HPC. By recreating the flow in the water channel using CFD, the solution can be compared with experimental measurements taken in the water channel using the methodology described in Chapter 2, thereby providing an assessment of the accuracy of the CFD method.

The same CFD methodology was also used to generate unsteady airwakes of the full-scale QEC aircraft carrier for analysis and for fixed- and rotary-wing piloted flight simulation. However, while the methodology, the mesh size and computational time were similar to that used for the small-scale model, an ABL velocity profile was applied at the inlet of the full-scale model, unlike the uniform profile that was present in the experiment. At defined WOD conditions, 30 seconds of unsteady airwake velocities were computed for integration with an aircraft flight dynamics model for piloted flight simulation. Airwakes were then scaled to provide a variety of wind speeds for each WOD azimuth. Each WOD CFD investigation produced approximately 4 TB of data.

The CFD of the full- and small-scale ship also allows any differences that may occur in the flow due to the different Reynolds numbers and inlet conditions to be observed. The following chapter will compare the CFD solutions with the experimental measurements.

Chapter 4

Comparison of Experimental Airwake Measurements with CFD

The principal method for modelling unsteady ship airwakes nowadays is CFD. However, due to the assumptions present in the turbulence modelling applied within the CFD solver, and error introduced by discretization, validation is required to provide confidence in the accuracy of the results. The airwakes generated by the twin-island QEC aircraft carriers will be characteristically different in size and content to airwakes previously produced for single-spot frigates and incremental changes in the turbulence model from the previously validated DES CFD method have also been implemented, further increasing the need for experimental validation.

Chapter 2 outlined the experimental setup used to measure mean and turbulent flow velocities present in the airwake of a 1:200 scale model of HMS Queen Elizabeth submerged in the UoL recirculating water channel. Chapter 3 described the CFD method used to produce the QEC airwakes for both the experimental setup and the full-scale ship. This chapter first compares the experimental measurements with the simulated CFD experiment, to demonstrate the accuracy and suitability of the CFD method. Mean velocity and RMS turbulence data were compared in locations of interest, such as along the approach path of the SRVL, or in regions which showed higher aerodynamic perturbations from the freestream conditions, to highlight any dissimilarities between the CFD method and experimental measurements. Two representative wind directions, Ahead and Green 10, were chosen for validation as aircraft carriers often head into the direction of the wind where possible, providing more favourable conditions for aircraft during take-off and landing. By examining separate wind conditions, a more thorough comparative study can be made for CFD validation [50].

The second part of this chapter, Section 4.2, compares the CFD of the experimental setup with the full-scale CFD to assess the effect of Reynolds number on the flow field in areas such as over the ski-jump, and to investigate any flow field changes due to the application of a non-uniform inlet boundary condition. Understanding how the differences in the Reynolds number and inlet conditions affects the overall ship airwake will provide additional confidence in the accuracy of the full-scale airwake data for use in high-fidelity flight simulations.

4.1 Comparison of Model-Scale CFD and Experiment

4.1.1 Headwind

This section compares the model-scale CFD results with measurements taken in the water channel. The flow was from Ahead with a uniform velocity profile of 1 m/s. Figure 4-1 shows the CFD-computed instantaneous flow over the ship where the turbulent vortical structures are presented as *Q*-criterion isosurfaces. The *Q*-criterion is defined as the second invariant of the velocity gradient tensor ∇u and is used as a vortex identification method; a positive value of Q is a region within the flow where the vorticity magnitude is larger than the strain-rate magnitude and is denoted as a vortex [128].

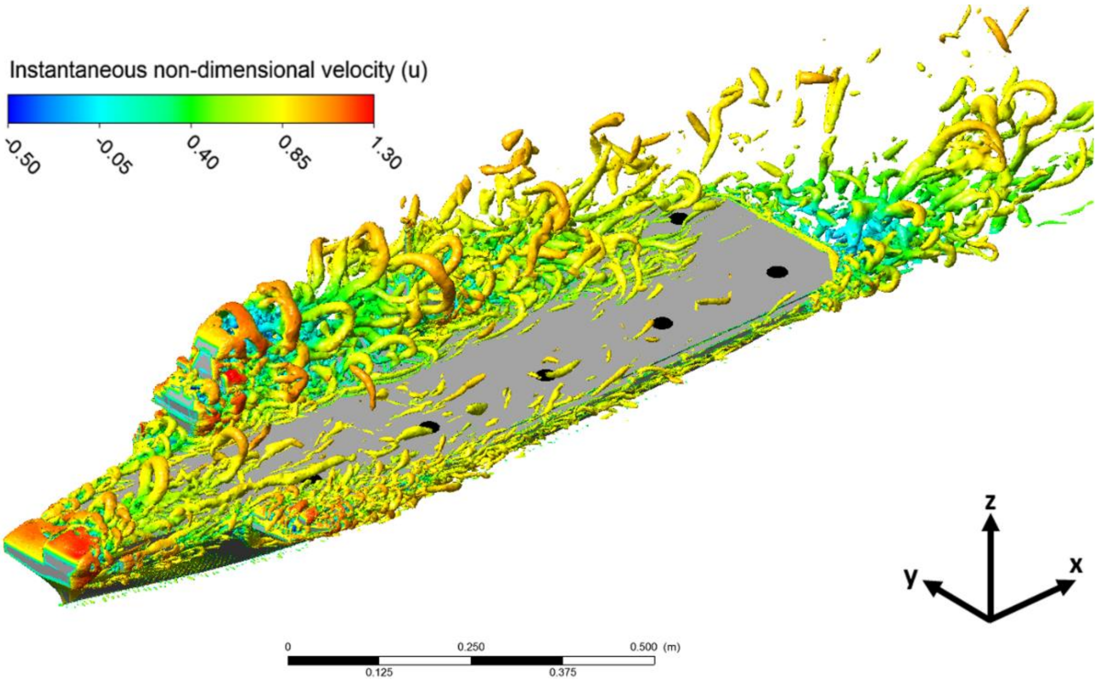

Figure 4-1 Headwind flow over QEC model presented as instantaneous iso-surfaces of Q-criterion coloured by *u*-velocity.

The results presented in Figure 4-1 were also used to inform the experiments. From an operational perspective the areas of interest are the landing spots, which are along the flight deck and are indicated as black dots. Spot 1 is the most forward, followed by spots 2 to 5; spot 6 is alongside spot 5 and situated behind the aft island (See Figure 1-5). In a headwind, there is little disturbance in the flow over the landing spots; the exception being spot 6 which is in the turbulent wake in the lee of the islands. In contrast, from the perspective of comparing experimental data with the CFD solution, the areas around the bow of the ship, the islands and astern of the ship are of greater interest; experimental velocity measurements were therefore concentrated in these key areas. Also shown in Figure 4-1 are the *x*, *y*, *z* axes relative to the ship; the corresponding velocities in these axes are *u*, *v* and *w*, respectively.

Figure 4-2 shows the unsteady airwake at an instant in time as contours of the streamwise *u*-velocity component. The vertical plane is parallel to the ship's longitudinal axis and passes through the centre of the islands and, therefore, is offset to the starboard side of the ski-jump.

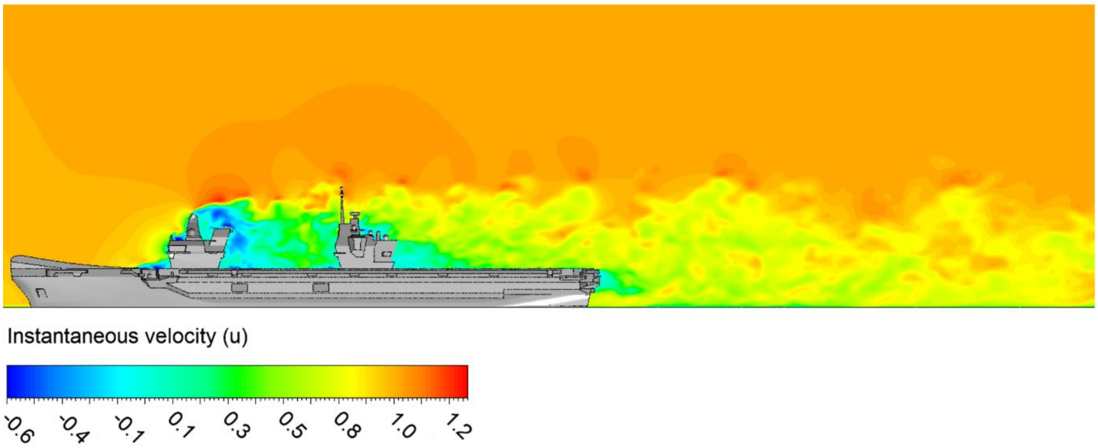

Figure 4-2 Contours of instantaneous *u*-velocity components (m/s) in a vertical plane through the centre of the islands.

Figure 4-3 shows a comparison between the measured and computed values of the mean streamwise velocities along vertical lines at each of the portside landing spots 1-5. In this case the airwake is illustrated by contours of turbulence intensity which, throughout this study, is defined as the Root Mean Square (RMS) of the turbulent velocity fluctuations divided by the freestream flow velocity, i.e. not the local velocity. For example, the turbulence intensity (Ti) presented as contours in Figure 4-3 is calculated by equation 4.1, where u', v', w' are the fluctuations in the three velocity components *u*, *v*, *w*.

$$Ti = \frac{\sqrt{\frac{1}{3}\left(u'^2 + v'^2 + w'^2\right)}}{U_\infty} \tag{4.1}$$

It can be seen in Figure 4-3 that the *u*-velocity profiles towards the stern of the ship is mostly undisturbed while spots 1 and 2 show a reduction in magnitude below 30 mm above the deck, which coincides with an area of turbulence in the order of 8%, which emanates from the bow of the ship. As can be seen in Figure 4-3 the agreement between the CFD (red line) and the ADV experimental data (black line) is mostly very good.

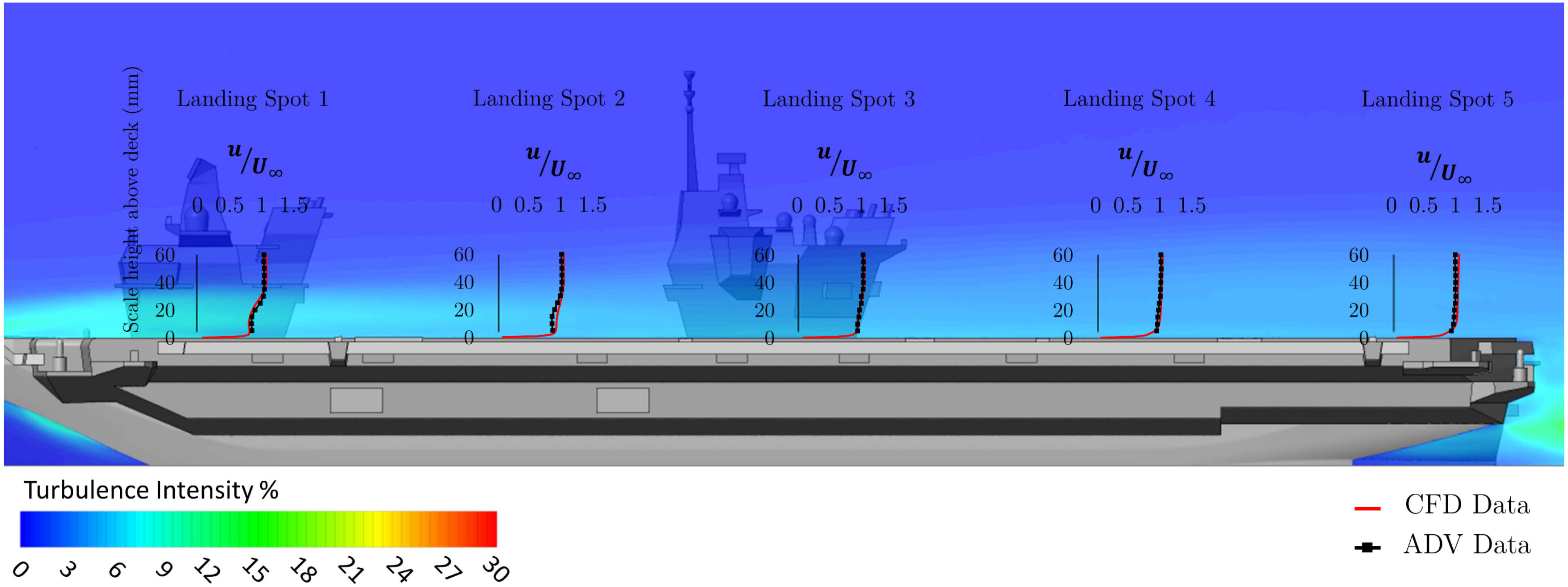

Figure 4-3 Comparison of experimental and CFD *u*-velocity components in a plane through the centre of the port-side landing spots.

Figure 4-4 compares the experimental and CFD values of the lateral, *v,* and vertical, *w,* mean velocity components and turbulence intensities at each port-side landing spot. In this case the turbulence intensity is the fluctuating velocity component divided by the mean freestream, i.e., w'/U_∞, consistent with equation 4.1. There is a greater proportional difference between the CFD and the experiment than in Figure 4-4; however, it should be noted that the mean velocities in these directions are very small, mostly less than 0.1 m/s.

Figure 4-5 compares the *u*-velocity profile of five vertical lines aligned with the centreline of the ship's ski-jump, and therefore in a different plane to Figure 4-4; a plane of turbulence intensity passing through each test point is also shown. These test points were included in the investigation as anemometer data was collected at these locations during Air Flow Air Pattern (AFAP) trials conducted as part of HMS Queen Elizabeth's sea trials. Similar to Figure 4-3, the *u*-velocity deviates little from the freestream wind conditions. The contours of turbulence intensity show a turbulence intensity at Spot 1 of around 8% which gradual reduces towards a value in the order of 5% at Spot 5, this time emanating from the front of the ski-jump. The small deviations from the freestream conditions shown in Figure 4-3 to Figure 4-5 correspond with the low flow disturbance visible over the deck and port-side spots in Figure 4-1.

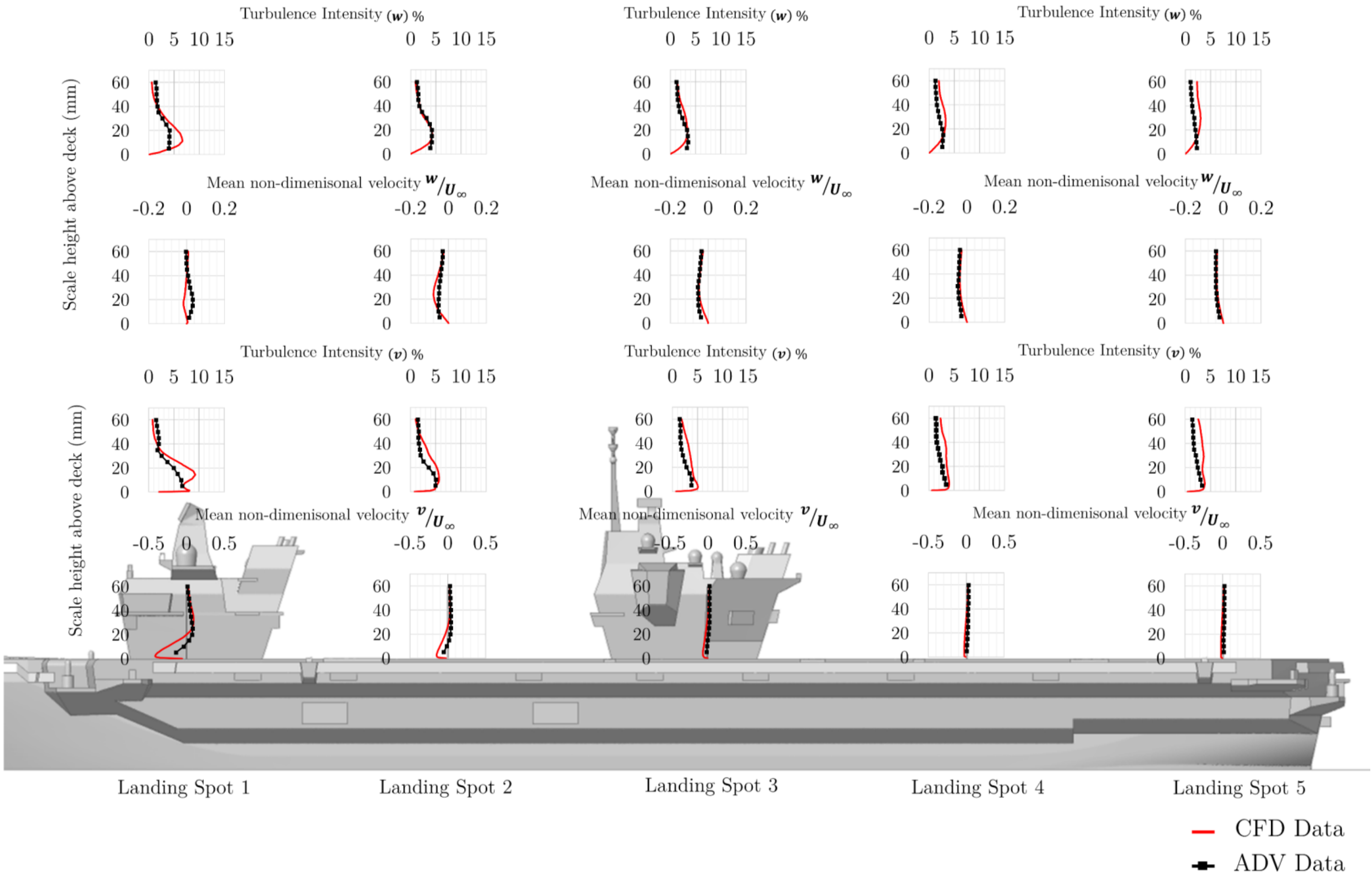

Figure 4-4 Comparison of experimental and CFD mean *v*- and *w*-velocity and RMS in a plane through the centre of the port-side landing spots.

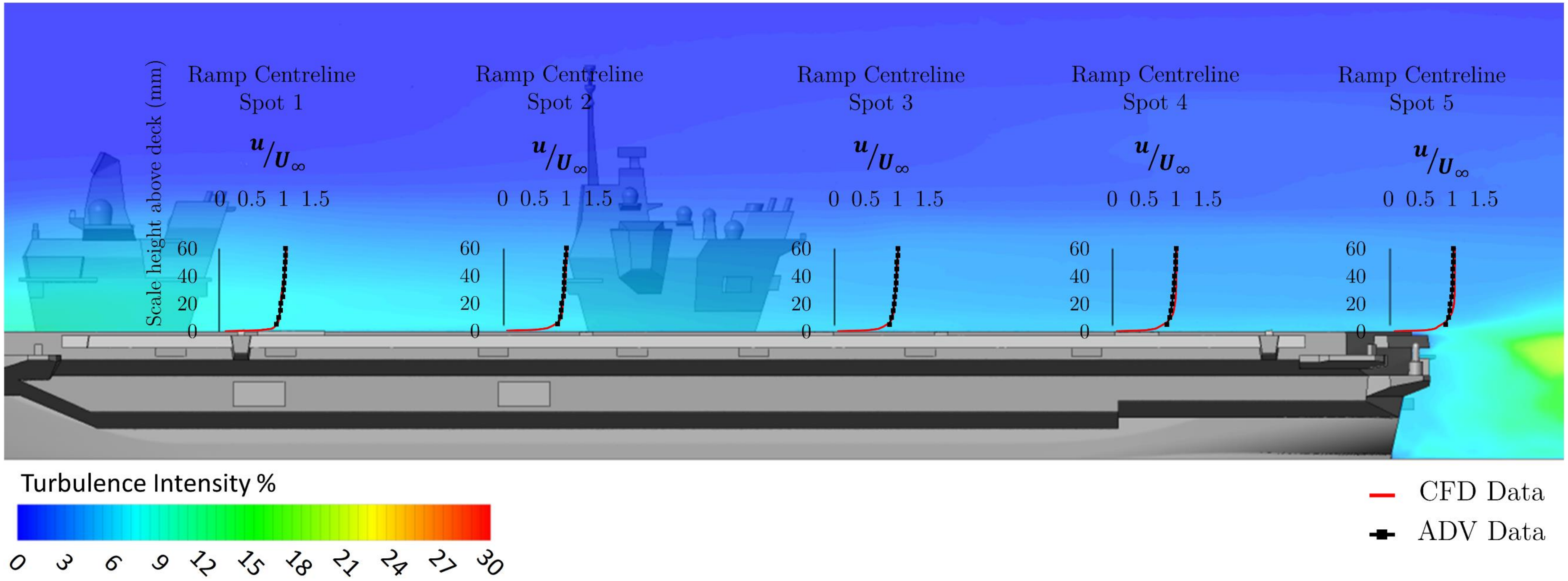

Figure 4-5 Comparison of experimental and CFD *u*-velocity components in a plane through the ski-jump's centreline.

Although the accuracy of the airwake over each port-side landing spot is essential for high-fidelity simulation, in a headwind there is very little deviation of the velocities from the freestream condition, which may not highlight dissimilarities between the CFD solution and experimental measurements. Figure 4-6 shows a comparison around the islands and the stern of the ship. It can be seen in Figure 4-6 that ahead of the forward island the *u*-velocity profile above the deck is largely undisturbed, whereas in the lee of each of the islands and at the stern of the ship there is a significant velocity deficit compared with the freestream. Also, referring to the contours of turbulence intensity, the turbulence between the islands is of the order of 20%. As can be seen in Figure 4-6 the agreement between the CFD (red line) and the experiment (black line) is mostly very good.

Figure 4-7 compares the experimental and CFD values of the lateral, *v,* and vertical, *w,* mean velocity components and turbulence intensities at various positions behind the islands. There is a greater proportional difference between the CFD and the experiment than in Figure 4-6; however, similar to Figure 4-4, it should be noted that the mean velocities in these directions are very small, mostly less than 0.1 m/s.

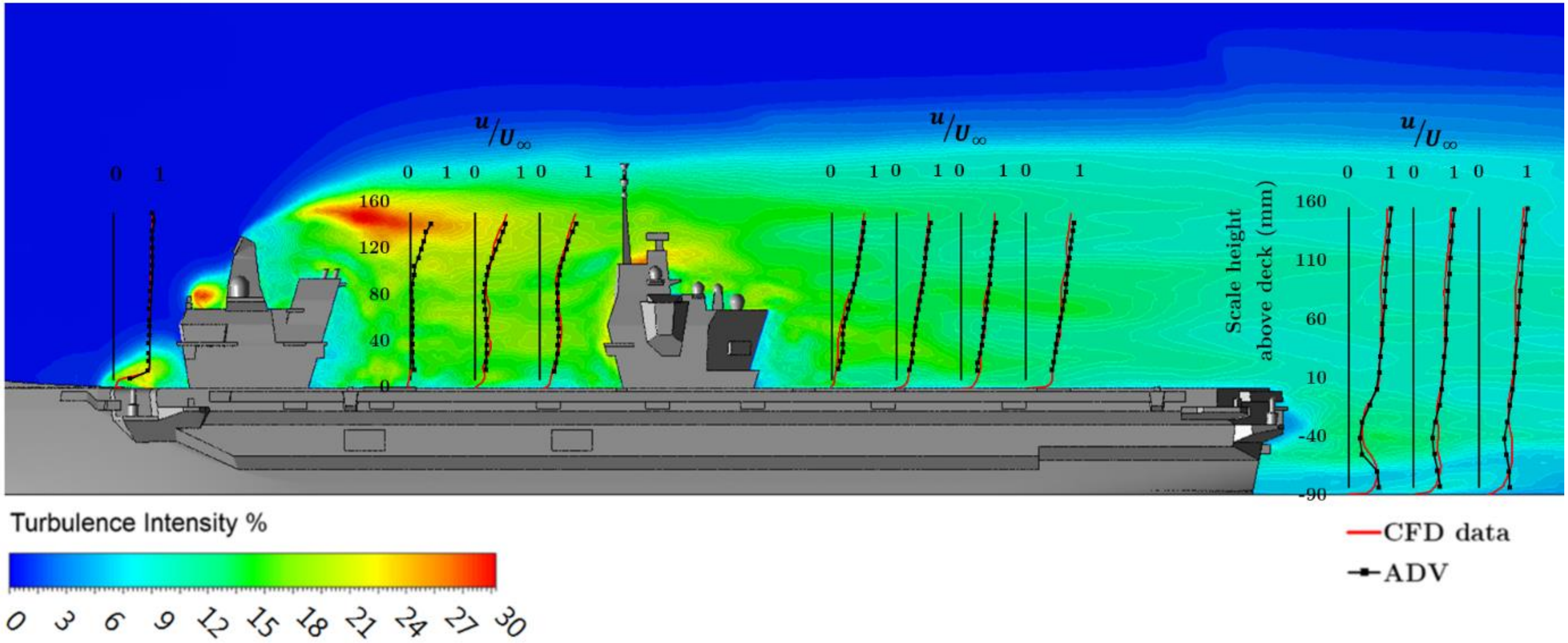

Figure 4-6 Comparison of experimental and CFD u-velocity components in a plane through the centre of the islands.

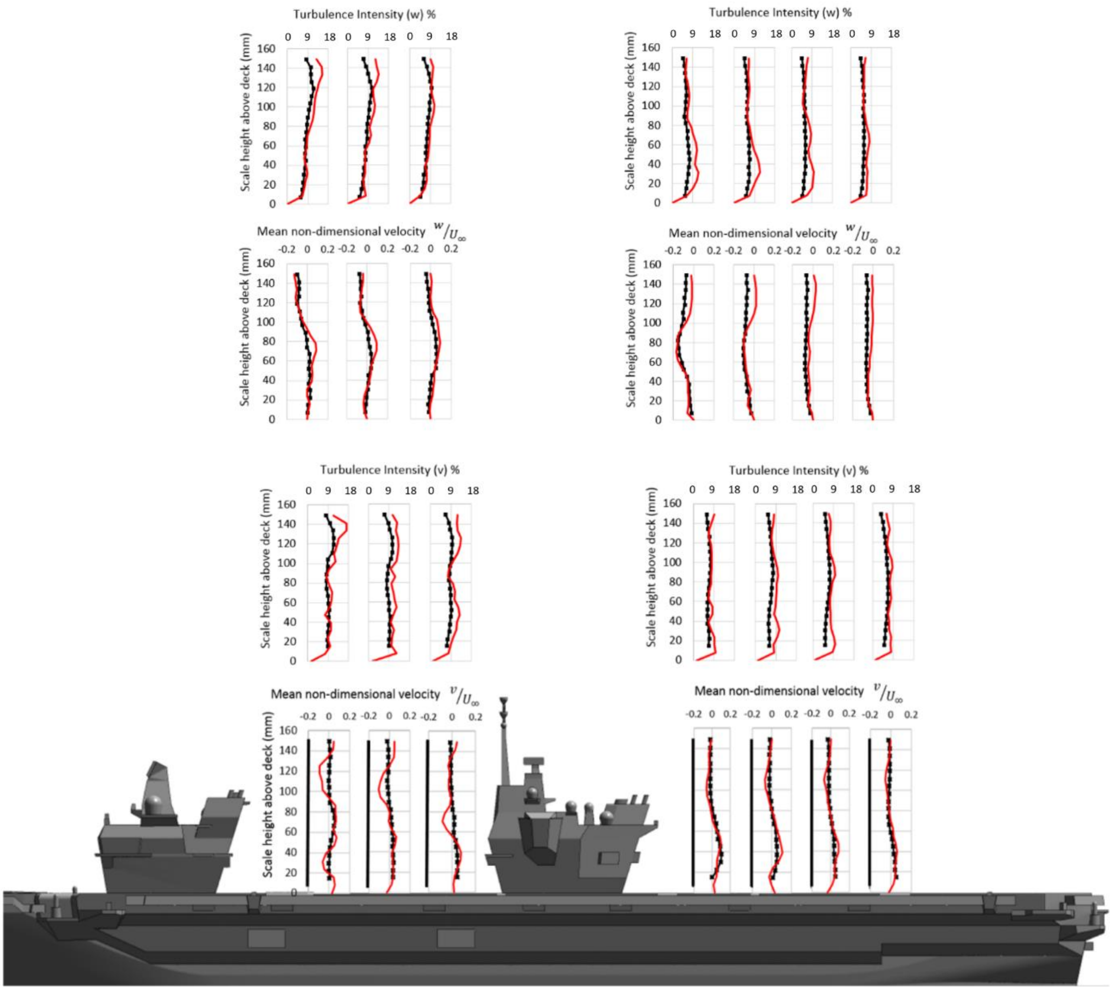

Figure 4-7 Comparison of experimental and CFD mean *v*- and *w*-velocity and RMS in the lee of the islands.

Figure 4-8 shows a comparison of the mean *u*-velocity component at three positions astern of the ship on the ship centreline (i.e. y=0) and, therefore, in a different plane to Figure 4-6 and Figure 4-7; contours of turbulence intensity are also shown. Again, there is good agreement between the CFD and the experiment, and the reverse flow region in this plane can be clearly seen as indicated by the knee in the curve. The higher levels of turbulence indicate the existence of a shear layer between the main flow and the recirculation zone.

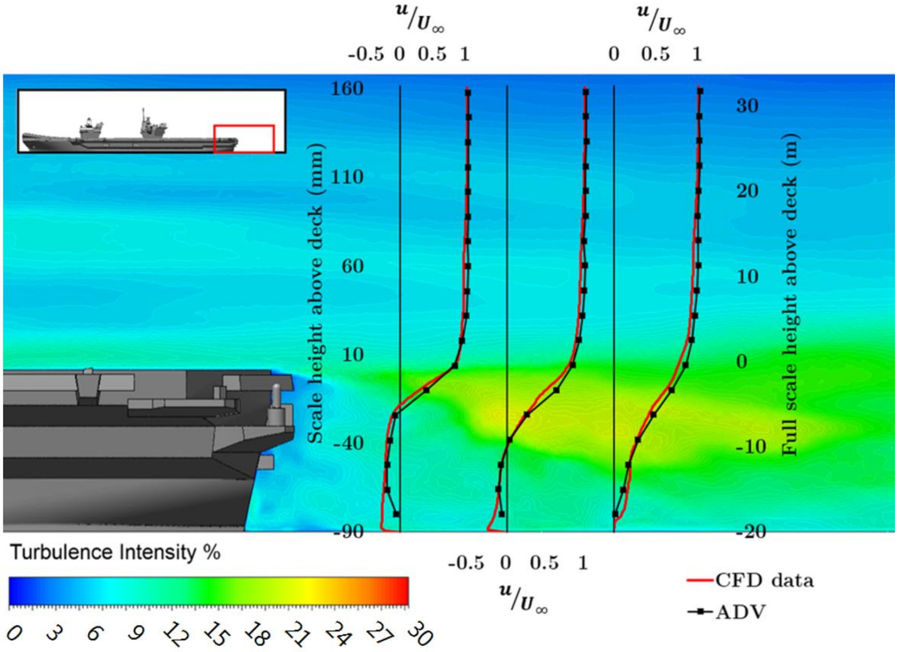

Figure 4-8 Comparison of experiment and CFD mean *u*-velocity component astern of the ship centreline.

Figure 4-9 shows the lateral and vertical velocity components along the vertical line in Figure 4-8 which is closest to the ship. The negative vertical velocity component, *w*, can be clearly seen. Because the line is at the centreline of the ship, the lateral velocity component, *v*, might be expected to be close to zero; however, the ship is not symmetrical and so, therefore, neither is the airwake astern of the ship. The comparison between the CFD and the measured points show reasonably good agreement, given that the velocities are small and will also be sensitive to the positional accuracy of the ADV probe.

Figure 4-10 shows the turbulence intensities corresponding to the mean velocities in Figure 4-9. The peak in the turbulence coincides with the shear layer indicated in Figure 4-8; again, the agreement between experiment and CFD is reasonably good.

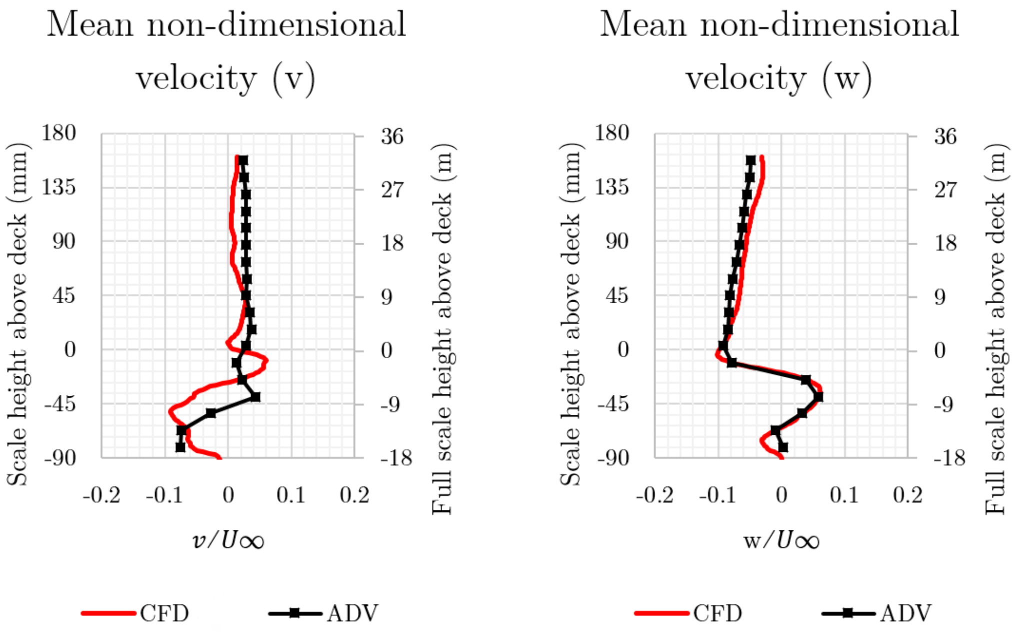

Figure 4-9 Comparison of experimental and CFD mean *v*- and *w*-velocity components at the rear of the ship centreline.

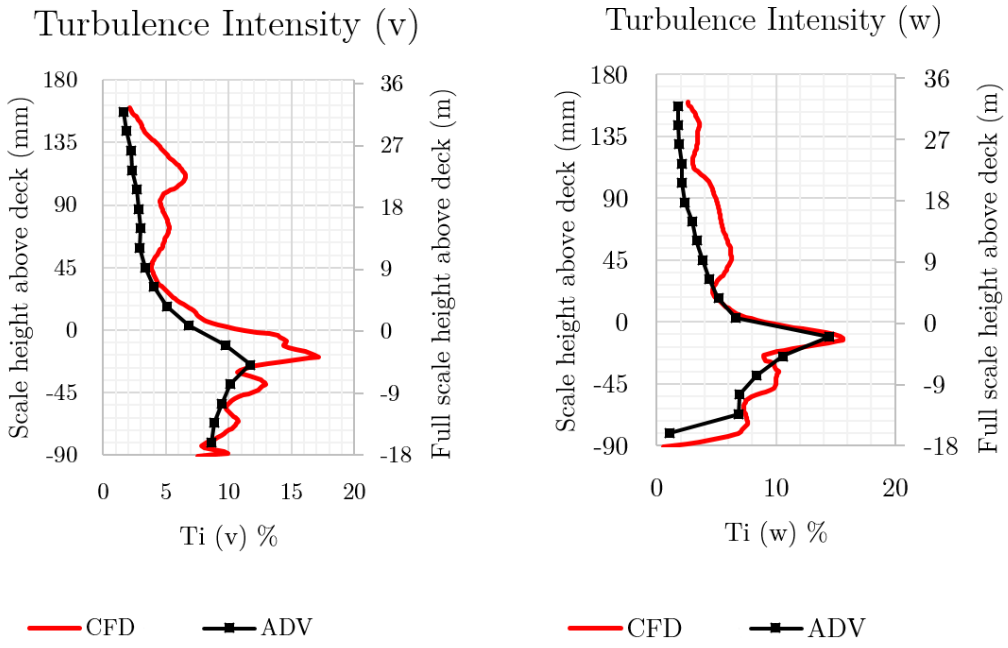

Figure 4-10 Comparison of experimental and CFD turbulence intensities in *v*- and *w*-velocity components at the rear of the ship centreline.

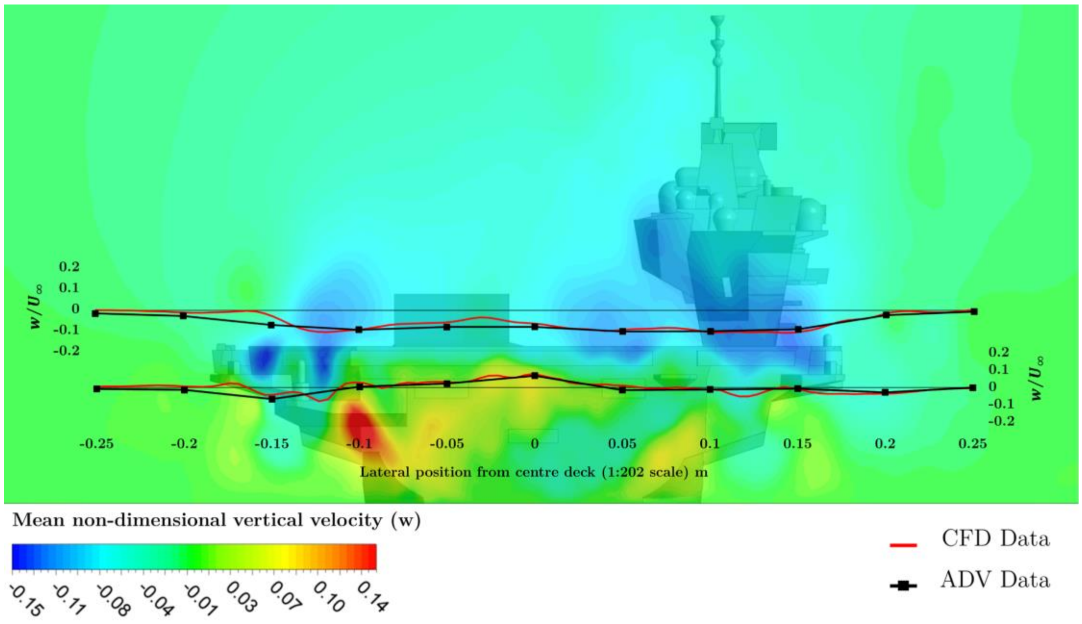

Figure 4-11 Comparison of experiment and CFD mean w-velocity along a lateral plane 24 cm (5 m full-scale) off the rear of the ship.

Figure 4-11 shows the vertical velocity along two lateral lines 24 cm (small-scale) behind the ship's stern; contours of the vertical velocities are also shown. The lateral line located above the ship's flight deck shows a negative vertical velocity across the width of the ship, whereas, the lateral line located beneath the ship's flight deck shows little vertical velocity except for a small positive region at the centreline of the ship. The comparison between the CFD and the measured points show reasonably good agreement.

The bow of the ship is also interesting from an aerodynamic perspective. Looking at the front of the ship in Figure 1-1 it appears to be blunt, but the leading edges of the flight deck-edge are rounded with a full-scale radius of 1 m. Turbulent flow cascading down the flight deck from separation at the bow can potentially impact aircraft operating downstream. Czerwiec and Polsky [129] investigated the unsteady flow over the flight deck of a LHA ship, which had a square leading edge. Wind tunnel tests and CFD showed that the flow over the deck was significantly improved by attaching a downward-deflected flap to the ship's bow. Bardera et al. [130] conducted an experimental wind tunnel study of the flow over an aircraft carrier's ski-jump, which had a leading edge that was relatively sharp, and showed that a significant flow separation took place. As discussed earlier in Section 1.9.1, the small-scale QEC model can be expected to exhibit flow separation at the bow and, with careful scrutiny, this can be seen in the CFD results in Figure 4-12, which shows the *u*-velocity along various vertical lines on a plane through the centre of the ski-jump, and which also shows that there is a separation bubble over the ski-jump.

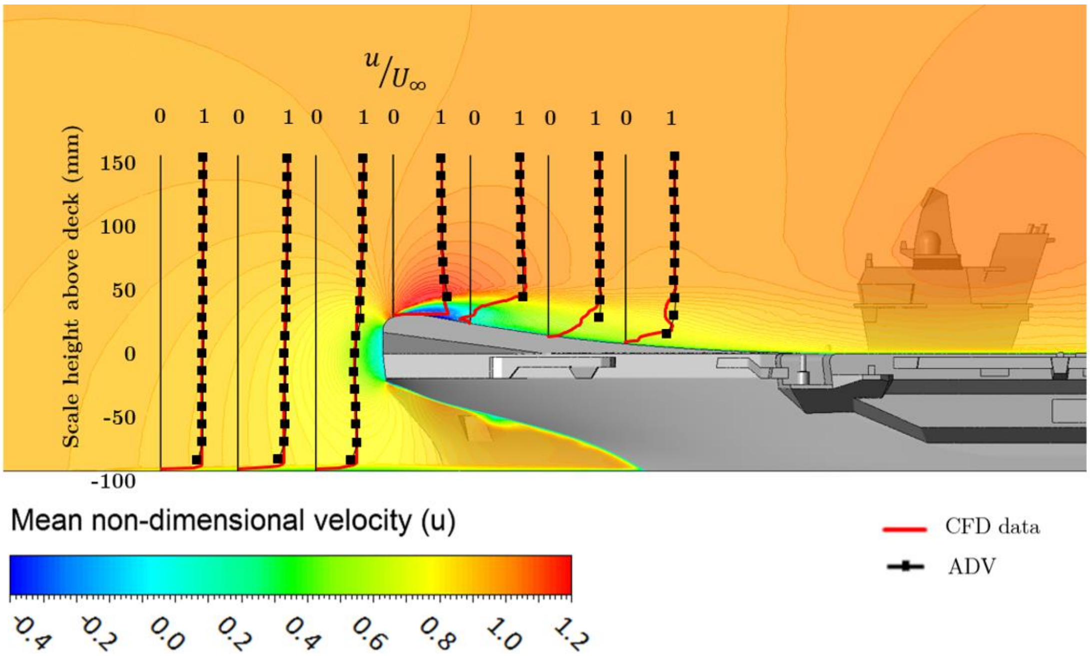

Figure 4-12 Comparison of experiment and CFD u-velocity over the ski-jump.

The outline of the ski-jump may resemble that of an aerofoil, but its purpose is to impart an upward vertical velocity and ballistic profile to the aircraft, providing additional time to accelerate to flying speed whilst ensuring it is on a safe trajectory. This additional time leads to either a reduced take-off length for a given weight, or an increased weight for a fixed take-off distance. The take-off benefits have to be balanced against the significant additional loads that are imparted to the landing gear and so the ski-jump profile is a balance between these two requirements [3]. The presence of flow separation over the ski-jump (or from the leading edge of the flight deck to the starboard of the ski-jump) will largely depend on the radius of the leading edge and on the flow Reynolds number [69]. As the Reynolds number reduces, the radius of the rounded edge must be increased to maintain attached flow [70]. As indicated earlier, it was expected that the small-scale CFD headwind flow would demonstrate separation, while the full-scale would not.

As well as the flow directly over the ship, it is also important that the flow astern of the ship is well modelled and validated. In this case, the challenge for the CFD is to maintain the turbulent eddies in the airwake for a significant distance downstream, covering the fixed-wing approach path. While conventional fixed-wing carrier-borne aircraft approach the carrier on a nominal 3 deg glideslope [131], the F-35B aircraft will approach along a steeper 7 deg glideslope during the SRVL approach [5], thus passing higher over the stern of the ship. Figure 4-13 shows the vertical *w*-velocity component plotted along the SRVL approach path; in this case the vertical plane corresponds with the centreline of the runway, since that is the pilot's line-up reference cue. For the experiments, the traverse system was programmed to collect velocity measurements along the approach path. As can be seen in Figure 4-13 there is a downward velocity component at the stern of the ship, as seen earlier in Figure 4-9; a feature known colloquially as the 'burble' [132]. The burble is characterised as a massively separated unsteady wake region in the lee of the ship. Fixed-wing aircraft approaching the flight deck will experience a sudden velocity downwash immediately aft of the ship due to the burble, which causes the aircraft to lose altitude and deviate from the desired glideslope.

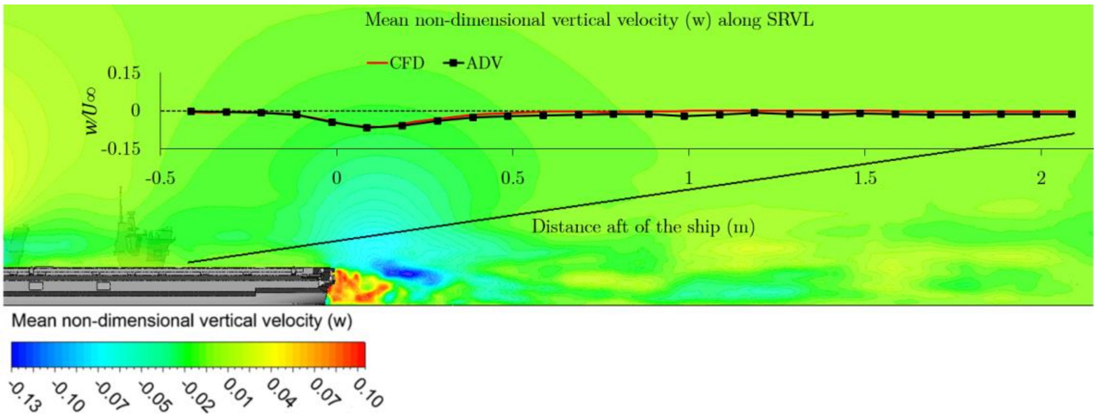

Figure 4-13 Comparison of experiment and CFD mean *w*-velocity along the SRVL approach path.

The experimental and computed streamwise, *u*, and lateral, *v*, mean velocity components along the glideslope are compared in Figure 4-14. Away from the direct influence of the ship the *u*-velocity component is essentially 1 m/s for both the experiment and the CFD. The lateral velocity component is close to zero, with some influence of the asymmetry of the ship apparent.

Figure 4-15 shows the comparison of experimental and CFD turbulence intensities in the lateral, *v*, and vertical, *w*, velocity components along the SRVL approach path. The agreement is reasonable, and the experimental values fall away towards the freestream value of approximately 1% after one ship length astern. It can be seen that despite the efforts taken to prevent turbulence dissipation, the computed turbulence does fall towards zero from around 1.5 ship lengths astern.

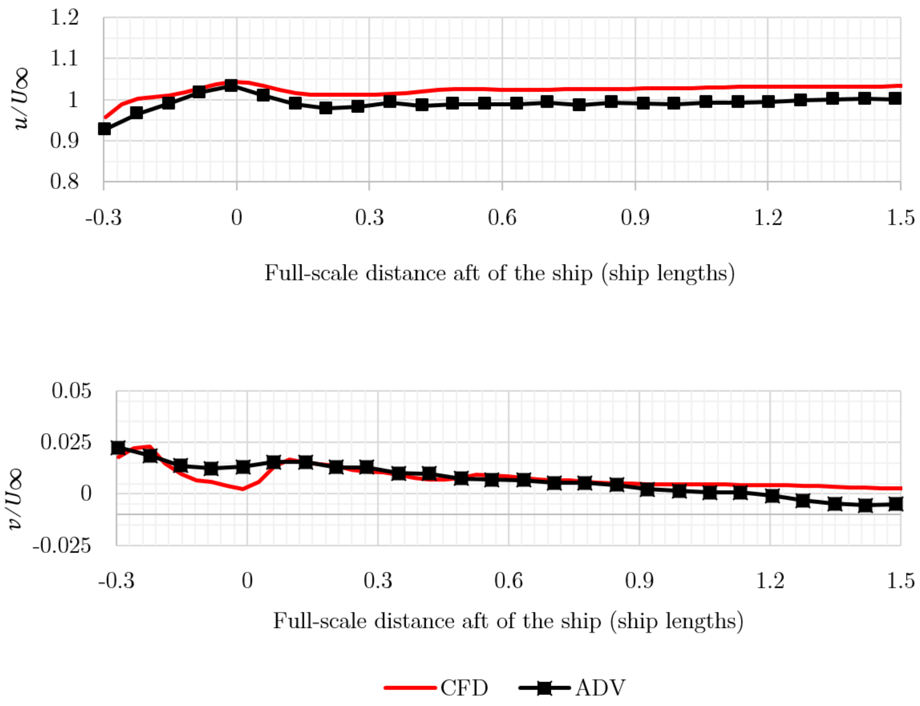

Figure 4-14 Comparison of experiment and CFD mean *u*- and *v*-velocity components along the SRVL approach path.

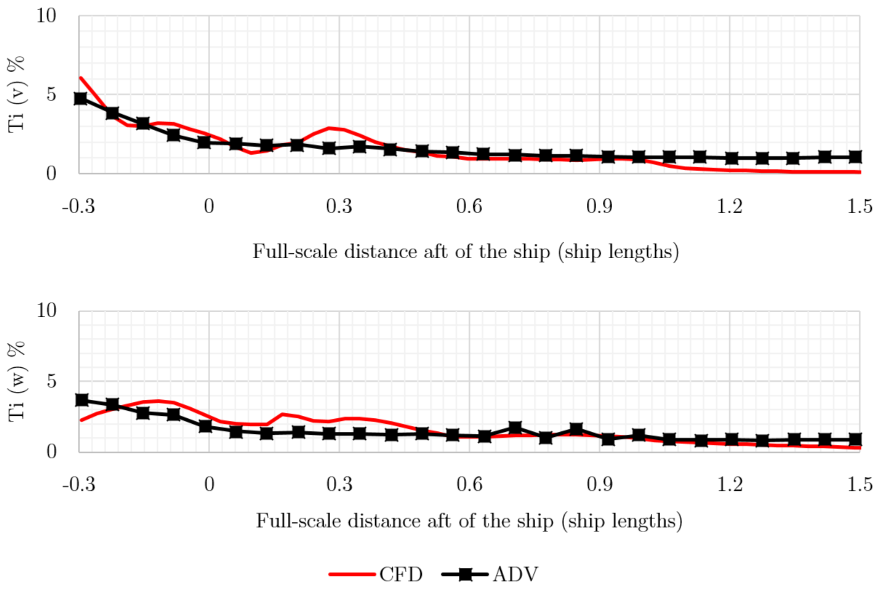

Figure 4-15 Comparison of experimental and CFD turbulence intensities in *v*- and *w*-velocity components along the SRVL approach path.

4.1.2 Green 10

To obtain a Green 10 WOD, the small-scale model of the ship was orientated in the water channel so the flow was from 10 deg off starboard. As the islands are located to the starboard side of the ship, their wakes will spread across some of the flight deck, creating larger deviations from the freestream. Figure 4-16 illustrates the airwake using instantaneous Q-criterion isosurfaces. The wake from the islands can be seen spreading across the flight deck, and there are also vortical structures which pass along the deck and over the landing spots from the side of the ski-jump, which is no longer aligned with the incoming flow.

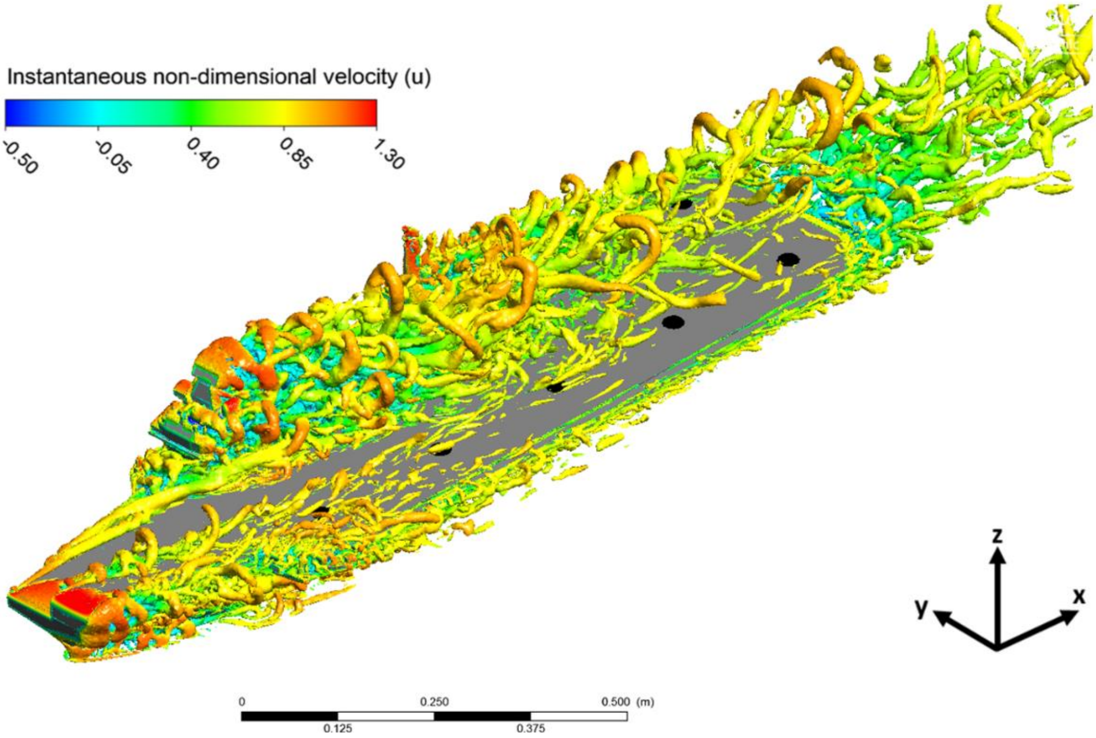

Figure 4-16 Green 10 flow over QEC model presented as instantaneous isosurfaces of Q-criterion coloured by *u*-velocity.

Figure 4-17, comparable to Figure 4-3 for the headwind case, shows the agreement between the experimental measurements of mean *u*-velocity component and the computed values in the vertical plane through the landing spots. As already defined, the direction of the *u*-component is parallel to the longitudinal axis of the ship, so the ADV probes were carefully rotated to an angle of 10 deg to the freestream flow and the traverse was programmed to follow the vertical plane parallel to the longitudinal axis of the ship while it was yawed at 10 deg. The velocity components from the CFD were similarly transformed. As can be seen in Figure 4-17, the agreement between the CFD and the experiment is good. The contours of turbulence intensity show an increase in turbulence at spots 3-5 which corresponds to the increased vorticity over these spots in Figure 4-16 due to the shedding of the flow from the islands.

Figure 4-18 compares the experimental and CFD values of the lateral, *v,* and vertical, *w,* mean velocity components and turbulence intensities at each port-side landing spot; reasonably good agreement between CFD and the experiment can be seen. Figure 4-19, similar to Figure 4-6, shows a comparison of mean *u*-velocity in the *u*-component measured in the experiment against the computed solution in a vertical plane through the centre of the islands. As can be seen, the agreement between the CFD and the experiment is good, although slightly less so along the vertical lines immediately aft of the islands and the stern of the ship, where there will be a greater effect on the airwake due to the oblique flow. Figure 4-20 also shows reasonably good agreement between the CFD values of the lateral, *v,* and vertical, *w,* mean velocity components and turbulence intensities along vertical lines in the lee of each island.

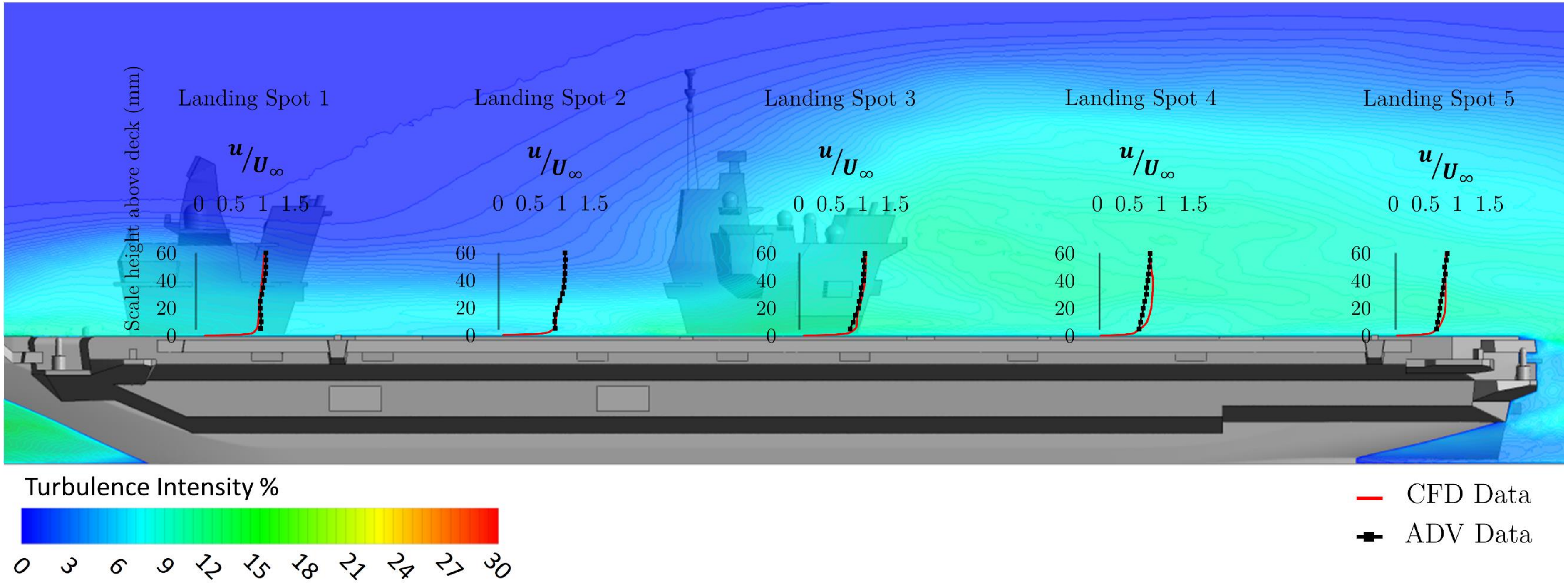

Figure 4-17 Comparison of experimental and CFD *u*-velocity components in a plane through the centre of the port-side landing spots in a Green 10 wind.

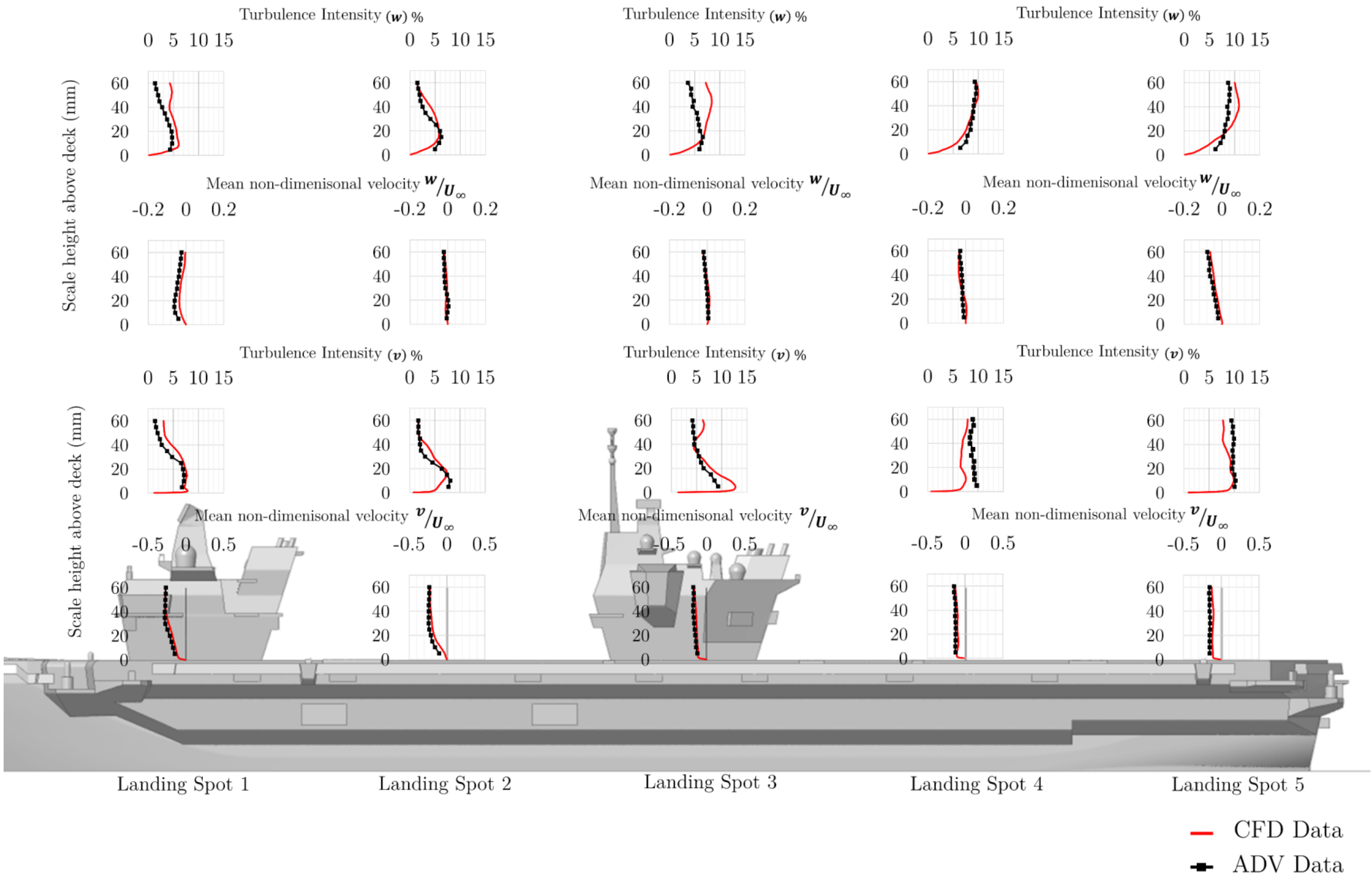

Figure 4-18 Comparison of experimental and CFD mean *v*- and *w*-velocity and RMS in a plane through the centre of the port-side landing spots in a Green 10 wind.

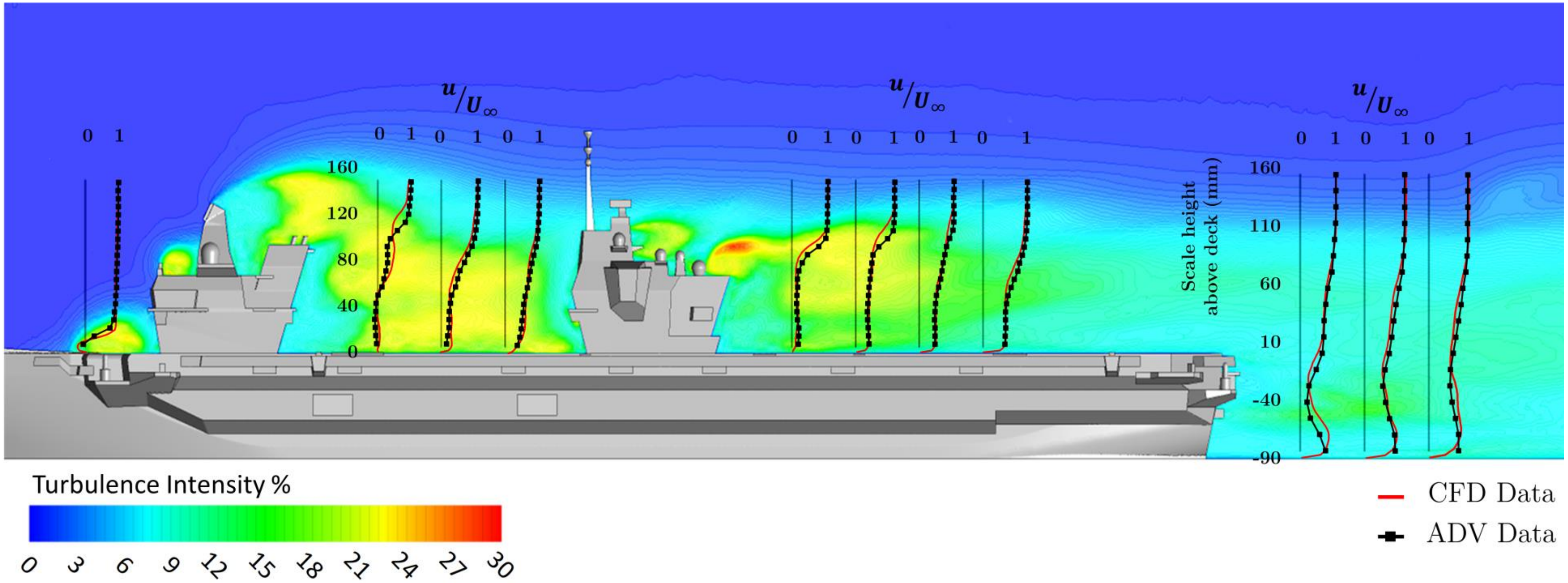

Figure 4-19 Comparison of experimental and CFD *u*-velocity components in plane through centre of islands in a Green 10 wind.

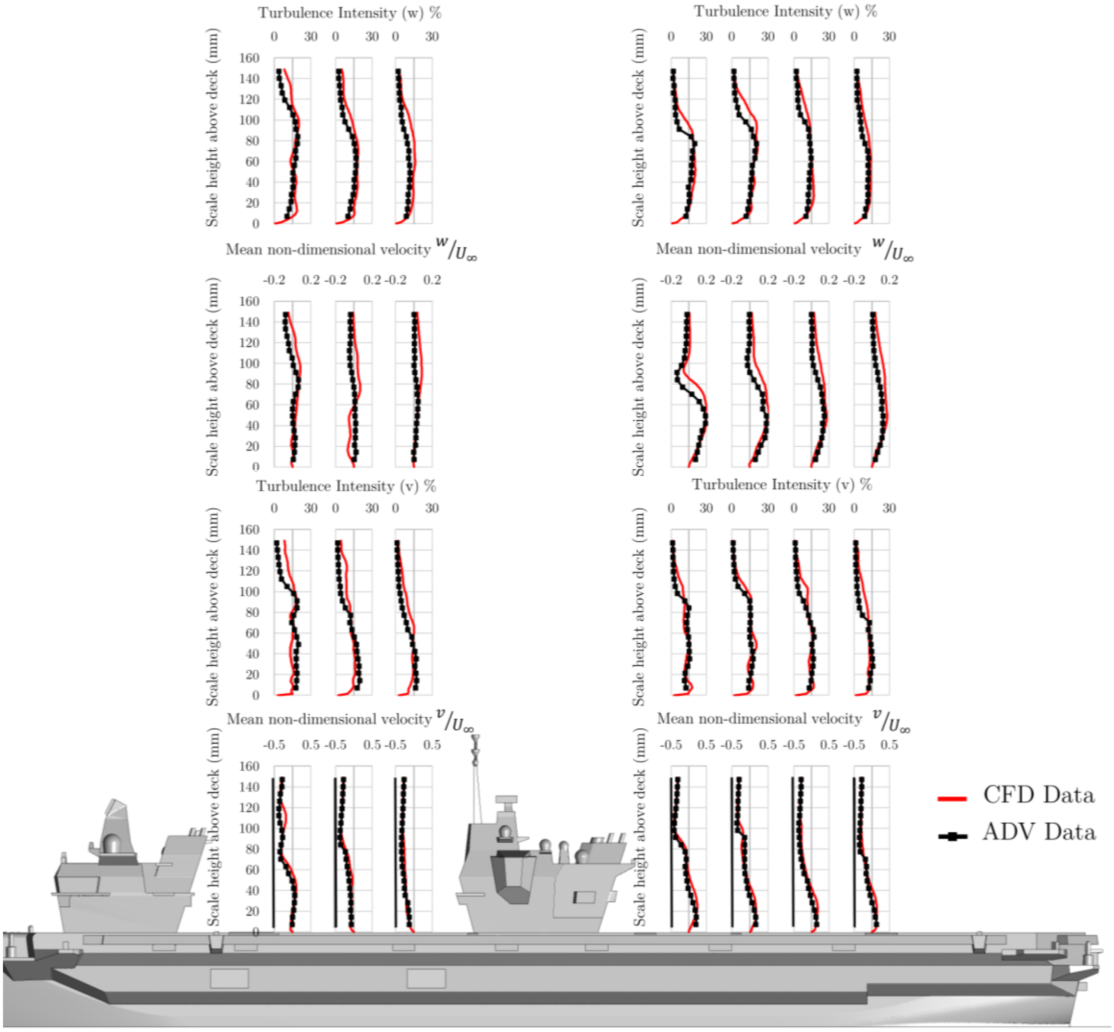

Figure 4-20 Comparison of experimental and CFD mean *v*- and *w*-velocity and RMS in the lee of the islands in a Green 10 wind.

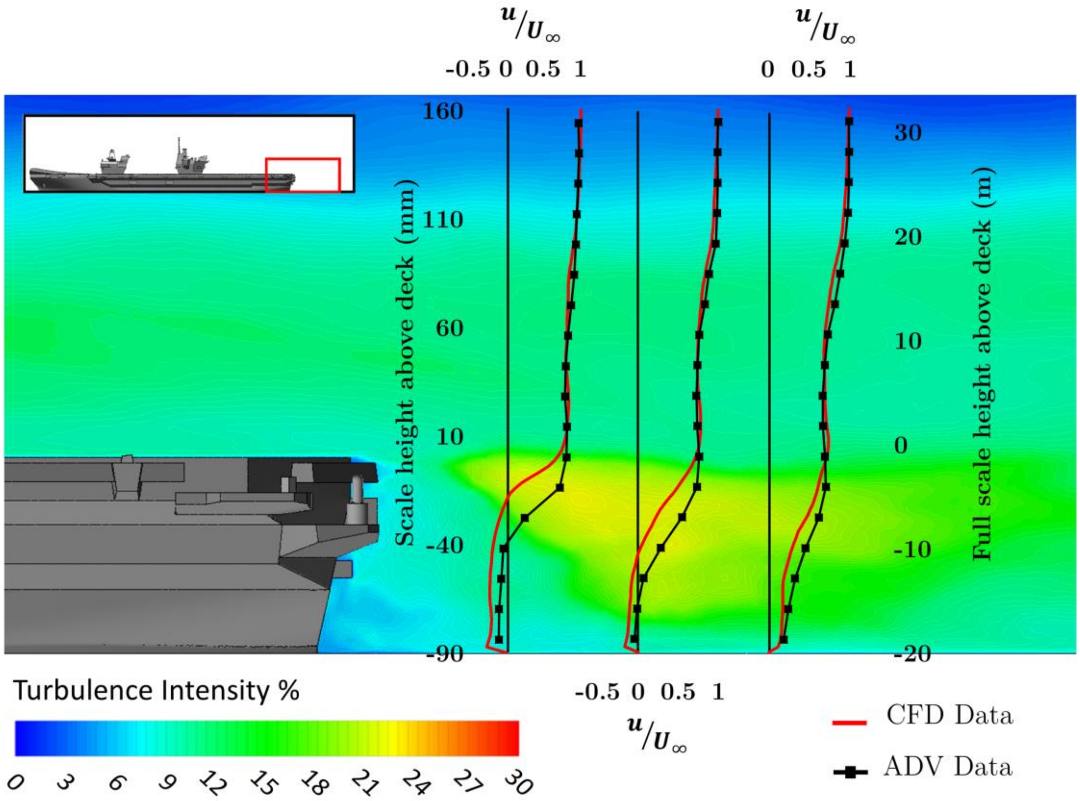

Figure 4-21 Comparison of experiment and CFD mean *u*-velocity component astern of the ship centreline in a Green 10 wind.

Figure 4-21 shows a comparison of the mean *u*-velocity component in a Green 10 wind at three positions astern of the ship on the ship centreline (i.e., $y=0$), comparable to Figure 4-8. The comparison between the experiment and CFD solution in Figure 4-21 shows generally good agreement. Figure 4-21 shows a shear layer between the main flow and the recirculation zone behind the ship, indicated by the increase in turbulence intensity as similarly shown in Figure 4-8.

Figure 4-22 shows the lateral and vertical velocity components along the vertical line in Figure 4-21 which is closest to the ship. The positive lateral velocity, v, beneath the height of the flight deck can be seen indicating a recirculation zone; a negative vertical velocity, w, can also be clearly seen. The comparison between the CFD and the measured points show reasonably good agreement, given that the velocities are small and will be sensitive to the positional accuracy of the ADV probe as discussed previously.

Figure 4-23 shows the turbulence intensities corresponding to the mean velocities in Figure 4-22. The peak in the turbulence coincides with the shear layer indicated in Figure 4-21; again, the agreement between experiment and CFD is reasonably good.

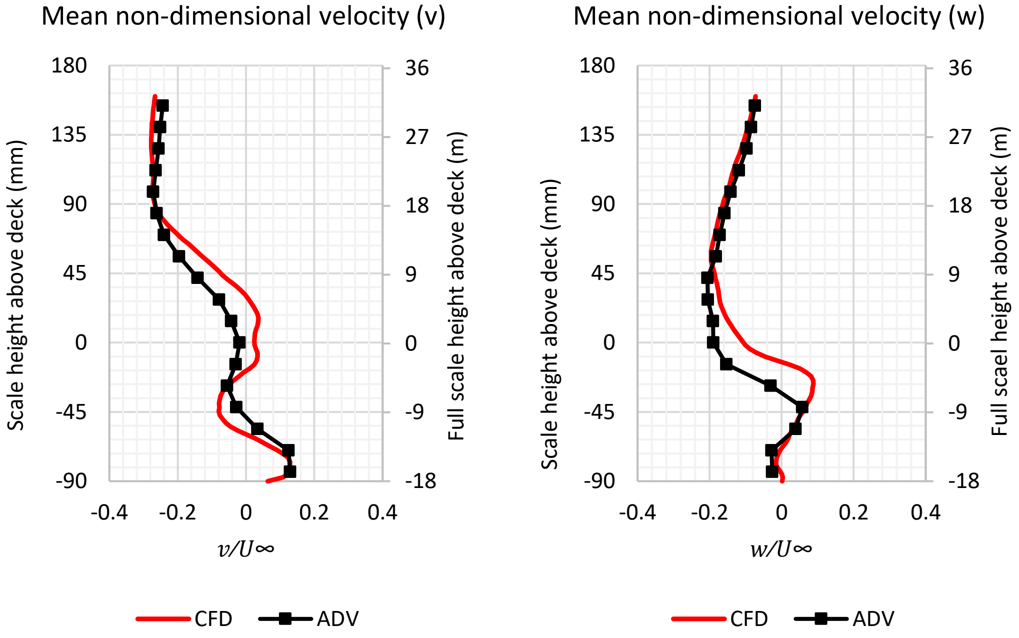

Figure 4-22 Comparison of experimental and CFD mean *v*- and *w*-velocity components at the rear of the ship centreline in a Green 10 wind.

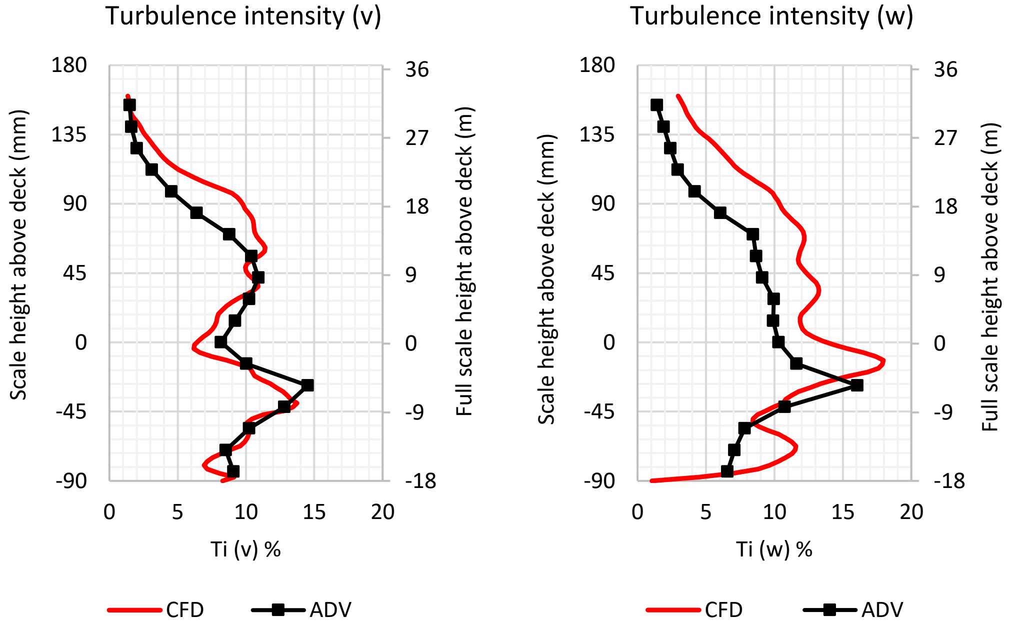

Figure 4-23 Comparison of experimental and CFD turbulence intensities in *v*- and *w*-velocity components at the rear of the ship centreline in a Green 10 wind.

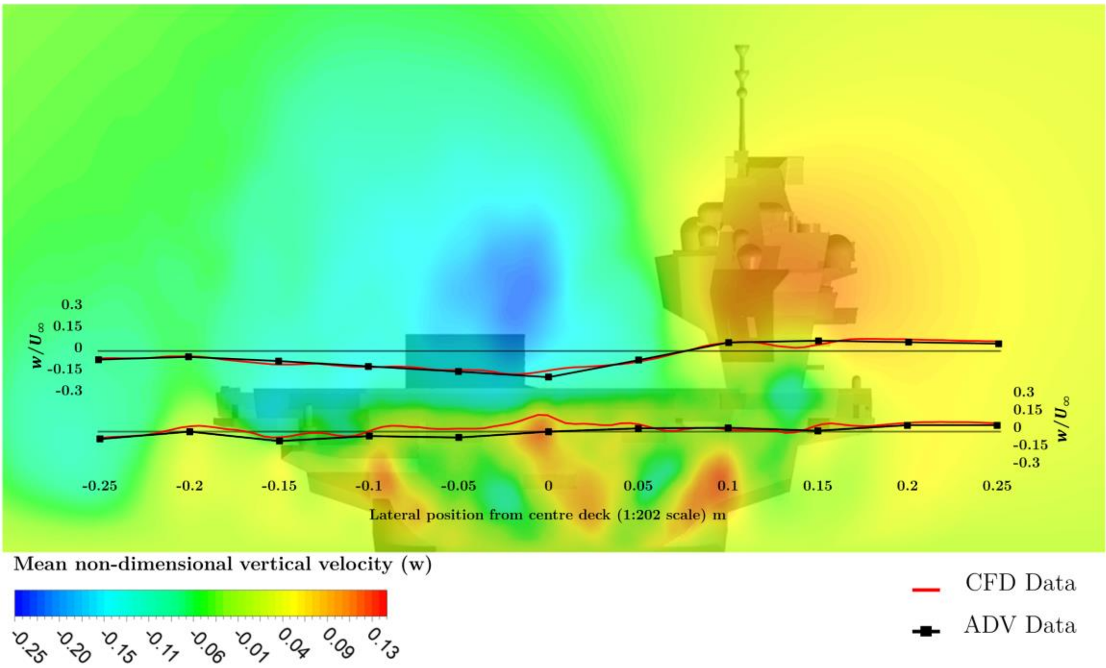

Figure 4-24 Comparison of experiment and CFD mean *w*-velocity along a lateral plane 24 cm (5 m full-scale) off the rear of the ship in a Green 10 wind.

Figure 4-24 shows the vertical velocity, *w*, in a Green 10 wind along two lateral lines 24 cm (small-scale) behind the ship's stern; contours of vertical velocities are also shown. The lateral line located above the ship's flight deck shows a positive vertical velocity, *w*, in the region behind the aft island. At the centreline and portside of the ship a negative vertical velocity can be seen. The vertical velocity profile indicates that the oblique flow caused and updraft from the upwind starboard side of the ship. The lateral line located beneath the ship's flight deck shows the vertical velocity, *w*, close to zero. The comparison between the CFD and the measured points show reasonably good agreement given that the velocities are small.

The vertical *w*-velocity component in a Green 10 wind measured along the SRVL approach path is shown in Figure 4-25; there is once again a good agreement between the CFD and the experiment. The maximum downward velocity component is 0.17 m/s, compared with 0.066 m/s in the case of the headwind. Figure 4-26 shows good agreement between the experimental measurements and computed solution of *u* and *w* mean velocity along the SRVL.

Figure 4-27 shows the corresponding vertical and lateral turbulence intensities along the SRVL approach path shown in Figure 4-25 in a Green 10 wind. Higher turbulence is shown in both the *w* and *v* component of turbulence over the headwind condition shown in Figure 4-15. Similar to the headwind case, a reduced turbulence intensity is computed in the Green 10 wind, close to 0% after about 1.5 ship lengths due to turbulence dissipation. The change in mean velocities and turbulence intensities in a Green 10 wind should be noticeable to pilots when the airwakes are integrated into the flight simulator. The preceding discussion for the comparison of the CFD computed velocities and the measured ones has used qualitative statements like ‘good’ or ‘reasonable’. The agreement can be observed in each figure but overall the differences between the CFD and experiment was mostly less than 5%.

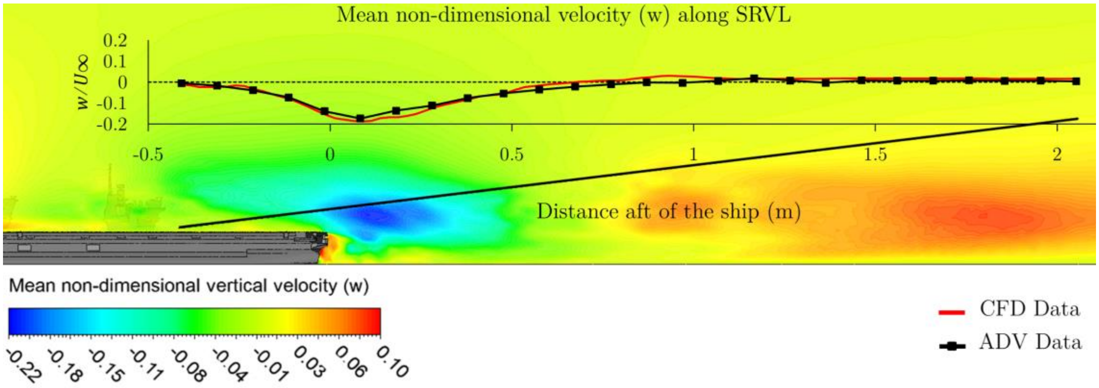

Figure 4-25 Comparison of experiment and CFD mean *w*-velocity along the SRVL approach path in a Green 10 wind.

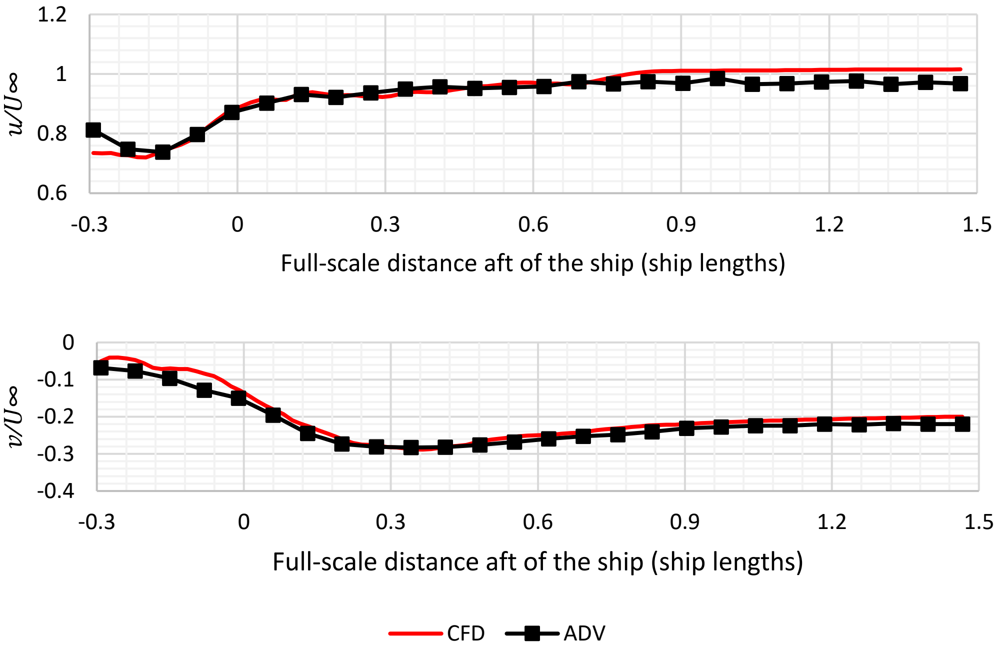

Figure 4-26 Comparison of experiment and CFD mean *u*- and *v*-velocity along the SRVL approach path in a Green 10 wind.

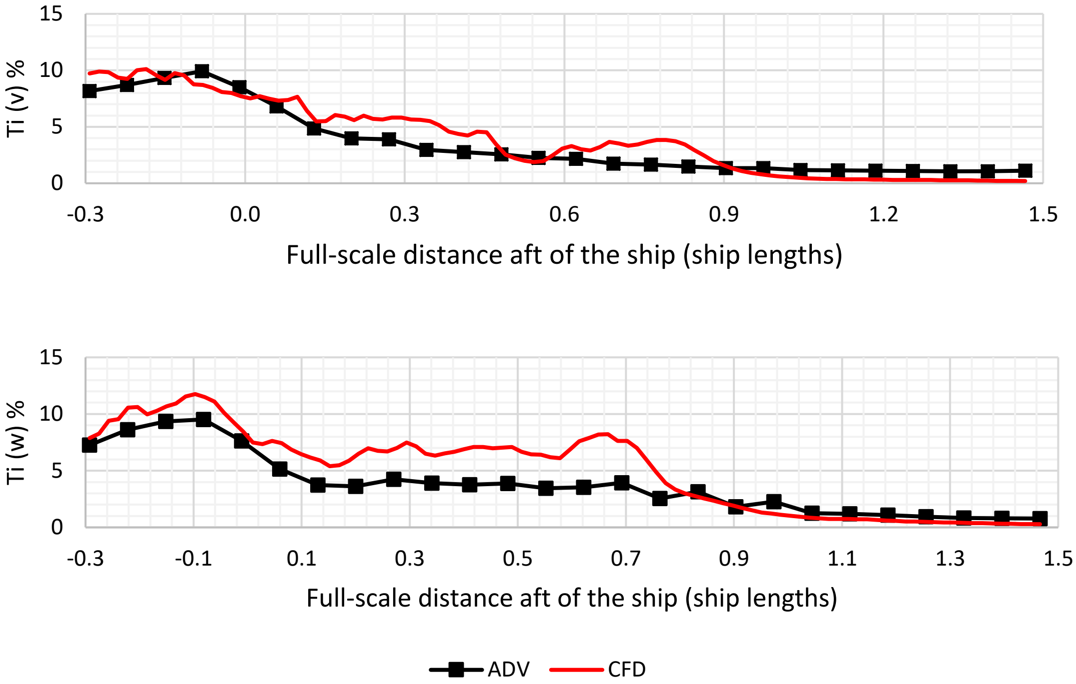

Figure 4-27 **Comparison of experimental and CFD turbulence intensities in *v*- and *w*-velocity components along the SRVL approach path in a Green 10 wind.**

4.2 Comparison of Full-Scale CFD and Experiment

As discussed earlier, the main difference between the full scale CFD and the model scale is the difference in Reynolds number, and the inclusion of an ABL; this section will compare the full-scale CFD and experiment results.

4.2.1 Headwind

Figure 4-28 shows the computed full-scale airwake for a headwind as contours of the mean *u*-velocity; the vertical plane is through the centre of the islands. Also included in this figure is the ABL velocity profile ahead of the ship. While in the small-scale study the flow had a uniform inlet velocity (1 m/s), in the full-scale case the inlet flow is described by the velocity at the mean height of the ship's three island-mounted anemometers, which is approximately 34 m above the sea surface. The velocity at anemometer height in Figure 4-28 is 25 kts (12.86 m/s).

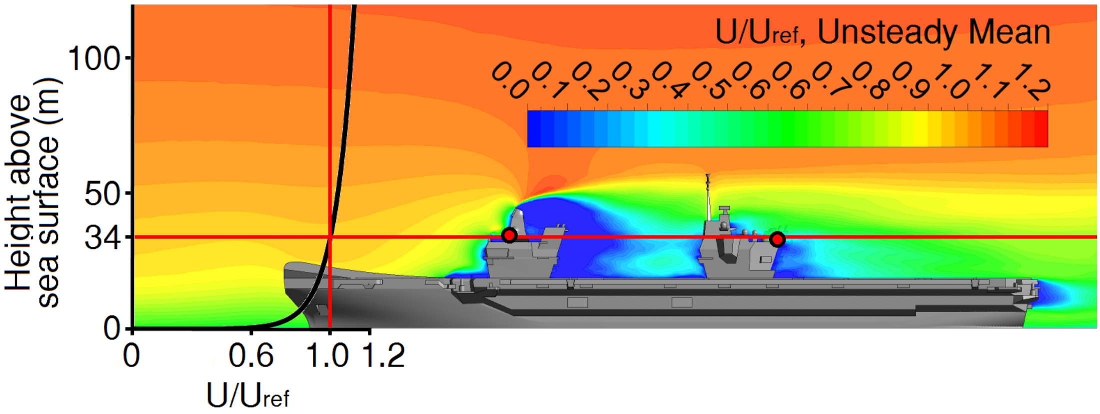

Figure 4-28 Contours of mean normalised *u*-velocity components in a plane through the centre of the islands, including the ABL inlet profile.

Considering the different inlet velocity profiles used for the full- and small-scale cases, a difference between the normalised airwakes is expected. As discussed earlier, the different Reynolds numbers (of the order of 10^6 at small-scale compared with 10^8 at full-scale) are also expected to have an effect on the separation of the air flow at the bow. Figure 4-29 shows a comparison of the full- and small-scale CFD at various locations in a plane through the centre of the islands for a headwind; the full-scale CFD has been normalised by the velocity at the anemometer height; turbulence contours are those for the small-scale ship. Ahead of the forward island and between the two islands there is some difference between the profiles of the *u*-velocity component, which is probably a result of the ABL inlet profile. The velocity profiles in the lee of the aft island and astern of the ship are very similar and this is probably because within this region the flow has been well mixed and the influence of the ABL has dissipated.

Figure 4-30 shows a comparison of the full- and small-scale CFD values of the lateral, *v,* and vertical, *w,* mean velocity components and turbulence intensities at various positions behind the islands; similar to the comparison given in Figure 4-29, reasonably good agreement is shown between the two CFD solutions.

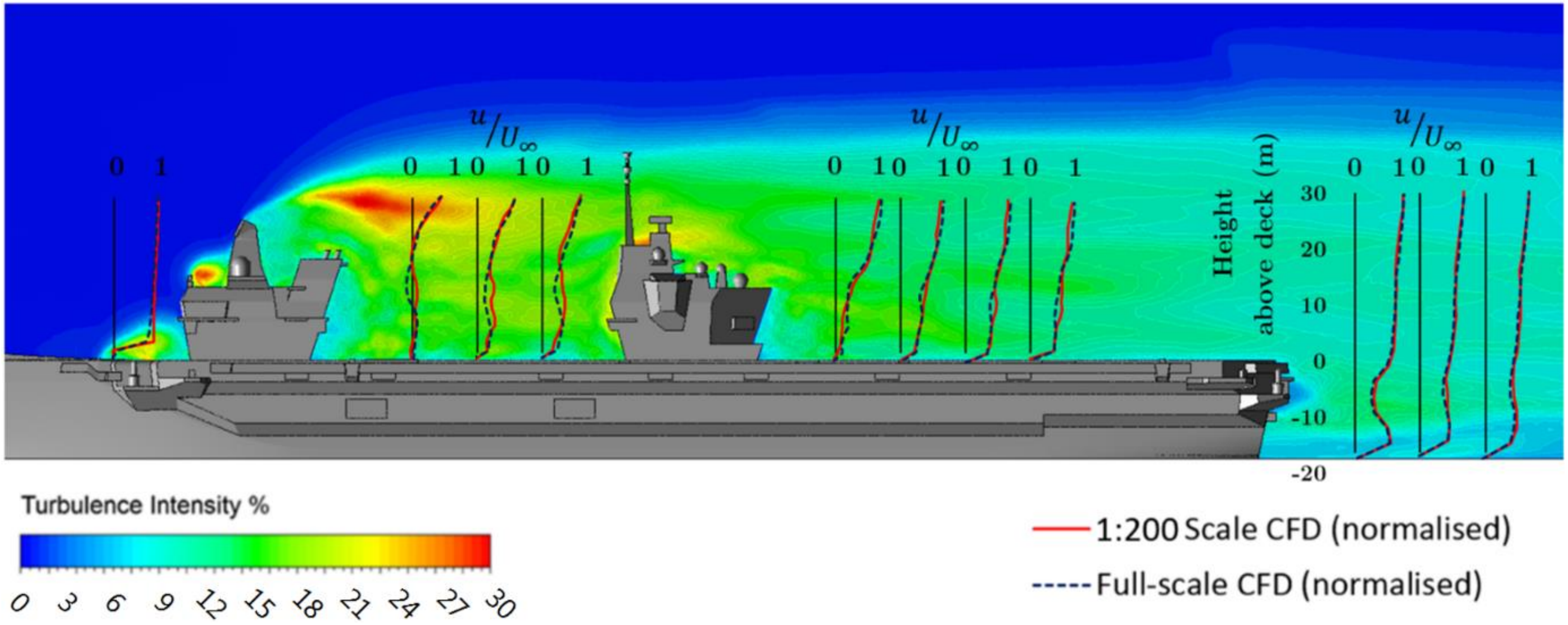

Figure 4-29 Comparison of small-scale and full-scale CFD results in *u*-velocity component.

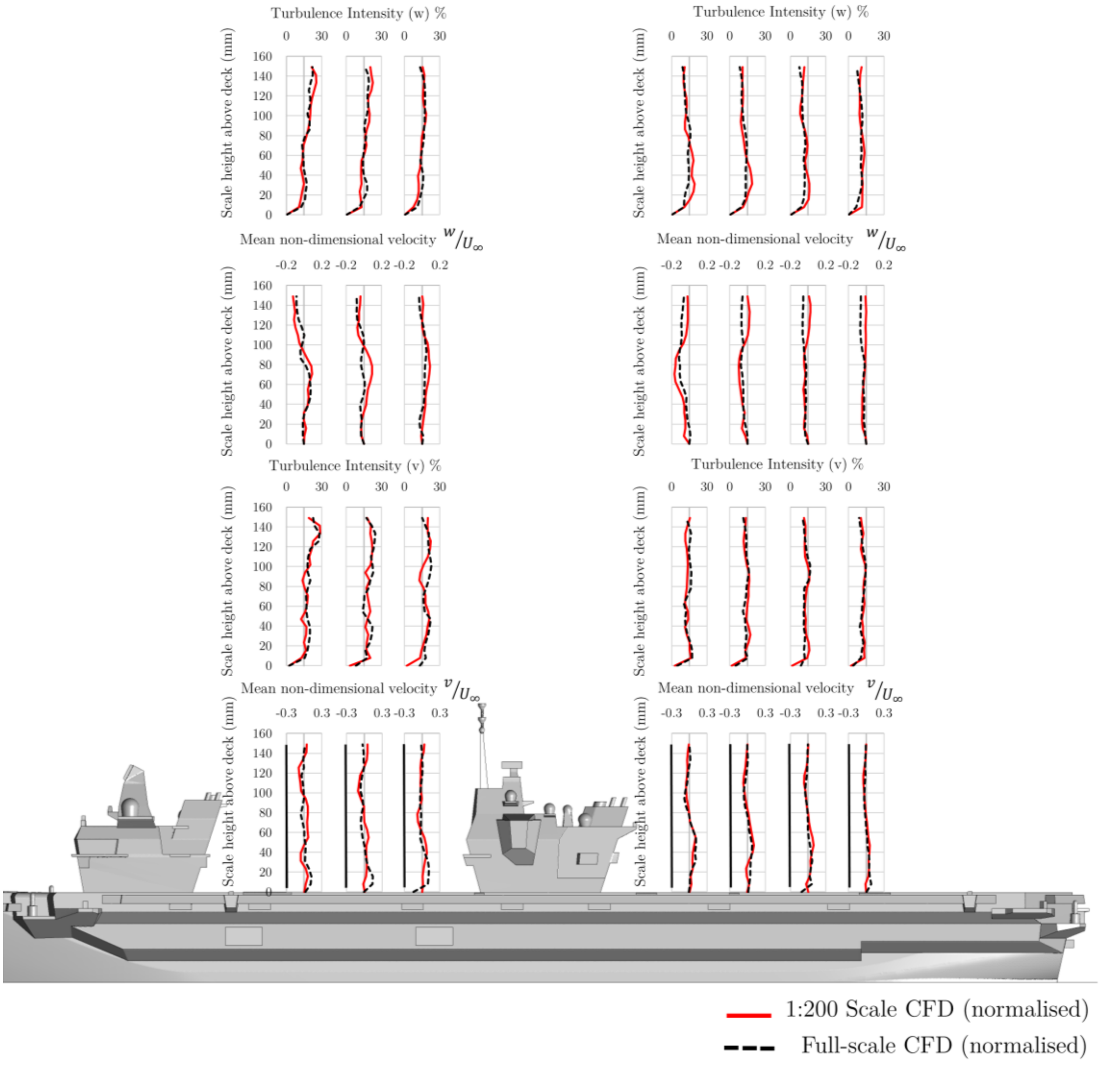

Figure 4-30 Comparison of small-scale and full-scale CFD mean *v*- and *w*-velocity and RMS in the lee of the islands.

Figure 4-31 shows a comparison of the full-scale and small-scale CFD results over the ski-jump at the bow of the ship. As discussed previously, due to the curved profile of the leading edge of the ski-jump, it can be expected that flow separation will be affected by the difference in Reynolds number at full-scale and small-scale, in addition to the presence of an ABL in the full-scale solution. As can be seen in Figure 4-31 there is no evidence of a separation bubble in the full-scale flow, and towards the end of the ski-jump the two velocity profiles are comparable. Furthermore, although not shown here, the full- and small-scale velocity profiles further down the flight deck and over the landing spots are very similar. Figure 4-32 shows computed mean streamlines over the bow of the ship in a headwind, demonstrating the smooth air flow and the effectiveness of the bow design.

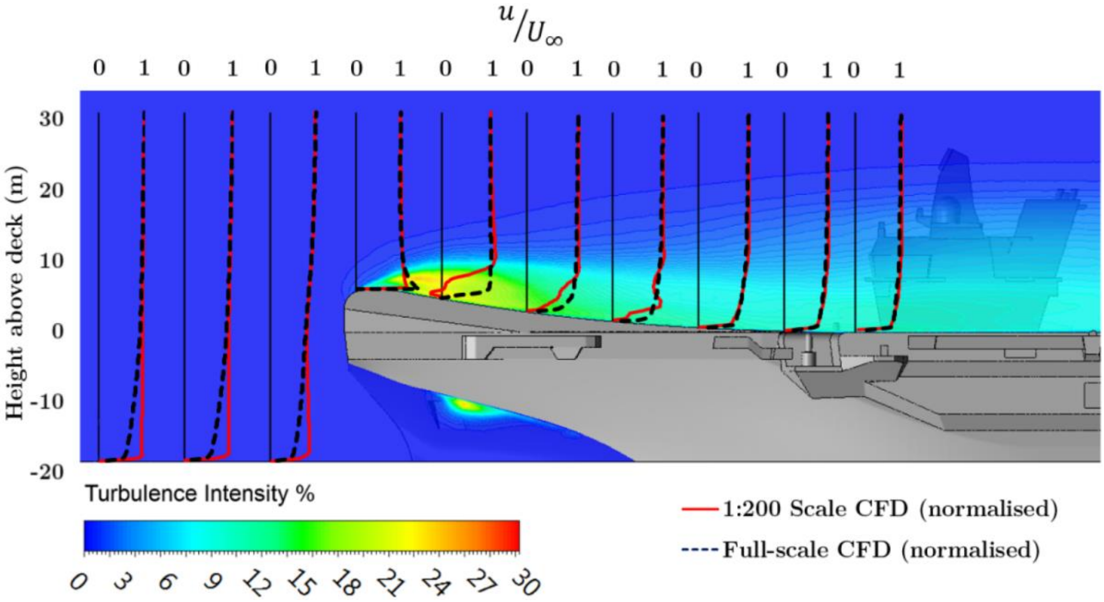

Figure 4-31 Comparison of full-scale and small-scale CFD results in *u*-velocity component over the ski-jump.

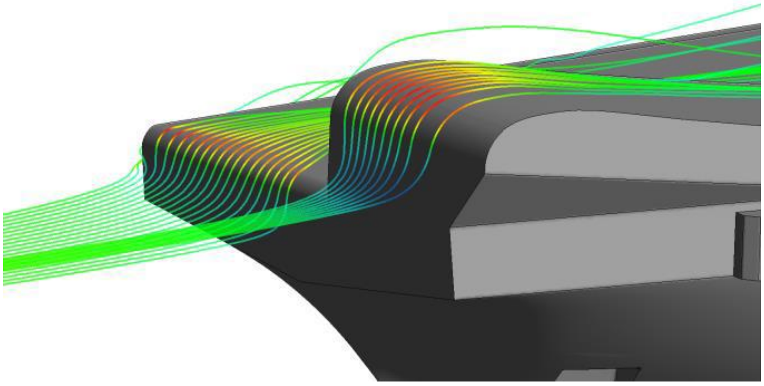

Figure 4-32 Mean streamlines over the full-scale bow in a headwind.

The *w*-velocity component measured along the SRVL approach path is shown in Figure 4-33 shows good agreement between the small- and full-scale CFD solutions.

The streamwise, *u*, and lateral, *v*, mean velocity components along the glideslope of the small- and full-scale CFD are compared in Figure 4-34 and good agreement between the CFD solutions is shown. However, near to the deck a lower *u* and *v* velocity is observed in the small-scale CFD.

Figure 4-35 shows the comparison of the small- and full-scale CFD turbulence intensities in the lateral, *v*, and vertical, *w*, velocity components along the SRVL approach path. The agreement is reasonable, and both CFD solutions show the computed turbulence falling towards zero from around 1.5 ship lengths astern, similar to Figure 4-15.

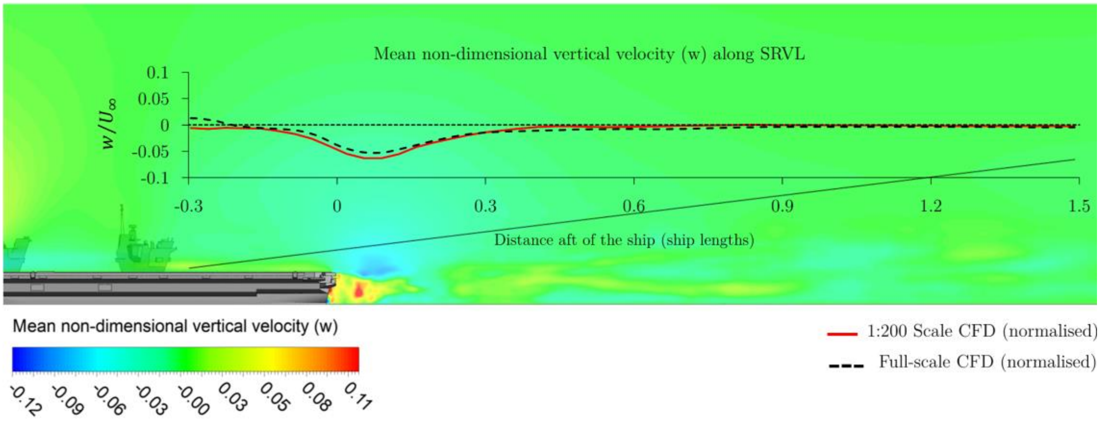

Figure 4-33 Comparison of small-scale and full-scale CFD mean *w*-velocity along the SRVL approach path.

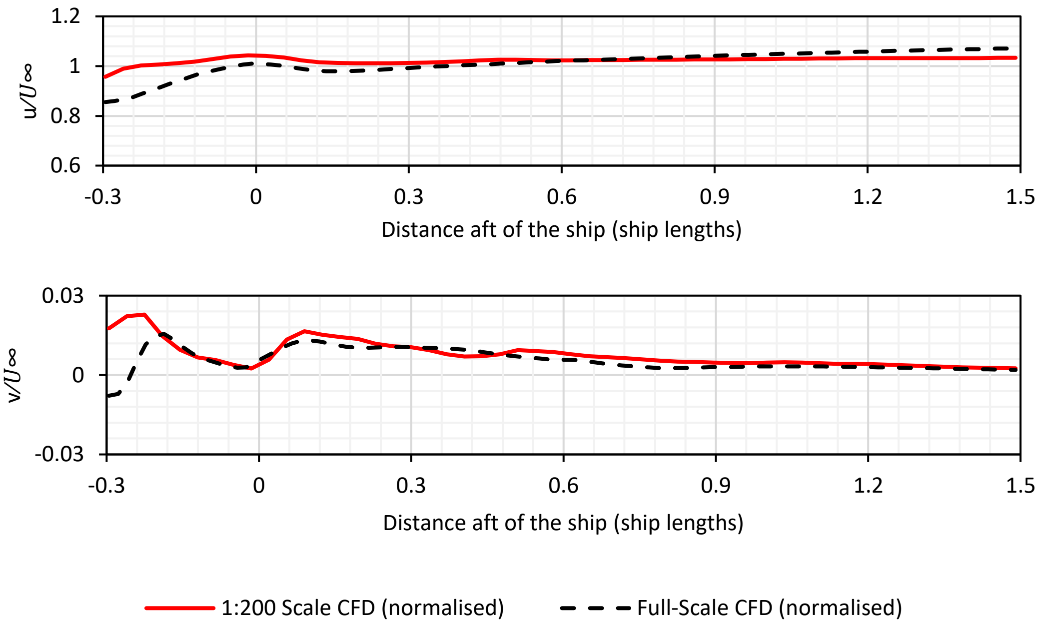

Figure 4-34 Comparison of small-scale and full-scale CFD mean *u*- and *v*-velocity along the SRVL approach path.

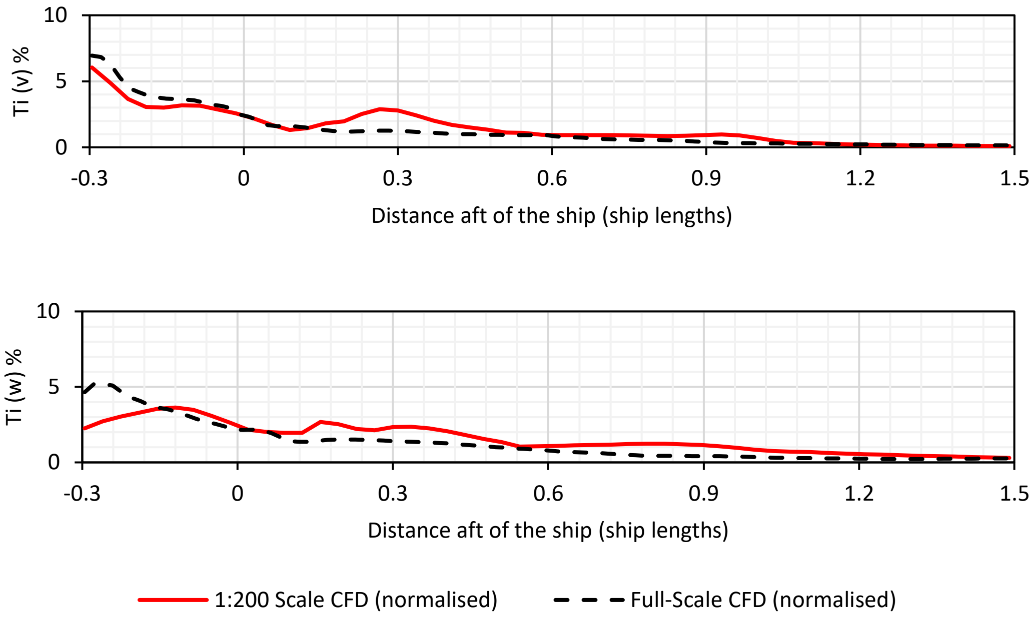

Figure 4-35 Comparison of small-scale and full-scale CFD turbulence intensities in *v*- and *w*-velocity components along the SRVL approach path.

4.2.2 Green 10 WOD

As for the full-scale headwind case, an ABL was applied at 10 deg off the starboard side of the ship with a 25 kts (12.86 m/s) velocity at anemometer height, and the direction of the *u*-velocity component is parallel to the centreline of the ship. Figure 4-36 shows a comparison of *u*-velocity in a plane along the centreline of the islands between the small- and full-scale CFD in a Green 10 wind; good agreement is seen. Furthermore, good agreement is also seen between the small- and full-scale CFD values of the lateral, *v,* and vertical, *w,* mean velocity components and turbulence intensities in Figure 4-37.

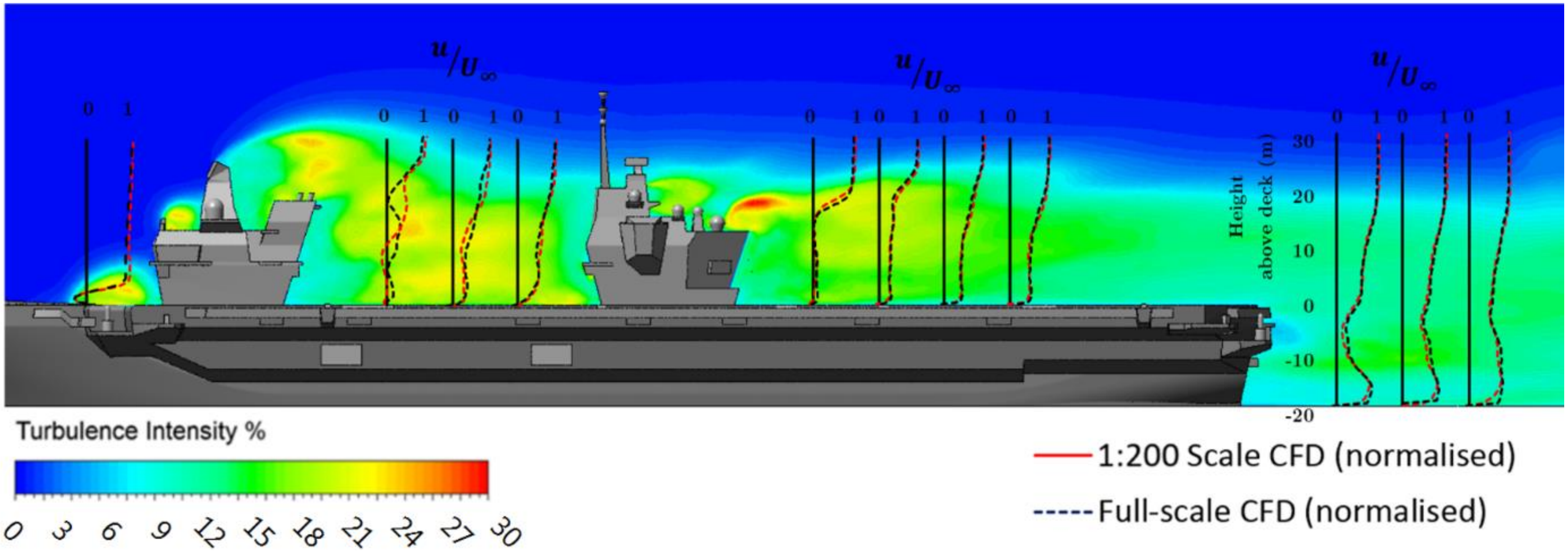

Figure 4-36 Comparison of small-scale and full-scale CFD results in *u*-velocity component in a Green 10 wind.

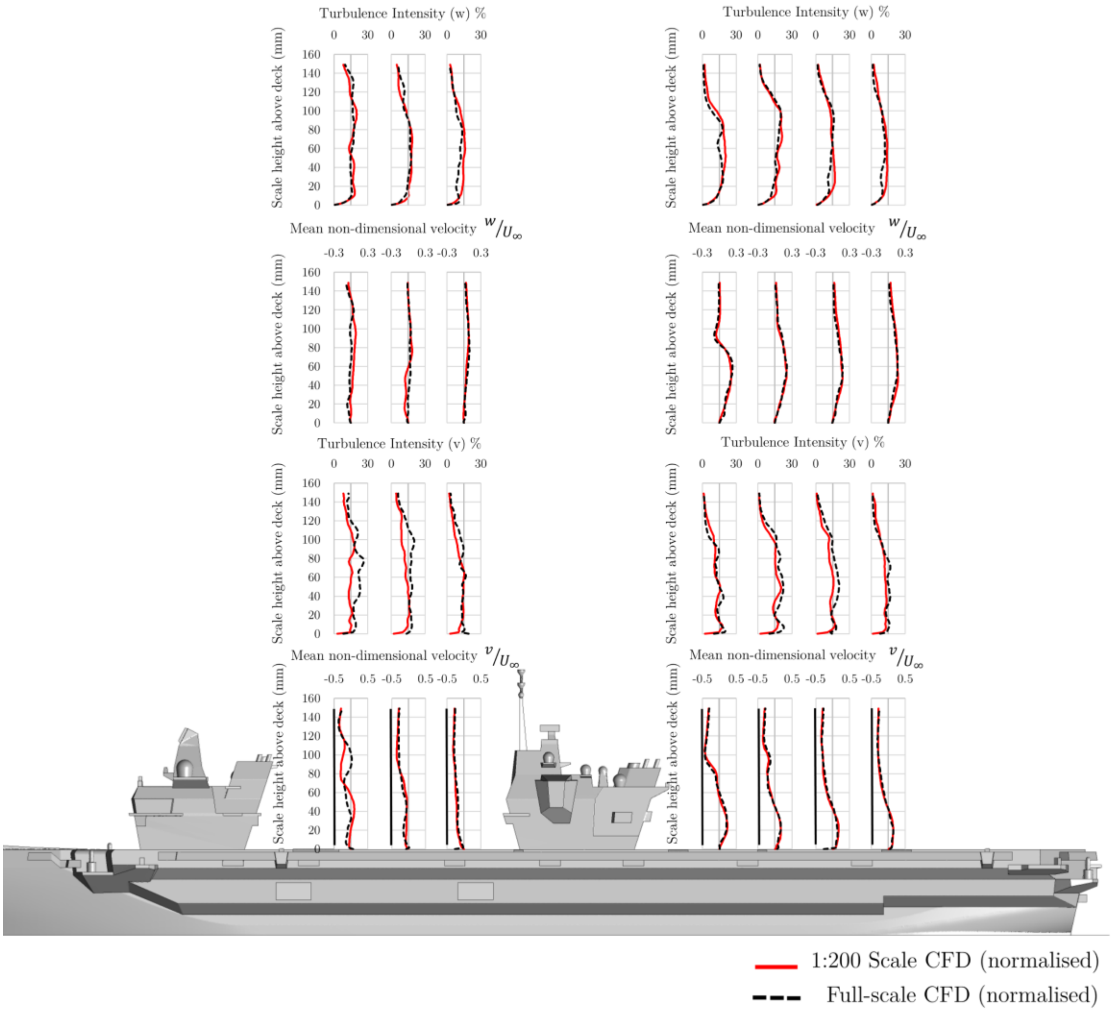

Figure 4-37 Comparison of small-scale and full-scale CFD mean *v*- and *w*-velocity and RMS in the lee of the islands in a Green 10 wind.

Figure 4-38 shows a comparison of mean vertical *w*-velocity along the SRVL approach path between the small- and full-scale CFD. A similar drop in the vertical velocity, *w*, in Green 10 wind compared to a headwind is experienced in the full-scale CFD as in the small-scale CFD. A comparison of each CFD solution of the mean *u*- and *v*-velocity along the SRVL approach path in a Green 10 wind is shown in Figure 4-39; good agreement is seen. The corresponding lateral and vertical turbulence intensities along the SRVL approach path for the small- and full-scale CFD solutions are shown in Figure 4-40. The agreement is generally good although an increase in turbulence intensity in the small-scale CFD is observed at 0.75 ship lengths aft of the ship.

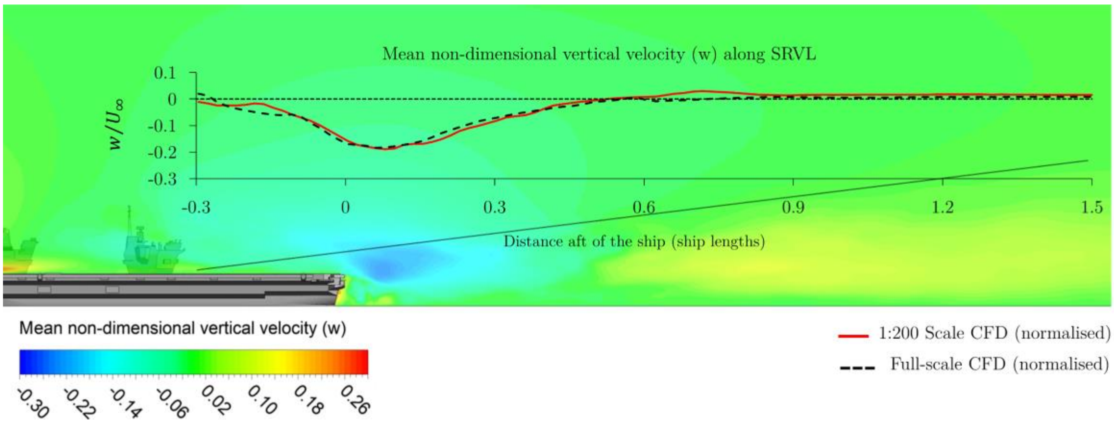

Figure 4-38 Comparison of small-scale and full-scale CFD mean *w*-velocity along the SRVL approach path in a Green 10 wind.

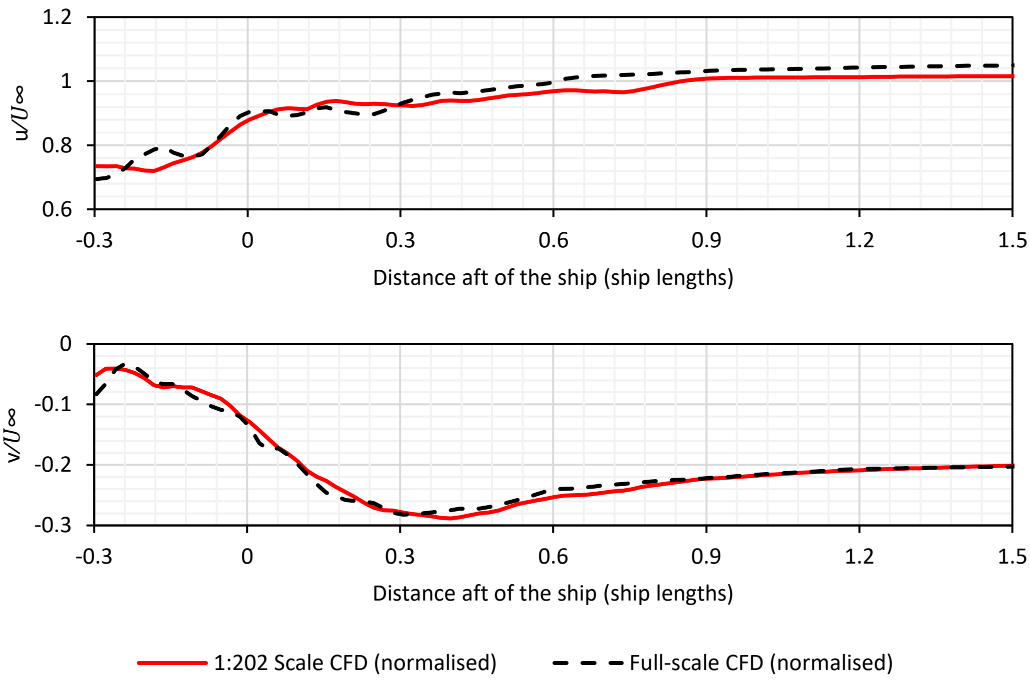

Figure 4-39 Comparison of small-scale and full-scale CFD mean *u*- and *v*-velocity along the SRVL approach path in a Green 10 wind.

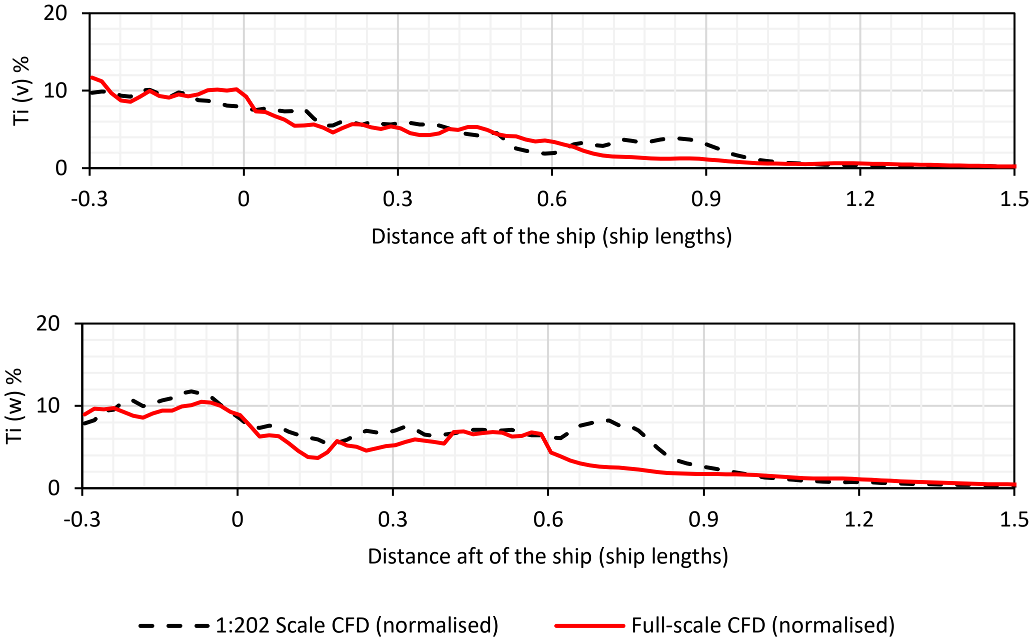

Figure 4-40 Comparison of small-scale and full-scale CFD turbulence intensities in *v*- and *w*-velocity components along the SRVL approach path in a Green 10 wind.

4.3 Air Flow over the Full-Scale Flight Deck

This section examines more closely a range of full-scale airwakes and discusses their possible effect on aircraft operating to and from the ship in those wind conditions. Figure 4-41 shows the mean air flow over the QEC carrier in a headwind, illustrated by mean streamlines in vertical planes that are aligned with the oncoming wind and pass through the landing spots (spots 1 to 5 along the length of the deck and spot 6 behind the aft island). The streamlines are coloured by turbulence intensity. The figure also contains contours of turbulence intensity in a horizontal plane that is located 10 m above the flight deck; the significance of the 10 m is that this is the approximate height of the centre of gravity for both fixed- and rotary-wing aircraft when translating across the deck during a vertical landing, according to [133]. As can be seen, in the headwind case there is little turbulence over the deck at 10 m and spots 1 to 5 are in largely undisturbed air flow.

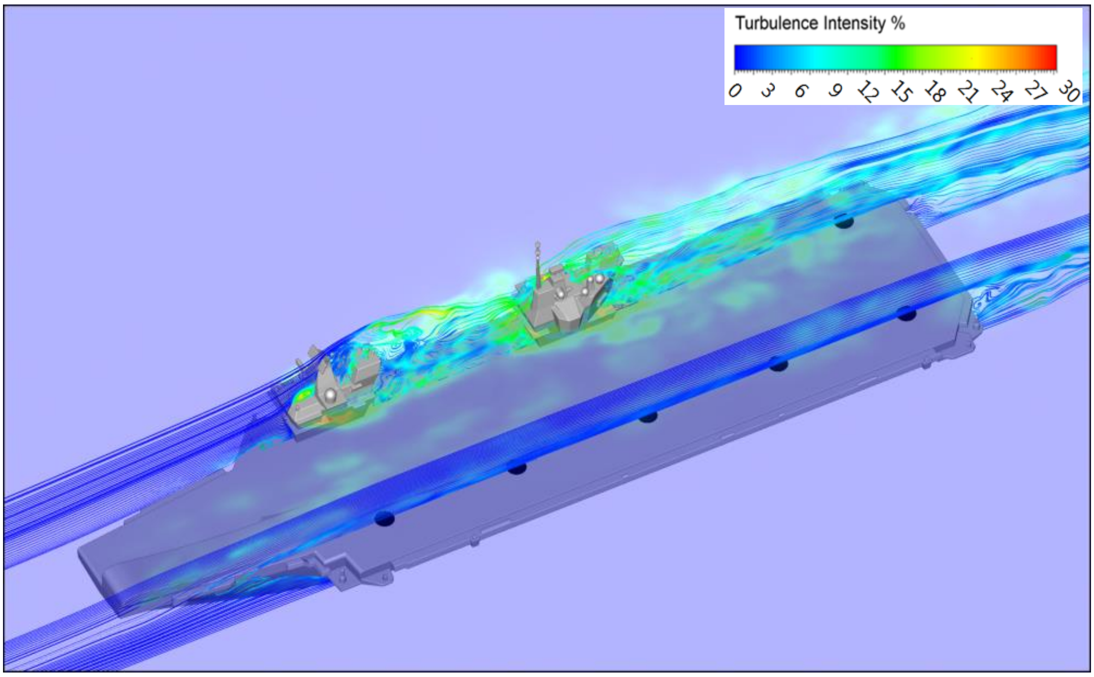

Figure 4-41 Full-scale airwake for a headwind as streamlines in vertical planes through the landing spots and turbulence intensity contours in a horizontal plane 10 m above the deck.

While it is preferable to launch and recover aircraft to the ship in a headwind, where there will be less flow disturbance over the flight deck and higher relative air speeds, and hence lift for the aircraft, there will inevitably be times when the relative wind will be from directions other than Ahead. It is important, therefore, to have an understanding of the air flow over the deck for all wind directions.

For winds from the starboard side of the ship, i.e., Green winds, an increased level of turbulence can be expected over the flight deck due to the air flowing over and around the island superstructures. Figure 4-42 shows examples of the ship airwakes over the flight deck from relative angles Green 25, Green 45 and Green 90 (beam wind). In these wind conditions the disturbed air flow from the two islands does indeed create more turbulence in the horizontal plane 10 m above the deck. The different orientation of the ship in each figure is to assist the reader in viewing each of the images.

Overall, it can be seen that as the wind moves around to the starboard, the profile presented by each island to the oncoming air flow is increasing, as is the width of the turbulent wake behind each island. Referring back to Figure 3-7, it can be seen that the vertical landing approach requires the aircraft, fixed- and rotary-wing, to come alongside the ship on the port-side, hold a hover position alongside the designated landing spot by matching the ship's forward speed, and to then translate sideways across the port deck-edge to the hover position above the landing spot, before descending to the deck. Therefore, the nature of the air flow off the port-side and over the flight deck is an important contributor to the handling qualities and pilot workload of aircraft operating in this region. Taking the three images in Figure 4-42 together, it can be seen that as the wind moves from Ahead to abeam, so the turbulent flow from the islands encroaches on more landing spots, becomes more turbulent at each landing spot, and more turbulent off the port-side. It can, therefore, be concluded that Green winds will increase pilot workload during vertical landings at each spot. A result that is not entirely unexpected for an aircraft carrier with its superstructure situated on the starboard side of the flight deck.

The beam wind in Figure 4-42 shows how the flow separating from the sides of the islands creates turbulent air in the vicinity of spots 1 to 4, where 25% to 30% turbulence intensity represents a significant disturbance. The islands also deflect the flow upwards and it can be seen that the separated flow over the forward island reattaches near to spot 1. Bearing in mind that the flow is represented by mean streamlines this means that the reattachment point and the flow direction at spot 1 could be fluctuating significantly. The flow deflected upwards from the aft island does not reattach to the deck and produces an area of highly turbulent air flow, although the most turbulent flow is 30 m above the deck and above the height of normal flying operations. Although spots 5 and 6 at the stern of the ship are not in the wake of the islands, the air flow separating from the starboard deck-edge of the ship still causes significant turbulence, particularly over spot 5 on the port side. The beam winds will also create significant turbulence off the port-side of the ship where the aircraft will take up their hover position before translating across the deck to the landing spot.

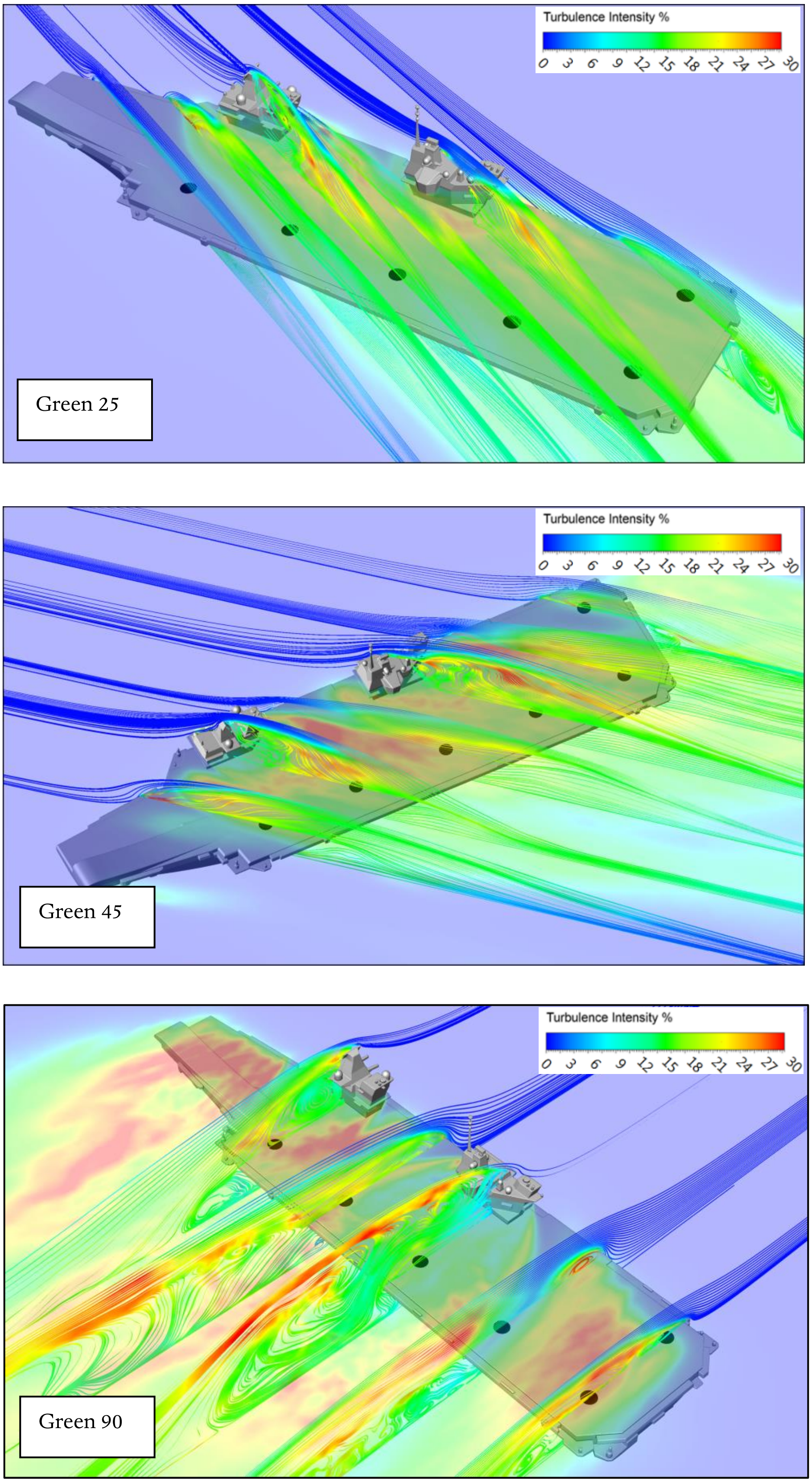

Figure 4-42 Full-scale airwakes for starboard winds illustrated as streamlines in vertical planes through landing spots and turbulence intensity contours in horizontal plane 10 m above deck.

In contrast, referring to Figure 4-43, Red winds (from the port side) create much less turbulence over the flight deck and will, therefore, be more favourable than Green winds. The possible exception is at spot 1, near the ski-jump, where the air flow in Red 25 and 45 winds could be affected by the corner formed by the deck-edge and the forward bow section. The Red 90 wind, however, still creates significant turbulence due to the flow separating from the ship's port deck-edge and, interestingly, the islands still have a significant influence on the flow over the flight deck. The combined effect of the two islands deflecting flow upwards means that the flow separating from the portside deck-edge does not reattach on the flight deck, except at spots 5 and 6 where the flow reattaches around one-third of the way across the flight deck. The channelling effect of the two islands can also be seen in the vertical plane through spot 2, where there is a large region of flow with turbulence intensities of 30%.

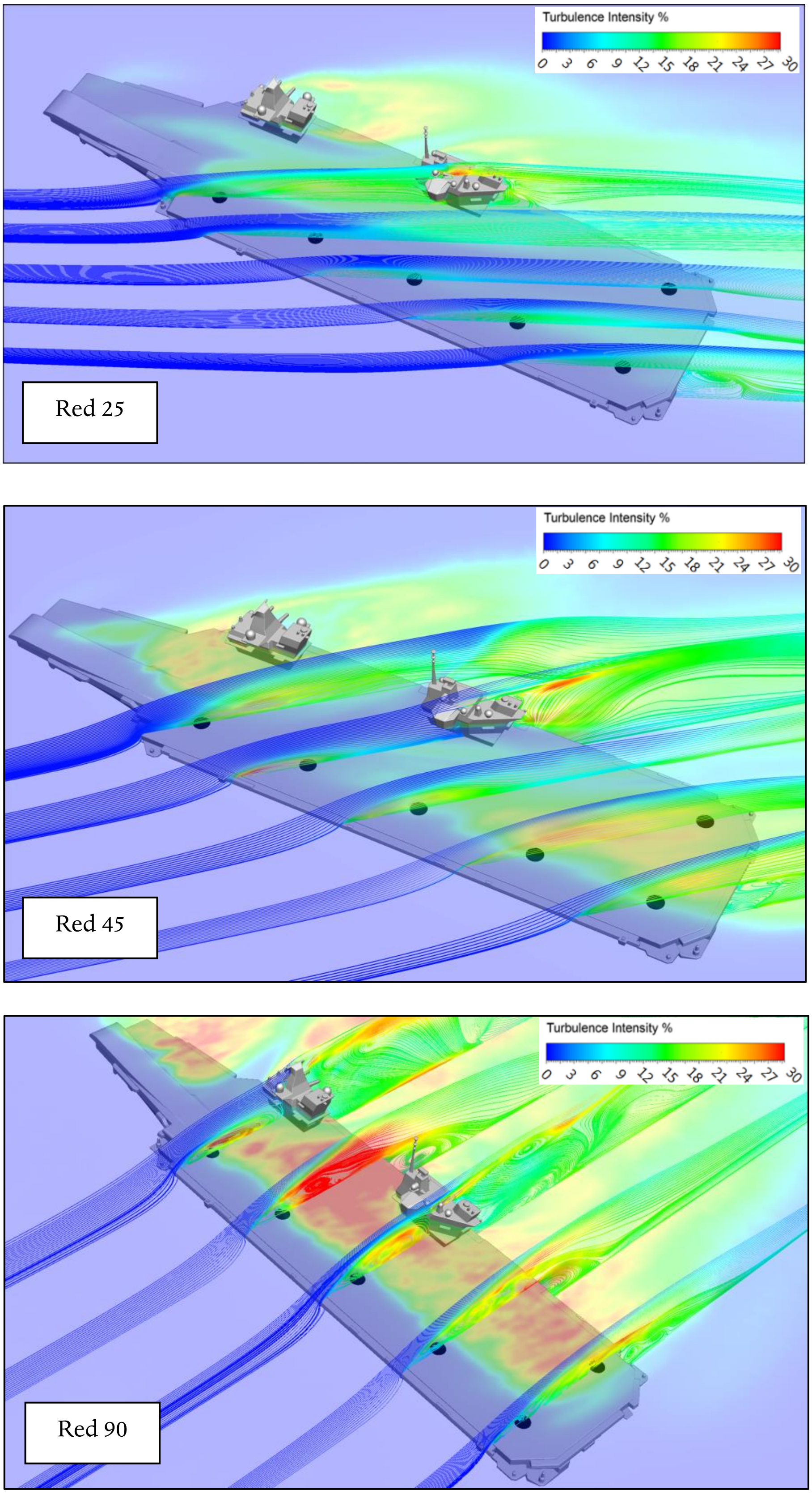

Figure 4-43 Full-scale airwakes for port winds illustrated as streamlines in vertical planes through landing spots and turbulence intensity contours in horizontal plane 10 m above deck.

4.4 Chapter Summary

Chapter 4 has provided a comparison between velocity and turbulence recorded in a large water channel of the airwake of a 1:200 scale model of the QEC submerged in a large water channel using ADV, and a CFD simulation of the experimental setup. Overall, excellent agreement between the model-scale experiment and CFD is observed for the two WOD conditions, providing confidence in the CFD method to accurately compute the ship's airwake. Comparison of the small-scale experiment and full-scale CFD solutions showed reasonable agreement, despite differences in Reynolds number and the different inlet velocity profiles. This latter observation suggests that the full-scale CFD is at least as representative of the full-scale situation as is the small-scale experiment, and that CFD is an effective tool for simulating the full-scale air flow over a large structure, such as an aircraft carrier.

As described in Chapter 1, the full-scale unsteady airwakes have been primarily computed for integration with the BAE Systems and UoL piloted flight simulators, and although the general characteristics of the flow over the deck can be described and commented upon as they have been above, the effect of the airwake on the aircraft and on pilot workload can only be assessed by trained test pilots either in the simulator or during real at-sea flight trials. Pilots are trained to operate in the challenging conditions encountered around the ship, including air turbulence and deck motion. Modern military aircraft, particularly the F-35B, have highly augmented flight control systems which are designed to alleviate pilot workload [134]. Nevertheless, it is clear from the airwake data presented here that the most favourable conditions under which to perform a vertical landing is in a headwind, when the disturbed air flow from the islands is least influencing the flow over spots 1 to 5, although it will affect spot 6. It has been shown that the rounded leading edges of the ski-jump and the adjacent deck-edge allows the flow from Ahead to remain attached and to create only a small disturbance along the length of the flight deck. It can also be deduced that Red winds are preferable to Green winds, and that as the Green winds approach the beam, the more turbulence they produce across the flight deck.

The full-scale airwakes described in this chapter, and for a wider range of wind angles, were implemented in the UoL full-motion flight simulator, HELIFLIGHT-R. The design, conduct and outcomes from the simulated flight trials are described in the following chapter.

Chapter 5

Piloted Simulated Helicopter Flight Trial

As outlined in Chapter 1, modelling and simulation of the SAI has the potential to de-risk FOCFTs, to provide training to flight deck operators and aircraft pilots, and to inform ship design. A significant milestone in the application of modelling and simulation to the launch and recovery of ship-borne aircraft was the use of piloted flight simulation in preparing for QEC/F-35B FOCFTs; the first time this had ever been done. This chapter describes how piloted flight simulation was used to investigate helicopter recovery operations to the deck of HMS Queen Elizabeth. A helicopter flight simulation environment was developed in which a flight dynamics model representative of a Sikorsky SH-60B Seahawk helicopter was integrated with CFD computed QEC airwakes and used to conduct real-time simulated deck landings. After recovering the aircraft to spots 5 and 6 towards the stern of the ship in varying WOD conditions, the pilot was asked to provide workload ratings which, along with recordings of pilot control input and helicopter relative position, gave a comprehensive assessment of how the airwake affects the helicopter. Performing an assessment of how the airwake affects the helicopter during recovery to a ship demonstrates the capability of piloted flight simulation to support both flight trials and helicopter clearance activities. It should be pointed out that this study was part of ongoing research into modelling and simulation of the ship-helicopter dynamic interface [1], and did not contribute directly to the helicopter/QEC FOCFTs.

5.1 Flight Simulation Environment

High-fidelity piloted flight simulation for helicopter landings to a ship ideally requires a six degree-of-freedom motion flight simulator with a dome projection system to provide motion and visual cues to the pilot in the highly dynamic flying environment over the ship's deck [135, 136]. It also requires effective modelling of the helicopter's flight dynamics, unsteady ship airwakes, and ship motion, along with realistic visual models, including sea surface, ship geometry, deck markings, and visual landing aids.

HELIFLIGHT-R, Figure 5-1, is a fully reconfigurable research simulator [51], consisting of a generic rotorcraft crew station housed inside a 12 ft diameter visual display dome, mounted on a six degree-of-freedom motion platform. The platform is a standard hexapod configuration, comprising six electric actuators, each with a 24 in stroke. The simulator dome houses a twin-seat cockpit, with a third seat at the rear for an instructor or simulator operator. The primary cockpit instruments are presented on two wide-screen flat-panel displays. A four-axis electronic control loading system provides the capability to configure the force-feel characteristics of both the pilot and co-pilot's cyclic, collective and pedal controls to represent a wide range of aircraft types. Three Digital Light Processing (DLP) projectors, with a resolution of 2,560 × 1,600 pixels, are used to project an outside-world image onto the inside surface of the dome. The three images are geometry-corrected and edge-blended, before being projected, to present a single continuous image to the pilot in the cockpit, as can be seen on the right in Figure 5-1. The projectors are equipped with wide-angle lenses and provide a horizontal field-of-view of 230 deg (±115 deg) and a vertical field-of-view of 70 deg (+30 deg/-40 deg). The visual scene was generated using Presagis Vega Prime software. Audio cues are presented to the pilot using a system of loudspeakers distributed throughout the cockpit.

Figure 5-1 QEC visual environment in the HELIFLIGHT-R flight simulator.

5.2 SH-60B FLIGHTLAB Model

Integration of the aircraft flight dynamics model with the HELIFLIGHT-R simulator is achieved using Advanced Rotorcraft Technology's FLIGHTLAB software [137], which provides a library of aircraft models and allows the user to define a rotorcraft via a library of pre-defined components such as those shown in Figure 5-2.

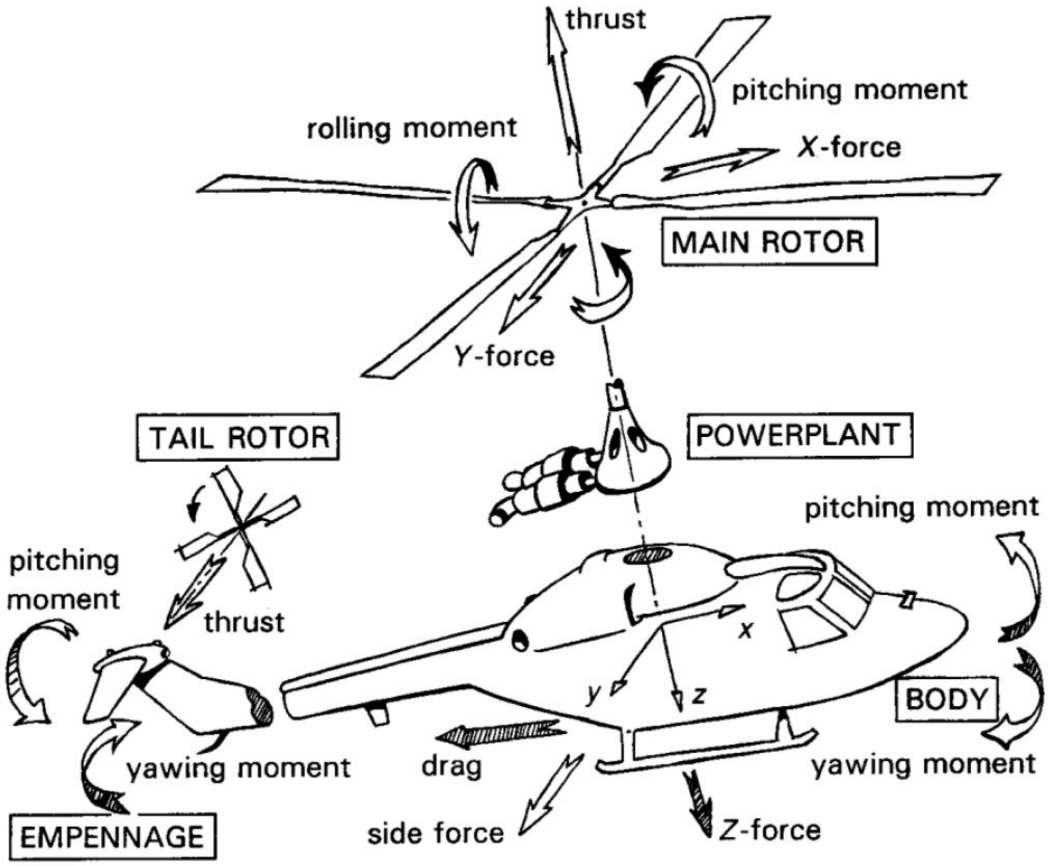

Figure 5-2 Components of a helicopter mathematical model [138]

A generic rotorcraft flight dynamics model has been configured derived from a model of the UH-60A Black Hawk utility transport helicopter, at UoL, to be representative of the Sikorsky SH-60B Seahawk. Although HELIFLIGHT-R may be configured to represent a large number of different rotorcraft, the SH-60B maritime helicopter has been used due to the availability of performance data of the UH-60 in the open literature [139]. The model was developed in FLIGHTLAB and comprises the following major subsystem components:

5.2.1 Main Rotor Model

Blade element theory is used to model the helicopter main rotor. Each rotor is divided into a number of segments. In the case of the SH-60B model each rotor blade has 10 segments. At each individual blade segment, the airspeed and incidence angle are calculated. Together, with look-up tables of non-linear lift, drag and pitching moment coefficients, the aerodynamic force and moment at each blade element is found. The total rotor forces and moments are calculated by integrating the elemental forces and moments of each blade segment on each rotor blade.

5.2.2 Inflow Model

The rotor blades induce a flow field at the rotor disk which changes the blade incidence and dynamic pressure, also changing the aerodynamic forces and moments at the blade elements. A more advanced inflow model, the finite-state Peters-He dynamic model, was used in the SH-60B helicopter simulation, which accounts for low frequency effects during manoeuvring flight and, the time delay associated with accelerating a large mass of air through the rotor disk [140]. The inflow model includes an empirical function for the rotor operating in proximity to a ground surface.

5.2.3 Tail Rotor Model

A Bailey disk was used to model the tail rotor. A simple model, the Bailey disk assumes the induced inflow is uniform across the rotor disk and is calculated using momentum theory.

5.2.4 Fuselage and Empennage Aerodynamic Models

The aerodynamics of the fuselage, vertical tail, and port and starboard horizontal stabilators are modelled via separate look-up tables. Coefficients of each airframe component, derived from wind tunnel data, are used to compute the aerodynamic forces and moments, dependent on the incidence and sideslip.

5.2.5 Engine Model

The engine is modelled as a simple turbo-shaft engine with a rotor speed governor.

5.2.6 Flight Control System

A SH-60B flight control system is included in the simulation with a primary mechanical flight control system and an Automatic Flight Control System (AFCS). The AFCS includes a Stability Augmentation System (SAS) with sensor and actuator models.

5.2.7 Landing Gear Model

A landing gear model is included in the FLIGHTLAB model to provide deck reaction cues on touchdown. The normal force developed by the oleo and tyre combination is modelled as a spring and damper system using a look up table and a velocity-squared function system respectively. Longitudinal and lateral forces on each tyre are also modelled using frictional force coefficients.

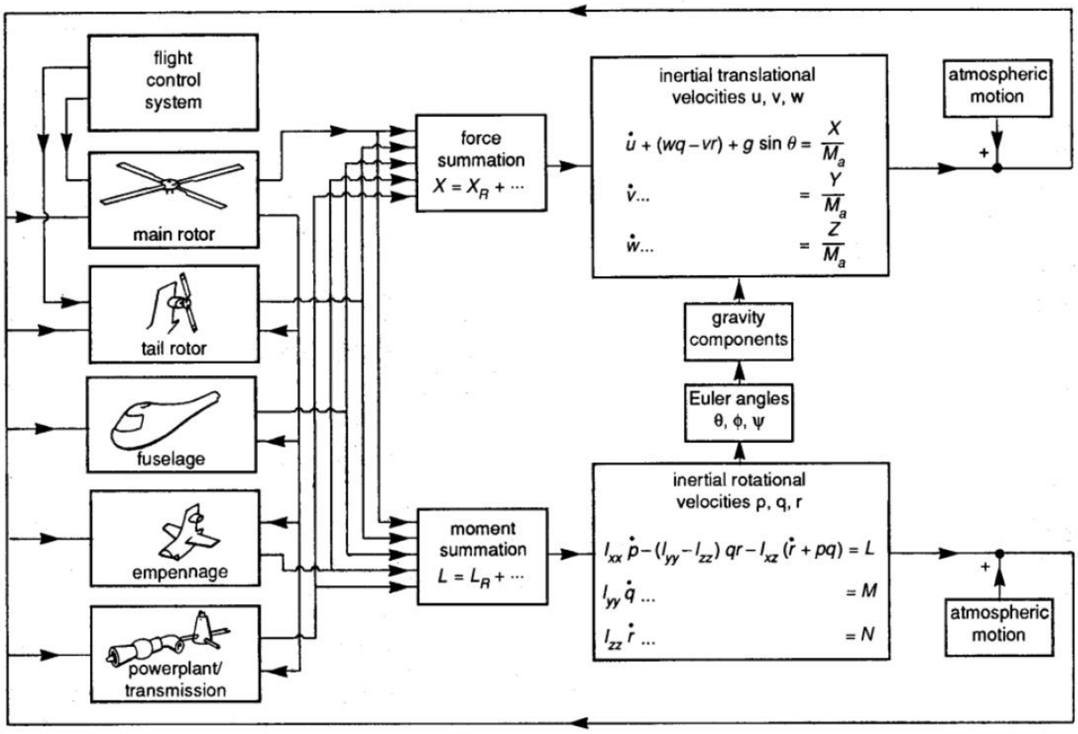

Figure 5-3 Integration of the helicopter model subsystem components [132].

Figure 5-3 shows how each of the helicopter's modelled subsystems are integrated with a standard atmosphere model and equations of motion. The forces and moments produced by each of the subsystem components are summed at the helicopter's centre of gravity. The total forces and moments are then used in the six degree-of-freedom rigid-body equations of motion to calculate the helicopter state vector.

Although it is recognised that the Seahawk is not in service with the UK Royal Navy, this aircraft model was used for these simulation trials due to its strong validation [141] and extensive use during previous research at UoL e.g., [17]. An important component of the simulation environment is the effect of the ship's airwake on the helicopter. CFD-generated airwakes can be integrated with FLIGHTLAB, enabling unsteady airwake velocities to be imposed upon the aircraft flight dynamics model at various locations on the rotor blades and airframe. During testing, the FLIGHTLAB software allows real-time data monitoring and recording which, together with in-cockpit video and audio recordings, are used for post-trial analysis.

The FOCFT process to determine the SHOL can be extremely costly, both financially and in the commitment of valuable assets, people and equipment over a number of weeks [142]. The opportunity to test over a suitable range of environmental conditions is heavily dependent on the prevailing wind and sea-state conditions. If these conditions are not available the trials may have to be extended or delayed, or the lack of testing can lead to a restricted SHOL in which the helicopter's operational envelope is constrained; SHOL diagrams determined using similar ship/aircraft types may be used conservatively to complete a SHOL, through a process called 'read-across', but this is undesirable.

Considering the large expense and uncertainty incurred in producing SHOLs for each ship-helicopter combination, a more cost-effective method would be highly beneficial. One method of reducing these costs may be through the use of modelling and simulation of the aircraft-ship dynamic interface, as an aid to real-world SHOL testing. This was demonstrated with the F-35B/QEC clearance trials, and is becoming a more feasible option due to the increasing fidelity of simulation, including research on motion tuning, pilot modelling and coupled rotor/airwake aerodynamics [135, 143].

5.2.8 Airwake integration with FLIGHTLAB

A selection of the QEC airwakes, whose computation and validation were described in Chapter 4, were used for the piloted simulation trials. It is important to have an understanding of the air flow over the deck for all wind directions due to the varying levels of disturbance in the air flow, e.g. [144]. Three wind directions were therefore used containing both disturbed and undisturbed air flow: Ahead, Green 45 and Green 90, for a range of wind speeds. These airwakes were illustrated earlier in Figure 4-41 to Figure 4-43.

The simulated deck landings were to spots 5 and 6, which are the two nearest to the stern; spot 6 being situated behind the island. The significance of these two spots is that they have been designated as primary landing spots for rotorcraft. Figure 4-41 (Chapter4) shows that the turbulence intensity level over spot 5 in an Ahead wind is low with an increase to approximately 10% at spot 6 due to the presence of the aft island in the freestream flow. As the wind approaches from 45 deg off the starboard side, the turbulence intensity increases at spot 5 and 6 to close to 20% as shown in Figure 4-42 (b). A further increase in turbulence intensity, to about 25%, can be seen in Figure 4-42 (c) over spot 5 in a Green 90 wind; however, the flow around a hover position at 10 m above spot 6 shows a turbulence intensity of less than 5% which increases as the height above the deck decreases.

The simulated flight trial was designed to evaluate the helicopter handling qualities and pilot workload when recovering to the QEC aircraft carriers for the three different wind directions. It was originally intended to use the same wind speeds at each wind angle; however, it was found during the trials that the Green winds were particularly challenging, so lower wind speeds were tested for the Green 45 and 90 conditions, as listed in Table 5-1.

Table 5-1 Test Conditions.

Azimuth (WOD)	Wind Speed (WOD), kts
Ahead	25, 35, 45
Green 45	15, 25
Green 90	15, 25, 35

Figure 5-4 illustrates the process of integrating the computed unsteady velocity components of the airwake with the FLIGHTLAB SH-60B helicopter flight dynamics model. Thirty seconds of unsteady airwake was computed for each wind direction at 100 Hz on an unstructured grid. The three-dimensional velocity components were then interpolated onto a smaller structured grid and down-sampled to 25 Hz. The structured grid is shown in Figure 5-4 with dimensions 300 m in length by 150 m in width by 50 m in height and a grid spacing of 1 m; all flying operations where constrained to take place within this rectangular volume. Airwakes were computed at each wind angle with a wind speed of 30 kts and then scaled to produce airwakes for wind speeds of 15 kts to 45 kts. As discussed earlier in Section 3.6, the scaling is possible because the ship is a bluff body and at the high Reynolds number the Strouhal relation can be used to scale the airwake frequency. The validity of Strouhal scaling of ship airwakes was demonstrated in [126].

The CFD-computed airwake is integrated into the flight dynamics model using Simulink. The velocity data for each WOD condition is converted into a series of lookup tables and applied to the helicopter flight dynamics model at Aerodynamic Computation Points (ACPs) in real-time within the FLIGHTAB software, as the pilot manoeuvres the aircraft within the airwake. As the presence of the helicopter and the downwash from the rotor has no effect on the airwake this integration is known as one-way coupling. The distribution of ACPs on the SH-60B model can be seen in the upper right of Figure 5-4. Ten ACPs are distributed along each of the four main rotor blades, one at the aircraft centre of gravity, one on each of the port and starboard stabilisers, two on the vertical tail, and a final ACP at the centre of the tail rotor hub, giving a total of 46 ACPs. Although two-way coupling has been achieved for a helicopter fixed in a hover position over a ship's flight deck [145], it is not currently feasible to compute the solution in real-time for piloted flight simulation [146].

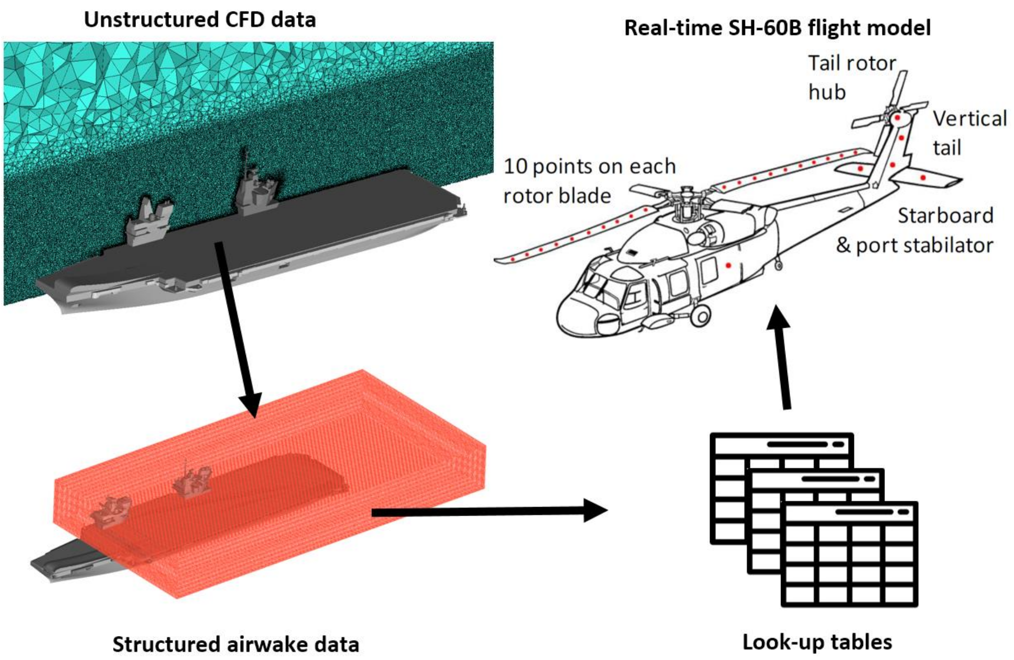

Figure 5-4 Integration of CFD airwake with helicopter flight dynamics model.

5.2.9 Ship Motion

Deck motion can be a major contributor to the difficulty of the landing task; furthermore, pilots use the ship's superstructure and deck to obtain visual cues when flying close to the ship, so realistic ship motion is required. A hull form and appendages representative of a generic 280 m long warship was used with the ship motion software, ShipMo3D, a well-validated ship motion potential-flow code developed at Defence Research and Development Canada (DRDC) – Atlantic [147] and made available to UoL. Ship motion was calculated in sway, surge, heave, pitch, roll and yaw axes for waves coming from Ahead and starboard aligning with the wind directions tested. Sea states were defined using the Bretschneider Spectrum [148]. Sea state 4 was used for the lower wind speeds and sea state 5 for the higher wind speeds. A typical ship speed through the seaway of 12 kts was applied.

Figure 5-5 shows deck motion data in heave (vertical), roll and pitch computed for spot 5 in sea state 5 for waves from Ahead and 45 deg from starboard, i.e., Green 45; spot 6 will have similar displacements. As expected, the greater motions are stimulated by the oblique waves. Heave motion, augmented by deck pitch and roll at spots away from the centre of rotation of the ship, is the most important motion for the pilot during recovery to the deck and, as can be seen in Figure 5-5, the vertical displacement at the landing spot was mostly less than 2 m. As will be seen in the flight test results in Section 5.3, the test pilot did not identify deck motion as a major factor contributing to workload during any of the deck landings performed in the simulator.

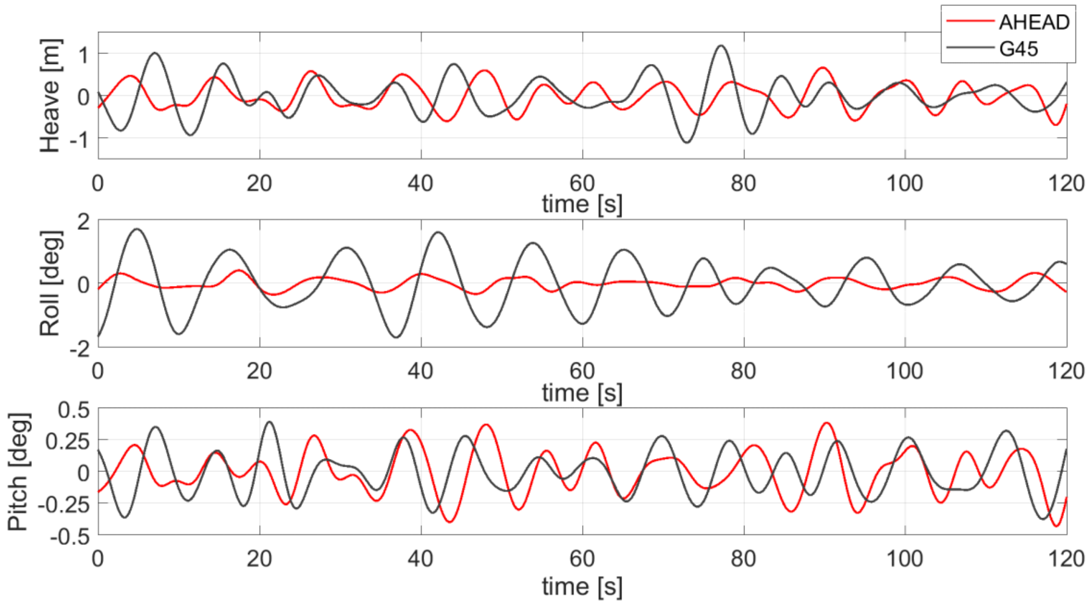

Figure 5-5 Computed ship motion at landing spot 5 for waves from Ahead and Green 45 in sea-state 5.

5.2.10 Flight Test Procedure

During the simulated flight trial, a highly experienced former Royal Navy (RN) helicopter test pilot was instructed to land at spots 5 and 6 in the eight WOD conditions at the wind speeds shown in Table 5-1. The pilot performed the standard UK port-side forward-facing recovery technique, which requires the pilot to guide the helicopter to a hover position off the port side of the ship, matching the ship's speed, followed by a lateral translation across the deck to hover over the landing spot, before descending to land on the flight deck. Each landing was split into three Mission Task Elements (MTE), illustrated in Figure 5-6. The first is the lateral traverse across the deck from the port side of the ship to a hover position over the landing spot. The second MTE requires the pilot to maintain the hover position for 30 seconds in preparation for landing and, finally, the third MTE is the descent from the hover position to touch down on the flight deck. The difficulty of the landing task was assessed by the test pilot using two subjective rating scales: a workload was assigned to each MTE using the Bedford workload rating scale, and a rating from the DIPES was given for the overall landing task. The two scales are shown in Figure 5-7 and Figure 1-9 (Chapter 1) respectively. Pilot assessment of their workload is a subjective process. In order to improve the reliability of workload ratings, the pilot is given the opportunity to acclimatize to the simulated flight environment by operating the helicopter freely within the airwake of the ship prior to the recovery task [15, 18].

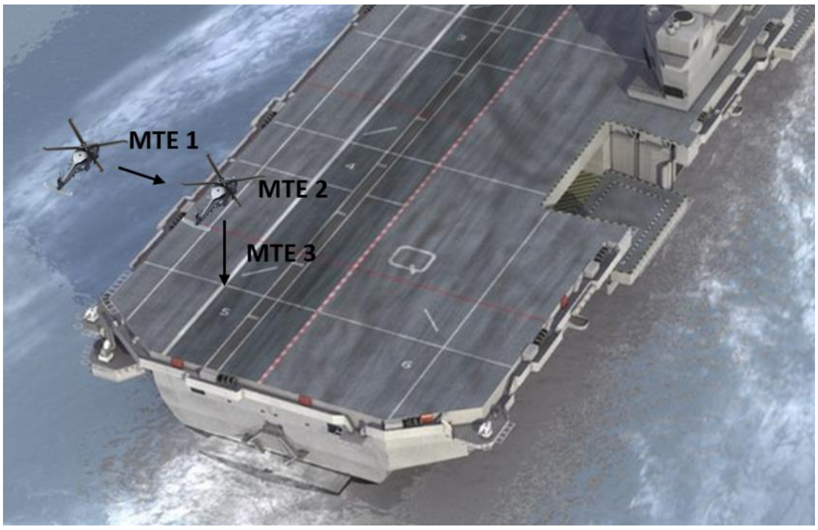

(a)

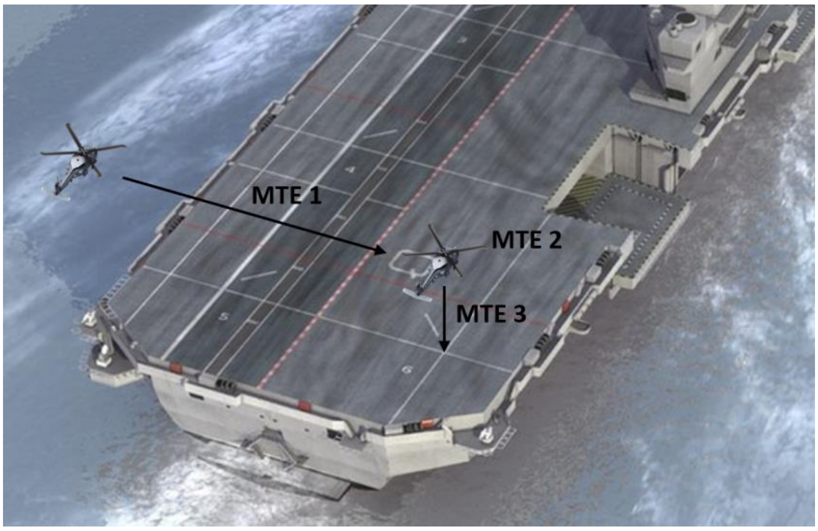

(b)

Figure 5-6 Mission task elements on recovery to QEC landing spots 5 (a) and 6 (b).

The Bedford workload rating scale assesses the pilot's perceived workload and is based on the pilot's spare capacity when performing a task, where workload is defined as the integrated physical and mental effort generated by the perceived demands of a specified piloting task [9]. As shown in Figure 5-7, the Bedford workload rating scale is a 10-point scale where a rating of 1-3 indicates that workload was satisfactory during the task. Ratings of 4-6 are awarded where the workload for a task was not satisfactory, reducing the pilot's capacity to perform ancillary tasks such as radio communication, while ratings of 7-9 are awarded where the task can be performed, yet the workload is deemed intolerable. Finally, a rating of 10 is awarded in situations where the pilot is unable to complete the task due to high workload, and so must abandon the task.

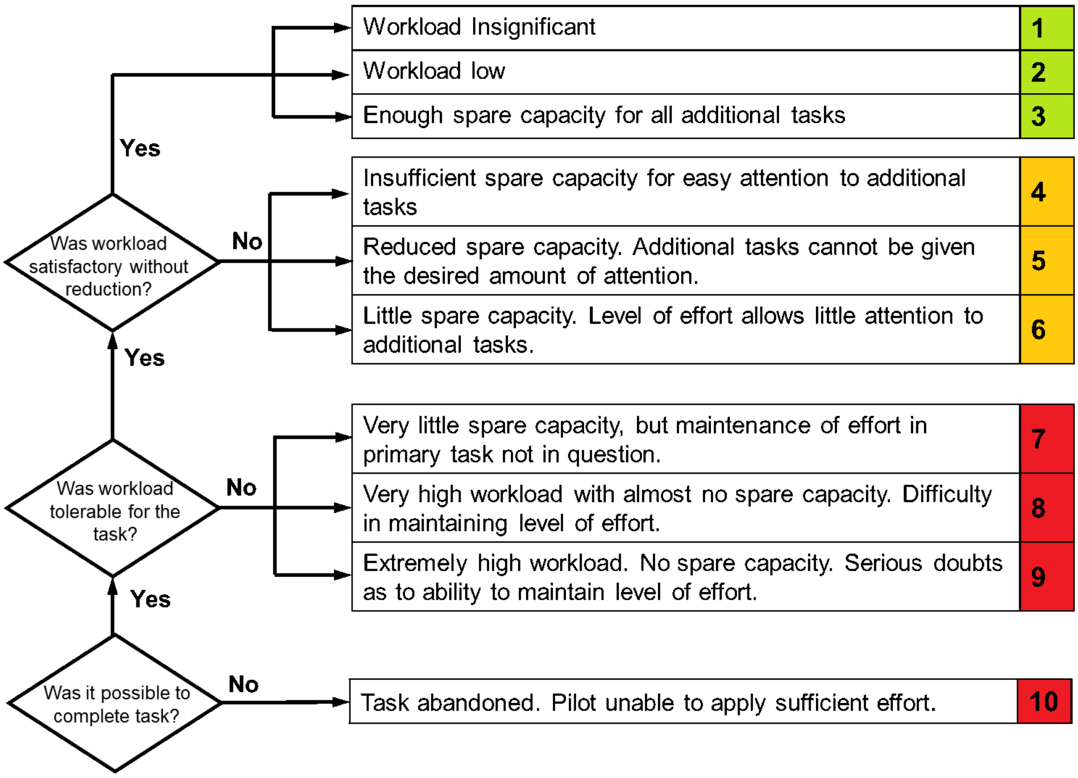

Figure 5-7 Bedford workload rating scale [9].

The DIPES (Figure 1-9) assesses the overall landing task and is widely used by NATO member countries to determine limiting conditions for ship-helicopter combinations. DIPES differs from the Bedford scale in that it is a coarser scale which also accounts for aircraft physical control activity and identifies environmental factors such as deck motion and turbulence [11]; DIPES is, therefore, particularly suited for at-sea qualification testing where, although pilot workload may be low, control limits can be encountered.

During the simulated flight trials, the pilot awarded Bedford workload ratings for each MTE, along with a DIPES rating for the total recovery to the ship; the pilot's comments were also documented for further analysis. In addition, flight test data was recorded providing time-stamped information for pilot input to the cyclic, collective and pedal controls, as well as aircraft position, attitude and accelerations in six degrees of freedom. The airwake velocity components at each of the 46 ACPs were also recorded.

5.3 **Flight Trial Results**

A selection of results from the flight trials are presented and discussed in the following sections. The results have been collated as tables of pilot ratings, and figures showing pilot control activity and aircraft position for both the overall landing task, and for each MTE.

5.3.1 Pilot Ratings for Deck Landing Task

The background colour in each of the following tables corresponds with those used in the Bedford workload scale in Figure 5-7 and denote the difficulty of the MTE.

5.3.1.1 Ahead

Table 5-2 presents the Bedford workload ratings for each MTE and the overall DIPES ratings when landing to spots 5 and 6 in winds from Ahead at speeds of 25 kts, 35 kts and 45 kts. The pilot gave workload ratings of 1 to 3 for each task in an Ahead wind indicating that the workload was satisfactory; a maximum DIPES rating of 2 in an Ahead wind was given during landing to spot 6 in winds of 35 kts and above.

Table 5-2 Bedford workload and DIPES ratings in Ahead WOD.

QEC Ahead						
			Bedford workload ratings			
Spot	DIPES suffixes	Wind	MTE 1	MTE 2	MTE 3	DIPES
5	none awarded	25 kts	1	2	2	1
	none awarded	35 kts	1	2	2	1
	none awarded	45 kts	1	2	2	1
6	none awarded	25 kts	1	2	2	1
	none awarded	35 kts	1	3	3	2
	none awarded	45 kts	1	3	3	2

5.3.1.2 Green 45

Table 5-3 presents the Bedford workload ratings for each MTE and the overall DIPES ratings when landing to spots 5 and 6 at speeds of 15 kts and 25 kts in a Green 45 WOD. After experiencing difficult flying conditions in the 25 kts wind, the pilot elected not to fly at a higher wind speed; an outcome that would correspond with establishing the operational limit during a real trial.

Table 5-3 Bedford workload and DIPES ratings in a Green 45 WOD.

QEC Green 45						
			Bedford workload ratings			
Spot	DIPES suffixes	Wind	MTE 1	MTE 2	MTE 3	DIPES
5	Y, H, T, F, L	15 kts	4	4	4	2
	Y, H, T, F, L	25 kts	5	6	6	3
6	Y, H, T, F, L, V	15 kts	4	5	4	3
	Y, H, T, F, L, V, Q	25 kts	5	7	8	4

All of the landing tasks in a Green 45 wind condition showed less than satisfactory workload conditions. Winds higher than 25 kts on landing to spot 6 caused intolerable workload for the pilot; this is reflected in a DIPES rating which exhibits excessive compensation required. Common causes of each DIPES rating given by the pilot in a Green 45 were as follows: Yaw control (Y), Height control (H), Turbulence (T), Forward/Aft positioning (F) and Lateral positioning (L) (letters refer to suffices in DIPES table, Figure 1-9).

5.3.1.3 Green 90

Table 5-4 presents the Bedford workload ratings for each MTE and the overall DIPES ratings when landing to spots 5 and 6 at speeds ranging from 15 kts to 35 kts in a Green 90 WOD, i.e., a beam wind. During the port-side forward-facing landing manoeuvre, the 90 wind presents a side wind to the helicopter thus requiring increased pedal and lateral cyclic inputs to maintain position. While the pilot did elect to land to spot 6 for a 35 kts wind, he did not do so for spot 5 due to the challenging conditions experience at 25 kts.

Table 5-4 Bedford workload and DIPES ratings in a Green 90 WOD.

QEC Green 90						
			Bedford workload ratings			
Spot	DIPES suffixes	Wind	MTE 1	MTE 2	MTE 3	DIPES
5	none awarded	15 kts	1	3	3	2
	Y, T, F, L	25 kts	3	4	4	4
6	Y, F	15 kts	1	3	4	2
	Y, T, F, L, P	25 kts	3	4	5	4
	Y, T, F, L, P, V, A	35 kts	9	8	8	5

The workload ratings for each task in a Green 90 condition for both landing spots shown in Table 5-4 increase with wind strength. Helicopter recovery was conducted to spot 6 in a 35 kts wind that would not have been attempted in a real FOCFT due to the large workload observed during the previous 25 kts test point; the recovery was attempted to observe the effects of operating in extreme workload conditions.

5.3.2 Aircraft Position During Deck Landing Task

Figure 5-8 to Figure 5-10 show the helicopter's lateral, longitudinal and vertical position over the deck whilst recovering to the ship in the three WOD conditions. The position is recorded at the aircraft's centre of gravity.

5.3.2.1 Ahead

In the Ahead WOD condition shown in Figure 5-8 the pilot was able to maintain a desired vertical height while translating across the edge of the deck to the hover position over landing spots 5 and 6. As the wind speed was increased from 25 kts to 45 kts the vertical position during the translation was similar. After the longer translation to spot 6, the aircraft had a longitudinal position which the pilot corrected by moving forward when in line with the landing spot; the longitudinal drift was greater in the stronger 45 kts wind.

5.3.2.2 Green 45

Although the pilot was able to maintain height throughout the translation in a 15 kts Green 45 WOD condition as shown in Figure 5-9, increasing the wind speed to 25 kts resulted in more flight path disturbances. The pilot was also required to correct the longitudinal drift and move the aircraft forward after the lateral translation to position over landing spot 6.

5.3.2.3 Green 90

Figure 5-10 shows the aircraft's position during recovery in a Green 90 WOD. Although the aircraft's vertical position was less disturbed while translating across the deck compared with the Green 45 WOD, the pilot was unable to maintain a precise longitudinal position during the traverse manoeuvre for the greater distance to spot 6.

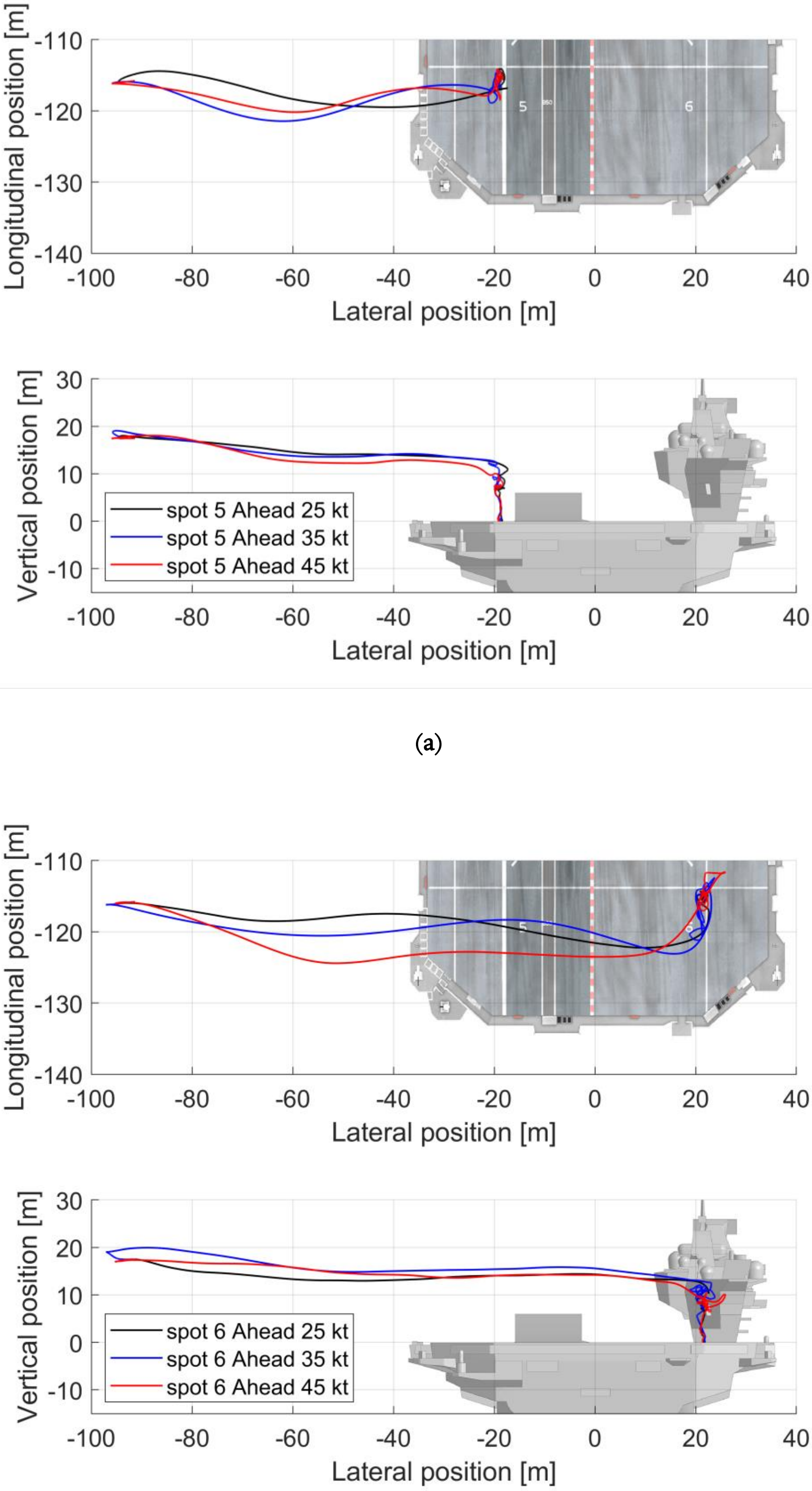

(a)

(b)

Figure 5-8 Helicopter position in an Ahead wind at spots 5 (a) and 6 (b).

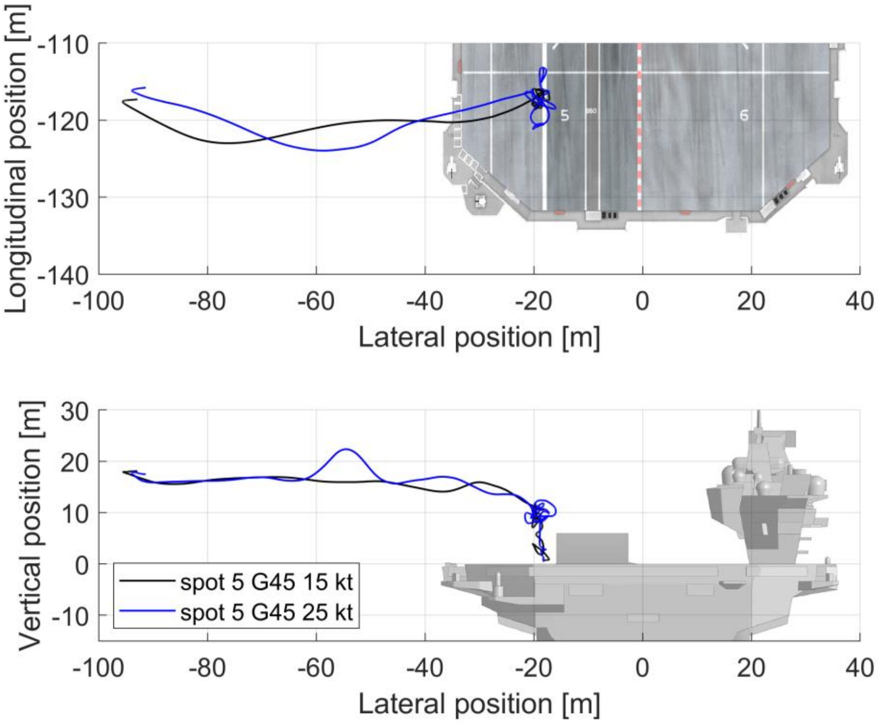

(a)

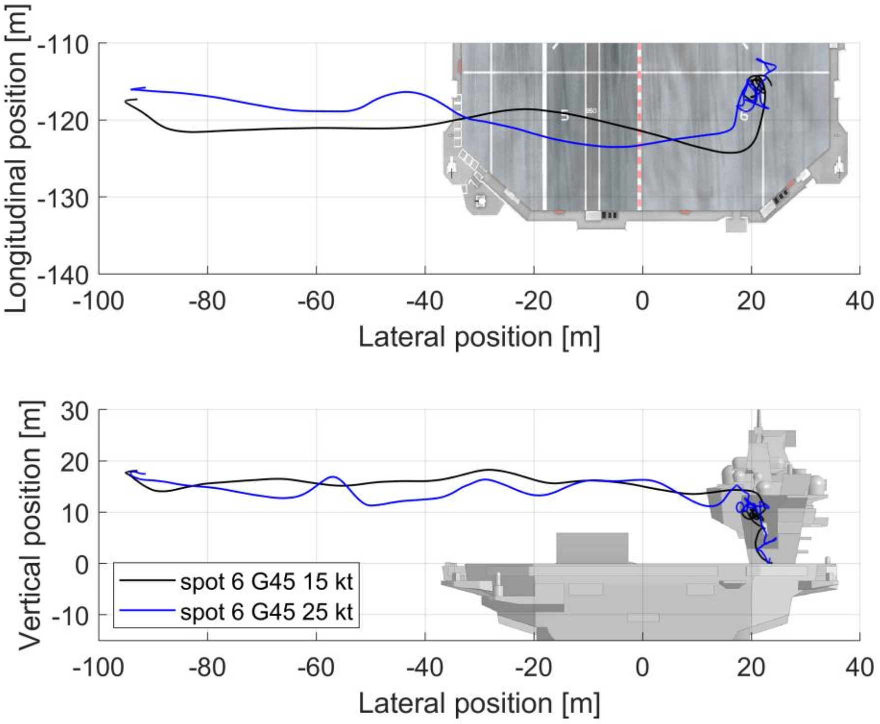

(b)

Figure 5-9 Helicopter position in a Green 45 wind at spots 5 (a) and 6 (b).

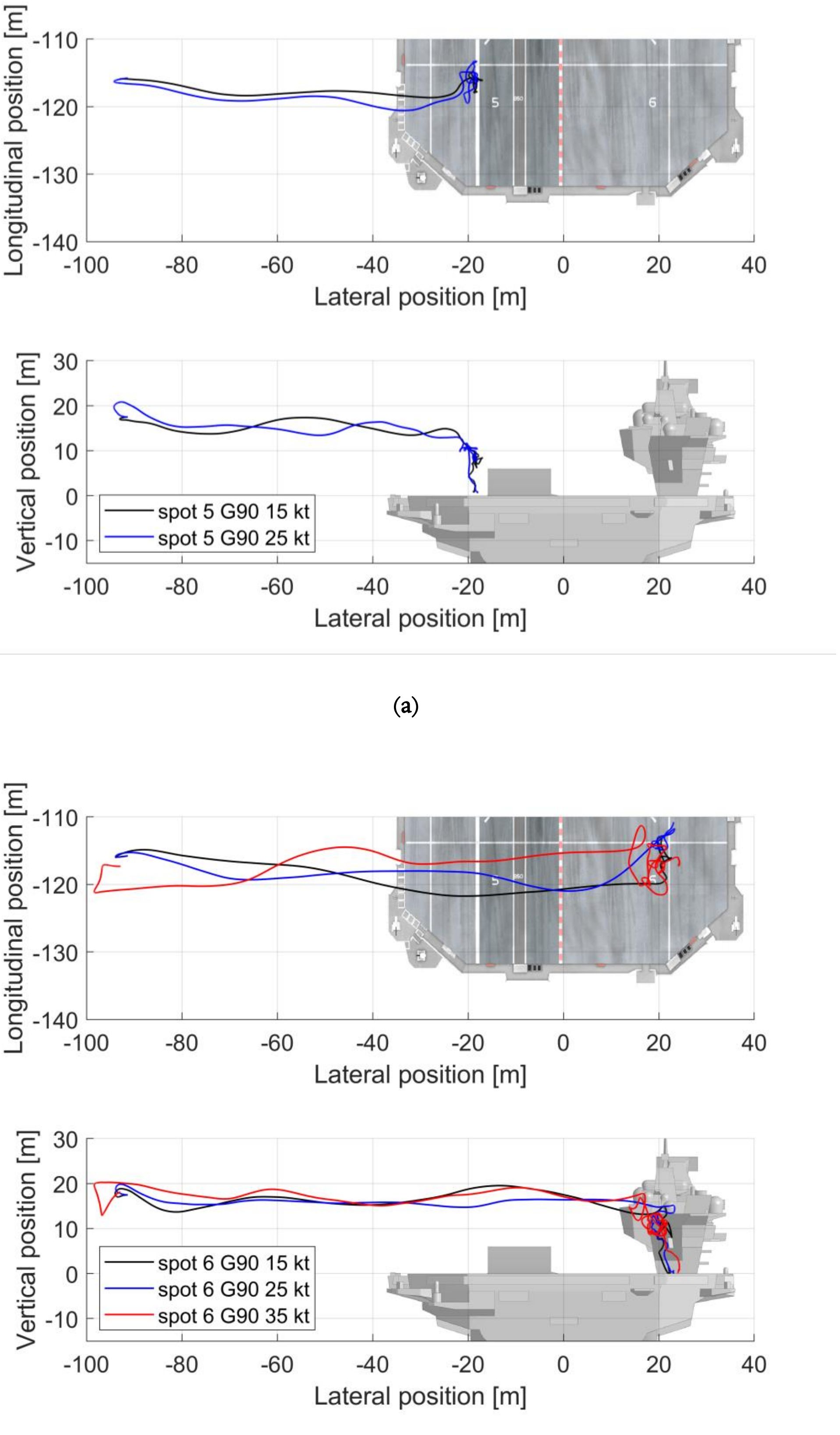

(a)

(b)

Figure 5-10 Helicopter position in a Green 90 wind at spots 5 (a) and 6 (b).

5.3.3 Collective Activity Control During the Landing Task

Although it is recognised that the aircraft controls are coupled, they have been presented separately to more easily compare the effect of the different WOD conditions at each spot location. Figure 5-11 to Figure 5-13 show the pilot's collective input and associated main rotor torque during recovery to the ship for each WOD condition at spot 6. Data for spot 5, which has a shorter translation and was less informative, has been omitted for the sake of brevity. In the figures the time histories are split by vertical dashed lines to show the three MTEs: lateral translation, hover and touchdown. The red horizontal dashed line indicates the 100% max continuous torque.

5.3.3.1 Ahead

The collective inputs and torque during aircraft recovery to the ship in an Ahead WOD at spot 6, Figure 5-11, shows that there was relatively little activity, although there is an increase in activity at the higher wind speeds.

5.3.3.2 Green 45

During recovery to spot 6 in a Green 45 WOD, much greater activity is observed in the pilot's collective inputs and torque for both wind speeds compared with winds from Ahead, as can be seen in Figure 5-12.

5.3.3.3 Green 90

Figure 5-13 shows that the pilot's collective control activity and torque during the landing task in the Green 90 winds were lower than those seen in the Green 45 winds. It is also noticeable that in the 45 kts wind the overall landing task, particularly MTEs 1 and 3, the translation and landing, took significantly longer with the pilot spending about one minute on MTE 1, a clear indicator of high workload.

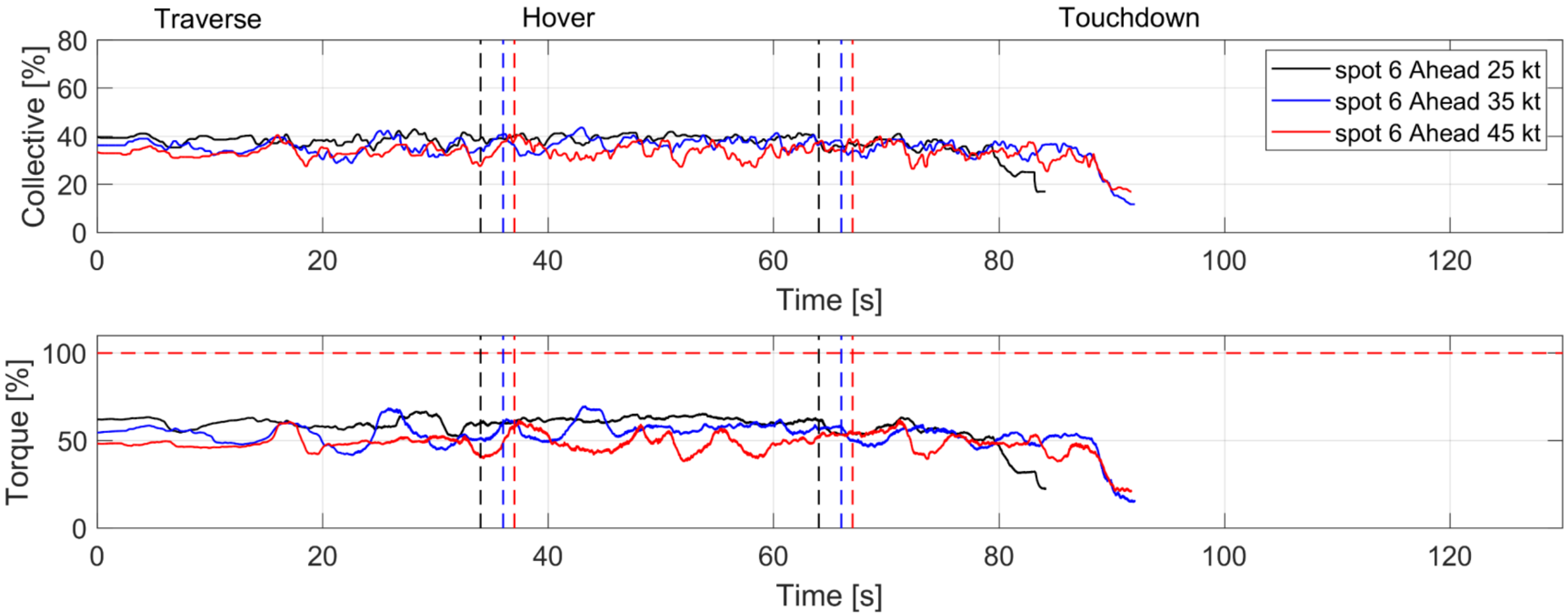

Figure 5-11 Collective control activity and Torque in an Ahead wind at spot 6.

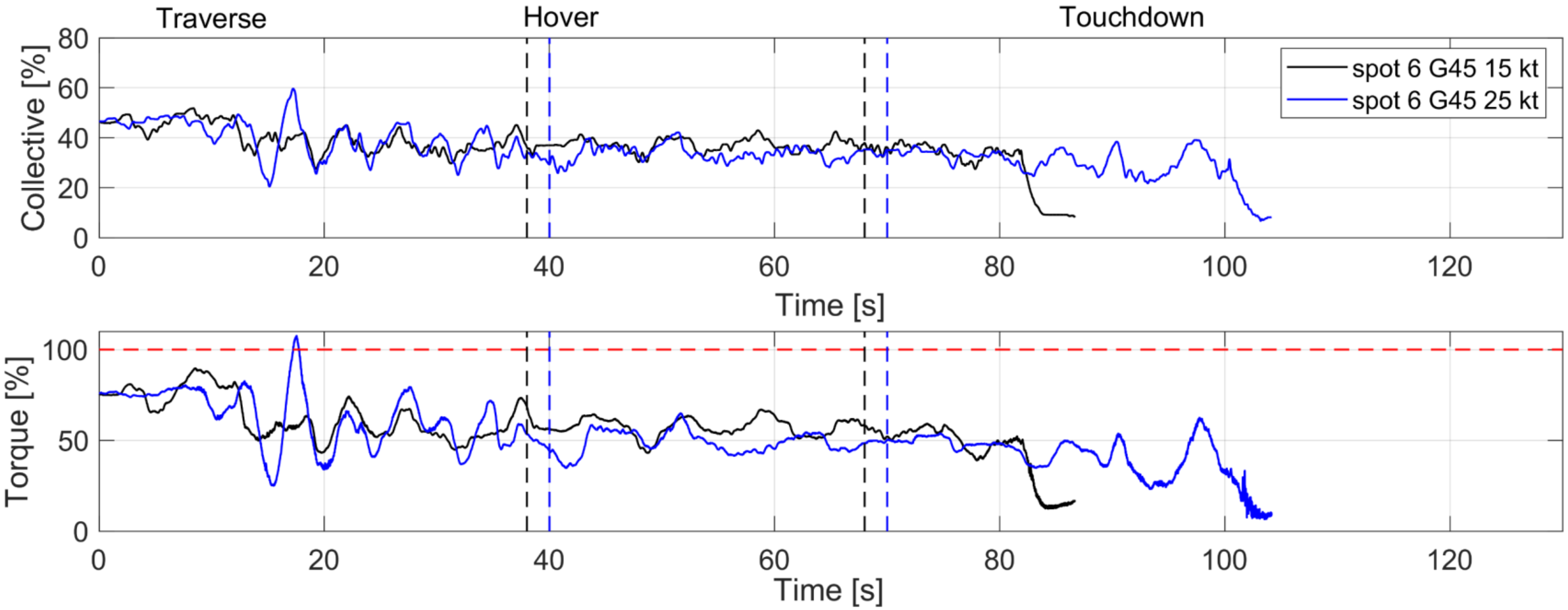

Figure 5-12 Collective control activity and Torque in a Green 45 wind at spot 6.

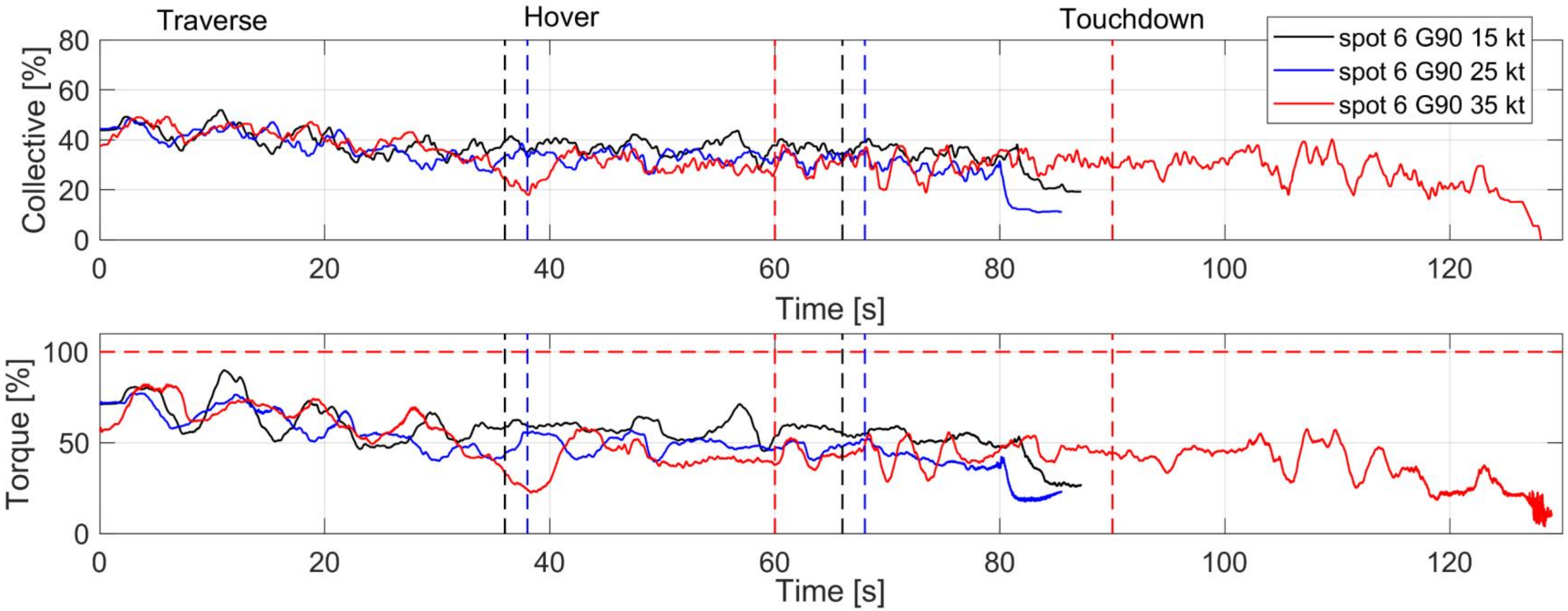

Figure 5-13 Collective control activity and Torque in a Green 90 wind at spot 6.

5.3.4 Pedal Inputs During Landing Task

During the simulated flight tests the pilot commented several times during recoveries in the Green 45 and Green 90 WOD conditions that the pedal limits had been reached. Figure 5-14 to Figure 5-16 show the pedal control inputs for each WOD condition; full right and left pedal are given as 50% and -50% respectively with the 10% pedal margins shown as horizontal dashed red lines.

5.3.4.1 Ahead

Figure 5-14 shows the limited pedal input on landing to spot 5 for 25 kts, 35 kts and 45 kts winds; increased activity is shown when landing at spot 6. Pedal activity is well within the pedal margins.

5.3.4.2 Green 45

The pedal input time histories on landing to spots 5 and 6 in a Green 45 WOD are shown in Figure 5-15. An increase in control activity can be seen compared with the headwind. Also, the control activity in the 25 kts wind was greater than in the 15 kts wind for both spots. As well as the control activity and greater excursions in the pedal controls, it can be seen that a significant left pedal input was applied for the majority of the mission to overcome the crosswind component in the Green 45 wind.

5.3.4.3 Green 90

Figure 5-16 shows the pilot's pedal control inputs for a Green 90. Similar to the winds from Green 45, an increase in the wind speed required the pilot to maintain a greater pedal input. The amplitude of pedal inputs on landing to both spots was less than that for the Green 45. Similar to the control activity exhibited in a Green 45, the pedal 10% margin was infringed several times in the Green 90 wind but for longer periods; at spot 6 in a 35kts wind full left pedal was required for much of the manoeuvre.

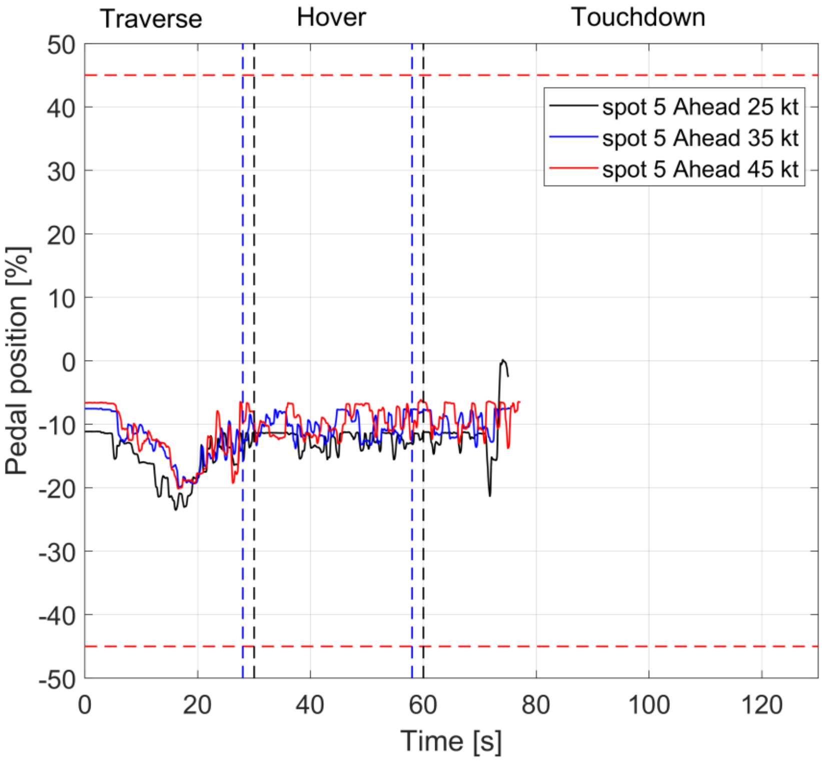

(a)

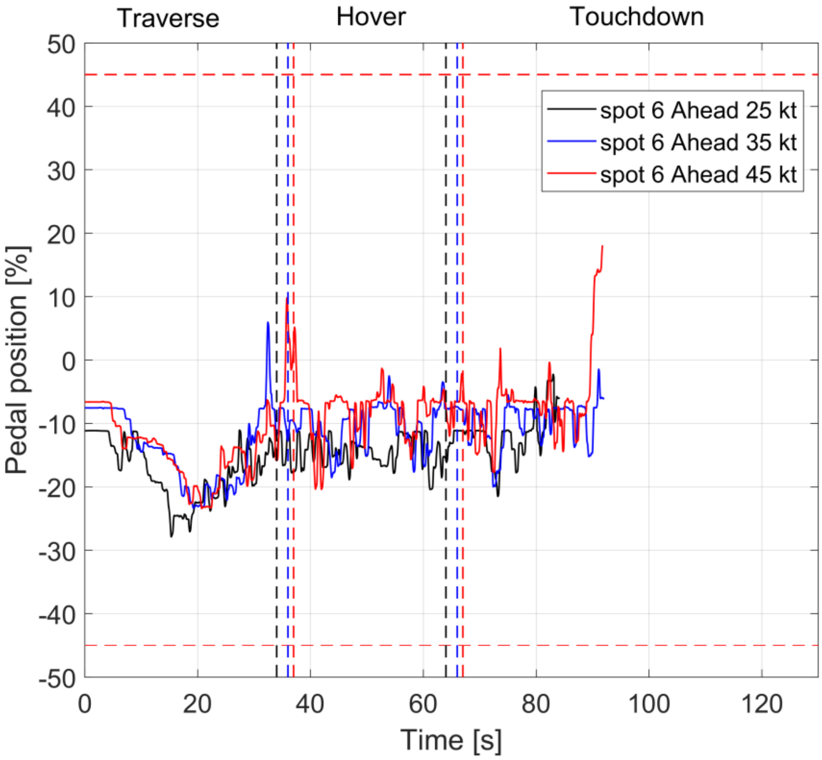

(b)

Figure 5-14 Pedal position in an Ahead wind at spots 5 (a) and 6 (b).

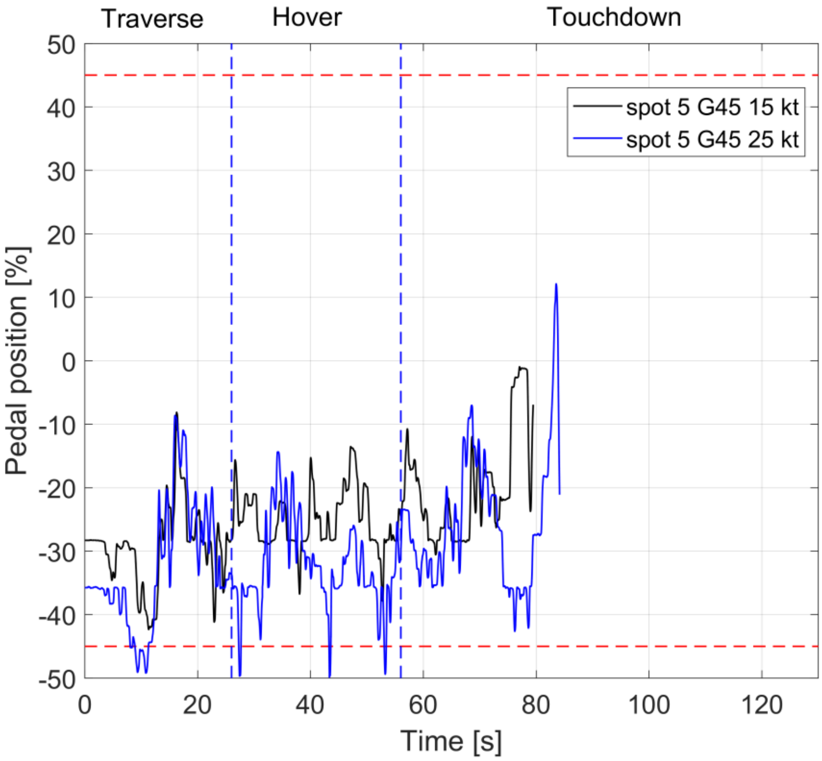

(a)

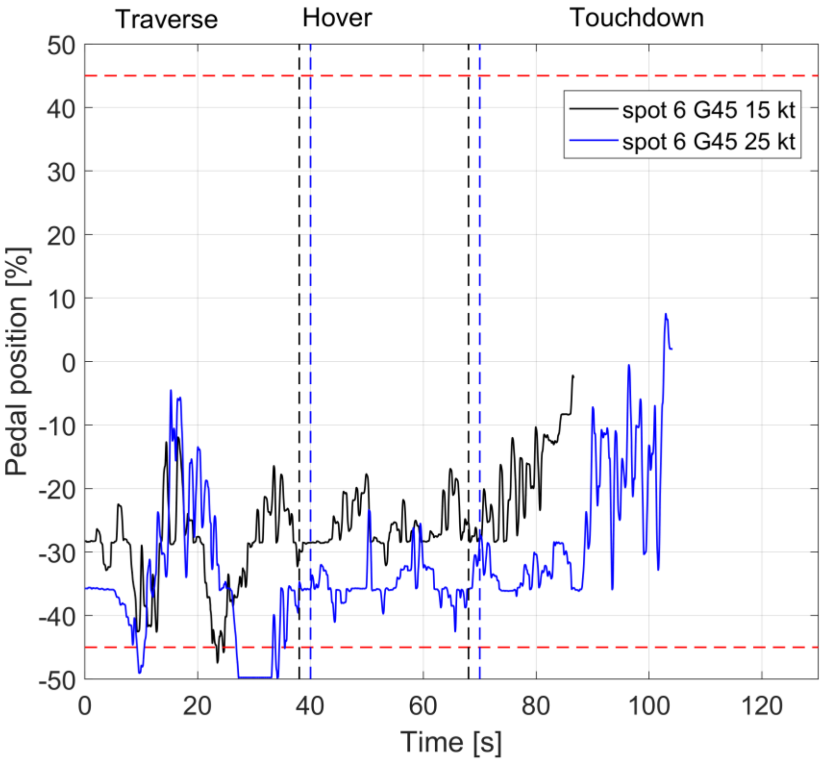

(b)

Figure 5-15 Pedal position in a Green 45 wind at spots 5 (a) and 6 (b).

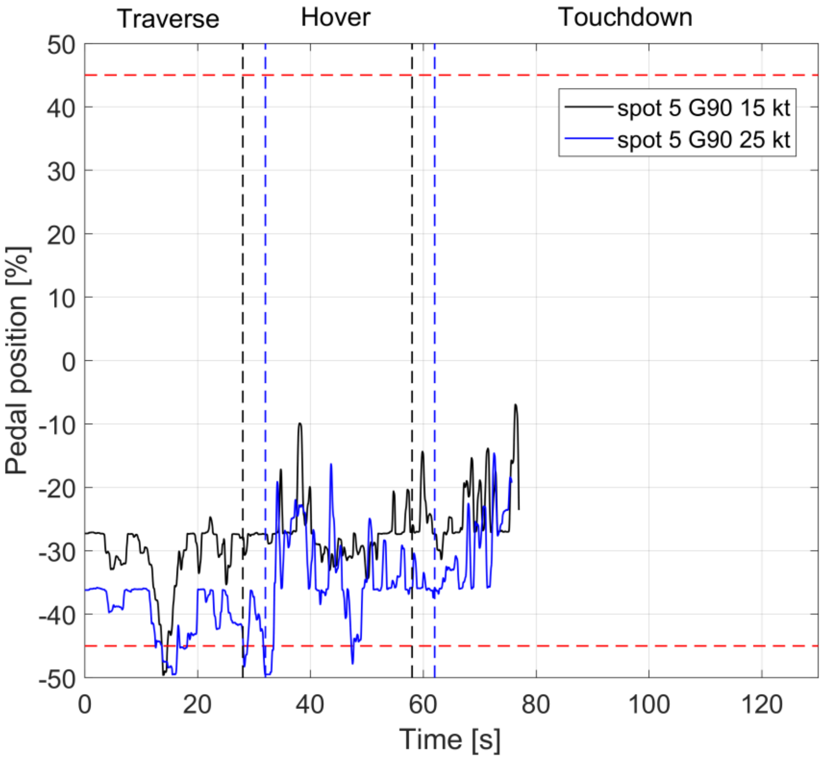

(a)

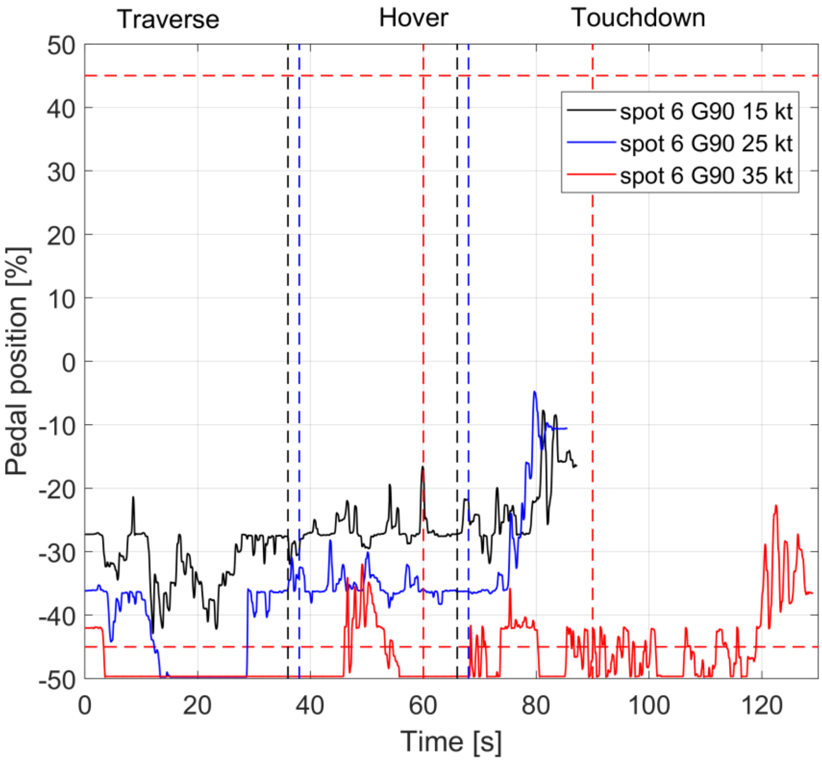

(b)

Figure 5-16 Pedal position in a Green 90 wind at spots 5 (a) and 6 (b).

5.3.5 Aircraft Position During Hover Task and Touchdown

The lateral and longitudinal position of the aircraft's centre of gravity during the hover and touchdown MTEs is shown in Figure 5-17 to Figure 5-19 for each WOD condition, they are a magnified of the congested final phase of the helicopter's positional scatter over the landing spot shown earlier in Figure 5-8 to Figure 5-10. In Figure 5-17 to Figure 5-19 a solid line is used to denote the position of the aircraft's centre of gravity during the hover MTE and a dotted line is used to show the position of the aircraft's centre of gravity during the touchdown MTE. The landing spots are marked on the ship's deck as the intersection of lines running fore/aft and port/starboard. Fore/aft lines for spots 5 and 6 are, respectively, at -18 m and +22 m, where the zero is the ship's centreline. The port/starboard line through both spots is -114 m, measured from the ship's centre of gravity. Pilots position themselves with these lines, but once in the hover position the spot cannot be seen. It should also be noted that the pilot sits about 3 m in front of the helicopter's centre of gravity; hence there is normally some variation in the aircraft's touchdown position, especially in the turbulent air flow.

Recommended limits for the amount of scatter during helicopter operations to single-spot and multi-spot RN ships are given in [149]. The deviation of the helicopter from the optimum flight path whilst positioning for landing or departing after take-off, known as airborne scatter, is determined by the rotor diameter of the helicopter. As the SH-60B aircraft has a rotor diameter about 15 m, and is operating to a multi-spot ship, the omnidirectional limit for airborne scatter is 3.5 m; this is shown in Figure 5-17 to Figure 5-19 as a solid green circle centred at the aircraft's centre of gravity. As the pilot positions themselves over the landing spot the aircraft's centre of gravity is aft of the landing spot.

Similarly, the landing scatter is determined by the helicopter's Maximum All Up Mass (MAUM) and defined as the deviation of the helicopter from the optimum flight path during the vertical phase of flight, which includes the descent manoeuvre post-hover during landing and climb manoeuvre pre-hover during take-off. The SH-60B operating to a multi-spot ship, having a MAUM in excess of 5400 kg, gives a landing scatter limit of 2.4 m. This is shown in Figure 5-17 to Figure 5-19 as a dashed green circle centred at the aircraft's centre of gravity relative to the pilot's seated position over the landing spot.

5.3.5.1 Ahead

Figure 5-17 shows the aircraft's position in an Ahead WOD. Over spots 5 and 6 at 25 kts there was little deviation from the chosen station-keeping hover position during the 30 second task and the descent. Over spot 5, even as the WOD speed was increased to 35 kts and 45 kts, although there are greater deviations in the longitudinal position, the pilot was still able to maintain an accurate horizontal position over the deck. At spot 5 the aircraft position was within both the airborne and landing scatter limits for 25 kts to 45 kts.

For spot 6 at the higher wind speeds, there is a greater deviation, particularly in the longitudinal axis. The large deviation in the 35 kts wind was not due to excessive workload, it was a corrective positioning manoeuvre by the pilot during the hover task, moving away from the spot, gaining situational awareness and then repositioning over spot 6. At spot 6 in each wind condition the aircraft's centre of gravity position was outside of the recommended RN airborne and landing scatter limits. At 25 kts the scatter is tightly clustered away from the nominal landing spot centre of gravity position, possibly indicating an issue with the pilot locating the landing spot.

5.3.5.2 Green 45

Figure 5-18 shows the aircraft's position during hover and touchdown MTEs over spots 5 and 6 in a Green 45 WOD. As the wind speed was increased from 15 kts to 25 kts, large deviations from the desired station-keeping position, both laterally and longitudinally, can be seen over both spots 5 and 6. At spot 5 in a 15 kts wind the aircraft's centre of gravity was within the airborne and landing scatter limits; however, as the wind speed increased to 25 kts the aircraft exceeded the limits. An increase in deviation can also be observed for spot 6 compared with spot 5 and the limits were exceeded for both wind speeds at spot 6.

5.3.5.3 Green 90

The Green 90 positions during hover and touchdown MTEs can be seen in Figure 5-19. The deviations from the desired station-keeping position are smaller than seen in the Green 45, with the exception of the 35 kts wind over spot 6 which, as mentioned previously, was outside of normal operational limits. Although the aircraft position was just beyond the airborne and landing scatter limits at spot 5, at spot 6 the aircraft far exceeded the respective scatter limits.

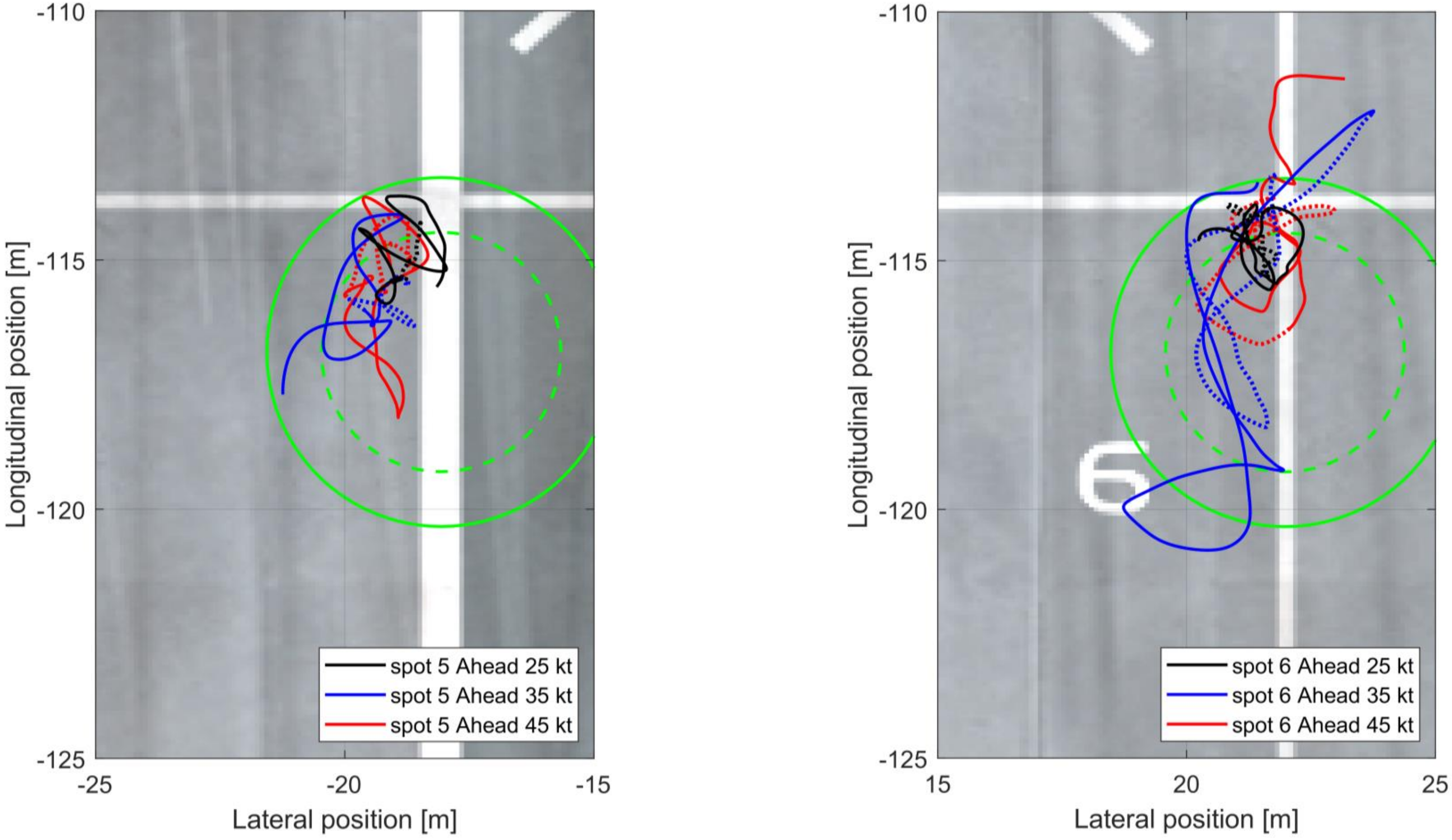

(a)

(b)

Figure 5-17 Helicopter position in hover (solid line) and descent (dotted line) in an Ahead wind at spots 5 (a) and 6 (b).

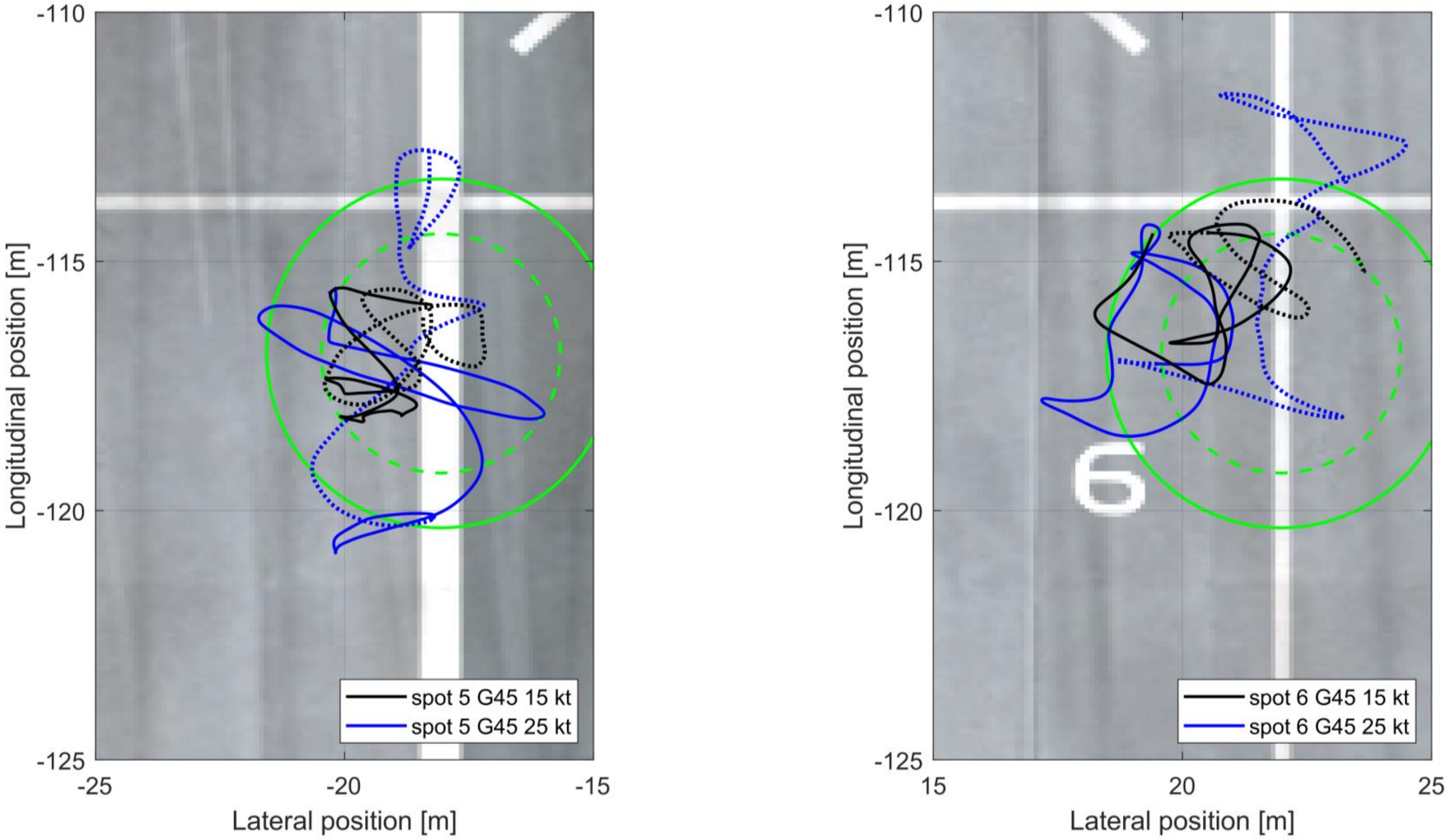

(a)

(b)

Figure 5-18 Helicopter position in hover (solid line) and descent (dotted line) in a Green 45 wind at spots 5 (a) and 6 (b).

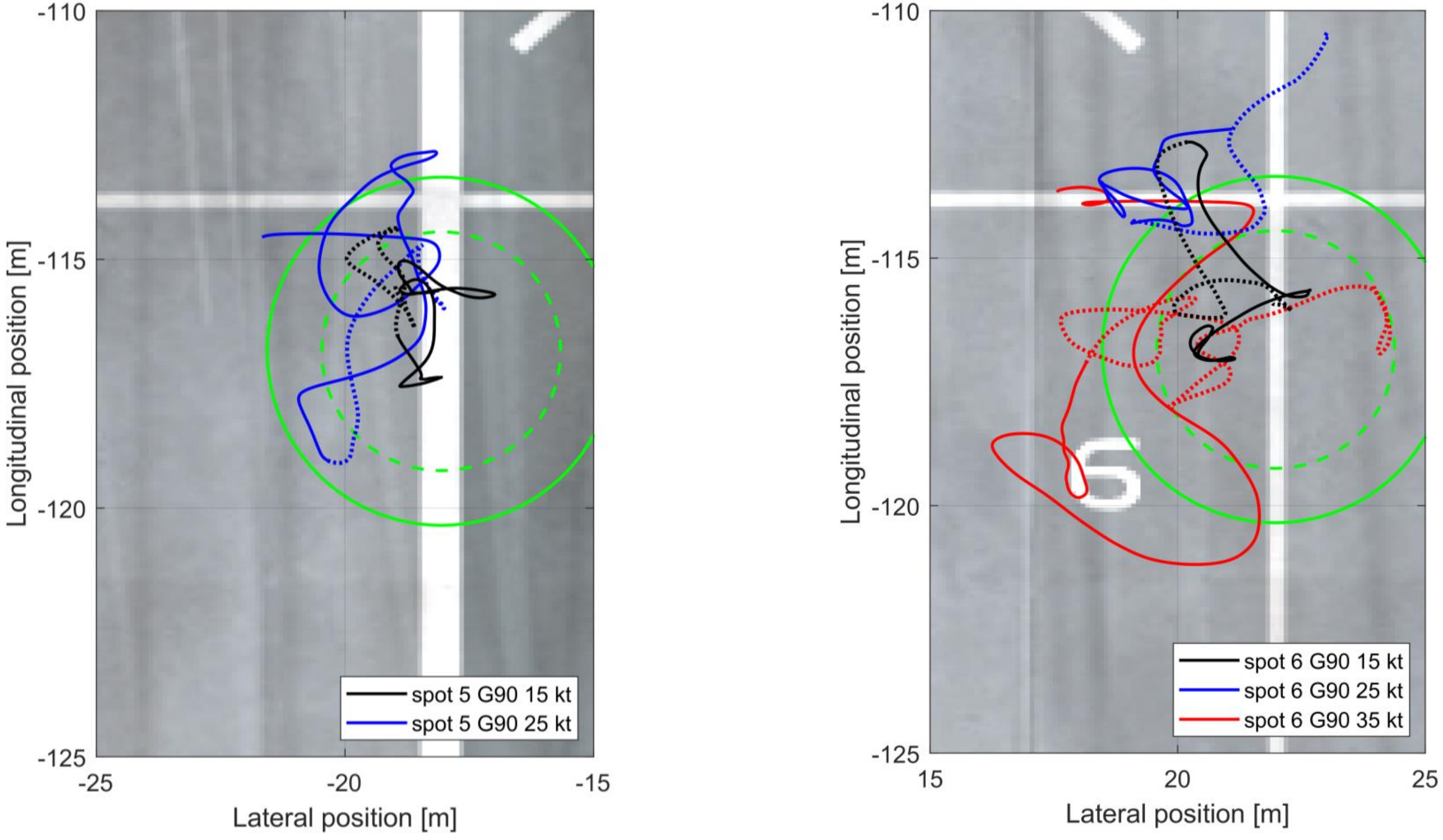

(a)

(b)

Figure 5-19 Helicopter position in hover (solid line) and descent (dotted line) in a Green 90 wind at spots 5 (a) and 6 (b).

5.3.6 Cyclic Control Activity During Hover Task

Figure 5-20 to Figure 5-22 to show the pilot's cyclic control activity during the hover task (MTE 2) where the pilot was asked to hold position for 30 seconds. The central graph shows the lateral/longitudinal cyclic displacement from the trim position, while the outer time-based graphs show how the lateral and longitudinal inputs changed with time. To highlight the maximum displacements from the trim position, a broken line box has been used to bound the edge of each data set.

5.3.6.1 Ahead

Results are shown for the lowest and highest wind speeds of 25 kts and 45 kts; data for 35 kts are omitted for clarity. Figure 5-20 shows little difference in the overall displacement of the cyclic from the trim position between spot 5 and 6 in a 25 kts Ahead WOD. As the WOD speed is increased to 45 kts an increase maximum displacement is seen from the trimmed cyclic position at spot 6 in comparison with spot 5.

5.3.6.2 Green 45

As the WOD moved around to Green 45, Figure 5-21 shows there was a significant increase in the maximum cyclic displacements from the trim position during the hover task, compared with the Ahead wind. There is greater activity in the displacements for the 25 kts WOD than the 15 kts on landing to spot 5 and spot 6.

5.3.6.3 Green 90

Figure 5-22 shows the cyclic inputs for 15 kts and 25 kts Green 90 WOD at spot 5, and at 15 kts and 35 kts at spot 6. An increase in the maximum displacement from the trim position can be seen for the higher wind speeds. At spot 6 in 35 kts, very large deviations from trim can be seen in cyclic activity.

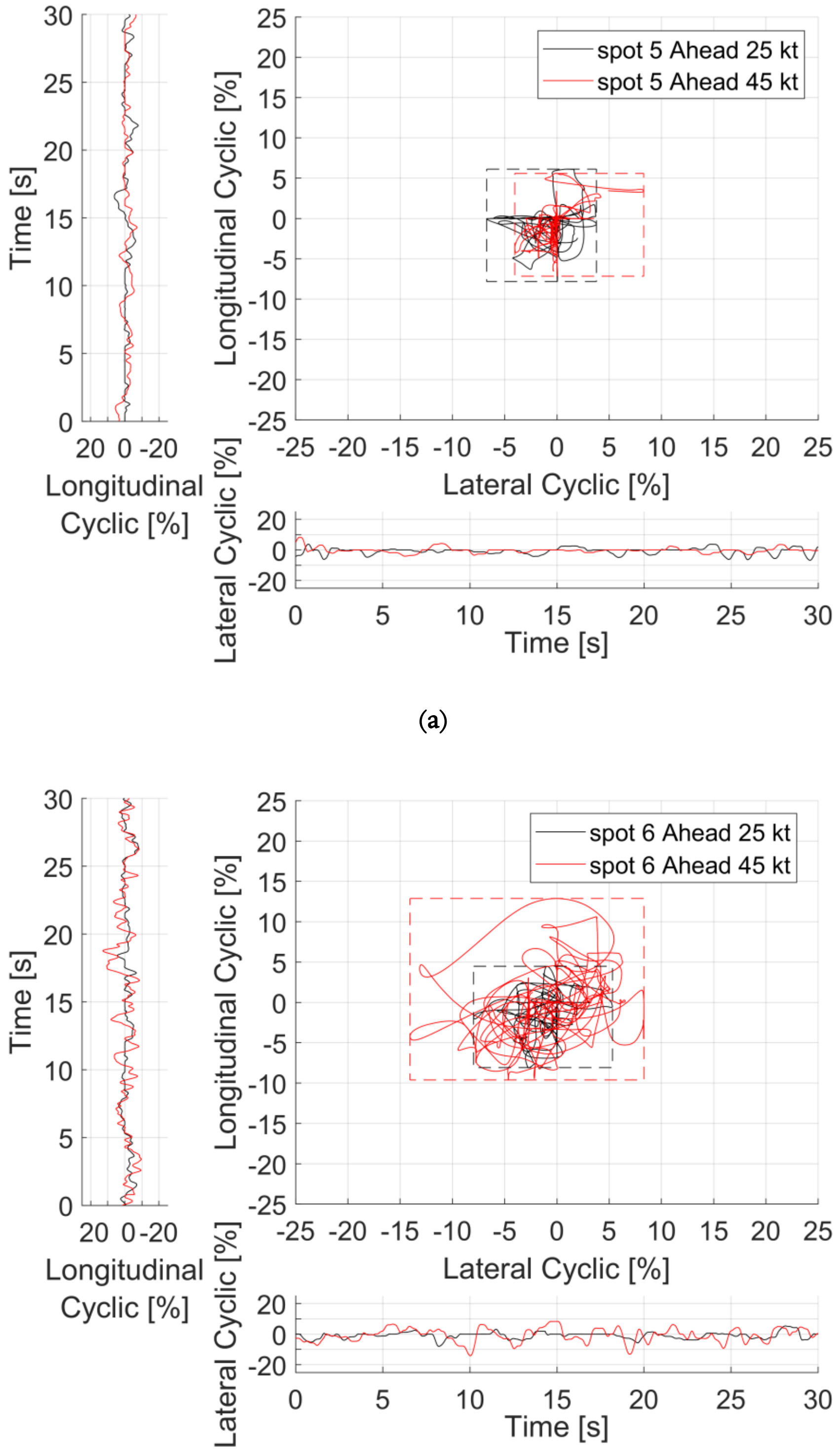

(a)

(b)

Figure 5-20 Longitudinal and lateral cyclic inputs during hover in an Ahead wind at spots 5 (a) and 6 (b).

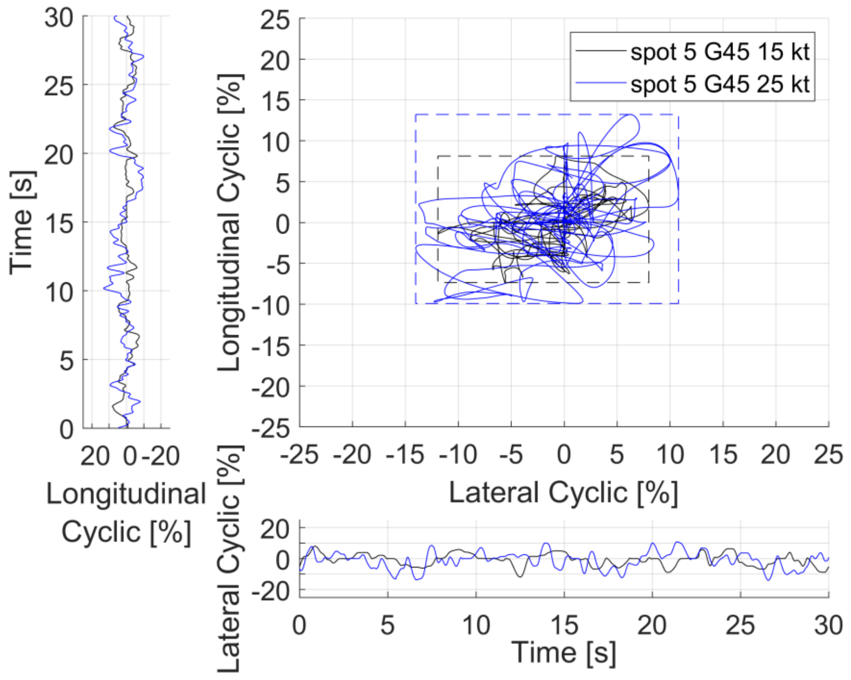

(a)

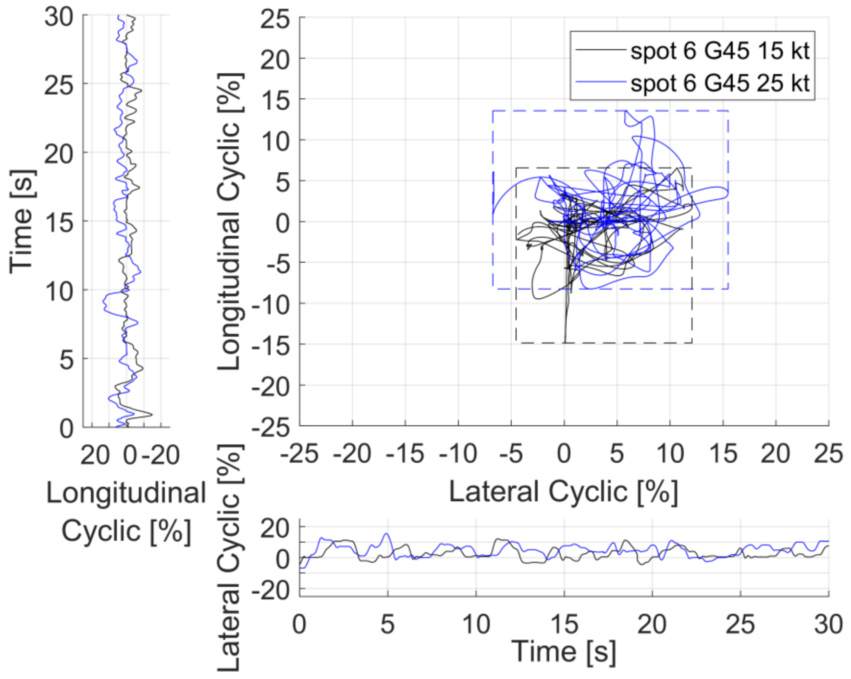

(b)

Figure 5-21 Longitudinal and lateral cyclic inputs during hover in a Green 45 wind at spots 5 (a) and 6 (b).

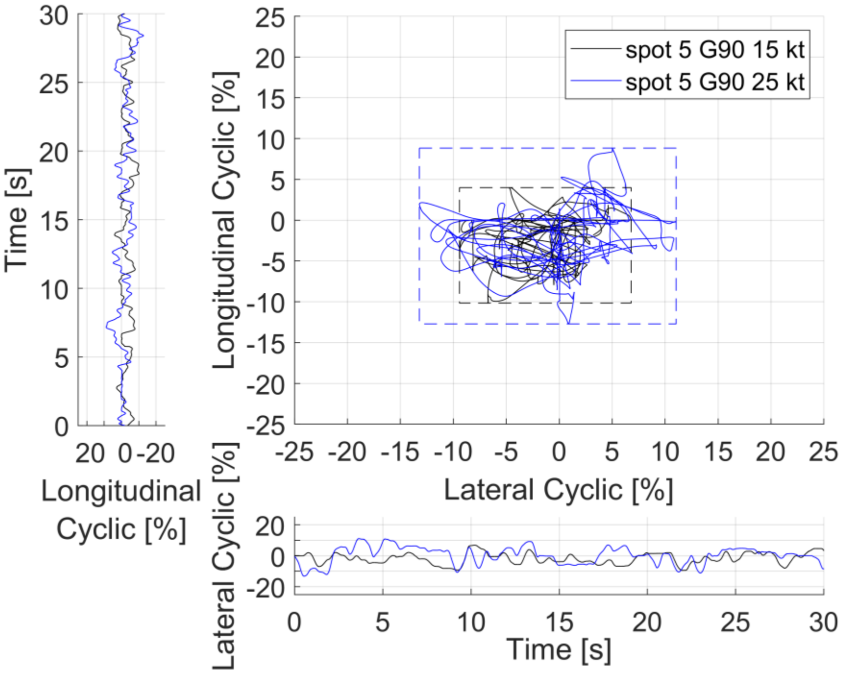

(a)

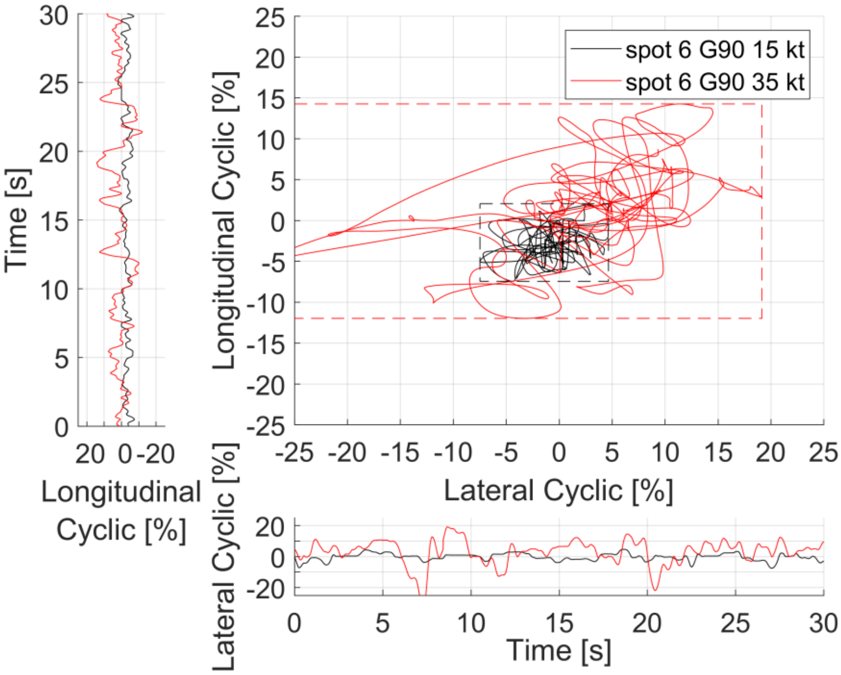

(b)

Figure 5-22 Longitudinal and lateral cyclic inputs during hover in a Green 90 wind at spots 5 (a) and 6 (b).

5.4 Piloted Simulation Flight Trial Discussion

A lot of data has been presented in the previous sections for the different aspects of control activity for different wind directions. This section seeks to coalesce the observations in the data for each wind direction.

5.4.1 Ahead

As expected from the low turbulence levels and undisturbed flow shown by the streamlines over spot 5 shown in Figure 4-41 in an Ahead wind, the Bedford workload for each mission task and DIPES ratings given by the pilot in Table 5-2 were relatively low. This is consistent with both the relative ease in maintaining the aircraft's position shown in Figure 5-8 (a) and Figure 5-17 (a) and the low level of pedal and cyclic activity by the pilot shown respectively in Figure 5-14 (a) and Figure 5-20 (a). Figure 4-41 shows spot 6 experiences higher airwake turbulence compared with spot 5, due to shedding of flow from the aft island, however, the flow disturbance didn't require high compensation by the pilot, consistent with the pilot's control inputs. Although the pilot had little to comment upon during the landings in an Ahead wind, hence the absence of DIPES suffixes in Table 5-2, it was commented that at spot 6 in winds stronger than 35 kts, turbulence could be felt. At 45 kts landing to spot 6, the pilot noted a greater angular displacement in heading compared with the 35 kts wind. The increase in Bedford workload and DIPES ratings at spot 6 corresponds to larger scatter in the longitudinal and vertical positions shown in Figure 5-8 (b) and Figure 5-17 (b); the associated control activity to stabilise on condition with the collective and pedal also increased (Figure 5-11 and Figure 5-14 (b)).

As the WOD speed is increased to 45 kts an increase in maximum displacement from the trimmed cyclic position is seen during hover at spot 6 that is not observed when in hover over spot 5, showing the larger effect wind speed has at spot 6. The airborne and landing scatter limits described above and defined in [149] were achieved for each condition at spot 5; at spot 6 in the higher winds the limit was exceeded due the corrective positioning manoeuvres made by the pilot.

5.4.2 Green 45

There is a significant increase in ratings for both spots in a Green 45 wind compared with an Ahead wind. In the forward-facing manoeuvre, the 45 deg wind presents a starboard oblique wind to the helicopter so increasing requirement for pedal input to control yaw, and lateral cyclic to overcome the crosswind component.

Referring to the CFD images in Figure 4-42 (b) for Green 45, it can be seen that neither landing spot is fully immersed in the turbulent airwake of the aft island, although turbulence from the aft vertical corner of the island will be shed across spot 5. Therefore, each spot, and the lateral translation paths, are in air flow that will not have been slowed by the blockage presented by the islands, hence the pilot's difficulty in maintaining heading. The aircraft will also experience turbulence and steep velocity gradients due to the shear layer formed by the air shedding from the starboard edge of the deck.

On landing to spot 5 in a 15 kts wind, the pilot was able to maintain low scatter during station-keeping but commented that although there was minor displacement in aircraft positioning the workload was consistent across the MTEs. The aircraft positioning is shown in Figure 5-9 (a) and is reflected in the DIPES rating of 2 given by the pilot. The pilot gave several causes for this increased workload: Yaw control (Y), Height control (H), Turbulence (T), Forward/Aft positioning (F) and Lateral positioning (L).

With an increase in WOD speed from 15 kts to 25 kts the workload and DIPES ratings increased on landing to spot 5. The causes of the DIPES rating for the 25 kts WOD were the same as for the 15 kts WOD. The pilot commented that the workload was consistent throughout with random disturbances felt; the deck motion was noticed but the majority of the pilot's attention was focussed on compensating for the turbulent fluctuations, due the steep velocity gradients due the shedding of the flow from the aft island. High activity in each control was reported with a large positional displacement, requiring considerable focus on the primary task. The difficulty in controlling the flight path and in maintaining a stable hover position, particularly in the 25 kts wind, is visible in Figure 5-9 (a) and, is consistent with the pilot ratings in Table 5-3 and the scatter limits in Figure 5-18 (a). The pilot also noted being close to the pedal limits during the task; it can be seen from the pedal activity that in a 25 kts wind, the pedal limits were exceeded momentarily several times, due to the strong lateral wind component relative to the aircraft as shown in Figure 4-42 (b). There was greater activity in the cyclic displacements for the 25 kts WOD than the 15 kts, consistent with the respective workload ratings of 4 and 6 given for hover over spot 5 in Table 5-3.

On landing to spot 6 in a 15 kts wind the workload ratings in the hover (MTE 2) increased from those given for the same task in the same wind over spot 5, as did the DIPES rating. The pilot commented that the DIPES rating was awarded due to the difficulty in translating across the deck caused by the turbulence over spot 6 being noticeably higher with random hover displacement also reported, which is consistent with the pilot's control inputs. The DIPES suffixes given were due to the same causes as those over spot 5 with the addition of Visual Cues (V), due to the aft island limiting the pilot's view of a fixed horizon, thereby affecting the pilot's ability to judge the ship's motion. The pilot also reported that turbulence over spot 6 abated a little and that as the aircraft descended vertically to land the turbulence changed with a noticeable increase in turbulence around one metre above deck, which will be due to the air flow separating from the landing deck horizontal edge.

With an increase of WOD from 15 kts to 25 kts for landings to spot 6, a large increase in workload was also experienced. Ratings in the hover and landing tasks increased to values such that the workload was no longer tolerable for the task; this was also reflected in the increased DIPES rating. An increase in wind speed from 15 kts to 25 kts for landings to spot 6 also corresponds with an increase in collective control activity and torque shown in Figure 5-12. The pilot commented that at 25 kts, on crossing the deck, the aircraft suddenly descended, due to the unsteady flow shedding from the aft island, and that on correction with a collective input the pilot reached the max continuous torque; Figure 5-12 shows this excursion over 100%.

Table 5-3 shows that the highest workload rating was given in a Green 45 WOD during touchdown at spot 6 in a 25 kts WOD, which corresponds with a large deviation from the desired longitudinal and lateral position during the descent to touchdown. The range of DIPES suffixes given were as seen in the 15 kts wind with the addition of Torque/Engine control (Q). It can also be seen that the final touchdown MTE took longer to execute in the higher wind speed, showing the additional time required by the pilot to complete the task. There was also increased pedal activity as seen in Figure 5-15 (b) which shows the 10 % control margin was exceeded during the lateral translation and hover, with one occurrence hitting the pedal limit for over 5 seconds to overcome the crosswind component during translation across the deck to spot 6. For spot 6 there was a corresponding increase in workload during hover from a rating of 5 to 7 as the wind speed increased from 15 kts to 25 kts; these higher workload ratings are again consistent with the increased cyclic activity for spot 6 seen in Figure 5-21 (b).

5.4.3 Green 90

Referring to the CFD image in Figure 4-42 (c) it can be seen that in the 90 deg wind there is a significant level of turbulence in the horizontal plane 10 m above the deck. During the lateral translation, and over spot 5, turbulence is in the region of 20-30 %, with significant velocity gradients caused by the flow separating from the starboard deck-edge. Landing to spot 5 in a 15 kts Green 90 WOD showed a reduction in overall workload compared with the 15 kts Green 45 WOD. No DIPES suffixes were given, reflecting the low workload at this condition.

At 25 kts Green 90 WOD there was an increase in workload ratings across all MTEs when landing to spot 5. The pilot commented that sharp gusts, turbulence and erratic disturbances were experienced due to the steep velocity gradients due to the shear layer formed by the air shedding from the starboard edge of the deck., leading to acceptance by the pilot of greater deck landing scatter. Significantly, the pilot also found it difficult to maintain heading in the crosswind and exceeded the pedal control limits on a number of occasions shown in Figure 5-16 (a), hence the higher DIPES rating in Table 5-4. Causes of the DIPES ratings were reported due to Yaw control (Y), Turbulence (T), Forward/Aft positioning (F) and Lateral positioning (L) and, as the pedal limit was reached, a DIPES of 4 was awarded for the overall landing. The difficulty in maintaining heading in the gusting side wind is consistent with the aerodynamic performance envelope of the aircraft which states that the sideward/rearward flight limit is 35 kts [150]. The pilot's cyclic activity was consistent with the Bedford workload ratings in Table 5-4 with an increase from a rating of 3 at 15 kts to a rating of 4 at 25 kts for spot 5. The reduced deviation of aircraft position during hover and touchdown at 15 kts and 25 kts compared with the Green 45 case is consistent with the cyclic and pedal activity for this wind direction and shows that the pilot was able to hold position, while at the same time concentrating on heading control due to the lack of pedal authority in the resulting crosswind.

Over spot 6 the turbulence level at hover height is less than 5% but increases towards the deck due the shear layer formed in the air flow separating from the deck edge. There was little change in workload ratings given on landing to spot 6 in a 15 kts Green 90 WOD compared with those given at spot 5 for the same conditions. A difference was only seen in the DIPES suffixes given by the pilot which included Yaw control (Y) and Forward/aft positioning (F). The pilot commented that heading accuracy was reduced with a difficult aircraft roll to account for due to the wind; a large lateral pedal input was also required to maintain heading.

With an increase of WOD speed from 15 kts to 25 kts on landing to spot 6 an increase in workload was seen, with the highest Bedford workload rating, a value of 5, awarded during landing (MTE 3). During this landing task the pilot was unable to maintain heading and the pedal limits were exceeded for 10 seconds during the lateral translation to spot 6 in the 25 kts wind as shown in Figure 5-16 (b), which is consistent with the high turbulence near the deck from the shear layer caused by shedding from the starboard side. The pilot commented that as the spot was behind the ship's aft island it was difficult to judge the deck motion due to a lack of horizon references. The pilot also commented that no lateral eddies were felt over the spot during the hover. The control activity data and aircraft position are consistent with the DIPES ratings awarded in Table 5-4, where in the 25 kts wind the pilot awarded a DIPES of 4 because the 10% control margin limits were exceeded and heading accuracy could not be maintained. The causes of the DIPES rating were attributed to Yaw control (Y), Turbulence (T), Forward/aft positioning (F), Lateral positioning (L) and Pitch control (P). Comparing the pilot ratings in the 25 kts Green

45 and 90 winds, conducting the landing task required less workload in the 90 deg wind, due to lower turbulence, but was awarded a higher DIPES due to the erosion of yaw pedal margin which, again, is consistent with the aircraft's aerodynamic performance referred to above.

On landing to spot 6 in a 35 kts Green 90 WOD the workload and DIPES ratings show an excessive and intolerable workload for a fleet pilot. Sharp gusts were experienced, causing significant loss of positional accuracy, and were compensated for by the pilot adopting a higher hover altitude. Additional causes of the DIPES in comparison to the 25 kts wind included Attitude control (A) and Visual cues (V). For much of the landing manoeuvre the pedal was against the limit and is the reason why the pilot had to abandon the requirement to maintain a forward-facing heading and instead adopt a 40 deg heading into wind (again consistent with the aircraft's aerodynamic envelope). Figure 5-23 shows the helicopter's heading throughout the entire landing manoeuvre. The time histories are split by vertical dashed lines showing the three MTEs: lateral translation, hover and touchdown. During the lateral translational phase in the 35 kts wind the pilot need to point the aircraft 40 deg into the wind to execute the MTE. While heading was recovered somewhat during the hover and landing MTEs, it can be seen that the aircraft still experienced a heading of up to 10 deg during the landing MTE.

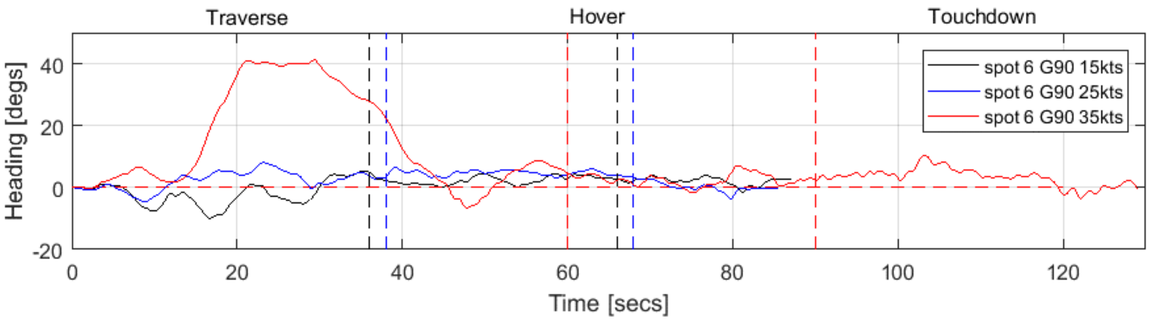

Figure 5-23 Helicopter heading in a Green 90 wind at spot 6.

Although the landing was completed and a DIPES 5 awarded, since the pilot was unable to maintain heading during the traverse the landing should, in reality, have been aborted. Figure 5-13 shows that the pilot's control activity in collective during the landing task in the Green 90 winds were lower than those seen in the Green 45 winds, consistent with the data shown above for the helicopter position during the landing task. However, as shown in Figure 5-23, the pilot was only able to hold position by pointing into the wind and ran out of pedal authority, hence the high DIPES rating in Table 5-4.

5.5 Aerodynamic Modelling of a Generic Fixed-wing STOVL Aircraft

This chapter has described the integration of a rotorcraft flight dynamics model with the unsteady velocities of QEC airwakes, computed using CFD, to conduct helicopter deck landings. A significant component of the workload encountered by the helicopter pilot in the simulator was due to the unsteady moments created by the non-uniform distribution of the airwake velocities across the aircraft. As described in Section 5.1, when the pilot 'flies' the aircraft in the simulator, the velocity components from the CFD airwake solution are applied in real-time to ACPs that are distributed along the individual blades of the main rotor, around the fuselage and at the tail rotor, as shown earlier in Figure 5-4. The judiciously placed ACPs enable the velocity field to influence the flight dynamics model and creates a more realistic flying experience for the pilot during simulated deck landings [17, 151].

Flight dynamics models for fixed-wing flight simulation also use look-up tables of airwake velocity components to create the forces generated by the aerodynamic surfaces. Usually these are based on a single angle-of-attack value for all points on the airframe [152]. The angle-of-attack is typically computed at a single location, the centre of gravity, where the air velocity components at that point are applied. Although moments may be generated by the inherent aerodynamic and stability characteristics of the aircraft, the model will ignore any velocity differentials across the lifting surfaces. While such an approach is suitable for a fixed-wing aircraft flying at typical cruise speeds, it will not be suitable for carrier-borne aircraft such as STOVL aircraft hovering in an unsteady three-dimensional air flow due to the ship's airwake.

Due to the expressed interest of the industrial sponsor in the complex interactions of the unsteady airwake produced by the ship on a fixed-wing aircraft, an aerodynamic model was developed based on generic Advanced STOVL (ASTOVL) aircraft using a modified strip theory. The model has then been subjected to unsteady airwakes produced by the QEC carrier to assess the effect of the airwake on the generic STOVL aircraft model. The development of the model and the analysis of the effect of QEC airwakes on the model are given in Appendix A.

5.6 Chapter Summary

This chapter has described how flight simulation has been used to investigate helicopter recovery operations to the deck of HMS Queen Elizabeth. A helicopter flight simulation environment has been developed, in which the unsteady airflow velocities present over a ship have been integrated with the flight dynamics model. The unsteady air flow over the ship was generated using the CFD method detailed in Chapter 3. A six degree-of-freedom motion flight simulator was used to conduct real-time piloted deck landings, where a helicopter flight dynamics model representative of a Sikorsky SH-60B Seahawk helicopter was recovered to the designated rotorcraft landing spots towards the stern of the ship. A test pilot was instructed to land the helicopter and to give workload ratings for the difficulty of the task when flying in relative winds from Ahead, and 45 deg and 90 deg from starboard. The workload ratings, along with the corresponding pilot control activity and helicopter positional accuracy, have been discussed in relation to the air flow to which the helicopter was subjected. The chapter demonstrates how flight simulation could be used to support flight trials and helicopter clearance activities. Characteristics flow features and disturbances of the ship airwake at different WOD conditions were felt by the pilot during recovery to the ship and shown in the pilot's control inputs. By computing the airwakes for individual ships and integrating the airwake velocities with a suitable rotorcraft flight dynamic model in a flight simulation environment, simulated piloted trials, such as the one described in this chapter, may be used to augment at sea flight trials, to interrogate certain WOD conditions, or to aid in ship design. It is, however, of note that real-world trials data is needed to compare with the simulations before the techniques can be beneficially deployed.

Chapter 6

Virtual Airdyn Analysis of the QEC Carrier Airwake

The development and highly successful application of the F-35B/QEC simulator at BAE Systems has shown that flight simulation can make a very significant contribution to the planning and execution of FOCFTs. While the simulated helicopter flight trials described in Chapter 5 were not used to inform the actual helicopter/QEC FOCFTs, their potential to do so has been demonstrated. The benefits of piloted flight simulation over FOCFTs is that they are substantially less expensive, they are not constrained by the weather conditions present during the trial period and test points can be repeated. As with the F-35B/QEC trials, it is not expected that the simulations will replace the FOCFTs, but they can have an important role in preparing for them and in understanding the results of the flight trials. However, while piloted simulation has its advantages, there are other simulation technologies, particularly for helicopter deck landings, being developed that do not involve a human pilot. The techniques are being developed to inform FOCFTs and to also assess the effect of ship superstructure design on the airwake and the ship's aircraft. These techniques involve using a flight dynamics model of an aircraft that flies through an airwake to the deck and is controlled either by an autopilot [153], or a model of a human pilot [154, 155].

One particular technique, that has been developed at UoL, is known as the Virtual AirDyn (VAD) [71]. The VAD uses the same FLIGHTLAB model of the Seahawk described in Section 5.1 but in this case the simulated helicopter is held stationary at various locations in the airwake to evaluate the unsteady aerodynamic loads imposed onto it by the airwake. A more complete description will be given in the following section.

A study was, therefore, conducted in which the VAD was used to provide an additional assessment of the effect of the airwake on a helicopter, and the results were then compared with the piloted flight trials in the HELIFLIGHT-R simulator. The trials were carried out for spots 1 to 5 for a Green 25 WOD. The purpose of the study, as well as gaining useful information on how the VAD analysis compares with piloted flight simulation, was to characterise the airwake over the deck of the QEC carriers to assess the effect of the twin islands on the flying environment over the deck.

6.1 The Virtual AirDyn

While the CFD results can give information on the unsteady air flow and steep velocity gradients in which the helicopter will operate, it is more important to understand how this will affect aircraft operating within the ship's airwake. During simulation piloted trials used to create SHOLs for different ships, it was observed that the helicopter loads and pilot workload was different for different ships [8]. To measure the effect of the unsteady loads imparted on a helicopter in an airwake a physical instrument called the Airwake Dynamometer, or AirDyn, was developed [23, 156]. The AirDyn consisted of a Merlin helicopter 1:54 scale-model with a motor driven rotor mounted on a six-axis force block, suspended over the flight deck of a ship, which was submerged in a large water tank similar to that described in Chapter 2. Immersed in the wake of the ship, the AirDyn was capable of measuring the unsteady loads imparted on the aircraft by the flow. Several experiments were conducted using the AirDyn as a tool to modify the ship geometry to provide better air flow conditions for the aircraft and pilot [18, 24].

The concurrent research into the integration of the CFD airwakes with flight dynamics models for flight simulation, and the AirDyn experiments, led to the development of the VAD, wherein the experimental helicopter was replaced by a helicopter flight model immersed in a simulated (CFD) airwake [71]. The VAD measures the impact of an unsteady airwake on a helicopter by integrating the unsteady velocity components with a helicopter flight dynamics model. For the helicopter model to be subjected to the effect of the ship's airwake in both piloted flight simulations and the VAD, the unsteady airwake velocities generated by CFD are imposed on the aircraft flight dynamics model at various locations on the rotor blades and airframe within FLIGHTLAB. In the previous chapter, Figure 5-4 shows schematically how the raw data produced in CFD is processed to enable the unsteady components of velocity in the ship's airwake to be applied to the flight dynamics model of the aircraft described in Section 5.2; the same method of integration is used in the VAD.

During real-time piloted simulations, the time-varying velocities in the airwake will produce unsteady forces and moments through the helicopter's flight dynamics model that will cause the aircraft to deviate from the trim condition, requiring the pilot to compensate for these disturbances through movement of the helicopter's controls. The helicopter model in the VAD is first trimmed in the prevailing freestream condition and then placed at a selected point in the airwake and fixed in that position. Since the helicopter is held at a fixed location, when the unsteady airwake velocities are applied, it will experience time-varying non-zero forces and moments. These forces and moments are recorded by the VAD over a selected time period. The thrust, side-force and drag forces align with the aircraft airframe as shown in Figure 5-2; similarly, the pitch, roll and yaw moments are defined around the aircraft's centre of gravity.

The resulting unsteady loads are created over a wide range of frequencies; however, it is known that loads in the range 0.2 to 2 Hz are the main contributors to pilot workload [125]. This range is known as the pilot closed-loop response frequency range; at disturbance frequencies within this range the pilot will respond to (compensate) with stick/pedal inputs. At frequencies much below this range disturbances will be 'quasi-steady' and manifest themselves as a drift which needs to be trimmed-out before resulting in large displacements. Frequencies above 2 Hz are experienced as vibrations through the airframe that will mainly impact ride quality.

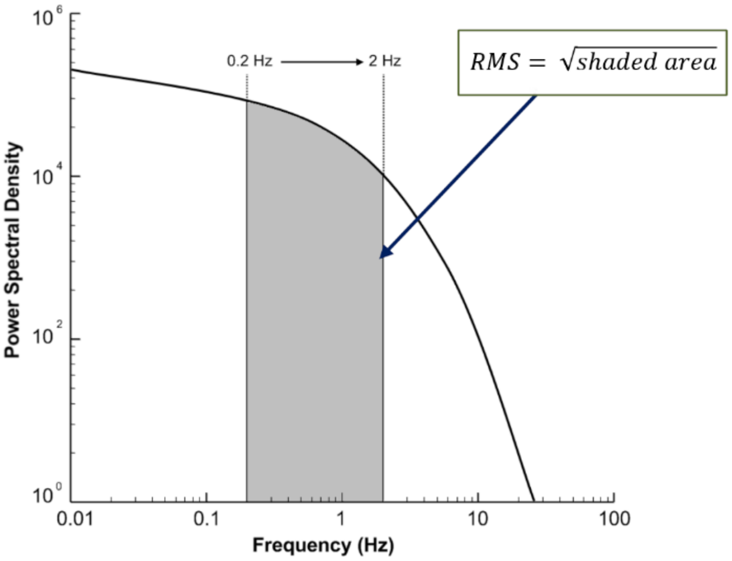

Figure 6-1 Method for calculating RMS forces and moments acting on helicopter flight dynamics model.

At each hover position, the root mean square (RMS) value in the three unsteady forces and moments are computed over the pilot's closed-loop response frequency range of 0.2 to 2 Hz by calculating the Power Spectral Density (PSD) plot of each time history and calculating the square root of the integral between the upper and lower bounds; this process is illustrated schematically in Figure 6-1.

Without the requirement of real-time control inputs from a pilot performing a task, the VAD provides a quantitative measure of the impact on the helicopter forces and moments from the ship's airwake. Previous research at UoL has employed the VAD for investigating the effect of a ship's superstructure design on helicopter handling qualities and pilot workload and for evaluating and comparing different ship designs [71].

6.2 **The QEC Green 25 Airwake**

The Green 25 WOD airwake was selected as the VAD study case detailed in this chapter to investigate how the two islands on the starboard side of the QEC affect the air flow over the flight deck when the wind comes obliquely from starboard, creating a turbulent air flow over the flight deck, and how it will impact a helicopter during a deck landing. The QEC airwake was generated using the CFD method detailed in Section 3.5.

6.2.1 CFD Analysis

To provide an understanding of the overall air flow over the landing deck, an examination of the CFD generated Green 25 QEC airwake was conducted prior to the investigation using the VAD and piloted flight simulation. Figure 6-2 shows the vortical structures in the CFD-generated airwake for a Green 25 WOD condition, using the *Q*-criterion vortex identification method, as iso-surfaces coloured by instantaneous streamwise *u*-velocity. Also shown in Figure 6-2 are the five landing spots along the port side of the ship and spot 6 behind the aft island (shown as black dots on the deck). It can be seen that in Green 25, landing spots 2 to 6, along the deck, are in mainly disturbed air flow. Figure 6-3 to Figure 6-5, further show the turbulent wakes from the islands in the Green 25 WOD. In Figure 6-3 the airwake in a Green 25 wind is illustrated in terms of turbulence intensities in vertical planes aligned with the 25 deg wind direction passing through landing spots 1 to 5. Figure 6-3 (a) shows a low turbulence intensity at the rotor hover position over spot 1, but in Figure 6-3 (b-d) the turbulence generated by the islands can be seen to encroach on the areas over landing spots 2 to 5. The CFD images also show the location of the SH-60B helicopter main rotor for a hover position above landing spots 1 to 5. The rotor height above the deck is 10 m, approximately the height the pilot holds the aircraft above the landing spot before descending to the deck to land.

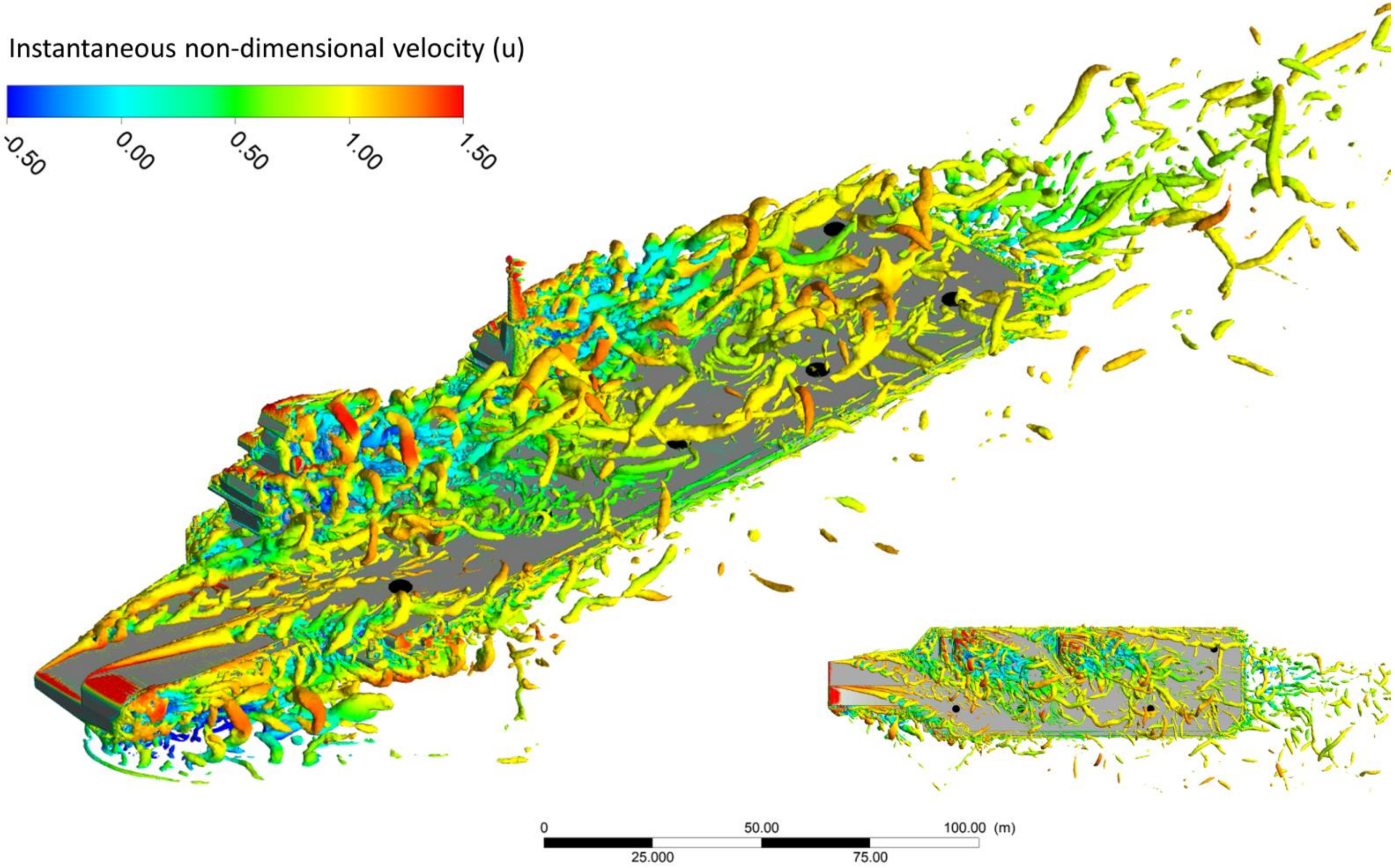

Figure 6-2 Green 25 flow over QEC model presented as instantaneous iso-surfaces of Q-criterion coloured by *u*-velocity.

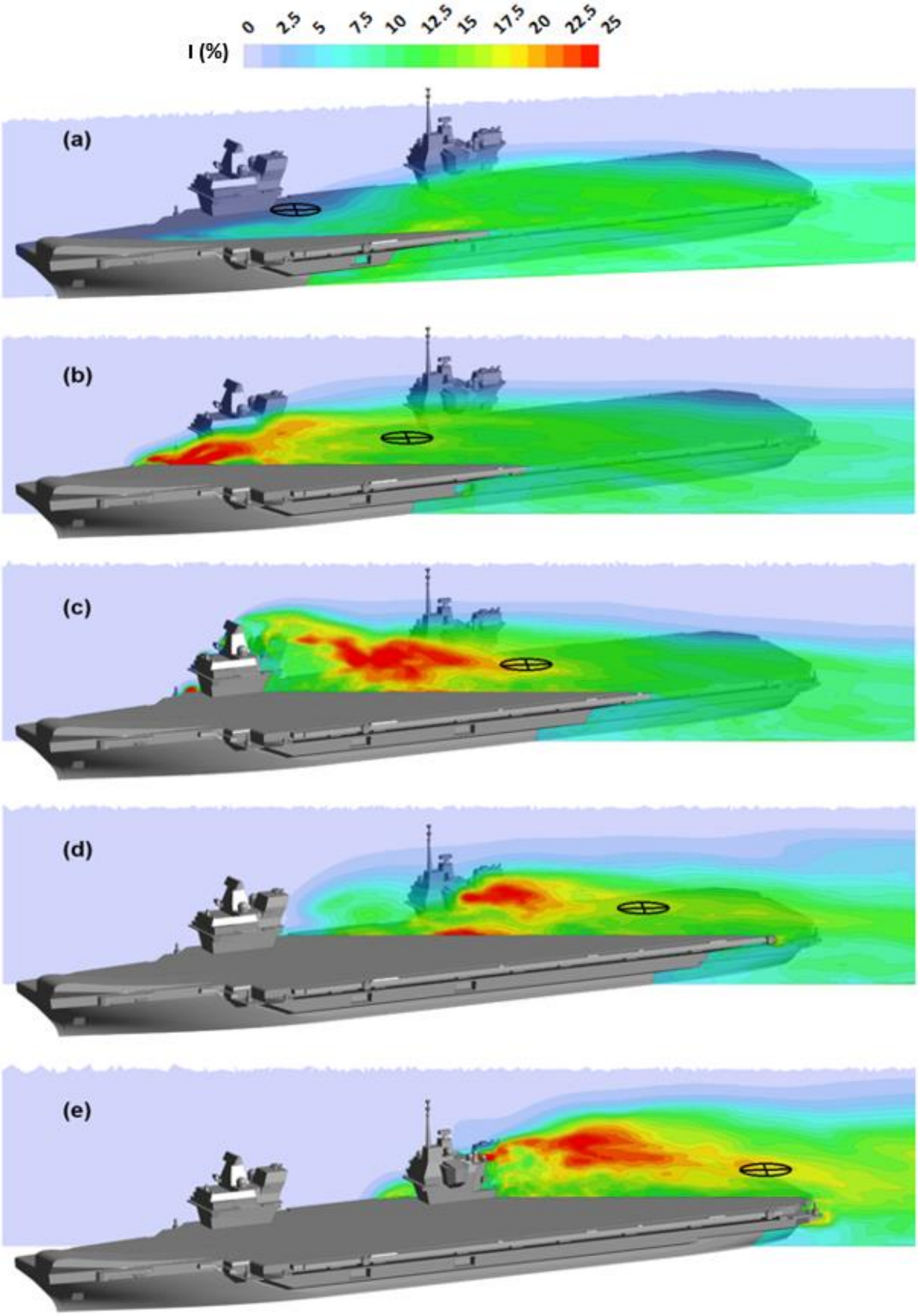

Figure 6-3 Ship airwake visualised as contours of mean turbulence intensity in streamwise vertical planes through landing spots 1 to 5.

Figure 6-4 shows the total non-dimensional velocity averaged over a 30 second sampling period in a horizontal plane at the 10 m hover height; streamlines in the horizontal plane are also included showing the direction of the flow. It can be seen that the flow velocity at spot 1 is largely unaffected by the ship's superstructure while spots 2 to 5 are within the wake of the two islands and show a large reduction and variability in velocity compared with the freestream flow.

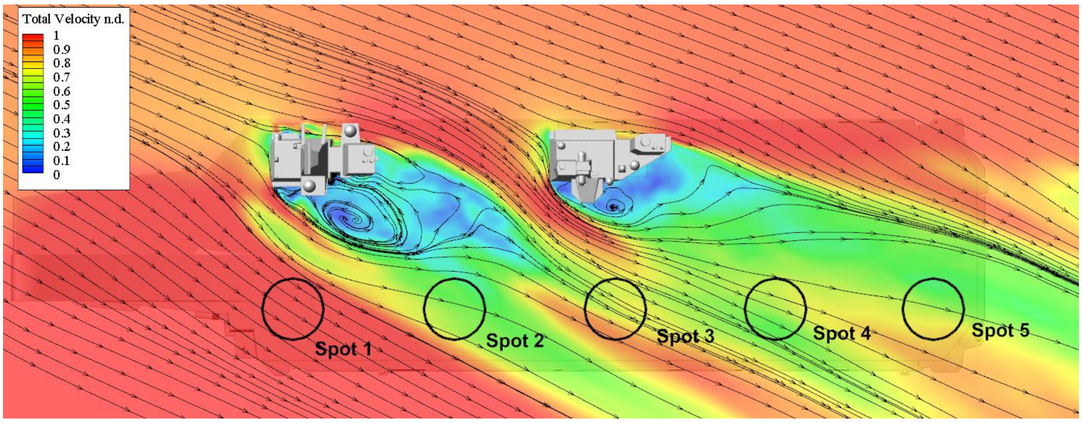

Figure 6-4 Mean total non-dimensional velocity in a horizontal plane at 10 m hover height.

Figure 6-5 shows the turbulence intensity in the 10 m horizontal plane. Again, spots 2 to 5 are in turbulent air flow; the turbulence varies between spots, and across the rotor disc, but are generally in the region of 15% to 20%. The two islands, and the gap between them, affect the air speed and turbulence over each landing spot, both of which will affect the aerodynamic loads on the helicopter, and hence the pilot workload; these two aspects were investigated separately in this chapter.

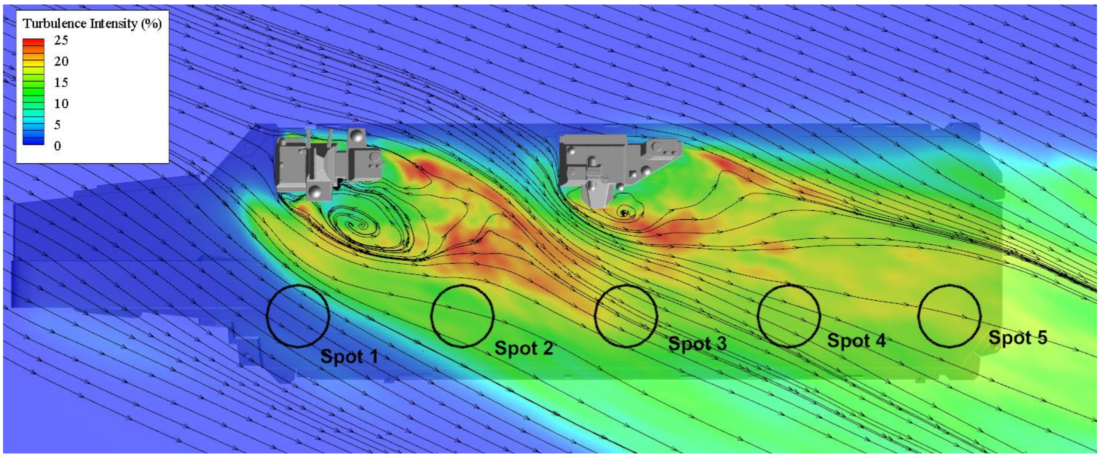

Figure 6-5 Mean turbulence intensity in a horizontal plane at 10 m hover height.

6.2.2 QEC VAD Analysis

The effect of a Green 25 airwake on a helicopter's forces and moments during hover above each of the landing spots was investigated using the VAD. The same FLIGHTLAB generic rotorcraft flight dynamics model configured to be representative of the Sikorsky SH-60B Seahawk, as described, and used in Chapter 5, was integrated with the QEC Green 25 airwake [141]. The helicopter model in the VAD was placed over landing spots 1 to 5 for 30 seconds and the forces and moments acting on the aircraft were recorded. Figure 6-6 shows an example of the down-sampled u and v velocity components from the QEC Green 25 airwake at points 10 m above spots 1 and 2. Off-line comparison of the data in Figure 6-6 with the original 100 Hz data showed insignificant differences. It can also be seen in the figure that the velocity components at spot 1, which is not within the wake of the islands, show a higher mean and much lower fluctuations in both velocity components compared with spot 2, consistent with the data shown in Figure 6-2 and Figure 6-5.

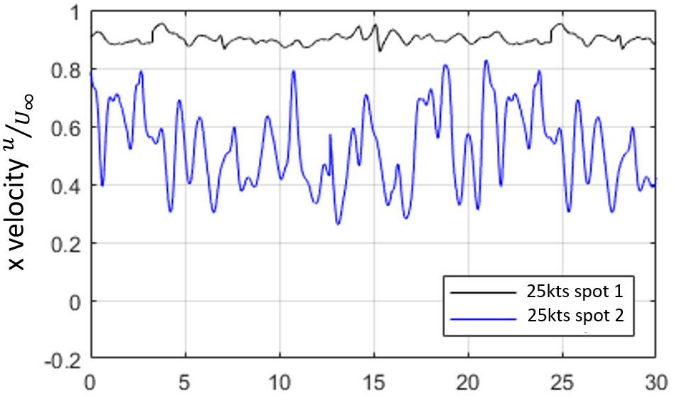

(a)

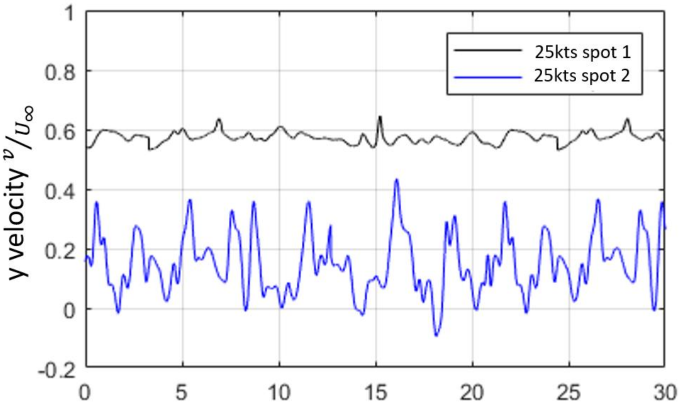

(b)

Figure 6-6 Airwake *u*-velocity (a) and *v*-velocity (b) components at points 10 m above spots 1 and 2 height.

An example of the unsteady thrust force (*Fz*) computed at the helicopter's centre-of-gravity during hover at spots 1 and 2 in a 25 kts Green 25 WOD condition is shown in Figure 6-7. The time-history of spot 2 in Figure 6-7 shows a larger deviation from the mean thrust in comparison with spot 1 over the 30 second time period; this is reflected in the PSD plot in Figure 6-8 which shows that the power at spot 2 is higher compared with spot 1 throughout the frequency range. The two dashed red lines in Figure 6-8 show the pilot's closed-loop response frequency range between 0.2 and 2 Hz, used as boundaries to calculate the area beneath each curve giving an RMS force value at spots 1 and 2 of 0.5 kN and 1.7 kN respectively. The higher RMS loads over spot 2 is consistent with the higher turbulence in the CFD results in Section 6.2.1.

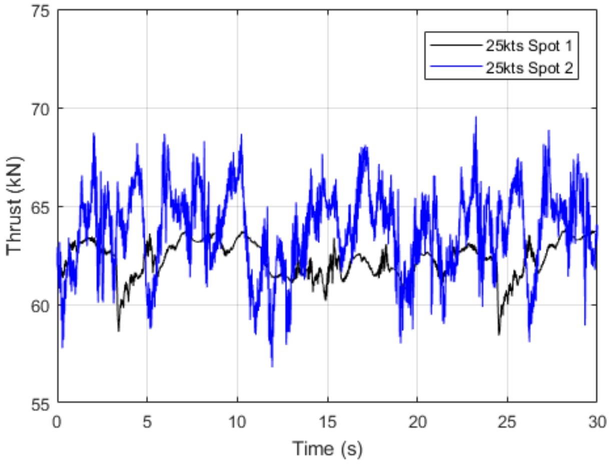

Figure 6-7 Unsteady thrust computed by Virtual AirDyn at spots 1 and 2 in 25 kts Green 25.

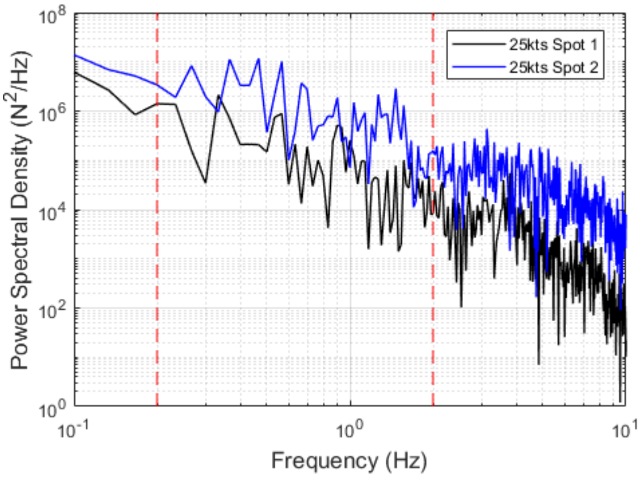

Figure 6-8 PSD of thrust computed by Virtual AirDyn at spots 1 and 2 in 25 kts Green 25 WOD.

Figure 6-9 shows the RMS value for each force calculated over the pilot's closed-loop response frequency range at spots 1 to 5 in a Green 25 WOD condition at 25 kts, 35 kts and 45 kts using the VAD. The RMS forces show a larger variation in the thrust force compared with the drag and side forces; this is to be expected since the production of thrust to counteract the weight of the aircraft is sensitive to any change in air velocity across the rotor disc. The forces required to counteract the drag and side force are relatively small and less sensitive to fluctuations in wind speed. As the wind speed is increased from 25 kts to 45 kts there is slight increase in the RMS drag and side force at each spot; as the wind speed increases the RMS thrust force varies slightly. Figure 6-9 shows an increasing level of RMS value in the thrust and drag forces from spots 1-4 with a drop in the RMS at spot 5.

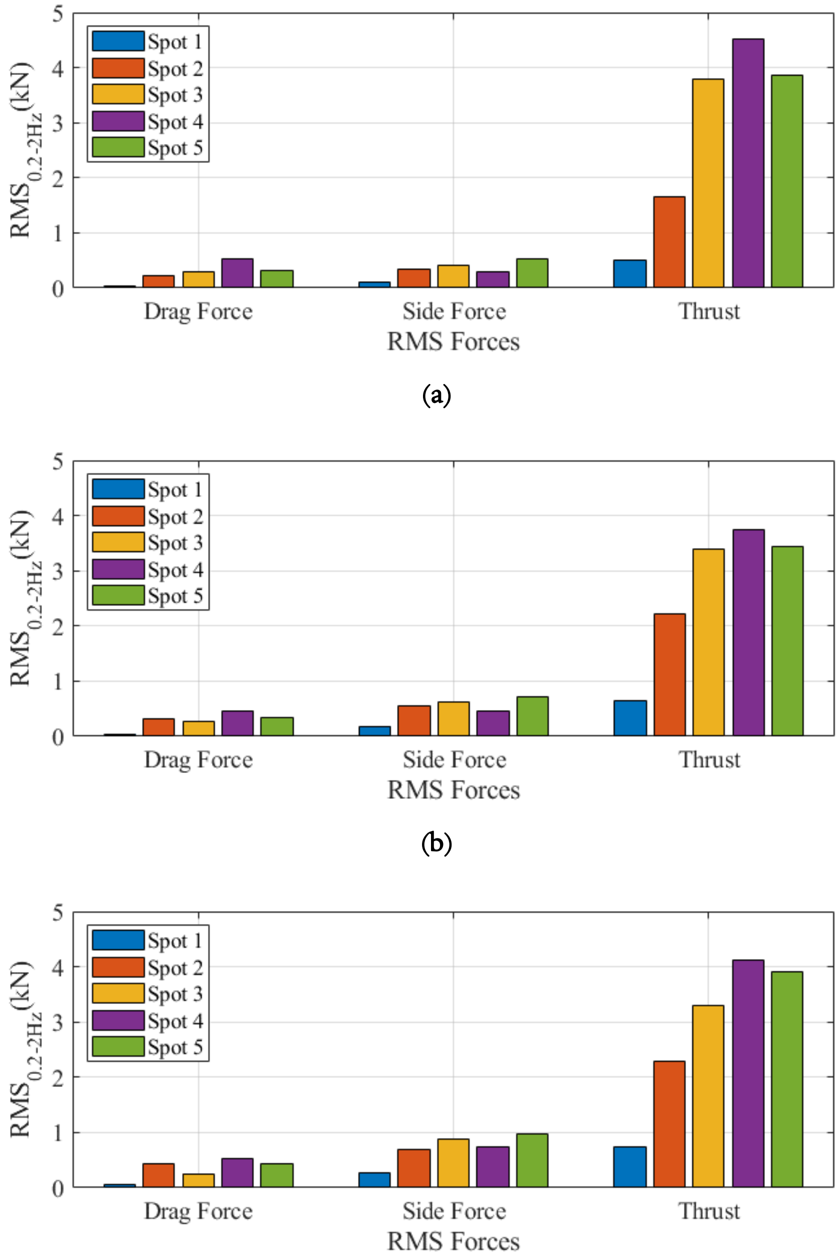

(a)

(b)

(c)

Figure 6-9 Virtual AirDyn RMS forces acting on aircraft fixed in hover in a Green 25 at (a) 25 kts, (b) 35 kts and (c) 45 kts height.

Figure 6-10 shows the RMS value for each moment calculated over the pilot’s closed-loop response frequency range at spots 1 to 5 in a Green 25 WOD condition at 25 kts, 35 kts and 45 kts using the VAD. A larger variation in moment is shown for yaw in Figure 6-10 than in roll or pitch; this is in part due to the reliance on the tail rotor to produce thrust in the horizontal plane to counteract the torque produced by the main rotor. As the wind speed is increase from 25 kts to 45 kts, an increase in the RMS moments is observed. As with RMS values for forces, the variations in moments for spot 1 is consistently the lowest; corresponding to the low level of air turbulence seen earlier. Consequently, it can be expected that the air flow over spot 1 will present less of a challenge to the pilot.

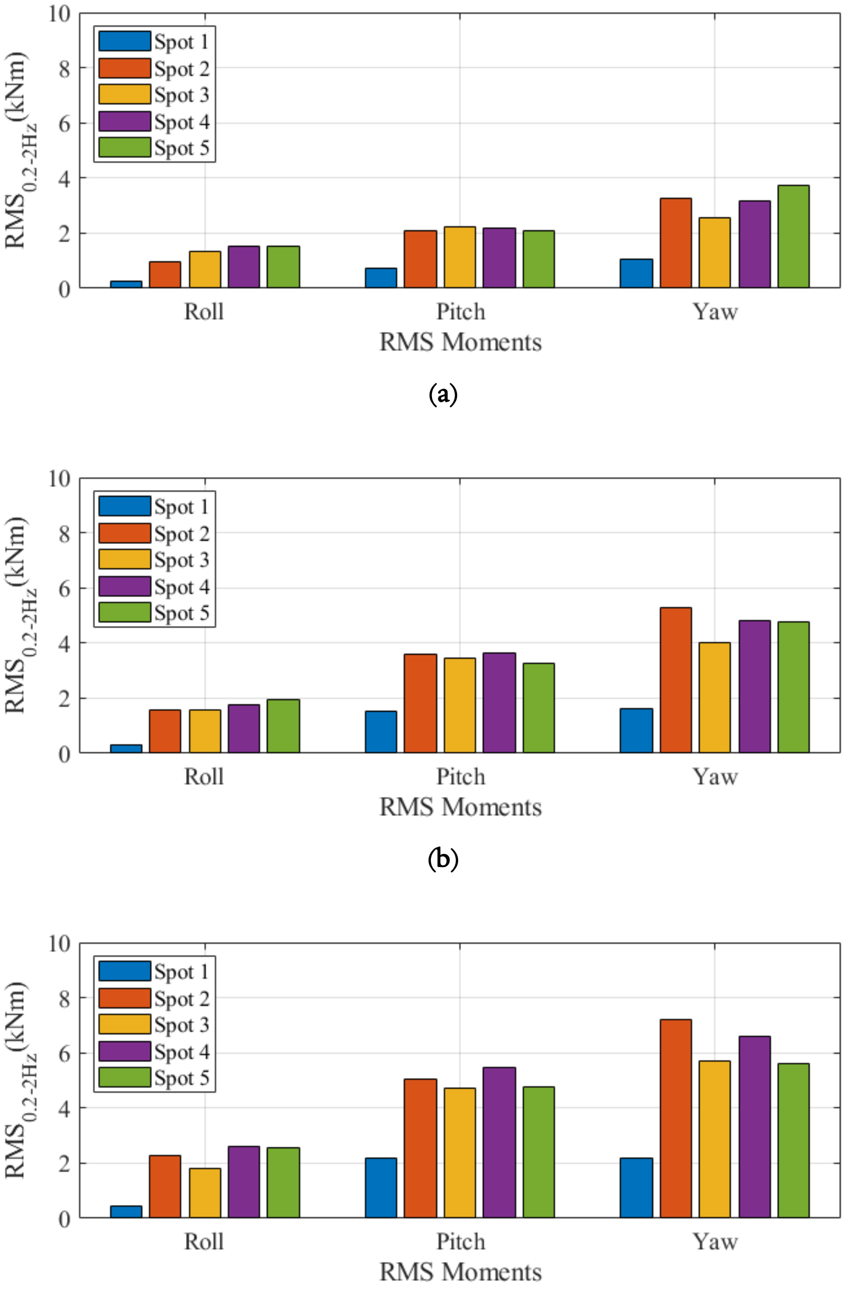

(a)

(b)

(c)

Figure 6-10 Virtual AirDyn RMS moments acting on aircraft fixed in hover in a Green 25 at (a) 25 kts, (b) 35 kts and (c) 45 kts.

6.3 Piloted Flight Simulation Trial for VAD Comparison

The VAD results shown section 6.2.2 enable the integrated effects of the unsteady airwake on the whole aircraft to be quantified at the different landing spots; an improvement on making a judgement of the air flow by simply examining the CFD airwakes. However, while the unsteady loads in the different axes at different wind speeds and direction have been individually evaluated for the different landing spots, the determination of pilot workload requires a pilot-in-the-loop to evaluate how the loads combine, along with other factors such as ship motion, to influence the pilot's overall workload. The HELIFLIGHT-R simulator, as described and used in Chapter 5, was used to assess the Green 25 QEC airwakes.

6.3.1 QEC Green 25 Piloted Flight Simulation Trial

To investigate pilot workload during recovery to the ship in a Green 25 WOD, a series of flight trials were conducted with an experienced former Royal Navy test pilot. Three wind speeds of 25 kts, 35 kts, and 45 kts were tested and, for each wind speed, the pilot was instructed to land at spots 1 to 5 using a port-side forward-facing recovery as shown in Figure 6-11, in the same manner as performed for the flight trial described in Chapter 5. Similar to Chapter 5, each landing evolution was divided into three contiguous MTEs. The landing was initiated with the helicopter positioned off the port side of the ship, facing forward and moving at the same speed as the ship; MTE 1 comprised the lateral translation from the port side to position over the landing spot; MTE 2 was a 30 second hover; MTE 3 was the descent and touch-down. The pilot was asked to provide a quantified rating of perceived workload for each of the three MTEs using the Bedford workload ratings scale shown in Figure 5-7 and to provide a rating for the difficulty of the overall landing task using the DIPES, shown in Figure 1-9. A description of each scale is detailed in Chapters 1 and 5, respectively.

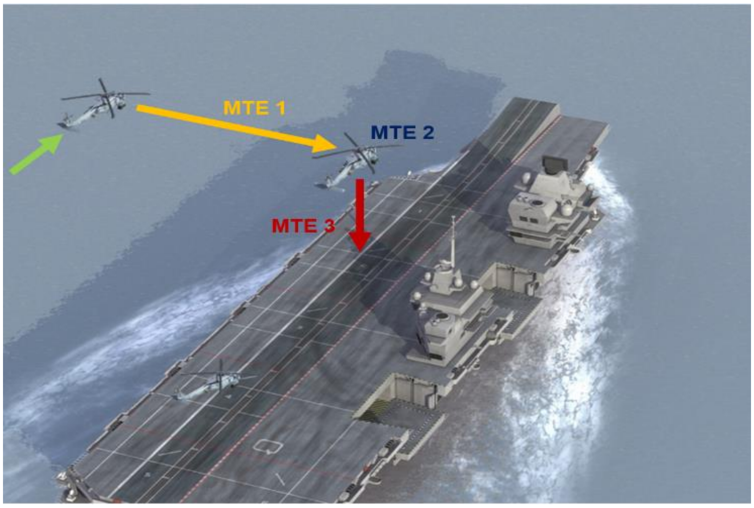

Figure 6-11 Port side helicopter recovery to QEC.

6.3.2 Simulation Trial Results

Figure 6-12 shows the workload ratings given by the test pilot for the hover task (MTE 2) at spots 1 to 5 in a 25 kts, 35 kts and 45 kts Green 25 WOD condition. The dashed red lines show the limit in the Bedford workload rating scale at which the level of spare capacity the pilot has for additional tasks is tolerable. As the wind speed is increased, the workload ratings given for the hover task at each spot also increases; for each wind speed the general trend is that workload increases from spot 1 to 4 and then either falls or remains constant for spot 5. This trend is consistent with the VAD results in Figure 6-9 where the RMS of the helicopter thrust load increases along the deck, peaking at spot 4, while at the same time pitch and yaw moments in Figure 6-10 are consistently higher over spots 2 to 5 compared with spot 1. As the wind speed increases from 25 kts to 45 kts the pilot workload in Figure 6-12 increases, consistent with the drag force RMS, side force RMS in Figure 6-9 and the RMS moments in Figure 6-10. In a 25 kts Green 25 WOD the hover task is within tolerable limits of workload for all spots. In a 35 kts wind the workload ratings for spots 1 and 2 are considered acceptable, while for spots 3 to 5 the workload is unsatisfactory. As the wind speed is increased to 45 kts, the workload for all spots, with the exception of spot 1, has become intolerable according to the Bedford workload rating scale.

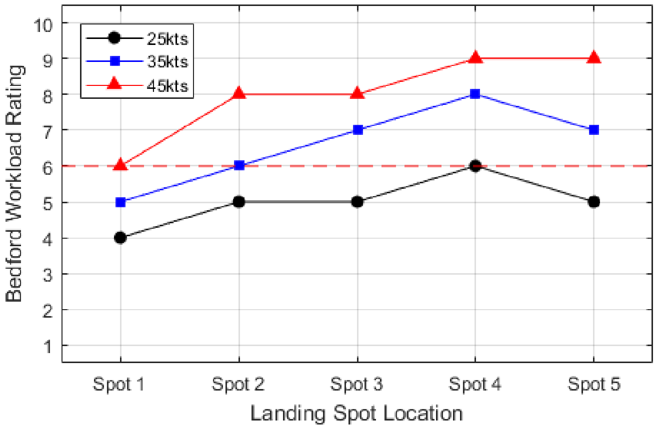

Figure 6-12 Bedford workload ratings for hover task over each landing spot.

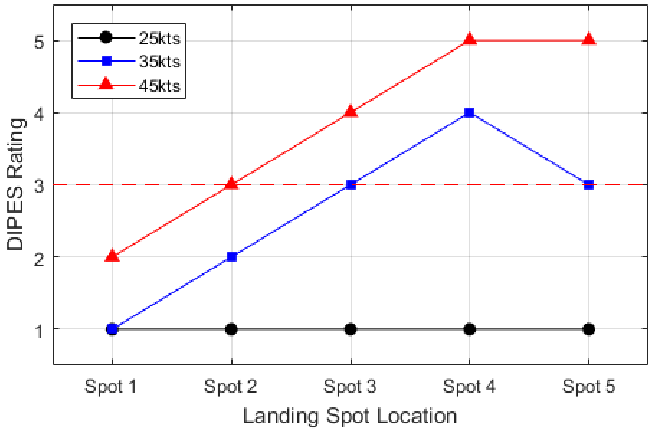

Figure 6-13 DIPES ratings for the complete landing task.

Figure 6-13 shows the DIPES rating given by the test pilot for the complete landing task at spots 1 to 5 in a 25 kts, 35 kts and 45 kts Green 25 WOD condition; the dashed red line corresponds with a DIPES rating of 3, which is the limit at which the level of effort during the task is acceptable. As a 5-point scale, the DIPES is coarser than the 10-point Bedford scale, it is also a measure of the difficulty of the overall landing task, not of discrete elements within it. Figure 6-13 shows that the difficulty of the landing task increases significantly with wind speed. For the 25 kts wind the pilot is not significantly challenged and awarded a rating of 1 for all spots. For the more challenging 35 kts and 45 kts winds the trend of the reported DIPES rating for landings at the different spots is similar to that of the Bedford ratings awarded for the hover task, i.e., workload increases from spot 1 to 4 and then either falls or remains the constant for spot 5. This trend is again consistent with the VAD results in Figure 6-9 and Figure 6-10. In the 35 kts wind, the landing to spot 4 was deemed too difficult for a fleet pilot to achieve consistently as was spot 3 in a 45 kts wind, while landings to spots 4 and 5 were deemed outside of safe operating limits.

Relatively high pilot workload in a Green wind at 45 kts for a carrier with a starboard superstructure is not an altogether surprising result. The workload ratings presented here are, of course, purely derived from simulation and, in addition, a simulation which makes use of a generic helicopter model, generic cockpit and limited visual and motion cues. Therefore, these results must not be taken as representative of any real-world scenario. Nevertheless, the study has shown promise in identifying areas where increased workload might be experienced and, as such, may prove a valuable tool in informing the planning of future flight test campaigns.

The results of the VAD show overall consistent agreement with workload ratings given by the pilot during the simulated flight trial. Therefore, the VAD is shown to be a suitable tool in assessing the effect of the airwake on the helicopter's forces and moments to inform both flight trials and ship design and is worthy of further development and application.

6.4 Chapter Summary

This Chapter has described an investigation of an oblique unsteady airwake over the landing deck of the QEC carrier, and how it could affect helicopter recovery. CFD was used to simulate the unsteady air flow over the ship in a wind approaching from 25 deg off the starboard which, due to the twin island superstructure, creates turbulent flow over much of the flight deck. Thirty seconds of unsteady CFD has been used to calculate the mean and turbulent velocities above the vertical landing spots used by both rotary- and fixed-wing aircraft. The effect of time-varying air flow on the unsteady loads imparted on a helicopter was assessed, using a technique known as the VAD, to quantify the unsteady forces and moments acting on the aircraft in the hover. How the unsteady air flow would affect the handling qualities of the helicopter and pilot workload, during a deck landing to each spot, was assessed through a series of simulated flight trials conducted in a full-motion flight simulator configured to represent a SH-60B Seahawk helicopter. The CFD analysis and piloted flight trial results were compared with the VAD analysis tool to evaluate the suitability of the VAD for assessing the effect of the aircraft carrier's airwake on helicopter performance and it's correlation with pilot workload. It was demonstrated that the VAD showed promise and could, therefore, be employed as a tool to inform future FOCFTs.

Chapter 7

Conclusions and Recommendations

This final Chapter will draw out the main conclusions from the research that has been reported in the thesis. A number of recommendations are also made on how modelling and simulation of the SAI may be developed further.

The use of simulation tools to inform or supplement at-sea trials to determine ship-aircraft operational limits requires high-fidelity modelling of the air flow over the ship's flight deck. The accuracy of the methods used to model the flow must be ensured through validation. The research reported in this thesis has assessed the accuracy of the CFD-generated airwakes for the QEC aircraft carriers through experimental validation. Furthermore, the effect of the QEC airwake on helicopter pilot workload when conducting deck landings in different wind and sea state conditions has been examined through piloted flight simulation. An offline flight simulation tool known as the Virtual AirDyn (VAD) was used to investigate how the QEC airwake affects the aerodynamic loads on a helicopter and the unsteady forces and moments were shown to be consistent with the helicopter pilot's workload when conducting deck landings in the same wind conditions.

A study was also conducted to investigate how the QEC airwake affects the forces and moments on a fixed-wing generic STOVL aircraft by developing an aerodynamic model of the aircraft in which airwake velocities can be distributed across its lifting surfaces. Although this was considered to be an important aspect of the research, particularly from the perspective of BAE Systems, the effort required to integrate the STOVL aerodynamic model with a STOVL flight dynamics model was beyond the scope of the PhD study. The aerodynamic model has therefore been included as an appendix so the research that was successfully completed can be further developed in the future.

7.1 Conclusions

The experimental study conducted using the ADV is believed to be the first time this instrument has been used for detailed velocity measurements for CFD validation. Ship airwake validation experiments are normally performed in wind tunnels, employing instrumentation such as pitot probes, hot wire anemometry, LDA, or PIV. The use of a water channel has been shown to be an effective alternative and the ADV is a suitable instrument for accurately providing validation data for CFD solutions of the ship airwakes. ADV has been demonstrated to be an effective tool for measuring the mean velocity in three components and the unsteady turbulence in two components.

The quality of the measured ADV data is affected by a number of variables. It was found that levels of SNR and Correlation of the recorded data must be sufficiently high and de-spiking of the raw data is required to provide high-quality velocity and turbulence measurement data for CFD validation. In particular, the quality of the ADV measurements conducted near boundaries is affected by the material composition of the surface, due to the reflection of the transmitted acoustic energy from the surface to the ADV probe's receivers. It was found that boundary materials composed of similar specific acoustic impedance to the fluid, in this case water, provide higher attenuation of the reflected signal reducing the acoustic noise at the ADV probes receivers. Furthermore, the quality of the ADV measurements obtained near boundaries is affected by the roughness of the surface material due to the scattering of acoustic energy from the surface and away from the ADV probe's receivers. It was found that boundaries with higher surface roughness scatter the reflected signal reducing the acoustic noise at the ADV probes receivers. The material of construction and surface roughness of the QEC carrier model was well-suited for near-wall ADV measurements.

The aircraft carrier airwake is highly dynamic and the unsteady flow field will at some stage impact on aircraft operating to the ship. It has been demonstrated that to accurately model the airwake, time-accurate CFD is required. DDES has been shown to be an effective CFD technique for this task, being more resistant to gird-induced separation in ambiguous boundary layer regions and is preferred over the standard DES model. The research has also shown how, when applying the DDES technique, a settling period is required, and the flow solution should be monitored to allow the unsteady flow to become 'settled'. It is also essential that cell growth is limited in areas of interest so that turbulent kinetic energy dissipation is minimized, ensuring accuracy of the modelled airwake.

In this research, the CFD methodology was applied to the model-scale experiments, for validation purposes, and to the full-scale ship to provide airwakes for flight simulation. For simulating the flow over the model QEC submerged in the water channel, the CFD domain was extended 2 m forward of the working section to ensure appropriate inlet conditions. It was also established that a time-step of 0.001 seconds was required to adequately capture flow frequencies of interest in the solution. For the full-scale ship, CFD was shown to be capable of creating full-scale airwakes for winds approaching from multiple WOD azimuths by placing the QEC carrier in the centre of a cylindrical domain. An atmospheric boundary layer was applied to be representative of the inflow conditions at sea, and to adequately capture flow frequencies of interest the solution was solved with a time-step of 0.01 seconds. The large size of the mesh (100-120 million cells) of both the small-scale and full-scale domains, combined with the DDES time accurate CFD method, requires the use of parallel computing to perform the simulations within reasonable timescales. A typical airwake simulation for one azimuth took 30 days to complete.

Comparing the experimental velocity measurements for flows from Ahead, and the equivalent of Green 10, with the corresponding CFD solutions demonstrated the validity of the CFD method. Overall, the small-scale experiment and CFD showed excellent agreement with average differences between measured and computed velocities being mostly less than 5%.

It has long been common practice in wind tunnel studies of large bodies to use small-scale experiments to represent full-scale conditions. It was revealing in this research that comparison of the small-scale experiment, the small-scale CFD and the full-scale CFD all showed reasonable agreement, despite differences in Reynolds number and the inlet velocity profiles. This observation suggests that the full-scale CFD is at least as representative of the full-scale situation as the small-scale experiment, and that it is an effective tool for simulating the full-scale air flow over a large structure such as an aircraft carrier.

The QEC is an unusual aircraft carrier in that it has two islands, compared with the normal single-island design; it also has a ski-jump ramp at the bow. Aerodynamically, the research has shown that the twin islands create complex air flows over the fight deck in oblique winds, while the rounded profiles of the ski-jump and the adjacent bow area allow the air flow from close to Ahead to remain attached to the deck surface and not create significant flow disturbances along the flight deck. The air flow being shed from the islands in starboard winds will create more challenging flying conditions. Other aircraft carrier designs, which have a single large island positioned on the starboard side of the flight deck, will also generate turbulent wakes, but ones that will be less complex than the twin-island configuration.

The effect of the unsteady airwakes over the flight deck of the QEC on helicopter operations was primarily assessed by piloted flight simulation. The pilot assessed the difficulty of the landing task by awarding workload ratings from recognised workload rating scales. Further experimental evidence of the difficulty of the landing task was obtained by recording the control inputs applied by the pilots during the deck landings, and by recording their comments. Winds up to 45 kts from Ahead presented little difficulty to the pilot when landing to the spots towards the stern of the ship that have been designated for rotorcraft operations. There was a greater level of turbulence observed in the CFD results for spot 6, which is in the lee of the aft island, but even so the workload was not reported as high by the pilot. The level of control activity in cyclic, pedal and collective, and the ability of the pilot to hold a hover position over the spot was consistent with this observation.

In Green 45 winds, conducting a forward-facing helicopter landing to spots 5 and 6 caused the pilot considerable workload in the simulated flight trials. The pilot deemed the workload associated with landing to spot 6 was not tolerable for a WOD of 25 kts because of a combination of high levels of turbulence and an inability to maintain heading due to insufficient yaw control authority. The control activity and positional accuracy was consistent with this observation and showed pedal margins had been exceeded on occasions. During recovery of the helicopter in a Green 90 beam wind the aircraft experienced turbulence and insufficient yaw control was available to maintain heading in these simulated trials. However, the pilot was able to conduct the landing task with lower workload than in Green 45 for the same wind speed, but at the expense of heading control, therefore while workload was lower, the DIPES rating was higher. In Green 45 and 90, the limiting wind speed for the simulated helicopter landing to spot 5 and 6 was 25 kts.

The research reported in this thesis has demonstrated how piloted flight simulation could be used to inform clearance trials for rotorcraft, which, together with the successful F35-B/QEC First-of-Class flight trials described in the thesis, bodes well for the future application of modelling and simulation for assisting and informing the conduct of aircraft/ship operations. The test pilots used in this research considered the overall simulation environment, including the integration of CFD airwakes into a real-time piloted simulation for rotorcraft operating to the QEC, to be a realistic representation of the at-sea flying experience. It is noted, however, that while the rotorcraft pilots who contributed to the simulated trials had specific experience of aircraft carrier landings, they had no specific experience of the QEC carrier environment, which is a new and unique ship. The simulated flight trials provided encouraging results, which have implications for the potential role of flight simulation in supporting future at-sea testing of maritime rotorcraft and for enhancing pilot training devices.

While the piloted simulation trails were the primary method for assessing the effect of the QEC airwakes on a helicopter, the trials were relatively lengthy and the ratings provided by the pilot were, by their very nature, subjective. Therefore, another simulation tool, the Virtual AirDyn, was used to quantify the unsteady loads on a helicopter when placed at a particular position in the airwake, thereby enabling a systematic assessment of the airwake on the aircraft. An analysis of the unsteady forces and moments imposed onto a helicopter by oblique starboard winds was conducted using the VAD and the measurements were compared with pilot workload and DIPES rating obtained from an equivalent piloted simulation in Green 25 winds. Winds up to 25 kts presented little difficulty to the pilot when hovering above spots 1 to 5. As the wind speed was increased above 25 kts the pilot workload and DIPES rating increased from spot 1 to spots 4 and 5, consistent with the unsteady loads recorded by the VAD. Overall, the VAD analysis showed that the unsteady loads imparted on the helicopter varied at each landing spot and were consistent with the pilot workload ratings. The VAD has therefore been shown to be an effective tool for distinguishing how different areas of a ship's airwake may impact on the unsteady loads on a helicopter and could offer a simple tool to inform the planning of helicopter flight trails.

Although the aerodynamic study of the fixed-wing STOVL analysis has been included as an appendix, the conclusions from that study are recorded here so their significance is not lost to future STOVL/QEC flight simulation research. Typical aerodynamic models for fixed-wing flight simulation assume that the aircraft is operating in a relatively steady airflow. A high-fidelity aerodynamic model has been developed, using strip theory, which enables a simulated fixed-wing aircraft to experience unsteady aerodynamic effects when operating at low speed and at hover in a complex three-dimensional air flow. The number of strips defined for each lifting surface in the strip theory method affects the ability of the model to accurately capture the unsteady velocity gradients in the wake. By observing the unsteady loads calculated for different numbers of strips, while the model was exposed to the unsteady air flow, it was determined that a minimum of ten strips are required. A corollary of this observation is that the more commonly used centre of gravity model, or the four-point model, are insufficient to adequately capture the forces and moments imposed by a highly three-dimensional air flow. In the QEC Green 25 wind, the wing and the canard of the generic STOVL model produced significant drag forces due to their large surface areas. The drag force and yawing moment produced by the body was small in comparison with the other three lifting surfaces, suggesting it is not necessary to include it in the aerodynamic modelling of such aircraft for flight simulation. The strip theory aerodynamic model is capable of capturing the unsteady forces and moments when immersed in the turbulent air flow of a ship's airwake.

7.2 Recommendations

During the course of the research, a number of observations have been made that would assist in the future development of research into the modelling and simulation of the SAI, including the application of the ADV as a velocity measurement device.

While the ADV has been shown to be an effective instrument for obtaining point measurements in a complex three-dimensional unsteady flow, in the present work two different probes (sideways and downward-looking) were applied separately. A natural progression for the method would be to apply the two probes simultaneously and to attempt to cross-correlate the measurements to obtain, for example, Reynolds stresses. Ship airwakes are characterised by separated flows and shear layers. This means that the velocity can vary across the relatively small measurement volume, which the instrument could interpret as a turbulent fluctuation. While such an effect was not evident in the current research, a supplementary study could be conducted to test the accuracy of the instrument in a one-dimensional flow with a steep velocity gradient. This would provide further supporting evidence for the use of the ADV close to boundaries and at separation points at corners.

The full-scale airwakes created in this study used a steady inlet velocity profile, which is a common approach. Oceanic winds are usually unsteady and so it is recommended that further research is conducted into the generation of an unsteady inlet flow within the CFD, and a comparison be made with experimental measurements.

While the F-35B/QEC simulation trials were an acknowledged success and a significant milestone in the used of piloted flight simulation to inform at-sea trials, the application to rotorcraft operations is not so well advanced. There is a need for at-sea flight trials data to compare with simulation to quantify how well simulated deck landings reflect the real-world so the potential benefits of the technology can be realised.

While the airwakes produced using CFD for large ships such as the QEC carrier are interpolated into a structured grid with a sufficient frequency for piloted flight simulation, they still represent a large amount of data. It is recommended that methods used to reduce the size of the airwake such as reduced order modelling be investigated.

The VAD has shown itself to be a quick and versatile tool for assessing the effect of a ship airwake on a helicopter. It would be beneficial to further utilise the VAD to conduct a sensitivity study of the effect of the flow on the helicopter over the flight deck spots. Further investigations of the flow off the portside edge before lateral translation over the deck could also be performed.

While acknowledging the usefulness of the VAD, it would be an even more useful tool if the unsteady helicopter loads that it measures could be used to predict pilot workload ratings. It is therefore recommended that further comparison of VAD analysis and ratings provided by piloted flight trials be used to determine if there is a correlation between the unsteady loads imparted on the helicopter and workload ratings.

Including the effects of unsteady airwake velocities over a helicopter in the flight simulation has emphasised how important it is to have an aerodynamic model of an aircraft that allows the effect of an unsteady three-dimensional flow field to be captured by the aerodynamic flight model. A future research area would be to include such a model in a fixed-wing simulation and so it is recommended that an in-depth investigation of the strip theory aerodynamic model be conducted to compare the strip theory model with a four-point aerodynamic model and centre of gravity model using QEC airwakes at various wind conditions. To properly exploit the new strip theory generic STOVL model, the next stage would be to combine the aerodynamic model with a flight dynamics model of a generic STOVL aircraft and to implement the integrated models in a piloted flight simulator to assess the impact of the enhanced aerodynamic modelling on the pilot experience.

References

[1] Owen, I., White, M. D., Padfield, G. D., and Hodge, S. J., "A Virtual Engineering Approach to the Ship-Helicopter Dynamic Interface - A Decade of Modelling and Simulation Research at the University of Liverpool," *The Aeronautical Journal*, Vol. 121, No. 1246, 2017, pp. 1833–1857.

https://doi.org/10.1017/aer.2017.102

[2] Kelly, M. F., White, M. D., Owen, I., and Hodge, S. J., "Using airwake simulation to inform flight trials for the Queen Elizabeth Class Carrier," *13th International Naval Engineering Conference (INEC)*, Institute of Marine Engineering Science & Technology, Glasgow, October 2018.

[3] Fry, A., Cook, R., and Revill, N., "CVF ski-jump ramp profile optimisation for F-35B," *The Aeronautical Journal*, Vol. 113, No. 1140, 2009, pp. 79-85.

https://doi.org/10.1017/S0001924000002803

[4] Bevilaqua, P. M., "Inventing the F-35 Joint Strike Fighter," *47th AIAA Aerospace Sciences Meeting Including the New Horizons Forum and Aerospace Exposition*, American Institute of Aeronautics and Astronautics, Orlando, Florida, January 2009.

https://doi.org/10.2514/6.2009-1650

[5] Cook, R., Atkinson, D., Milla, R., Revill, N., and Wilson, P., "Development of the Shipborne Rolling Vertical Landing (SRVL) Manoeuvre for the F-35B Aircraft," *International Powered Lift Conference*, American Institute of Aeronautics and Astronautics, Philadelphia, 2010.

[6] Atkinson, D. C., Brown, R., Potts, R., Bennett, D., Ward, J. E., and Trott, E., "Integration of the F-35 Joint Strike Fighter with the UK Queen Elizabeth Class Aircraft Carrier," *International Powered Lift Conference*, American Institute of Aeronautics and Astronautics, Los Angeles, California, August 2013.

https://doi.org/10.2514/6.2013-4267

[7] Lumsden, B., and Padfield, G. D., "Challenges at the helicopter-ship dynamic interface," *24th European Rotorcraft Forum*, Marseilles, France, September 1998.

[8] Forrest, J. S., Owen, I., Padfield, G. D., and Hodge, S. J., "Ship-Helicopter Operating Limits Prediction Using Piloted Flight Simulation and Time-Accurate Airwakes," *Journal of Aircraft*, Vol. 49, No. 4, 2012, pp. 1020–1031.

https://doi.org/10.2514/1.C031525

[9] Roscoe, A., and Ellis, G. "A Subjective Rating Scale for Assessing Pilot Workload in Flight: A decade of Practical Use," RAE report TR90019, Royal Aircraft Establishment, Farnborough, UK, March 1990.

[10] Lee, D., and Horn, J. F., "Simulation of Pilot Workload for a Helicopter Operating in a Turbulent Ship Airwake," *Proceedings of the Institution of Mechanical Engineers, Part G: Journal of Aerospace Engineering*, Vol. 219, No. 5, 2005, pp. 445–458. https://doi.org/10.1243/095441005X30298

[11] Carico, G. D., Fang, R., Finch, R. S., Geyer Jr., W. P., Cdr. (Ret.) Krijns, H. W., and Long, K., "Helicopter/Ship Qualification Testing," *RTO AGARDograph 300 Flight Test Techniques Series*, Vol. 22, Research and Technology Organisation, NATO, France, February 2003, pp. 1-126.

[12] Kelly, M. F., White, M. D., Owen, P. I., and Hodge, S. J., "The Queen Elizabeth Class Aircraft Carriers: Airwake Modelling and Validation for ASTOVL Flight Simulation," *American Society of Naval Engineers Launch & Recovery Symposium*, American Institute of Aeronautics and Astronautics, Linthicum Heights, Maryland, 2016.

[13] Save The Royal Navy, "Successful flight trials period vindicates design of HMS Queen Elizabeth," [Online]. [Accessed 9 January 2021]. Available from: https://www.savetheroyalnavy.org/successful-flight-trials-period-vindicates-design-of-hms-queen-elizabeth/

[14] Padfield, G. D., "The Making of Helicopter Flying Qualities: A Requirements Perspective," *The Aeronautical Journal*, Vol. 102, No. 1018, December 1998.

[15] Roper., D. M., Owen, I., Padfield, G. D., and Hodge, S. J., "Integrating CFD and piloted simulation to quantify ship-helicopter operating limits," *The Aeronautical Journal,* Vol. 110, No. 1109, 2006, pp. 419-428. https://doi.org/10.1017/S0001924000001329

[16] Forrest, J. S., and Owen, I. "An investigation of ship airwakes using Detached-Eddy Simulation," *Computers & Fluids*, Vol. 39, No. 4, April 2010, pp. 656-673. https://doi.org/10.1016/j.compfluid.2009.11.002

[17] Hodge, S. J., Forrest, J. S., Padfield, G. D., and Owen, I., "Simulating the environment at the helicopter-ship dynamic interface: research, development and application," *The Aeronautical Journal*, Vol. 116, No. 1185, November 2012, pp. 1155-1184. https://doi.org/10.1017/S0001924000007545

[18] Forrest, J. S., Kääriä, C. H., and Owen, I., "Evaluating ship superstructure aerodynamics for maritime helicopter operations through CFD and flight simulation," *The Aeronautical Journal*, Vol. 120, No. 1232, 2016, pp. 1578-1603. https://doi.org/10.1017/aer.2016.76

[19] Roscoe, M. F., and Wilkinson, C. H., "DIMSS - JSHIP's M&S process for ship helicopter testing & training," *AIAA Modeling and Simulation Technologies Conference and Exhibit*, Monterey, CA, 2002.

[20] Wilkinson, C. H., Roscoe, M. F., and Vandervliet, G. M., "Determining fidelity standards for the shipboard launch and recovery task," *AIAA Modeling and Simulation Technologies Conference and Exhibit*, Montreal, Canada, 2001.

[21] Mateer, R., Scott, P., White, M., and Owen, I., "A CFD Study of the Aerodynamics of a Ship's Bulky Enclosed Mast," *American Society of Naval Engineers (ASNE) Launch and Recovery Symposium*, Linthicum Heights, Maryland, 2016.

[22] Zan, S. J., "On Aerodynamic Modelling and Simulation of the Dynamic Interface," *Proceedings of the Institution of Mechanical Engineers, Part G: Journal of Aerospace Engineering*, Vol. 219, No. 5, 2005, pp. 393–410. https://doi.org/10.1243/095441005X30315

[23] Kääriä, C. H., Wang, Y., Curran, J., Forrest, J., and Owen, I., "AirDyn: An Airwake Dynamometer for Measuring the Impact of Ship Geometry on Helicopter Operations," *36th European Rotorcraft Forum*, Paris, France, 2010.

[24] Kääriä, C. H., "Investigating the Impact of Ship Superstructure Aerodynamics on Maritime Helicopter Operations," University of Liverpool PhD Thesis, August 2012.

[25] Fortenbaugh, R. L., "Mathematical Models of the Aircraft Operational Environment of DD 963 Class Ships," Vought Report- 2-55800/8R-3500, 1978.

[26] White, H. E., and Chaddock, D. R., "Comparison of Full Scale and Model Data of the Wind Velocity over the CVS-16 Flight Deck," Aerodynamic Report 1128, DTNSRDC, 1967.

[27] Reddy, Jr., W., "Ship Airwake Measurement and Flow Visualization," *6th AIAA Biennial Flight Test Conference*, American Institute of Aeronautics and Astronautics, Hilton Head, South Carolina, 1992. https://doi.org/10.2514/6.1992-4088

[28] Garnett, Jr, T. S., "Investigation to Study the Aerodynamic Ship Wake Turbulence Generated by a DD963 Destroyer," *Report D210-11545-1, Boeing Vertol*, August 1979.

[29] Rhoades, M. M., "A Study of the Airwake Aerodynamics Over the Flight Deck of an AOR Model Ship," *Naval Postgraduate School,* September 1990.

[30] Rhoades, M. M., and Healey, J. V., "Flight Deck Aerodynamics of a Nonaviation Ship," *Journal of Aircraft*, Vol. 29, No. 4, 1992, pp. 619–626. https://doi.org/10.2514/3.46210

[31] Johns, M. K., "Flow Visualization of the Airwake Around a Model of a DD-963 Class Destroyer in a Simulated Atmospheric Boundary Layer," *Naval Postgraduate School*, September 1988.

[32] Anderson, G. A., "Mapping the Airwake of a Model DD-963 along Specific Helicopter Flight Paths," *Naval Postgraduate School*, December 1989.

[33] Nave, R. L., "Development and Analysis of a CVA and 1052 Fast Frigate Air Wake Model," *Technical Report 78182-60,* Naval Air Development Centre, Philadelphia, September 1978.

[34] Moore, G. E., "Cramming More Components Onto Integrated Circuits," *Proceedings of the IEEE*, Vol. 86, No. 1, 1998, pp. 82–85. https://doi.org/10.1109/JPROC.1998.658762

[35] Shukla, S., Sinha, S. S. S., and Singh, S. N. N., "Ship-Helo Coupled Airwake Aerodynamics: A Comprehensive Review," *Progress in Aerospace Sciences*, Vol. 106, 2019, pp. 71–107. https://doi.org/10.1016/j.paerosci.2019.02.002

[36] Syms, G. F., "Numerical Simulation of Frigate Airwakes," *International Journal of Computational Fluid Dynamics*, Vol. 18, No. 2, 2004, pp. 199–207. https://doi.org/10.1080/10618560310001634159

[37] Tai, T. C., and Carico, D., "Simulation of DD-963 Ship Airwake by Navier-Stokes Method," *Journal of Aircraft*, Vol. 32, No. 6, 1995, pp. 1399–1401. https://doi.org/10.2514/3.46892

[38] Liu, J., Long, L. N., and Modi, A., "Higher Order Accurate Solutions of Ship Airwake Flow Fields Using Parallel Computer," *American Helicopter Society 54th Annual Forum*, Washington, D.C., May 1998, pp. 58–70.

[39] Syms, G. F., "Simulation of Simplified-Frigate Airwakes Using a Lattice-Boltzmann Method," *Journal of Wind Engineering and Industrial Aerodynamics*, Vol. 96, No. 6–7, 2008, pp. 1197–1206. https://doi.org/10.1016/j.jweia.2007.06.040

[40] Polsky, S., and Bruner, C., "Time-Accurate Computational Simulations of an LHA Ship Airwake," *18th Applied Aerodynamics Conference*, American Institute of Aeronautics and Astronautics, Denver, Colorado, 2000.

https://doi.org/10.2514/6.2000-4126

[41] Polsky, S., "A Computational Study of Unsteady Ship Airwake," *40th AIAA Aerospace Sciences Meeting & Exhibit*, American Institute of Aeronautics and Astronautics, Reno, Nevada, January 2002.

https://doi.org/10.2514/6.2002-1022

[42] Polsky, S., "CFD Prediction of Airwake Flowfields for Ships Experiencing Beam Winds," *21st AIAA Applied Aerodynamics Conference*, American Institute of Aeronautics and Astronautics, Orlando Florida, June 2003.

https://doi.org/10.2514/6.2003-3657

[43] Sharma, A., and Long, L., "Airwake Simulations on an LPD 17 Ship," *15th AIAA Computational Fluid Dynamics Conference*, American Institute of Aeronautics and Astronautics, Anaheim, California, June 2001.

https://doi.org/10.2514/6.2001-2589

[44] Tai, T., and Carico, D., "Simulation of DD-963 Ship Airwake by Navier-Stokes Method," *23rd Fluid Dynamics, Plasmadynamics, and Lasers Conference*, American Institute of Aeronautics and Astronautics, Orlando, Florida, July 1993.

https://doi.org/10.2514/6.1993-3002

[45] Wilkinson, C. H., Zan, S. J., Gilbert, N. E., Funk, J. D., "Modelling and simulation of ship air wakes for helicopter operations - a collaborative venture," NATO RTO Applied Vehicle Technology Panel (AVT) Symposium on Fluid Dynamics Problems of Vehicles Operating Near or in the Air-Sea Interface, Amsterdam, The Netherlands, October 1998

[46] Cheney, B. T., and Zan, S. J., "CFD code validation data and flow topology for the technical co-operation program AER-TP2 simple frigate shape," NRC-CNRC report LTR-A-035, National Research Council Canada Institute for Aerospace Research, 1999.

[47] Zan, S. J., "Surface Flow Topology for a Simple Frigate Shape," *Canadian Aeronautics and Space Journal*, Vol. 47, No. 1, 2001, pp. 33–43.

[48] Reddy, K. R., Toffoletto, R., and Jones, K. R. W., "Numerical Simulation of Ship Airwake," *Computers and Fluids*, Vol. 29, No. 4, 2000, pp. 451–465.

https://doi.org/10.1016/S0045-7930(99)00033-X

[49] Lee, R., "SFS2 Code Validation Update," *TTCP AER TP-2 Dynamic Interface Workshop*, 2003.

[50] Zan, S., "Technical Comment on 'Computational-Fluid-Dynamics Based Advanced Ship-Airwake Database for Helicopter Flight Simulation,'" *Journal of Aircraft*, Vol. 40, No. 5, 2003.

https://doi.org/10.2514/2.6890

[51] White, M. D., Perfect, P., Padfield, G. D., Gubbels, A. W., and Berryman, A. C., "Acceptance Testing and Commissioning of a Flight Simulator for Rotorcraft Simulation Fidelity Research," *Proceedings of the Institution of Mechanical Engineers, Part G: Journal of Aerospace Engineering*, Vol. 227, No. 4, 2013, pp. 663–686. https://doi.org/10.1177/0954410012439816

[52] Kelly, M. F., "*The Development, Validation, and Integration of Aircraft Carrier Airwakes for Piloted Flight Simulation*," University of Liverpool Thesis, 2018.

[53] Lison, A., "Integrating the Joint Combat Aircraft into the Queen Elizabeth Class Aircraft Carriers - Design Challenge or Opportunity?," *RINA, Royal Institution of Naval Architects International Conference - Warship 2009: Airpower at Sea*, London, June 2009.

[54] Hodge, S. J., "Validation of Shipborne Visual Landing Aids Through Piloted Simulation," *RAeS Flight Simulation Group Conference on 'Simulation of Onboard Systems,* Royal Aeronautical Society, London, 2004.

[55] Allison, G., "Royal Navy pilot hails 'unique simulator' supporting first of class F-35 flight trials," [Online]. [Accessed 9 January 2021]. Available from: https://ukdefencejournal.org.uk/royal-navy-pilot-hails-unique-simulator-supporting-first-of-class-f-35-flight-trials/

[56] Hodge, S. J., and Wilson, P. N., "Operating JSF from CVF the Reality of Simulation.," *Proceedings of the International Powered Lift Conference*, Royal Aeronautical Society, London, 2008.

[57] Hodge, S. J., Spencer, M. P., and Southworth, M. R., "A Collaborative Simulation Environment for Investigating Aircraft-Ship Operations," *RAeS Flight Simulation Group Conference on 'Mission Training and Flight Simulation – Technology, concepts and collaboration*, Royal Aeronautical Society, London, 2013.

[58] Moorhouse, Captain S., "HMS Queen Elizabeth carrier strike group returns home from jet trials," [Online]. [Accessed 9 January 2021]. Available from: https://www.royalnavy.mod.uk/news-and-latest-activity/news/2019/december/04/190412-carrier-units-homecoming

[59] Oberkampf., W. L., Trucano, T. G., "Verification and Validation in Computational Fluid Dynamics," *Progress in Aerospace Sciences*, Vol. 38, No. 3, 2002, pp. 209–272. https://doi.org/10.1016/S0376-0421(02)00005-2

[60] Zan, S. J., and Garry, E. A., "*Wind tunnel measurements of the airwake behind a model of a generic frigate,*" NRC-IAR-LTR-AA-13, June 1994.

[61] Zan, S. J., Syms, G. F, and Cheney, B. T., "Analysis of Patrol Frigate Air Wakes," RVO AVT Symposium on Fluid Dynamics of Vehicles Operating Near or In the Air-Sea Interface". Amsterdam, October 1998.

[62] Greenwell, D., and Barrett, R., "Inclined Screens for Control of Ship Air Wakes," *3rd AIAA Flow Control Conference*, American Institute of Aeronautics and Astronautics, San Francisco, California, June 2006.

https://doi.org/10.2514/6.2006-3502

[63] Nacakli, Y., and Landman, D., "Helicopter Downwash / Frigate Airwake Interaction Flowfield PIV Surveys in a Low Speed Wind," *67th Annual Forum of the American Helicopter Society*, Virginia Beach, Virginia, 2011.

[64] Rosenfeld, N., Kimmel, K., and Sydney, A. J., "Investigation of Ship Topside Modeling Practices for Wind Tunnel Experiments," *53rd AIAA Aerospace Sciences Meeting, AIAA Science and Technology Forum,* American Institute of Aeronautics and Astronautics, Kissimmee, Florida, January 2015.

https://doi.org/10.2514/6.2015-0245

[65] Rahimpour, M., and Oshkai, P., "Experimental Investigation of Airflow over the Helicopter Platform of a Polar Icebreaker," *Ocean Engineering*, Vol. 121, 2016, pp. 98–111.

https://doi.org/10.1016/j.oceaneng.2016.05.023

[66] Mora, R. B., "Flow Field Velocity on the Flight Deck of a Frigate," *Proceedings of the Institution of Mechanical Engineers, Part G: Journal of Aerospace Engineering*, Vol. 228, No. 14, 2014, pp. 2674–2680.

https://doi.org/10.1177/0954410014524739

[67] Lim, H. C., Castro, I. P., and Hoxey, R. P., "Bluff bodies in deep turbulent boundary layers: Reynolds-number issues," *Journal of Fluid Mechanics*, Vol. 571, Issue 1, 2007, pp. 97-118.

https://doi.org/10.1017/S0022112006003223

[68] Anon, "Fluid Forces, Pressure and Moments on Rectangular Blocks," *Engineering Science Data Unit Item 71016*, 1978.

[69] Cooper, K. R., "The Effect of Front-Edge Rounding and Rear-Edge Shaping on the Aerodynamic Drag of Bluff Vehicles in Ground Proximity," SAE Technical Papers, 1985.

https://doi.org/10.4271/850288

[70] Hucho, W. H., Janssen, L. J., and Emmelmann, H. J., "The Optimization of Body Details-A Method for Reducing the Aerodynamic Drag of Road Vehicles," SAE Technical Papers, 1976. https://doi.org/10.4271/760185

[71] Kääriä, C. H., Forrest, J. S., and Owen, I., "The Virtual AirDyn: A Simulation Technique for Evaluating the Aerodynamic Impact of Ship Superstructures on Helicopter Operations," *The Aeronautical Journal*, Vol. 117, No. 1198, 2013, pp. 1233-1248. https://doi.org/10.1017/S0001924000008836

[72] Millward, A., Nicholson, K., and Preston, J. H., "The Use of Jet Injection to Produce Uniform Velocity in a High Speed Water Channel," *Journal of Ship Research*, Vol. 24, No. 2, 1980.

[73] Barlow, J. B., Rae, W. H. & Pope, A., "Low-Speed Wind Tunnel Testing," New York John Wiley & Sons, 3rd edition, 1999.

[74] White, F. M., *"Fluid Mechanics, 7th Edition,"* McGraw-Hill, New York, 2011.

[75] ABB, Mint Workbench Version 5 [Computer software], 2018.

[76] National Instruments, LabVIEW [Computer software], 2020.

[77] Kraus, N. C., Lohrmann, A., and Cabrera, R., "New Acoustic Meter for Measuring 3D Laboratory Flows," *Journal of Hydraulic Engineering*, Vol. 120, No. 3, 1994, pp. 406–412. https://doi.org/10.1061/(ASCE)0733-9429(1994)120:3(406)

[78] Lohrmann, A., Cabrera, R., and Kraus, N. C., "Acoustic Doppler Velocimeter (ADV) for Laboratory Use," *Fundamental and Advancements in Hydraulic Measurements and Experimentation*, Buffalo, New York, 1994.

[79] Nortek, "*The Comprehensive Manual for Velocimeters*," 2018.

[80] Nikora, V. I., and Goring, D. G., "ADV Measurements of Turbulence: Can We Improve Their Interpretation?," *Journal of Hydraulic Engineering*, Vol. 124, No. 6, 1998, pp. 2–6. https://doi.org/10.1061/(ASCE)0733-9429(1998)124:6(630)

[81] Poindexter, C. M., Rusello, P. J., and Variano, E. A., "Acoustic Doppler Velocimeter-Induced Acoustic Streaming and Its Implications for Measurement," *Experiments in Fluids*, Vol. 50, 2011, pp. 1429–1442. https://doi.org/10.1007/s00348-010-1001-2

[82] Lane, S. N., Biron, P. M., Bradbrook, K. F., Butler, J. B., Chandler, J. H., Crowell, M. D., McLelland, S. J., Richards, K. S., and Roy, A. G., "Three-Dimensional Measurement of River Channel Flow Processes Using Acoustic Doppler Velocimetry," *Earth Surface Processes and Landforms*, Vol. 23, No. 13, 1998, pp. 1247–1267. https://doi.org/10.1002/(SICI)1096-9837(199812)23:13<1247::AID-ESP930>3.0.CO;2-D

[83] Wong, G. S. K., and Zhu, S. M., "Speed of Sound in Seawater as a Function of Salinity, Temperature, and Pressure," *Journal of the Acoustical Society of America*, Vol. 97, No. 3, 1995, pp. 1732–1736.

https://doi.org/10.1121/1.413048

[84] Nortek, "*Nortek Vectrino Velocimeter Technical Specification*," 2019.

[85] Chanson, H., "Acoustic Doppler Velocimetry (ADV) in the Field and in Laboratory: Practical Experiences," *International Meeting on Measurements and Hydraulics of Sewers*, IMMHS'08, Summer School GEMCEA/LCPC, Bouguenais, France, August 2008.

[86] Goring, D. G., and Nikora, V. I., "Despiking Acoustic Doppler Velocimeter Data," *Journal of Hydraulic Engineering*, Vol. 128, No. 1, 2002, pp. 117–126.

https://doi.org/10.1061/(asce)0733-9429(2002)128:1(117)

[87] Whal, T. L., "Discussion of '"Despiking Acoustic Doppler Velocimeter Data"' by Derek G. Goring and Vladimir I. Nikora," *Journal of Environmental Engineering*, Vol. 129, No. 6, 2003. https://doi.org/10.1061/(ASCE)0733-9429(2003)129:6(484)

[88] Voulgaris, G., and Trowbridge, J. H., "Evaluation of the Acoustic Doppler Velocimeter (ADV) for Turbulence Measurements," *Journal of Atmospheric and Oceanic Technology*, Vol. 15, No. 1, 1998, pp. 272–289.

https://doi.org/10.1175/1520-0426(1998)015<0272:EOTADV>2.0.CO;2

[89] McLelland, S. J., and Nicholas, A. P., "A New Method for Evaluating Errors in High-Frequency ADV Measurements," *Hydrological Processes*, Vol. 14, No. 2, 2000, pp. 351–366. https://doi.org/10.1002/(SICI)1099-1085(20000215)14:2<351::AID-HYP963>3.0.CO;2-K

[90] Khorsandi, B., Mydlarski, L., and Gaskin, S., "Noise in Turbulence Measurements Using Acoustic Doppler Velocimetry," *Journal of Hydraulic Engineering*, Vol. 138, No. 10, 2012, pp. 829–838.

https://doi.org/10.1061/(asce)hy.1943-7900.0000589

[91] García, C. M., Cantero, M. I., Niño, Y., García, M. H., Garcia, C. M., Cantero, M. I., Nino, Y., and Garcia, M. G., "Turbulence Measurements with Acoustic Doppler Velocimeters," *Journal of Hydraulic Engineering*, Vol. 131, No. 12, 2005, pp. 1062–1073.

https://doi.org/10.1061/(asce)0733-9429(2005)131:12(1062)

[92] Chanson, H., Trevethan, M., and Koch, C., "Discussion of 'Turbulence Measurements with Acoustic Doppler Velocimeters' by Carlos M. García, Mariano I. Cantero, Yarko Niño, and Marcelo H. García December," *Journal of Hydraulic Engineering*, Vol. 133, No. 11, 2007, pp. 1283–1286.

https://doi.org/10.1061/(ASCE)0733-9429(2007)133:11(1286)

[93] Rusello, P. J., "*Near Boundary Measurements with a Profiling Acoustic Doppler Velocimeter*," *Nortek*, 2013.

[94] Koca, K., Noss, C., Anlanger, C., Brand, A., and Lorke, A., "Performance of the Vectrino Profiler at the Sediment–Water Interface," *Journal of Hydraulic Research*, Vol. 55, No. 4, 2017, pp. 573–581.

https://doi.org/10.1080/00221686.2016.1275049

[95] Jackson, D. R., Richardson, M. D., Isakson, M. J., and Wilson, P. S., "High-Frequency Seafloor Acoustics," *The Journal of the Acoustical Society of America*, Vol. 122, No. 5, 2007. https://doi.org/10.1121/1.2782933

[96] Greenspan, M., and Tschiegg, C. E., "Speed of Sound in Water by a Direct Method," *Journal of Research of the National Bureau of Standards*, Vol. 59, No. 4, 1957.

https://doi.org/10.6028/jres.059.028

[97] John Wiley & Sons, I., "*Properties and Behavior of Polymers, Volume 2*," 2011.

[98] Granta Design, CES EduPack, [Computer software], 2019.

[99] Young, A. D. and Paterson, J. H., "Aircraft Excrescence Drag," AGARDograph No. 264, 1981.

[100] Klebanoff, P. L., "Characteristics of turbulence in a boundary layer with zero gradient," National Advisory Committee for Aeronautics, Report No. 1247, 1995.

[101] Ogilvy, J. A., "Computer Simulation of Acoustic Wave Scattering from Rough Surfaces," *Journal of Physics D: Applied Physics*, Vol. 21, No. 2, 1988, pp. 260–277.

https://doi.org/10.1088/0022-3727/21/2/006

[102] Ticconi, F., Pulvirenti, L., and Pierdicc, N., "Models for Scattering from Rough Surfaces," *Electromagnetic Waves*, IntechOpen, June 2011.

https://doi.org/10.5772/19318

[103] Strutt, J. W., *"The Theory of Sound,"* Macmillan and co., 1877.

[104] Anderson, J., "Computational Fluid Dynamics: The Basics with Applications. 1995," McGraw-Hill Inc, 1995.

[105] Institute, C. M., "*Millennium Problems Navier-Stokes Equation,*" [Online]. [Accessed 9 January 2021]. Available from https://claymath.org/millennium-problems/navier%E2%80%93stokes-equation.

[106] Bakker, A., *"Applied Computational Fluid Dynamics,"* [Online]. [Accessed 9 January 2021]. Available from http://www.bakker.org/dartmouth06/engs150/10-rans.pdf.

[107] Launder, B. E., and Sharma, B. I., "Application of the Energy-Dissipation Model of Turbulence to the Calculation of Flow near a Spinning Disc," *Letters in Heat and Mass Transfer*, Vol. 1, No. 2, 1974, pp. 131-137.

https://doi.org/10.1016/0094-4548(74)90150-7

[108] Wilcox, D. C., "Reassessment of the Scale-Determining Equation for Advanced Turbulence Models," *AIAA Journal*, Vol. 26, No. 11, 1988, pp. 1299-1310. https://doi.org/10.2514/3.10041

[109] Menter, F. R., Kuntz, M., and Langtry, R., "Ten Years of Industrial Experience with the SST Turbulence Model Turbulence Heat and Mass Transfer," *4th Internal Symposium, Turbulence, heat and mass transfer*, Antalya, Turkey, 2003.

[110] Tu, J., Yeoh, G. H., and Liu, C., "Computational Fluid Dynamics: A Practical Approach," Elsevier, Oxford, UK, 1st edition, 2008.

[111] Forrest, J. S., Owen, I., Padfield, G. D., Hodge, S. J., "Detached-Eddy Simulation of Ship Airwakes for Piloted Helicopter Flight Simulation," *International Aerospace CFD Conference*, Paris, France, June 2007.

[112] Yesilel, H., and Edis, F. O., "Ship Airwake Analysis by CFD Methods," *AIP Conference Proceedings*, Vol. 936, No. 674, 2007. https://doi.org/10.1063/1.279023

[113] Forrest, J. S., "*Predicting Ship-Helicopter Operating Limits Using Time-Accurate CFD Ship Airwakes and Piloted Flight Simulation*," University of Liverpool Thesis, 2009.

[114] Smagorinsky, J., "General Circulation Experiments with the Primitive Equations: 1. The Basic Experiment," *Monthly Weather Review*, Vol. 91, No. 3, 1963, pp. 99-164. https://doi.org/10.1175/1520-0493(1963)091<0099:gcewtp>2.3.co;2

[115] Spalart, P. R., Jou, W. H., Strelets, M. K., and Allmaras, S. R., "Comments on the Feasibility of LES for Wings and on a Hybrid RANS/LES Approach," *Advances in DNS/LES: Direct numerical simulation and large eddy simulation*, Ruston, Louisiana, 1997.

[116] Menter F. R., Kuntz M., "Adaptation of Eddy-Viscosity Turbulence Models to Unsteady Separated Flow Behind Vehicles," *The Aerodynamics of Heavy Vehicles: Trucks, Buses, and Trains. Lecture Notes in Applied and Computational Mechanics*, vol 19. Springer-Berlin Heidelberg, 2004. https://doi.org/10.1007/978-3-540-44419-0_30

[117] Spalart, P. R., Deck, S., Shur, M. L., Squires, K. D., Strelets, M. K., and Travin, A., "A New Version of Detached-Eddy Simulation, Resistant to Ambiguous Grid Densities," *Theoretical and Computational Fluid Dynamics*, Vol. 20, No. 181, 2006. https://doi.org/10.1007/s00162-006-0015-0

[118] Spalart, R., "Young-Person's Guide to Detached-Eddy Simulation Grids," NASA/CR-2001-211032, 2001.

[119] ANSYS Inc., "*ANSYS Fluent User Guide*," 2016.

[120] ANSYS Inc., "ANSYS Fluent User Guide," 2003.

[121] ANSYS Inc., "Theory Guide Release 12.0," 2009.

[122] Roper, D. M., "*Integrating Computational Fluid Dynamics and Piloted Simulation to Quantify Ship-Helicopter Operating Limits*," University of Liverpool Thesis, 2006.

[123] Kelly, M. F., White, M. D., Owen, L., and Hodge, S. J., "Piloted Flight Simulation for Helicopter Operation to the Queen Elizabeth Class Aircraft Carriers," *43rd European Rotorcraft Forum,* Milan, Italy, 2017.

[124] Garratt, J. R., "The Atmospheric Boundary Layer," Cambridge University Press, 1992.

[125] McRuer, D. T., "Interdisciplinary Interactions and Dynamic Systems Integration," *International Journal of Control*, Vol. 59, No. 1, 1994, pp. 3-12. https://doi.org/10.1080/00207179408923067

[126] Scott, P., Owen, I., and White, M. D., "The Effect of Ship Size on the Flying Qualities of Maritime Helicopters," *70th American Helicopter Society Forum,* Montreal, Canada, May 2014.

[127] Polsky, S. A., and Bruner, W. W., "Computational Study of Unsteady Ship Airwake," *RTO AVT Symposium on "Advanced Flow Management: Part A –Vortex Flows and High Angle of Attack for Military Vehicles*, Leon, Norway, 2001.

[128] Hunt, J. C. R., Wray, A. A., and Moin, P., "Eddies, Streams, and Convergence Zones in Turbulent Flows," *Center for Turbulence Research, Proceedings of the Summer Program*, 1988, pp. 193-208.

[129] Czerwiec, R. M., and Polsky, S. A., "LHA Airwake Wind Tunnel and CFD Comparison with and without Bow Flap," *22nd Applied Aerodynamics Conference and Exhibit,* American Institute of Aeronautics and Astronautics, Providence, Rhode Island, 2004. https://doi.org/10.2514/6.2004-4832

[130] Bardera, R., Rodríguez-Sevillano, A., León-Calero, M., and Nova-Trigueros, J., "Three-Dimensional Characterization of Passive Flow Control Devices over an Aircraft Carrier Ski-Jump Ramp," *Proceedings of the Institution of Mechanical Engineers, Part G: Journal of Aerospace Engineering*, Vol. 232, No. 15, 2018, pp. 2737-2744. https://doi.org/10.1177/0954410017716195

[131] Urnes, J. M., Hess, R. K., Moomaw, R. F., and Huff, R. W., "H-Dot Automatic Carrier Landing System for Approach Control in Turbulence," *Journal of Guidance and Control*, Vol. 4, No. 2, 1981, pp. 177–183.

https://doi.org/10.2514/3.56069

[132] NAVAIR, "NATOPS Landing Signal Officer Manual, NAVAIR-00-80T-104," 2009.

[133] Denham, J. W., Krumenacker, J. L., W., D. G., and Lewis, M., "Taking Advanced STOVL Flight Control to Sea: The VAAC Follow-on Research Programme," *American Helicopter Society Aerodynamics, Acoustics, and Test and Evaluation Technical Specialists Meeting*, San Francisco, California, 2002.

[134] Denham, J. W., "Project MAGIC CARPET: 'Advanced Controls and Displays for Precision Carrier Landings,'" *54th AIAA Aerospace Sciences Meeting*, American Institute of Aeronautics and Astronautics, San Diego, California, 2016.

https://doi.org/10.2514/6.2016-1770

[135] Memon, W. A., Owen, I., and White, M. D., "Motion Fidelity Requirements for Helicopter-Ship Operations in Maritime Rotorcraft Flight Simulators," *Journal of Aircraft*, Vol. 56, No. 6, 2019, pp. 2189–2209.

https://doi.org/10.2514/1.C035521

[136] Wang Y., White M. D., Owen I., Hodge S. and Barakos G., "Effects of Visual and Motion Cues in Flight Simulation of Ship-Borne Helicopter Operations," *CEAS Aeronautical Journal*, Vol. 4, No. 4, 2013, pp. 385–396.

https://doi.org/10.1007/s13272-013-0085-9

[137] Du Val, R. W., and He, C., "Validation of the FLIGHTLAB Virtual Engineering Toolset," *Aeronautical Journal*, Vol. 122, No. 1250, 2018, pp. 519-555.

https://doi.org/10.1017/aer.2018.12

[138] Padfield, G. D., "Helicopter Flight Dynamics," Blackwell Science, Oxford, UK, 1996.

[139] Beck, C. P., and Funk, J. D., "Development and Validation of a Seahawk Blade Element Helicopter Model in Support of Rotorcraft Shipboard Operations," *RAeS Rotorcraft Group Conference on 'Rotorcraft Simulation,* Royal Aeronautical Society, 1994.

[140] Peters, D. A., and He, C., "Finite State Induced Flow Models Part II; Three Dimensional Rotor Disk", *Journal of Aircraft*, Vol. 32, No. 2, 1995, pp. 323-333.

https://doi.org/10.2514/3.46719

[141] Howlett, J. J., "UH-60A Black Hawk Engineering Simulation Program: Volume I - Mathematical Model," *NASA Contractor Report 66309*, 1981.

[142] Hoencamp, A., "An Overview of SHOL Testing within the Royal Netherlands Navy," *35th European Rotorcraft Forum*, Hamburg, Germany, 2009.

[143] Advani, S., and Wilkinson, C., "Dynamic Interface Modelling and Simulation - A Unique Challenge," *Royal Aeronautical Society Conference on Helicopter Flight Simulation*, Royal Aeronautical Society, London, November 2001.

[144] Bardera-Mora, R., León Calero, M., and García-Magariño, A., "Aerodynamic Effect of the Aircraft Carrier Island on Flight Deck Flow with Cross Wind," *Proceedings of the Institution of Mechanical Engineers Part M: Journal of Engineering for the Maritime Environment*, Vol. 232, No. 2, 2017, pp. 145-154.

https://doi.org/10.1177/1475090216689172

[145] Crozon, C., Steijl, R., and Barakos, G. N., "Coupled Flight Dynamics and CFD-Demonstration for Helicopters in Shipborne Environment," *Aeronautical Journal*, Vol. 122, No. 1247, 2018, pp. 42-82.

https://doi.org/10.1017/aer.2017.112

[146] Oruc, I., Horn, J. F., Shipman, J., and Polsky, S., "Towards Real-Time Pilot-in-the-Loop CFD Simulations of Helicopter/Ship Dynamic Interface," *International Journal of Modeling, Simulation, and Scientific Computing*, Vol. 8, No. 4, 2017, paper 1743005. https://doi.org/10.1142/S179396231743005X

[147] McTaggart, K., "*Validation of ShipMo3D Version 1.0 User Applications for Simulation of Ship Motion,*" Technical Memorandum DRDC Atlantic TM 2007-173, August 2007.

[148] ITTC Seakeeping Committee Report, "Bretschneider spectrum," The Hague, 1978.

[149] Ministry of Defence, "*Defence Standard 00-133 Part 3 Issue 2 Aviation Arrangements in Surface Ships: Design, Construction and Provision (Flight Deck)*," DEF STAN 00-133: Part 3, August 2015.

[150] Naval Air Systems Command, "*NATOPS Flight Manual Navy Model SH-60B Helicopter*," A1-H60BB-NFM-000, 2008.

[151] Memon, W. A., "*The Development of High-Fidelity Modelling & Simulation for the Helicopter Ship Dynamic Interface*," University of Liverpool Thesis, 2019.

[152] L. T. Nguyen, M. E. Ogburn, W. P. Gillert, K. S. Kibler, P. W. Brown and P. L. Deal, "Simulator Study of Stall/Post-Stall Characteristics of a Fighter Airplane with Relaxed Longitudinal Static Stability", *NASA Technical Paper 1538*, 1979.

[153] Lee, D., Sezer-Uzol, N., Horn, J. F., and Long, L. N., "Simulation of Helicopter Shipboard Launch and Recovery with Time-Accurate Airwakes," *Journal of Aircraft*, Vol. 42, No. 2, 2005, pp. 448–461.

https://doi.org/10.2514/1.6786

[154] Hess, R. A., "Simplified Technique for Modeling Piloted Rotorcraft Operations near Ships," *Journal of Guidance, Control, and Dynamics*, Vol. 29, No. 6, pp. 1339-1349, 2006. https://doi.org/10.2514/1.18711

[155] Memon, W. A., Owen, I., and White, M. D., "SIMSHOL: A Predictive Simulation Approach to Inform Helicopter–Ship Clearance Trials," *Journal of Aircraft*, Vol. 57, No. 5, 2020, pp. 854-875.

https://doi.org/10.2514/1.C035677

[156] Wang, Y., Curran, J., Padfield, G. D., and Owen, I., "AirDyn: An Instrumented Model-Scale Helicopter for Measuring Unsteady Aerodynamic Loading in Airwakes," *Measurement Science and Technology*, Vol. 22, No. 4, 2011.

https://doi.org/10.1088/0957-0233/22/4/045901

[157] Polsky, S., and Naylor, S., "CVN Airwake Modeling and Integration: Initial Steps in the Creation and Implementation of a Virtual Burble for F-18 Carrier Landing Simulations," *AIAA Modeling and Simulation Technologies Conference*, American Institute of Aeronautics and Astronautics, San Francisco, California, 2005.

https://doi.org/10.2514/6.2005-6298

[158] Birckelbaw, L. G., McNeill, W. E., and Wardwell, D. A., "Aerodynamics Model for a Generic ASTOVL Lift-Fan Aircraft," NASA/TM-1995-110347, April 1995.

[159] Smith, W. G., and Lazzeroni, F. A., "Experimental and Theoretical Study of a Rectangular Wing in a Vortical Wake at Low Speed," NASA TN D-339, October 1960.

[160] McMillan, O. J., Schwind, R. G.; Nielsen, J. N., and Dillenius, M. F. E., "Rolling Moments in a Trailing Vortex Flowfield," *Journal of Aircraft*, Vol. 15, No. 5, 1978, pp. 280-286. https://arc.aiaa.org/doi/10.2514/3.58356

[161] Hastings, E. C., Jr., and Keyser, G. L, "Simulation Study of Vortex Encounters by a Twin-Engine, Commercial, Jet Transport Airplane," NASA TP-1966, February 1982.

[162] Rossow, V. J., "Estimate of Loads During Wing-Vortex Interactions by Munk's Transverse-Flow Method," *Journal of Aircraft*, Vol. 27, No. 1, 1990, pp. 66-74. https://doi.org/10.2514/3.45897

[163] Reimer, H. M., and Vicroy, D. D., "A Preliminary Study of Wake Vortex Encounter Hazard Boundary for a 737-100 Airplane," NASA TM-110223, April 1996.

[164] Hallock, J. N. "Aircraft Wake Vortices: An Assessment of the Current Situation". DOT-FAARD-90-29, January 1991.

[165] Stewart, E. C., "A Parametric Study of Accelerations of an Airplane Due to a Wake Vortex System". NASA/TM-1999-208745, May 1999.

[166] Birckelbaw, L. G., McNeill, W. E., and Wardwell, D. A., "Aerodynamics Model for a Generic ASTOVL Lift-Fan Aircraft". NASA/TM-1995-110347, April 1995.

[167] Williams, J. E.; and Vukelich, S. R., "The USAF Stability and Control Digital DATCOM; Volumes I, II, and III". AFFDL-TR-79-3032, April 1979.

[168] Gloudemans, J. R., Davis, P. C., and Gelhausen, P. A., "A rapid geometry modeler for conceptual aircraft", *The 34th Aerospace Sciences Meeting and Exhibit*, American Institute of Aeronautics and Astronautics, Reno, Nevada, January 1996.
https://doi.org/10.2514/6.1996-52

[169] Montgomerie, B., "Methods for Root Effects, Tip Effects and Extending the Angle of Attack Range to ±180°, with Application to Aerodynamics for Blades on Wind Turbines and Propellers", Swedish Defence Research Agency Scientific Report FOI-R—1305-SE, 2004.

[170] Denham, J. W., Krumenacker, J. L., D'Mello, G. W., and Lewis, M., "Taking Advanced STOVL Flight Control to Sea: The VAAC Follow-on Research Programme," *American Helicopter Society Aerodynamics, Acoustics, and Test and Evaluation Technical Specialists Meeting*, San Francisco, California, 2002.

[171] Harris, J. J., and Stanford, J. R., "F-35 Flight Control Law Design, Development, and Verification," *The F-35 Lightning II: From Concept to Cockpit*, American Institute of Aeronautics and Astronautics, Inc., 2019, pp. 287–311.
https://doi.org/10.2514/5.9781624105678.0287.0312

Appendix A Aerodynamic Modelling of a Generic Fixed-wing STOVL Aircraft

The introduction to this thesis explained how a major objective in the research project was to supply unsteady airwakes for the full-scale QEC carrier to be implemented in the F-35B/QEC simulator at BAE Systems, Warton. The simulated flight trials were conducted and feedback from the test pilots who had conducted the trials indicated that the experience in the simulator was an excellent preparation for what they encountered at sea (see pilot feedback comment in Section 1.8). Having created, and validated, the airwakes, this research then went on to integrate them into the HELIFLIGHT-R simulator to conduct helicopter deck landings, as reported in Chapters 5 and 6. Flight dynamics models for fixed-wing flight simulation typically use a single angle of attack at the centre of gravity to calculate the forces generated by the aerodynamic surface using look-up tables [152]. Any change in airwake velocity across the span of the lifting surfaces is not accounted for. This approach is suitable for aircraft flying at typical cruise speeds and altitudes, however, carrier-borne aircraft such as STOVL aircraft hovering above the deck typically encounter unsteady three-dimensional air flow with non-uniform flow fields. Other fixed-wing flight dynamics models, such as the four-point model, have been used to investigate the turbulent wind and its effect on flight, although it is considered only suitable for applications where the flow field gradients are uniform [157]. Unfortunately (and understandably), it was not possible to access the highly-sensitive F-35B flight model to investigate the effect of non-uniform velocities across the aircraft and, therefore, a generic STOVL model was adapted for this purpose. The aerodynamic model is based on the generic Advanced STOVL (ASTOVL) concept aircraft developed by NASA [158] and uses a modified strip theory. The model has then been subjected to unsteady airwakes produced by the QEC carrier to assess the effect of the airwake on the generic STOVL aircraft model.

A.1 Aerodynamic Model

To accurately model an aircraft for flight simulation, the underlying aerodynamic model must capture both the aerodynamic characteristics of the aircraft itself and the flow field in which it operates. Typical aerodynamic models for fixed-wing flight simulation assume that the aircraft is operating in a relatively steady airflow. Although this assumption holds true for most scenarios, where any change in the flow field is generally uniform, it becomes invalid when the aircraft encounters complex three-dimensional flow fields such as those produced by the presence of a large body upstream of the aircraft. Examples of these flight environments include a fixed-wing aircraft operating in the wake generated by another aircraft, e.g., air-to-air refuelling, during take-off, or, as in this case, in the wake generated by a ship's superstructure. The unsteady wakes result in air velocities which vary across the aircraft's lifting surfaces. The choice of aerodynamic model then becomes significant, since more simplistic models are not able to resolve this non-uniform flow field and may produce incorrect forces and moments acting on the aircraft. Several studies have investigated the interaction of fixed-wing aircraft in the wake of other bodies using a variety of techniques of varying complexity [157-164]. However, for piloted flight simulation the modelling of aerodynamic loads on the aircraft must be computed in real-time, prohibiting the use of more computationally demanding techniques.

Figure A-1 shows examples of aerodynamic models for aircraft that can be applied for flight simulation in real-time: the centre of gravity model, the four-point model and a generic strip theory model. The more generally adopted aerodynamic model for flight simulation shown in Figure A-1 (a) uses look-up tables to calculate the aerodynamic forces and moments, which are dependent on the effective angle-of-attack at the centre of gravity. This model is insufficient for aircraft flying in highly unsteady three-dimensional air flow as the effective angle-of-attack may vary across the airframe. The more complex four-point aerodynamic model shown in Figure A-1 (b) has been used to investigate turbulent air flow but is only considered suitable for applications in which the flow field gradients are uniform. The generic strip theory model shown in Figure A-1 (c) has an advantage over the other two models in that the local flow velocity is applied at many points along each lifting surface, therefore, enabling the total forces and moments acting on the aircraft to be calculated.

(a) (b) (c)

Figure A-1 Aerodynamic models: (a) Centre of gravity model, (b) Four-point model, (c) Strip theory model.

The model used in this study to calculate the aerodynamic loads on the aircraft is based on a generic strip theory method used previously by Stewart [165] in a study of aircraft accelerations in a wake vortex system. The model uses three axis systems: the aerodynamic surface axis system, the body axis system and the earth axis system, as shown in Figure A-2. The aerodynamic surface axis system is used to model the wing, canard, tail and fuselage panels. Each panel is segmented into *N* incremental areas or strips parallel to the *x*-axis. The aerodynamic surface axis systems are located at defined locations in *x, y, z* and rotation angle η (about the *x*-axis) relative to the airplane body axis; the body axis is located at the aircraft's centre of gravity and angular orientation relative to the earth axis system is specified as the standard aircraft Euler angles (φ, θ, ϕ) for aircraft yaw, pitch and roll.

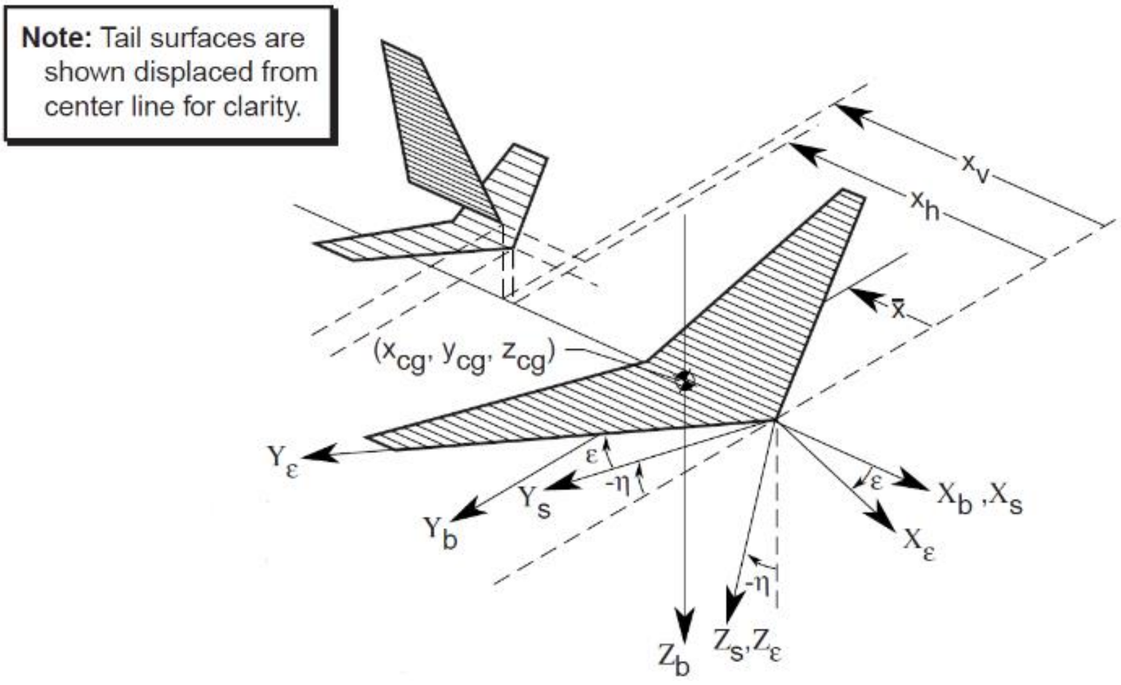

Note: Tail surfaces are shown displaced from center line for clarity.

Figure A-2 Strip theory axis systems [165].

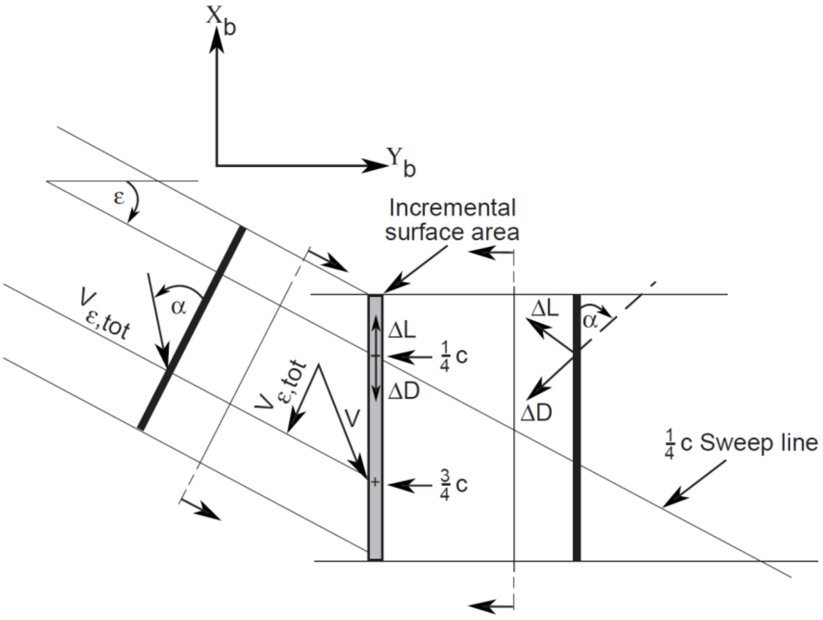

Figure A-3 Detail of geometry of an incremental surface area showing flow angles and aerodynamic forces [165].

At the three-quarter-chord point of each incremental strip, the effective angle-of-attack and sideslip is computed from the local air velocity components independent from neighbouring strips, as shown in Figure A-3. Using defined lift and drag polars for each panel, the lift and drag coefficients are calculated for each strip. The area of the local strip is calculated in equation A.1 and used to compute the lift and drag for the section in equations A.2 and A.3 accounting for the effect of sweep; the lift and drag forces are then integrated over the whole surface to produce the overall magnitude and direction of force.

$$\Delta Area = \frac{|l_y|}{N} c_r \left[1 + \frac{(\lambda - 1)|y_s|}{|l_y|} \right] \tag{A.1}$$

$$\Delta L = \frac{1}{2} \rho V_{\varepsilon,tot}^2 \cdot \Delta Area \cdot c_l \tag{A.2}$$

$$\Delta D = \frac{1}{2} \rho V_{\varepsilon,tot}^2 \cdot \Delta Area \cdot c_d \tag{A.3}$$

$$\begin{bmatrix} M_x \\ M_y \\ M_z \end{bmatrix} = \begin{bmatrix} y_b \cdot F_z - z_b \cdot F_y \\ z_b \cdot F_x - x_{b4} \cdot F_z \\ -y_b \cdot F_x + x_{b4} \cdot F_y \end{bmatrix} \tag{A.4}$$

Similarly, the forces acting at each strip location from the aircraft's centre of gravity provide the moment acting on that section calculated in equation A.4. The lifting forces and moments for each surface are summed and then combined to give the overall forces and moments acting on the aircraft. In this study the fuselage was also modelled as a lifting surface to assess its contribution to the aircraft's overall forces and moments. The relative simplicity of this method allows the aerodynamic loads over multiple lifting surfaces to be calculated in real-time using a look-up table of the airwake velocity field, as required for piloted flight simulation. A complete listing of the symbols in Figure A-2 and Figure A-3 and equations A.1 to A.4 is provided in the Nomenclature.

A.2 **NASA Advanced STOVL Model**

Supporting the development of an advanced STOVL demonstrator aircraft, NASA Ames Research Centre developed a mathematical model for simulation of an ASTOVL concept aircraft [166], the geometry of which is given in Table A-1. The ASTOVL model was designed as a single engine fighter/attack aircraft featuring a wing-canard arrangement with two vertical tails, as shown in Figure A-4. The power-off aerodynamics data for the ASTOVL concept was generated using DATCOM and Vortex Lattice Method (VLM) [167] at low speeds ($M \sim 0.2$) as the simulation was focused on the transition and hover flight regimes only. The ASTOVL model was chosen for the present investigation as it is the most complete and well documented model available in the public domain, which allows the effect of unsteady turbulent wakes to be investigated.

Table A-1 NASA ASTOVL aircraft geometry.

Aircraft	Overall length	16.9 m
	Overall height	4.3 m
	Weight	13600 kg
Wing	Area	48.6 m^2
	Span	11.0 m
	Leading edge sweep	40 deg
	Aerofoil	NACA 64A005
Canard	Area	22.6 m^2
	Span	7.5 m
	Leading edge sweep	40 deg
	Aerofoil	NACA 64A004.5

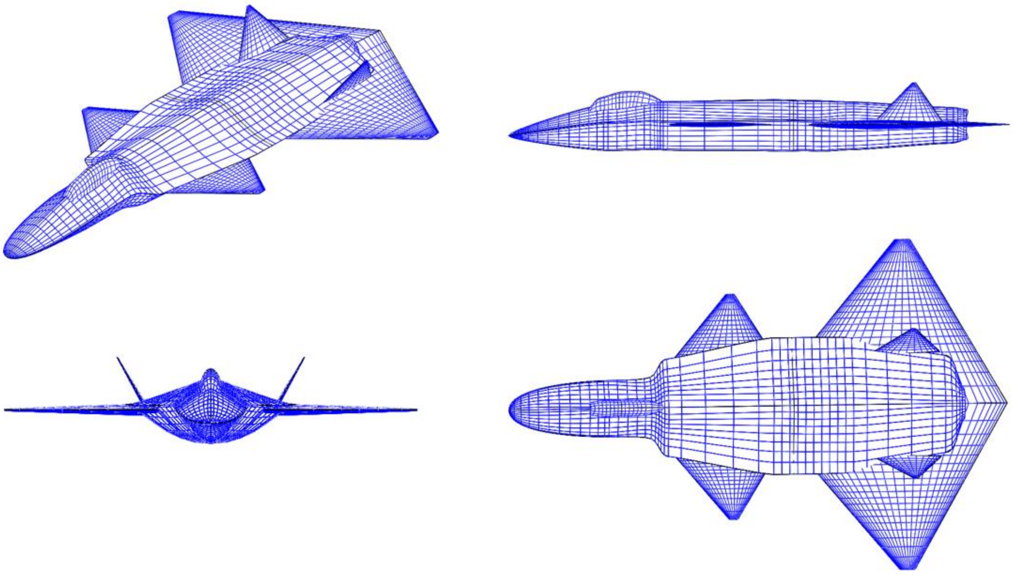

Figure A-4 NASA ASTOVL model geometry in VSPAERO.

As previously discussed, the strip theory method requires the aerodynamic characteristics of each lifting surface to be defined in order to compute the lift and drag at each surface strip. Although aerodynamic data was available for the ASTOVL model, it was limited to lift and drag polars for two separate entities only: the canards and the total aircraft without the canard. VSPAERO, an open source VLM method similar to the one used to produce the original NASA report data [168], was therefore employed in the present study to generate the additional aerodynamic data that was required. A 3D model of the ASTOVL aircraft was first created in the aircraft geometry software tool, OPENVSP, using the aerofoil profiles given in the NASA report; VSPAERO was then used to compute the coefficient of lift for each of the individual lifting surfaces over a range of angles-of-attack. Although the VLM method is unable to predict stall, VSPAERO permits the user to include an estimate of the $C_{l_{max}}$ derived from the original data. A comparison between the original ASTOVL lift polar and the VSPAERO generated data is presented in Figure A-5. The gradient of each lift curve slope is shown to be in good agreement, however, as higher angles-of-attack are reached, near the region of stall, some differences can be observed.

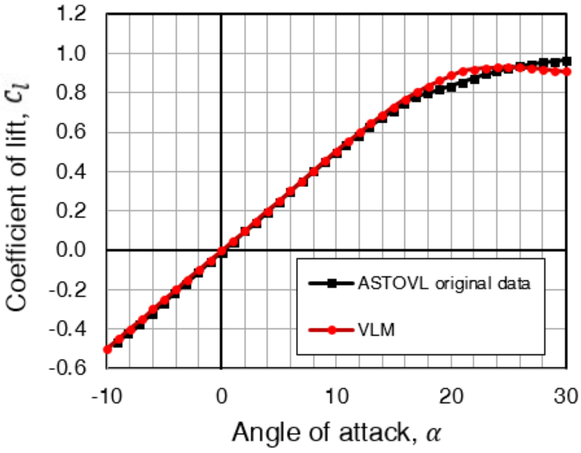

Figure A-5 Comparison of NASA ASTOVL and VLM computed lift polar.

Typically, a fixed-wing aircraft's flight envelope includes a minimum forward operating speed to produce enough lift. As STOVL aircraft are able to maintain height using vertical thrust vectoring they do not require any forward speed. In areas of separated or disturbed air, this reduction in freestream flow can create large, and even significantly negative, effective angles-of-attack over the lifting surfaces as vertical and lateral velocity components become more significant. To account for any large effective angles-of-attack, along the generic STOVL lifting surfaces, during hover in the disturbed wake of a ship's superstructure, the lift and drag polars were extended beyond -10 deg to 30 deg. Due to the complexity of modelling the lifting surfaces beyond the stall and at high angles-of-attack, the lift polar was extended using an approximation combining the effects of thin-plate theory and potential flow, as described by Montgomerie in [169]. The drag polar was also extended using the drag for a thin-plate. Both extended polars for the generic STOVL wing are shown in Figure A-6. The generated VLM lift curve slope is shown on the left as a solid black line with a maximum lift coefficient of approximately 1.0 at 40 deg angle-of-attack. Similarly, the data for drag from the original NASA report is shown in black

Figure A-6 (b) with a maximum drag coefficient identified as just over 1.2. The aerodynamic characteristics of each lifting surface was defined using Montgomerie's thin-plate approximation, allowing large effective angles-of-attack to be modelled and accounted for in the strip theory simulation.

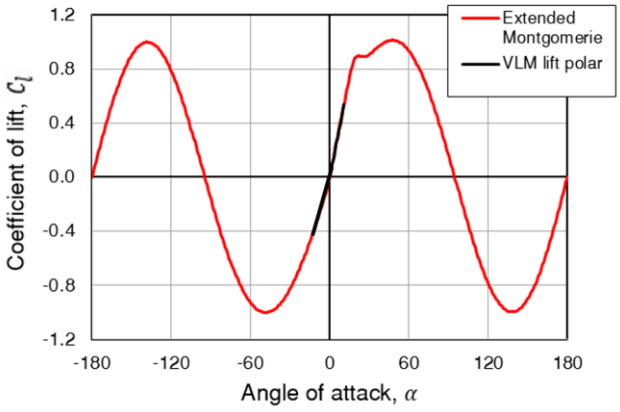

(a)

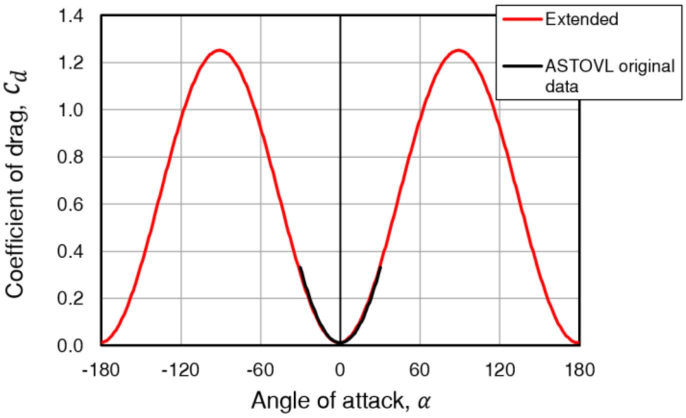

(b)

Figure A-6 Extended lift (a) and drag (b) polars for the generic STOVL wing surface.

A.3 Generic STOVL-QEC Analysis

Having developed the generic STOVL aerodynamic model, it was then used with the air velocities from QEC carrier airwakes to assess how the unsteady, non-uniform air flow affects the forces and moments on the model aircraft.

A.3.1 QEC Ship Airwake

The generic STOVL strip theory model was implemented in a relatively steady flow and an unsteady one to provide a comparison. Figure 4-41, Chapter 4, shows the flow over the QEC carrier in a headwind and Figure 4-42 (a) in a wind coming from 25 deg off the starboard side i.e., a Green 25 wind over deck. The airwakes are illustrated by mean streamlines in vertical planes that are aligned with the oncoming wind and pass through the landing spots. Horizontal planes coloured by turbulence intensity were also placed at 10 m as the approximate height of the centre of gravity for fixed-wing aircraft when translating across the deck during a vertical landing [170]; the streamlines are also coloured by turbulence intensity. The generic STOVL aircraft model was located 10 m above spot 3, the third spot from the bow of the ship along the portside edge, in a 35 kts Ahead and a 35 kts Green 25 WOD; the aircraft was aligned with the ship's centreline. As can be seen in Figure 4-41, in Ahead the flow over spot 3 is largely undisturbed, while the flow over spot 3 in a Green 25 wind is turbulent, because it is in the lee of the forward island. To illustrate this further, Figure A-7 shows the three normalized velocity components recorded for 30 seconds at the point 10 m above spot 3 in both the headwind and the Green 25 WOD. In the headwind the lateral and vertical (*v* and *w*) velocity components are close to zero, as expected, while the *u*-velocity component is relatively steady. However, in the Green 25 35 kts wind the velocity components are varying significantly with time. To integrate the airwake with the generic STOVL model for each wind condition, the local CFD velocities, such as those shown in Figure A-7, were applied at each strip along each of the lifting surfaces to produce the overall forces and moments on the aircraft at each time-step of the 30 second sample time of the CFD solution; the effect on the flow from the generic STOVL vectored thrust jets is not accounted and is, therefore, a one-way coupled model.

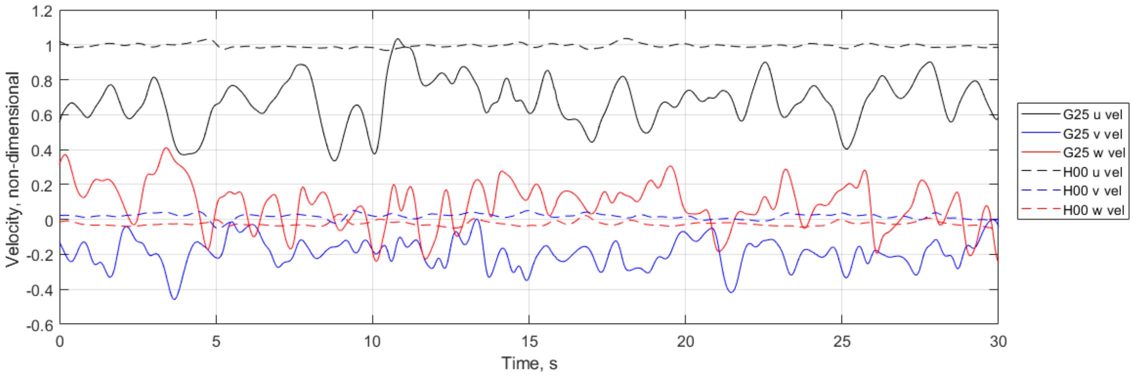

Figure A-7 Unsteady velocity components at a point 10 m above spot 3 in a 35 kts headwind and Green 25 WOD.

A.3.2 Integration of ASTOVL model with Ship Airwake

The process for integrating the velocity components of the CFD-generated airwake with the strip theory aerodynamic generic STOVL model is illustrated in Figure A-8 and is based on the more complex integration of the helicopter and airwake within FLIGHTLAB, illustrated earlier in Figure 5-4 The CFD solution produces 30 seconds of velocity data for each cell throughout the whole domain on an unstructured grid as shown in the top left of Figure A-8. The velocity components from the large overall domain are interpolated onto a structured grid of 1 m spacing in the region of interest over and around the flight deck, as shown in the bottom left of Figure A-8. To enable the playback of the data in real-time and to reduce the overall storage requirements, the data is down-sampled from the computed solution of 100 Hz to 25 Hz. The structured airwake data is then converted into a series of look-up tables from which the unsteady velocity components are applied to the strips in the generic STOVL strip theory aerodynamic model to produce the overall forces and moments acting on the aircraft.

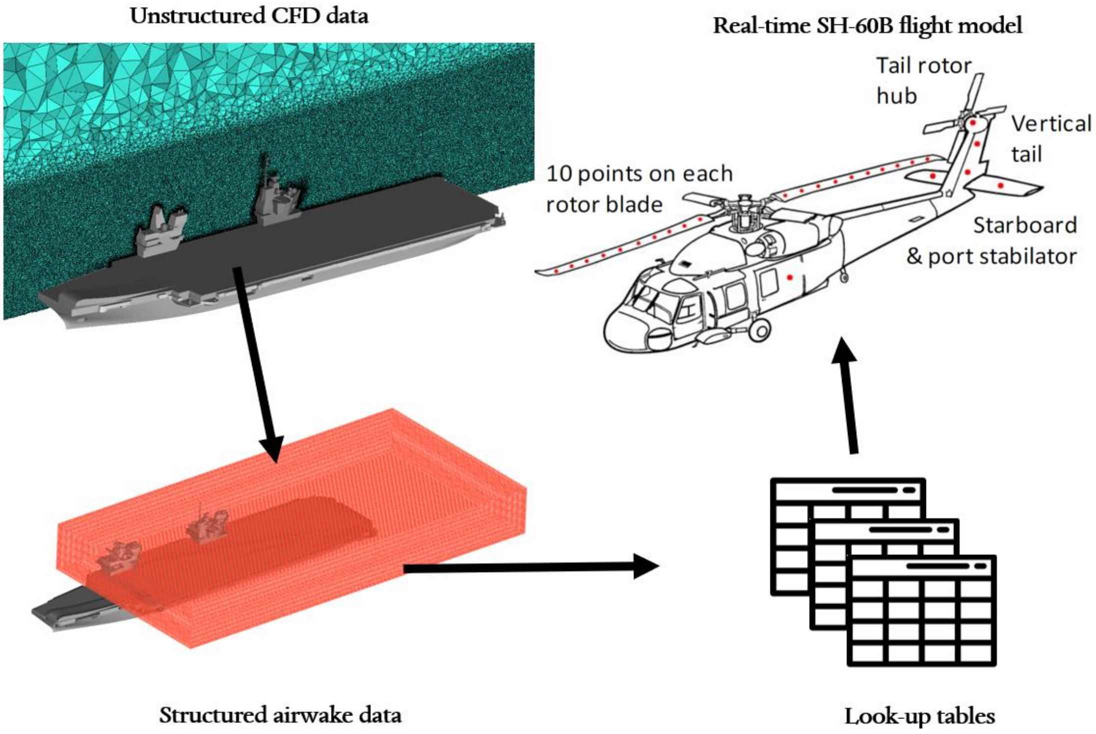

Figure A-8 Integration of CFD airwake with the generic STOVL strip theory model.

The number of strips on each surface of the aircraft is defined in the strip theory aerodynamic model. Figure A-9 shows each surface on the generic STOVL model; the wing, canard, vertical tails and body are each split into 5 strips, i.e., $N=5$. The forces and moments on each strip act at the one-quarter chord location, shown as red dots; the summation of the contributions from each strip produces the total forces and moments acting on the aircraft. The number of strips for each aircraft lifting surface may be varied according to the application; for this investigation the number of strips on all the surfaces was kept the same. To create an aerodynamic model for piloted flight simulation, the mathematical model must capture the applied forces and moments adequately with relatively low computing resources to allow processing in real-time. The number of strips chosen for each surface will affect how well the strip theory model responds to large gradients in the flow velocity along the lifting surfaces, and the amount of computer processing needed. A larger number of strips will more accurately, to a point, capture the velocity gradients in the airwake, however, as the number of strips is increased, the resultant computational time will also increase.

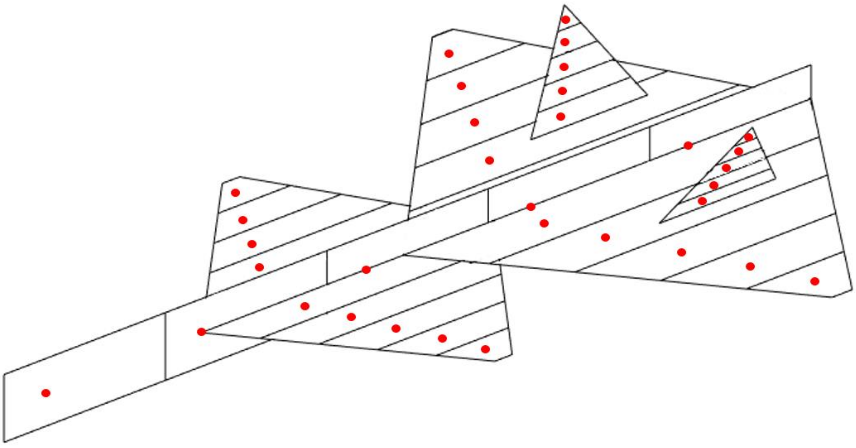

Figure A-9 Strip theory model of the generic STOVL aircraft (N = 5).

A.4 Analysis of QEC-STOVL integration

The generic STOVL strip theory aircraft model was held stationary at a hover position 10 m above spot 3 on the carrier deck, aligned with the centreline of the ship, in the 35 kts headwind and Green 25 WOD conditions. At each time step the local angle-of-attack at each strip was computed from the velocity components to give the lift and drag forces acting on each strip along the different surfaces and integrated to produce the overall forces and moments acting on the aircraft. The time-varying forces and moments acting on the aircraft in the unsteady airwake were calculated over a period of 30 seconds to determine the overall disturbance on the airframe while it was held stationary in a hover position. Figure A-10 shows an instantaneous coefficient of lift distribution across the total wing with a different number of strips, i.e., 10 and 100, across each span at spot 3 in a Green 25 wind. It can be seen that the highly disturbed air flow in the lee of the islands has caused a non-uniform lift distribution across the wing, with a predominately positive lift on the right wing and a negative lift on the left wing.

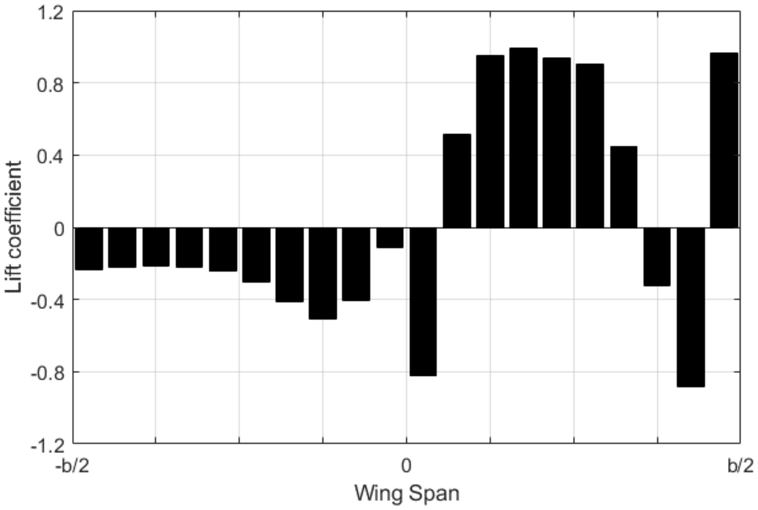

(a)

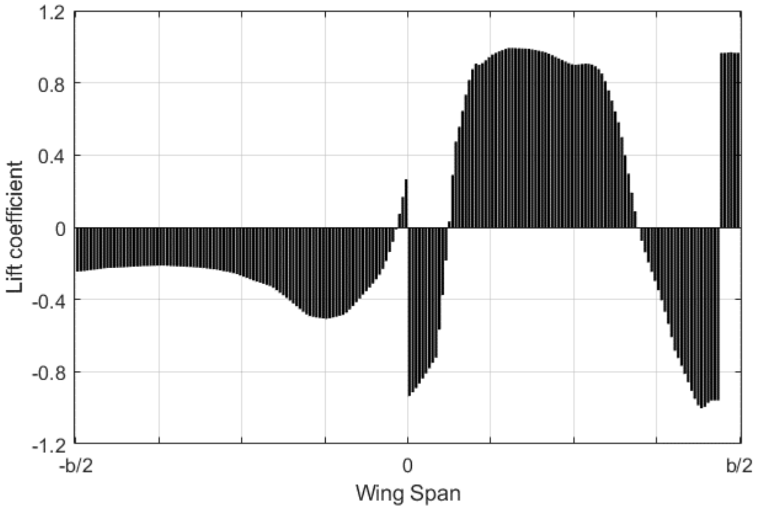

(b)

Figure A-10 Instantaneous coefficient of lift across wing for (a) 10 and (b) 100 strips.

To evaluate how many strips are required to fully capture the non-uniform air flow, Figure A-11 shows how the unsteady forces and moments vary with the number of strips across the main wings when the aircraft was exposed to the 35 kts Ahead WOD. The unsteady loads are represented by the root-mean-square (RMS) calculated from the 30 seconds of data, again for the aircraft hovering over spot 3. It can also be seen in Figure A-11 that the largest disturbance in force and moment is in lift and pitch, respectively.

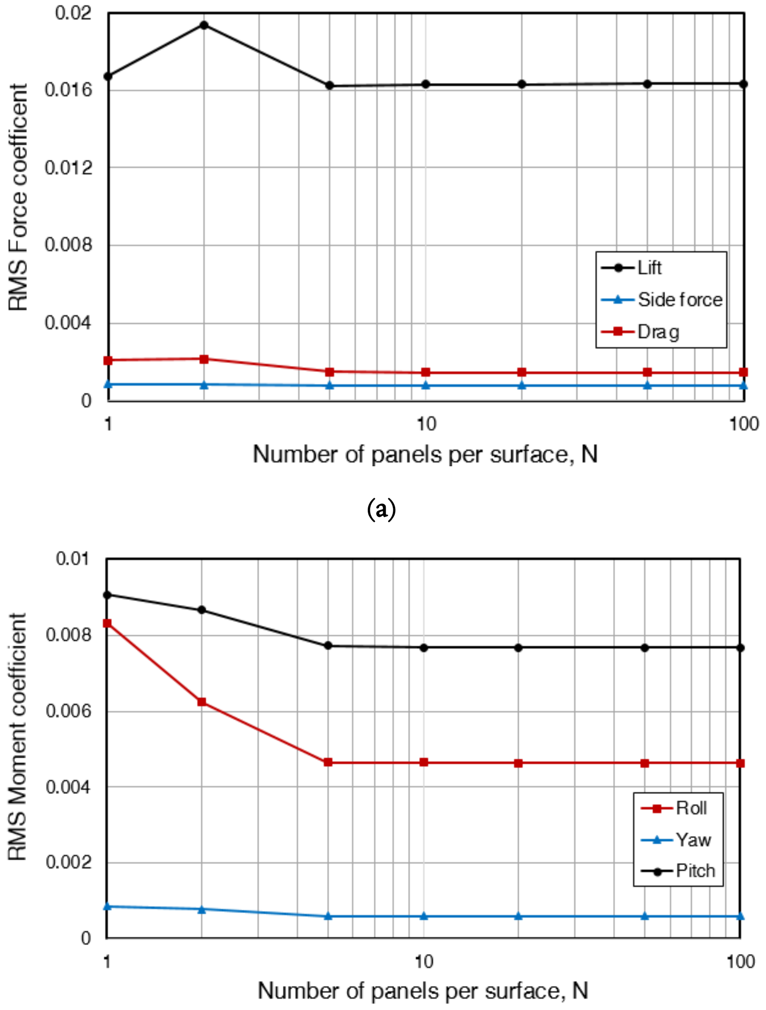

(a)

(b)

Figure A-11 RMS force (a) and moment (b) coefficients for different numbers of strips during hover in a headwind.

The unsteady forces and moments on the aircraft for different numbers of strips while the aircraft is in the more turbulent Green 25 airwake is shown in Figure A-12. The magnitude of the unsteady forces and moments in the more turbulent flow are greater than those shown in Figure A-11 for the headwind, as expected. Similar to the headwind, it can be seen that the RMS forces and moments converge as the number of strips is increased. The data in Figure A-11 and Figure A-12 show that the RMS forces and moments converge to constant values after ten strips and this value was, therefore, adopted. From this observation, it follows that neither the centre of gravity model nor the four-point model would accurately capture the effects of the unsteady airwake.

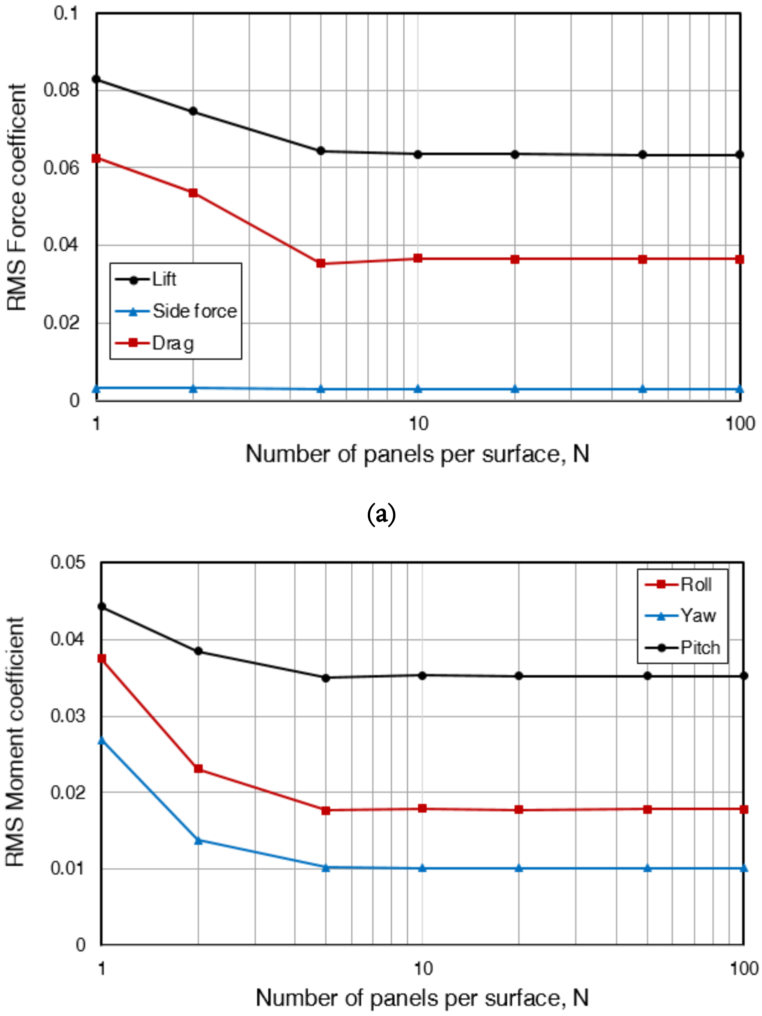

(a)

(b)

Figure A-12 RMS force (a) and moment (b) coefficients for different numbers of strips during hover in a Green 25 WOD.

With N=10, Figure A-13 shows the contribution of each lifting surface to the aircraft's unsteady drag force and yawing moment for 30 seconds in hover above spot 3 in the 35 kts Green 25 WOD condition. The largest contributor to the overall drag is the wing lifting surface, followed by the canard; this is expected because of their larger surface areas. A similar trend can be seen in the yawing moment, with the wing providing a larger contribution to the moment than the canard. The contribution from the two tail fins to the overall drag is small in comparison to the wing and canard but is more significant in the total yawing moment; since the tail is primarily for controlling yaw angle, this influence is expected. Interestingly, the body exerts little influence on either the drag or the yawing moment even in an oblique highly turbulent airflow generated in a Green 25 35 kts wind.

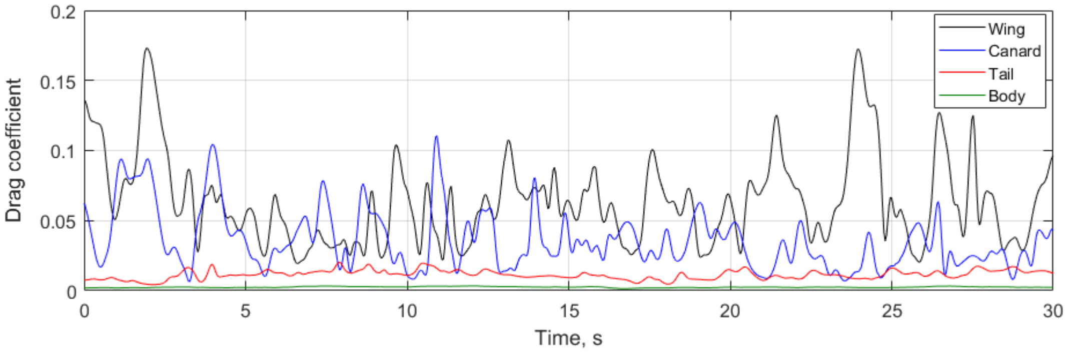

(a)

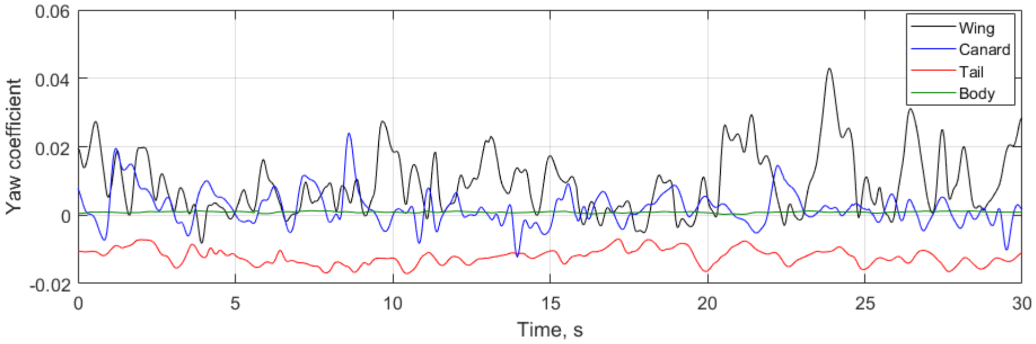

(b)

Figure A-13 Surface contribution to total drag force (a) and yawing moment (b) in a 35 kts Green 25 WOD.

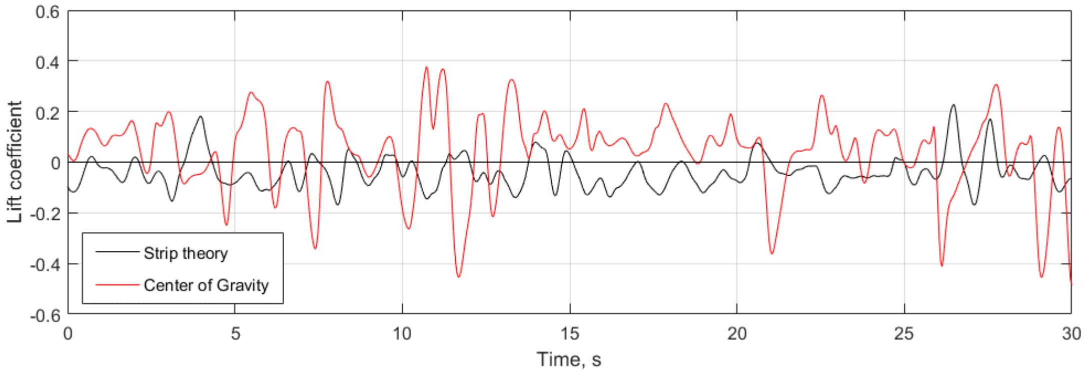

(a)

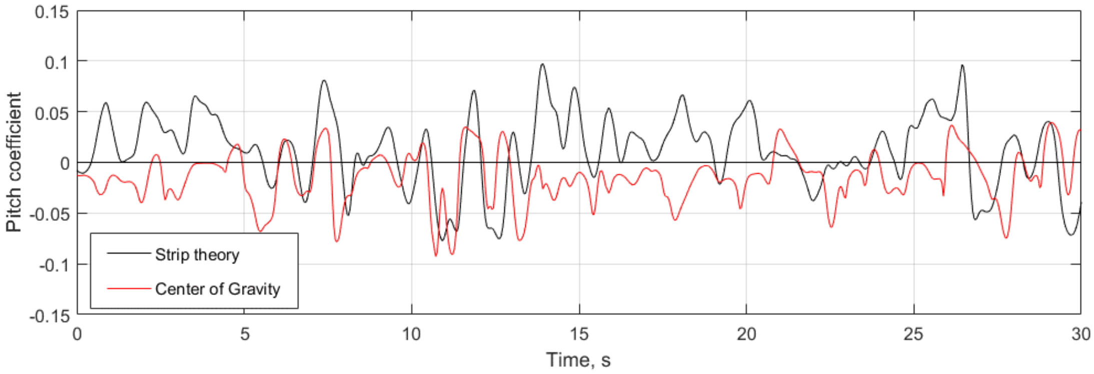

(b)

Figure A-14 Comparison of total unsteady lift force (a) and pitching moment (b) time histories for two aerodynamic modelling methods in a Green 25 wind.

Figure A-14 shows a comparison of the overall lift force and pitching moment acting on the aircraft during hover at spot 3 in a Green 25 wind, computed using both the centre of gravity and strip theory methods. The lift force computed using the centre of gravity method shows larger deviations from the mean value in comparison with the strip theory method; this is consistent with Figure A-12 which shows a larger RMS value at a lower number of strips. The value of lift produced by the centre of gravity model shown in Figure A-14 is predominantly positive with large negative deviations; the lift computed by the strip theory method is mostly negative. In the lower graph in Figure A-14, the pitching moment calculated by the centre of gravity method is generally lower than that calculated by the strip theory method. It can also be seen that between 6 and 12 seconds, the pitching moment computed using the two methods are similar; however, at other time intervals, such as between 12 and 20 seconds, the pitching moments produced by the two methods are dissimilar with a positive pitching moment for the strip theory model and a negative pitching moment for the centre of gravity model.

In the context of the F-35B simulations, it is not known what is included in the flight model aerodynamics; however, it is clear from this study that in order to adequately capture the moments imposed on the aircraft, the centre of gravity model is deficient. It should be noted though, that the F-35B is a very sophisticated aircraft with an advanced flight control system which compensates for aerodynamic disturbances to such a degree that the pilot may not feel them [171]. In terms of extending this research with respect to the effect of ship airwakes on fixed-wing STOVL aircraft, the next step would be to develop a flight model which includes elements such as the aircraft flight controls, propulsion systems, actuators, landing gear and vehicle management systems, however, such an extensive study was beyond the scope of the present research.

A.5 Summary

This Appendix has described the results of an investigation into the effect of unsteady turbulent wakes on a generic STOVL aircraft model where there is a one-way coupling between the air flow and the aircraft. The airwakes were created using CFD for the QEC in a 35 kts wind, from Ahead and Green 25. To capture and investigate the effect of the large temporal and spatial variation in air velocity within an unsteady wake, the generic strip theory method was applied to a STOVL aircraft model using aerodynamic data produced for a concept aircraft reported by NASA. As the aircraft characteristics of the NASA model were limited, each lifting surface on the generic STOVL aircraft was modelled using a VLM method, providing the lift polar for each surface. Due to the nature of the complex three-dimensional flow in the ship's airwake, the lifting surfaces on the aircraft may experience large effective angles-of-attack; to account for this the lift and drag polars were extended to ±180 deg with approximations using data from the aerodynamic characteristics of a flat-plate. The study showed that the aerodynamic perturbations from the QEC airwakes are better represented by a strip theory model, with 10 strips on each surface, than by a single-point centre of gravity model. It was not possible to take this aspect of the research further within the present project, but it is a good starting point for future research into the effect of ship airwakes on fixed-wing aircraft.

Appendix B CFD Computations

Table B-1 CFD computations.

	WOD	Computation	Interpolation
QEC Experimental CFD	H00	Watson	n/a
	G10	Watson	n/a
	G90	Watson	n/a
	R10	Watson	n/a
QEC Full-scale CFD	H00	Kelly	Kelly
	G05	Kelly	Kelly
	G10	Kelly	Kelly
	G25	Kelly	Watson
	G45	Kelly	Watson
	G90	Kelly	Watson
	R05	Kelly	Kelly
	R10	Kelly	Kelly
	R25	Kelly	Kelly
	R45	Kelly	Kelly
	R90	Kelly	Watson
	R135	Watson	Watson
	H180	Kelly	Kelly